X-ray Observations of AGN Masers

Bachelor Thesis at the Chair of Astronomy
of
Maximilian Norbert Günther

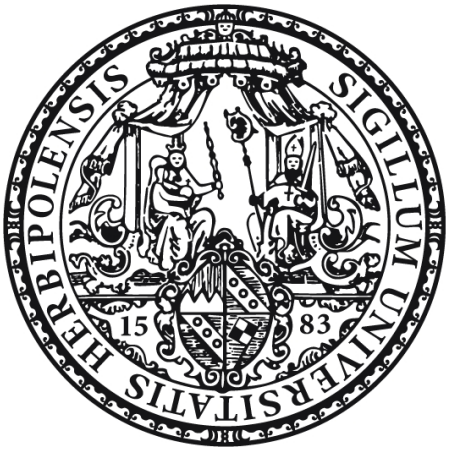

Department of Physics and Astronomy
Julius-Maximilians-University Würzburg
Am Hubland, 97074 Würzburg

Professor in charge
Prof. Dr. Matthias Kadler

24^{th} July 2012

Statement of authorship

I, Maximilian Günther, confirm that the work presented in this bachelor's thesis has been performed and interpreted solely by myself and that information and aids which have been directly or indirectly taken from other sources have been noted as such. Furthermore, I confirm that this work is submitted in partial fulfilment for the degree of Bachelor of Science in Physics at the University of Würzburg and has not been submitted elsewhere in any other form for the fulfilment of any other degree or qualification.

Würzburg, 24$^{\text{th}}$ July 2012

Maximilian Günther

Acknowledgements

My special thanks go to Professor Matthias Kadler, not only for offering me this topic, but also for his personal mentoring and support.

Furthermore, I like to thank Eugenia Litzinger and Felicia Krauss, who have advised me in the work with ISIS and have always been always available for any kind of questions about spectral model fitting.

In the same way I wish to thank Jürgen Walther for the constant exchange on the field of masers during our bachelor's theses.

This research has made use of the XRT Data Analysis Software (XRTDAS) developed under the responsibility of the ASI Science Data Center (ASDC), Italy.

Abstract

We have a lot of unresolved questions left in astronomy. The main question of cosmological research, the expansion of the universe, is still based on very uncertain measurements of the Hubble parameter. Furthermore, different astronomical objects have been studied intensively over the past years, but are still not reliably understood. For example, it is still unclear where Active Galactic Nuclei (AGNs) gain their activity from and what is the origin of their jets. A great possibility for answering those questions about cosmology as well as AGNs is offered by AGN masers.

A maser is the microwave equivalent of the nowadays well known laser, its name stands for "microwave amplification by stimulated emission of radiation". Molecular gas clouds emitting maser radiation are very bright and narrow lined sources of microwave radiation and can be located in AGNs or starforming regions. AGN masers offer successful methods for analyses of the central object, the jet or the nuclear outflow of the hosting AGN. If they appear on the accretion disk cycling around the nucleus, one can estimate its size. Simple methods based on Kepler's laws allow estimations of its mass and consequently of an lower limit for its density. Thereby, masers can give proof of the central object being a black hole. Moreover, they allow direct redshift analyses and reliable distance determinations. With a combination of these values they can even be used for good estimations of the Hubble parameter, which is the main task of the Megamaser Cosmology Project. If they appear as jet masers, an analysis allows to study the jet on milliarcsecond scales and to determine the density and velocity of the jet material. Outflow masers are very rare yet, but they are the first indications for molecular gas in a nuclear outflow and allow detailed studies of the velocities and characteristics of nuclear winds.

Obviously, AGN masers offer a lot of possibilities. However, the restrictive factor is that only a small number of 136 AGN masers have been identified yet. A promising way to detect more of them is their weak correlation with the absorbing hydrogen column density of the hosting AGNs, which can be determined by X-ray spectral analyses. Furthermore, it is still not proofed, whether there is a direct correlation of X-ray and maser luminosity. In order to increase the significance of these results a bigger sample of X-ray covered AGN masers is crucial. Currently only 93 of them have been analysed in the X-ray band.

It is therefore the basic motivation of this bachelor's thesis to contribute some information about the X-ray luminosity and the AGN hydrogen column densities. For this purpose an overview of the present information coverage is given, followed by a detailed analysis of maser hosting AGNs which have not been previously studied in the X-ray band, but have been observed with *Swift*/XRT meanwhile.

Abstract (German translation)

Wir haben viele ungeklärte Fragen in der Astronomie. Die größte Frage der Kosmologie, die Expansion des Universums, basiert noch immer auf recht ungenauen Messungen des Hubble-Paramaters. Zudem gibt es verschiedene astronomische Objekte, die intensiv über die letzten Jahre hinweg untersucht wurden, aber nach wie vor nicht komplett verstanden sind. Zum Beispiel ist weiterhin unklar, woher Aktive Galaxienkerne (AGNs) ihre Aktivität beziehen und was der Ursprung ihrer Jets ist. Eine großartige Möglichkeit diese Fragen sowohl der Kosmologie als auch über AGNs zu beantworten wird durch AGN Maser eröffnet.

Ein Maser ist das Mikrowellen-Äquivalent des heutzutage sehr gut bekannten Lasers, sein Name steht für "microwave amplification by stimulated emission of radiation" (Verstärkung von Mikrowellenstrahlung durch Stimulierte Emission von Strahlung). Jene Molekülgaswolken, die Maserstrahlung emittieren, sind sehr helle und schmallinige Quellen dieser Mikrowellenstrahlung und können entweder in AGNs oder Sternentstehungsgebieten auftreten. AGN Maser wiederum bieten erfolgreiche Methoden für Analysen des zentralen Objekts, des Jets oder des Outflows des beherbergenden AGNs. Falls sie auf der Akkretionsscheibe, die um den Kern kreist, auftreten, kann man dessen Größe abschätzen. Einfache Methoden basierend auf Keplers Gesetzen erlauben Schätzungen für die Masse des zentralen Objekts und demzufolge für eine Untergrenze seiner Dichte. Dadurch kann man mit Masern beweisen, dass es sich bei bestimmten Zentralobjekten um Schwarze Löcher handelt. Weiterhin erlauben sie zugleich direkte Analysen der Rotverschiebung als auch verlässliche Distanzbestimmungen. Durch eine Kombination dieser Größen können sie sogar für gute Abschätzungen des Hubble-Parameters genutzt werden, was das Hauptziel des Megamaser Cosmology Projects ist. Falls sie als Jet Maser auftreten, erlaubt eine Analyse den Jet auf Millibogensekunden-Skalen zu studieren und die Dichte und Geschwindigkeit des Jet Materials herauszufinden. Outflow Maser wiederum sind bisher sehr selten, waren aber die ersten Indikatoren für Molekülgas in einem nuklearen Outflow und erlauben detailierte Studien der Geschwindigkeiten und Charakteristiken von nuklearen Winden.

Offensichtlich eröffnen AGN Maser also zahlreiche Möglichkeiten. Allerdings ist der beschränkende Faktor, dass bisher nur die geringe Anzahl von 136 AGN Masern identifiziert wurde. Ein vielversprechender Weg eine größere Anzahl zu detektieren ist ihre schwache Korrelation mit den absorbierenden Wasserstoff-Säulendichten des beherbergenden AGNs, welche über Röntgenspektralanalysen bestimmt werden können. Außerdem ist es noch immer nicht bewiesen, ob es eine direkte Korrelation zwischen Röntgen- und Maserleuchtkraft gibt. Um die Signifikanz dieser Resultate zu erhöhen ist eine größere Stichprobe an AGN Masern

mit Röntgenbeobachtungen unerlässlich. Derzeit wurden nämlich lediglich 93 von ihnen im Röntgenbereich beobachtet.

Daher ist es die grundlegende Motivation dieser Bachelorarbeit, einige Informationen über die Röntgenleuchtkraft und die AGN Wasserstoff-Säulendichten beizutragen. Aus diesem Grund wird zunächst eine Übersicht über die derzeitige Informationslage gegeben, gefolgt von einer detailierten Analyse derjenigen AGNs, die Maser beherbergen und vorher noch nicht im Röntgenbereich studiert, aber mittlerweile mit *Swift*/XRT beobachtet wurden.

Contents

1. Introduction

Masers are very important astrophysical objects since they are extremely bright radio sources (see e.g. Lo 2005). They can appear in starforming regions, referred to as SF Masers, or nearby Active Galactic Nuclei (AGNs). Such AGN masers can amongst others be setted on the accretion disk cycling around the center of the AGN, which is presumed to be a black hole. In this special formation their radio data can be used to get fundamental information about the massive object in the center, e.g. the redshift, the mass or an upper limit for the size. This data can be used to confirm the current AGN model by providing evidence of the central object being a black hole. One can consequently say that the analysis of masers could help us to reveal some of the most mysterious objects in the universe. Moreover, AGN disk masers can even be helpful to gain a better accuracy of the Hubble parameter, what will lead to a better understanding of cosmology. That is why AGN disk masers are the most important special case of an astrophysical maser. Nevertheless, just a part of astrophysical masers are AGN disk masers and it is often hard to define their type. Therefore it is necessary to find more sources for a better understanding and for more reliable detections of AGN disk masers.

Unfortunately, the maser detection rate is relatively low, even though the Megamaser Cosmology Project has made enormous proceedings in the last years (see e.g. Reid et al. 2009; Braatz et al. 2010; Kuo et al. 2011). Since masers are becoming more and more important in modern astrophysics, it is necessary to find more of them. A promising approach is given by the theory that the X-ray radiation powered by the nucleus is the energy source for the maser emission (Neufeld et al. 1994). In the last years a number of publications studied the connection between AGN X-ray and maser radio luminosities, some of them with good prospects (Kondratko et al. 2006), but it has not been proofed yet (Kandalyan and Al-Zyout 2010). However, a weak correlation of X-ray absorbing hydrogen column densities and maser luminosity has been found (Zhang et al. 2006). AGN megamasers, the brightest AGN masers, are mainly appearing at AGNs with a column density $N_{\mathrm{H}} > 10^{24}\,\mathrm{cm}^{-2}$, referred to as Compton-thick. Upcoming all-sky X-ray surveys like eROSITA (Predehl et al. 2010) can therefore be used to increase the number of maser detections. Additionally, these correlations can also be used the other way around. Radio surveys are less expensive and relatively unbiased compared to X-ray surveys. Hence, ground-based radio surveys of AGN megamasers could be used to find presumably Compton-thick AGNs and thereby help to classify their type (Greenhill et al. 2008). Moreover, the combination of X-ray and radio data complements one another and deeper insights in the nature of AGNs can be drawn in this way. However, a big sample is crucial for the significance of a correlation and the number of AGN masers has increased by nearly a third since the last studies.

Based on that recent research, the main motivation for this bachelor's thesis has been to collect X-ray information for some of the recently detected masers in order to contribute to a more significant correlation of the AGNs' X-ray and the masers' radio data.

This thesis begins in section 2 with an overview of the basic physical principle of a maser and an astrophysical maser in detail. A short excursus follows to introduce the origin areas of masers, namely starforming regions and AGNs. Moreover, the categorization of masers according to their occurrence as well as luminosity is discussed. In this context, the particular importance of AGN disk masers is explained in more detail. Afterwards, the focus is set on the possibilities offered by the combined analysis of X-ray and radio data of AGN masers. This section emphasizes the importance of including X-ray studies for several purposes and can therefore be seen as the main motivation of this bachelor's thesis.

Secondly, in section 3 the currently most important satellites with X-ray telescopes are introduced, namely *Swift*, *XMM-Newton*, *RXTE*, *Chandra* and *Suzaku*. Afterwards, it is shown which 136 AGN disk masers have been identified in the radio band yet. For the 43 ones of them which have not been analysed in the X-ray band before, a HEASARC search for data of the five main X-ray satellites has been performed and the results are given. Moreover, the overlap with hard X-ray observations of *Swift*/BAT is discussed. In the following, the main focus lies on the *Swift*/XRT telescope and it is described, which ways of analysis could be performed for which *Swift*/XRT observation. The different spectral model fitting methods, fitting statistics and the calculation of the standard derivations and upper limits are discussed in more detail and it is summarized which results could be drawn from that work.

Thirdly, section 4 gives a discussion of these results. The different fitting models are compared with one another and the final parameter values are discussed by considering the scientific background, for example the AGN type.

At last, some conclusional words about the theoretical background, the analyses and the results of this bachelor's thesis are given in section 5. Finally, this section ends the thesis with a short outlook on future perspectives.

2. Scientific background

The following sections give a short summary of the basics of masers and AGNs. At first, we look at the physical principles of maser radiation, which was discovered under laboratory conditions. Secondly, we go into the details of astrophysical masers. Thirdly, an excursus about the regions of maser obscuration follows and explains the characteristics of starforming regions and the zoo of AGNs. Next, a categorization of masers according to their appearance is given and the terms mega- and kilomasers are defined. Afterwards, the special importance of AGN disk masers is emphasized by explaining the possibilities they offer. At last the key idea behind this thesis is explained, namely the new perspectives offered by a combination of X-ray and radio analyses of masers.

2.1. Physical principle of a maser

The theoretical phenomenon of a maser was discovered by the American physicist Charles Townes and his assistants James Gordon and Herbert Zeiger in 1951, two years later they presented the first functional ammonia maser (Gordon et al. 1954). The term maser is actually an acronym standing for "microwave amplification by stimulated emission of radiation" (Lo 2005). Thus, it is the microwave equivalent of the nowadays well-known laser, which was actually invented based on the ideas of Townes' maser. The difference is that atoms have gaps between electronic energy orbits in the range of optical light, whereas molecules have not just electronic, but also vibrational, torsional and rotational energy levels. Those have gap energies in the range of microwaves. Typical wavelengths are 21 cm (1.4 GHz) for a H maser, 1.35 cm (22 GHz) for a H_2O maser or 18 cm (1.6 GHz) for an OH maser.

The essential physical principle of a maser is the stimulated emission (Gordon et al. 1954; Lo 2005). The necessary condition for this effect is a local disturbance of the thermal equilibrium, referred to as population inversion. In this case, more molecules are in a semi-stable excited state than in the stable ground state. This can only happen, if the density of the gas is below a critical density, under which the de-excitation due to collisions is negligible. Under laboratory conditions a constant energy pumping is necessary to produce such a non-equilibrated state. Since only selected energy levels may be excited, the pumping has to be selective. Given a population inversion, stimulated emission becomes possible. If then a microwave photon with an energy equal to the gap energy hits an excited molecule, it collapses back to it's ground state by emitting a second, totally coherent photon, as it is illustrated in Figure 1. This process is the reason for the high intensity of maser radiation.

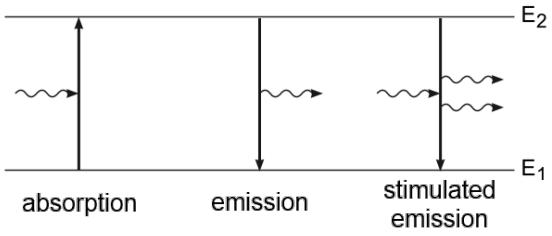

Fig. 1.— Comparative illustration of absorption, emission and stimulated emission processes (University of Goettingen, revised)

2.2. Astrophysical masers

For a long time researchers thought a maser could just work under controlled laboratory conditions, because the population inversion needs a constant and selective energy supply to exist (Lo 2005). In addition, the density and temperature of the gas must have the right values. For example, the temperature of a H_2O maser must exceed 300 K with a gas density between $10^8\,\mathrm{cm}^{-3}$ and $10^{11}\,\mathrm{cm}^{-3}$. An OH maser instead needs a gas temperature of around 160 K at a gas density lower than $10^7\,\mathrm{cm}^{-3}$. It was not conceivable how all those conditions could be satisfied in nature.

Nevertheless, a group of researchers around Alan Barrett discovered the first indications of astrophysical masers in 1963 (Weinreb et al. 1963). His detection of OH molecules in the interstellar medium was of great importance, because the advantages of masers known from laboratory experiments promised new observation possibilities for astronomers (Lo 2005). In fact, the measurement techniques for masers that were developed in the following years confirmed that hope. Especially their high luminosity makes maser sources a helpful instrument for observational astronomy as we will see in section 2.5. Moreover, they are characterized by a very narrow line spectra. The light emitted by the molecules is actually monochromatic, but due to Doppler broadening and the influence of intermediate material the lines are a bit broadened when the spectrum is observed from earth.

2.3. Regions of maser appearance

Masers are related with either starforming regions or AGNs (Lo 2005). A short summary of the main facts about those different areas of maser obscuration is given in the following. At first, some compact information about starforming regions is given. Secondly, AGNs are discussed in more detail, since AGN masers are most useful and the main topic of this thesis.

2.3.1. Starforming regions

Areas of star formation are located inside interstellar clouds and have a high density of molecular gas (Osterbrock 2005). If the pressure gets too high, the gas collapses into plasma, out of which stars can be formed. Famous examples for such clouds are the Orion Nebula or the Eagle Nebula.

2.3.2. Active Galactic Nuclei (AGN)

AGNs are centers of galaxies with a significantly high luminosity in the radio band, up to four orders of magnitude higher than that of normal galaxies (Peterson 1997; Krolik 1998; Kadler 2012). The source of the intense radiation is furthermore concentrated on a scale of less than 1 pc from the center. Considering their emission-line spectra, differences from typical starforming galaxies can be observed. Moreover, star densities in such small regions would get too high and the system would become unstable, before such luminosities could be reached. Hence, the luminosity of AGNs can not be due to stars. That is why generally accepted AGN models assume a supermassive black hole in the center. The reason for the high luminosity can then be described by strong accretion of material leading to intense synchrotron radiation. A dense torus of obscuring dust surrounds the accretion disk. Perpendicular to it a stream of material forms two antisymmetric jets, which can be observed in the radio band. This material has relativistic speed and can be ejected up to a few megaparsec away from the black hole.

Since a lot of questions about AGN are still open, they can not be categorized according to their physical background. Rather, they are defined based on observations, like it is the general case in astronomy. It is often talked of the zoo of AGN, in which AGNs are classified by their radio luminosity, the line width in their spectra and their luminosity (Peterson 1997; Krolik 1998; Kadler 2012). The resulting subclasses are described in the following.

- Seyfert and LINER galaxies

  Seyfert galaxies are described according to their ultraviolet and optical spectra, since they are radio-quiet. Hence, no jets can be observed for them. They are differed in Seyfert 1 and Seyfert 2 types. The former are characterized by broad as well as narrow emission lines. In contrast, Seyfert 2 galaxies have a weaker continuum and, most notably, no broad emission lines. Furthermore, their spectra can show absorption lines from underlying galaxies. Low-Ionization Nuclear Emission Line Region (LINER) galaxies have similar optical spectra to Seyfert 2 types, but an even weaker continuum. All of these three types appear mostly in early type spiral galaxies.

- Quasars/QSOs

  Quasi-Stellar Radio Sources (Quasars), also referred to as Quasi-Stellar Objects (QSOs), always show some radio emission. Nevertheless, usually no jets can be observed. Quasars are mainly radio quiet, less than ten percent of them are identified as radio loud. This is also due to the fact, that they generally have a higher magnitude than Seyfert types, namely $M \lesssim -22$. Apart from that, their optical spectra are similar to that of Seyfert galaxies with weaker absorption features and narrow lines. Analogue to them they are categorized as Type 1 and Type 2 Quasars.

- General Radio-loud galaxies

  Radio-loud AGNs are mainly observed in elliptical galaxies. On the one hand they can be categorized according to their spectral lines, on the other hand depending on their luminosity. If the spectra shows as well broad as narrow lines, they are referred to as Broad Line Radio Galaxies (BLRG), if the broad lines are not observed, as Narrow Line Radio Galaxies (NLRG). These types can be seen as the radio-loud counterparts of Seyfert galaxies. As jets can be observed here, they can furthermore be distinguished according to their jets as well as radio luminosity. If they generally have a low luminosity and as well a jet as a counterjet, they are referred to as Fanaroff-Riley 1 (FR1) types. If they otherwise are very luminous and have a missing counterjet, they are categorized as FR2 galaxies.

- Blazars

  Blazars are also radio-loud galaxies, but they can not be classified as FR1 or FR2, since their luminosity can vary on time scales of down to hours. They can be futhermore categorized in BL Lac Objects and Flat-Spectrum Radio Quasars (FSRQs), depending on their luminosity. BL Lac Objects are named after the first discovered Blazar in the formation Lacerta, which was originally believed to be a variable star, and are not as luminous as FSRQs.

For some AGNs it has turned out to be very difficult to decide as which type they should be classified (Peterson 1997; Krolik 1998; Kadler 2012). This continuum of AGNs gave a first hint, that they all may be based on the same physical structure. The so called unification model, which gives an explanation for the zoo of AGNs, was first proposed by Urry and Padovani (1995). It claims that the different types of AGNs are not due to different physical models, but can be explained by different viewing angles onto the same type of object. An illustration of the connection between the line of sight into the AGN and the observational classification is given in Figure 2.

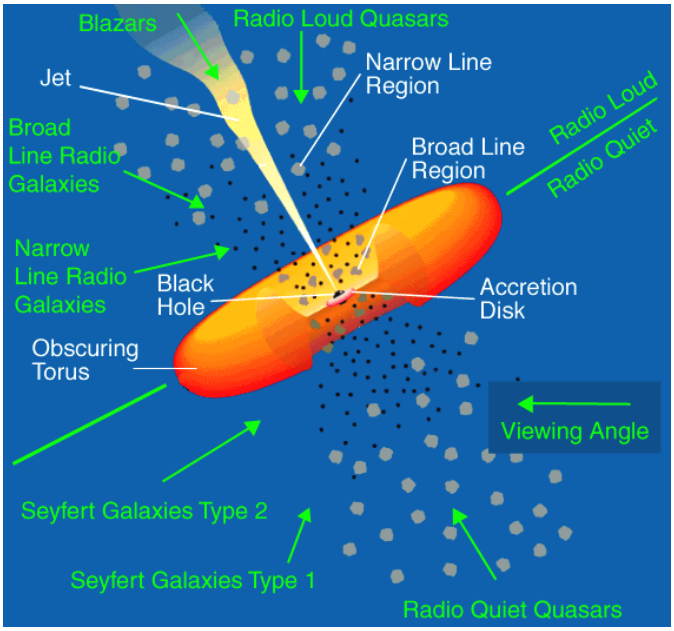

Fig. 2.— Illustration of the unification model for AGNs on logarithmic length scales. The different types of AGNs can be explained by different viewing angles on the same type of object. (Illustration by NASA, adapted from Urry and Padovani 1995)

Above and below the accretion disk the Broad Line Region (BLR) is located (Peterson 1997; Krolik 1998; Kadler 2012). Those areas are heated up by synchrotron radiation due to the black hole. Ionized gas clouds in these areas emit intense radiation while moving at high speeds. That is why the lines are broadened due to Doppler shifts. No broad lines can be observed, when the obscuring torus surrounding the accretion disk lies in the line of sight. The gas clouds in the Narrow Line Region (NLR) are moving at much lower speeds. Hence, the Doppler broadening is negligible and they contribute the narrow lines to the spectra.

For example, one can compare the characteristics of a Seyfert 2 galaxy with Figure 2. Their weak continuum and lack of broad emission lines can be explained by the viewing angle, because there is nearly no radiation of the BLR passing the torus. The other types can be discussed analogue.

2.4. Classification of astrophysical masers

2.4.1. AGN and SF masers

As already mentioned above, astrophysical masers can occur in AGNs, referred to as AGN masers, or in starforming areas, referred to as SF masers. Furthermore, AGN masers can be divided into three subgroups, namely disk masers, jet masers and outflow masers (Lo 2005; Tarchi 2012).

AGN disk masers are the most important subclass, since they can offer a lot of possibilities (Lo 2005; Tarchi 2012). They are located on a circumnuclear rotation disk within a sub-parsec distance to the black hole. Most so far known AGN disk masers show a triple-peak pattern, a so called systemic maser, located in the line of sight, and two maser spots at his sides, which are observed red- and blueshifted due to the rotation velocity of the disk. This alignment is illustrated at the case of the prototype disk maser galaxy NGC 4258 in Figure 3. If the disk is stable and not warped too much it can be seen as a Keplerian disk (Wardle and Yusef-Zadeh 2012). These types offer a lot of possibilities which we therefore want to discuss in more detail in section 2.5. Nevertheless, there are also unstable systems, which could lead to calculation errors and hence are not qualified for determinations. It is unknown yet, how to distinguish those types from each other reliably. An indicator for the stability of the disk seems to be the hydrogen column density. Presumably the disk is unstable, if the AGN is Compton-thick, which means that $N_{\mathrm{H}} > 10^{24}\,\mathrm{cm}^{-2}$. For that reason, it is very important to find out about the column density of the AGN to be able to make reliable calculations based on the disk structure. They can be determined by spectral model fitting of X-ray data, which therefore is one of the main points of this bachelor thesis.

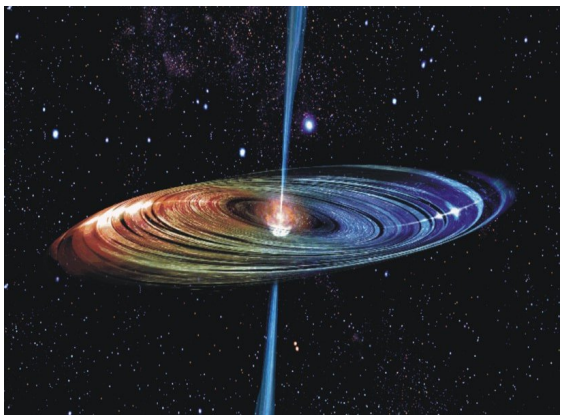

Fig. 3.— Illustration of the accretion disk of NGC 4258. The measured maser spots are charted as very bright spots in the red- and blueshifted areas of the disk as well as in line of sight towards the nucleus (NRAO/AUI and J. Kagaya)

AGN masers are not necessarily cycling around the black hole. They can also occur connected with jets in two different ways (Tarchi 2012). The first model states that the jet interacts with an encroaching gas cloud and thereby directly transfers the necessary energy for maser radiation. A prototypical example for this appearance is Mrk384, which was discussed by Peck et al. (2003). Even with only a small number of epochs it was possible for them to gather important information about the jet itself. They were able to study the jet evolution on milliarcsecond scales and to determine the density as well as shock velocities of the jet material. However, not all jet masers seem to be directly interacting with the jet. In a second model the radio continuum of the jet heats up a foreground gas cloud, which thus becomes a maser source. This seems to be the case for NGC 1052 according to the studies of Sawada-Satoh et al. (2008). Figure 4 shows a radio map of its jet where the two maser spots are marked. Consequently, there is observational evidence for both kinds of scenarios and hence there probably exist two types of jet masers.

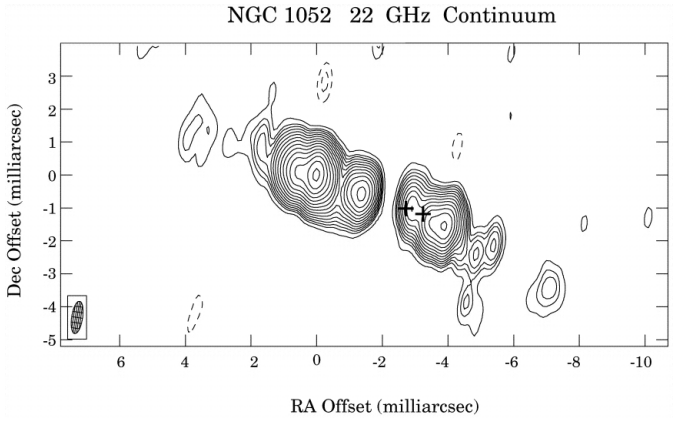

Fig. 4.— Two maser spots (marked with "+") on the jet axis of NGC 1052 (Claussen et al. 1998)

There is just one case of an AGN outflow maser detected yet, namely in the galaxy Circinus (Tarchi 2012). In addition to the sub-parsec disk masers some less dense and cooler spots can be observed at parsec scales in the surrounding torus. Those masers are the first evidence of such material in a nuclear outflow. Thereby, they offered the possibility to determine physical quantities of the nuclear winds.

In contrast to those three AGN maser types, SF masers are not associated with black holes (Lo 2005). They get their energy from starforming processes in interstellar clouds (see section 2.3.1). While AGN masers are concentrated few parsec of the black hole, SF masers are widespread over 100 pc around the center of the starforming region. They can be used for determinations of the chemical composition of the hosting galaxy, for example in order to measure the amount of water as it was done for Arp 220, where the first maser, an OH maser, was discovered.

Fig. 5.— Image of Arp220 with the Hubble Space Telescope (NASA, ESA, and C. Wilson)

Until now, mainly two kinds of extragalactic molecular gases which emit maser radiation are detected, namely H_2O and OH (Zhang et al. 2010; Greenhill 2007; Lo 2005). H_2O masers occur in nearly every case as AGN masers and are strongly connected with Seyfert 2 or LINER galaxies. In contrast, OH masers are preferentially driven by starforming processes, typically located in ultra-luminous infrared galaxies. The reason for this can be seen in the different pumping mechanisms for H_2O and OH masers.

H_2O masers are presumably driven by collisional pumping, which means that collisions of the molecules provide the energy for the population inversion (Lo 2005). That is why it is so important that the gas is not to dense, since otherwise it would be thermalized by the collisions and the population inversion would be destroyed. Additionally, a strong energy source needs to be nearby to drive the pumping, so H_2O masers appear generally in AGNs.

OH masers may also be driven by collisional pumping, but the appropriate density and temperature values do not fit the measured circumstances in the interstellar medium (Lo 2005). Therefore, it is more probable that they are driven by radiative pumping. In this model the molecular gas absorbs infrared radiation, which is consistent with their appearance in ultra-luminous infrared galaxies.

2.4.2. Mega- and kilomasers

Masers show a wide range of luminosity (Lo 2005). Thereby, one can differ between galactic and extragalactic maser sources. Galactic masers have a mean luminosity of $10^{-4}\,L_\odot$, with a few exceptions rising up to a order of magnitude of $10^{-1}\,L_\odot$. In contrast, extragalactic masers typically range from 10^2 to $10^4\,L_\odot$, so they are in average at least 10^6 orders of magnitude more luminous than their galactic equivalents. That is why they are often referred to as megamasers. Nonetheless,

there are also a lot of extragalactic masers which only have a luminosity up to a few $L_\odot$. According to their more luminous equivalents, they are called kilomasers. As maser radiation presumably was stronger in the beginning of the universe, it is probable that there are also gigamasers detectable at high redshifts.

As discussed above, H_2O megamasers need very strong energy sources in close on regions and therefore can normally not be driven by starforming processes. Hence, they are generally AGN masers and thus very good indicators for AGNs. H_2O kilomasers instead can be weaker AGN masers as well as SF masers. Moreover, OH masers are generally weaker sources of radiation, since radiative pumping is not as efficient as collisional pumping (Lo 2005). For that reason they appear in general as kilomasers in starforming regions.

It is important to emphasize the details of the maser taxonomy. AGN masers as well as SF masers can be megamasers as well as kilomasers. In literature it is often simplified written of megamasers, when the special case of AGN masers or even AGN disk masers is meant. That is due to the fact that most works concentrate on megamasers in a disk formation. Even though all kinds of masers can be used for astronomical purposes, we also focus on AGN disk masers in the following chapter, since they offer the greatest advantages for astronomers.

2.5. New Perspectives offered by AGN disk masers

It was already written a lot in the previous sections about the promising possibilities offered by masers and AGN disk masers in particular. The main benefits and calculation methods are explained in the following. For this work simplified approaches are used in order to emphasize the elementary physics underlying the AGN disk maser analysis. The most of the following calculations are therefore based on the assumption of stable non-warped Keplerian disks, so that the basic physical ideas get clear and are not covered by more complex geometrical problems. The referenced sources in each section go into more detail for more complicated structures.

2.5.1. Indicator for supermassive black holes

Black holes are one of the most fascinating objects in the universe, as well for scientists as for the broad public. Since they can not be observed directly, they have kind of a mysterious character. Therefore, one has to use other methods to identify an object as a black hole, for example an indirect mass determination using Kepler's laws. In this connection, it is necessary to have good detectable

objects cycling around the black hole candidate. A very good possibility is offered by circumnuclear gas disks which are sources of intense maser radiation (Miyoshi et al. 1995).

If one knows the radius of the disk maser orbit r, one can easily approach the mass of the black hole candidate at its center (Miyoshi et al. 1995). Assuming the masers rotate on a Keplerian disk around the center with a constant tangential velocity v_{rot}, one can use the balance of centripetal and gravitational forces,

$$\frac{mv_{rot}^2}{r} = \frac{GMm}{r^2}, \tag{1}$$

where G is the gravitational constant, m is the mass of a cycling maser spot and M is the mass of the object in the center. As the radius r is not a directly measured quantity, it can be expressed by $r = D \cdot \tan\Theta$. For small angles Θ and a constant distance D, which both is reasonable for extragalactic sources, this leads to $r \approx D\Theta$ and one gets

$$M = \frac{D\Theta v_{rot}^2}{G}. \tag{2}$$

Combined with Kepler's second law $v_{rot} \propto r^{-1/2}$, the linear dependence of r and Θ leads to the relation $v_{rot} \propto \Theta^{-1/2}$. Therefore, equation (2) is independent of the chosen maser spots and orbits respectively.

Anyway, enormous masses M could not only be explained by black holes, but also by supermassive star clusters. Nevertheless, the latter may be excluded by the combination of M and r (Miyoshi et al. 1995). If the mass density in this area is too high, the stars will hit each other and unbalance the cluster. In such cases, the simple equation (2) is a very good indicator for a black hole in the center of the studied AGN.

2.5.2. Determination of the redshift

For an AGN disk maser the gas clouds rotate around the center of the galaxy like it is shown in Figure 6. The components A are termed as systemic masers, while the components B are termed as red- and blueshifted masers, according to their additional Doppler shift due to the rotation of the disk (see e.g. Lo 2005). However, for the determination of the redshift it is not necessary to observe both kinds of components, but only the systemic masers. Their rotation velocity v_{rot} is not contributing, because it is perpendicular to the recessional velocity of the galaxy. Since we only can measure the line of sight velocity from earth, those velocity components are not contributing. Hence, the cosmological redshift z of

the galaxy can be measured directly using the relation

$$z = \frac{\lambda - \lambda_0}{\lambda}, \tag{3}$$

where λ is the redshifted wavelength of the systemic masers and λ_0 is the original wavelength (Weigert et al. 2009), which is well known from laboratory masers. For low redshifts one can calculate the recessional velocity of the galaxy from its redshift by using the simplified approximation

$$v_{rec} \approx cz, \tag{4}$$

where c is the speed of light. For higher redshifts equation (4) has to be replaced by relations that depend on the chosen cosmological model.

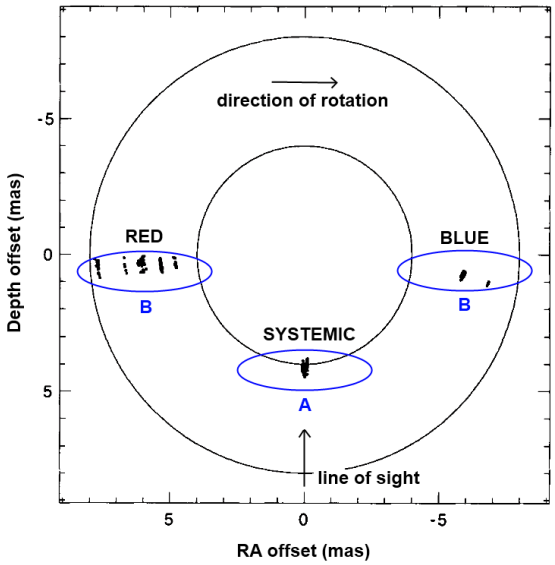

Fig. 6.— Top view of the AGN disk maser NGC4258. The components A are systemic masers, B are red- and blueshifted masers respectively. The x-axis shows the RA offset, which was measured using VLBI technique. The depth offset, which was calculated from measured velocities, is given on the y-axis (Miyoshi et al. 1995, revised)

2.5.3. Distance determination

For the determination of the galaxy's distance from earth D the regions B in Figure 6 are needed (Braatz et al. 2010). One can determine the distance D as

$$D = \frac{r}{\tan \Theta}, \tag{5}$$

in which r again is the radii of the chosen maser orbit and Θ is the corresponding observation angle between the center of the galaxy and the masers. If the galaxy is

far away from earth, a small-angle approximation can be used to linearise equation (5) to the form

$$D = \frac{r}{\Theta}. \tag{6}$$

As done in chapter 2.5.1, one can again use the centripetal acceleration $a = v_{rot}^2/r$ to express r and get the relation

$$D = \frac{v_{rot}^2}{a\Theta}. \tag{7}$$

As we will see in the next section, this formulation of the equation has the advantage that it becomes directly dependent on measurable quantities.

2.5.4. Measurement of Θ and v_{rot}

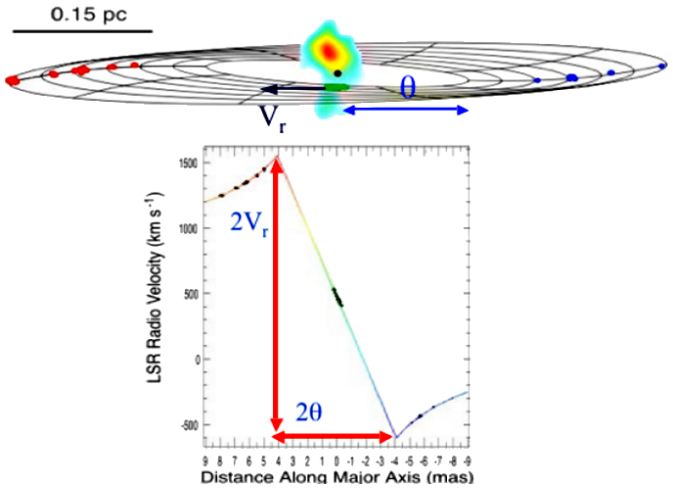

Fig. 7.— Upper graphic: AGN disk maser components cycling around a black hole with the rotational velocity $v_r \equiv v_{rot}$. The observation angle Θ between the black hole and the innermost orbit is illustrated. Bottom graphic: Kepler profile of this disk maser. The x-axis shows Θ as an indicator for the distance of the maser spots to the center in mas. The y-axis shows the Local Standard of Rest velocity in km s^{-1}. (Braatz et al. 2010, revised)

In the sections 2.5.1 and 2.5.3 we have rewritten the equations (2) and (7) to have a dependence on Θ and v_{rot}. The reason is, that both quantities can be determined directly. By measuring the velocities of the single maser spots of the disk, one can generate a Kepler profile, like the one shown in Figure 7 (Herrnstein et al. 1999; Braatz et al. 2010). The LSR velocity is the combination of the recessional velocity, which is determined via equation (4), and the measured rotational velocity component of the specific maser point, which is determined by its Doppler shift. As explained in chapter 2.5.2, only the line of sight components of the rotational velocity are contributing, so $v_{LSR} = v_{rec}$ for systemic masers and $v_{LSR} = v_{rec} + v_{rot} \cdot \sin\Theta$ for red- and blueshifted masers.

In order to gain high local resolution for large distances, radio astronomers use the Very Long Baseline Interferometry (VLBI) (see e.g. Lo 2005). At this technique observations of radio telescopes on the hole globe are computationally correlated, which results in a highly improved resolution. As maser galaxies are mainly observed in the radio band the angles Θ can be measured very precise.

As Figure 7 shows, the rotational velocity v_{rot} and the angle Θ, which are both needed for equations (2) and (7), can then directly be read out of the Kepler profile (Herrnstein et al. 1999; Braatz et al. 2010). That is, why it is practical to rewrite those equations.

2.5.5. Determination of the centripetal acceleration

It is still necessary to determine the centripetal acceleration to be able to derive the galaxy's distance from earth D from equation (7) (Greenhill et al. 1995; Herrnstein et al. 1999; Braatz et al. 2010). In this connection, masers of the regions B in Figure 6 are observed over several years and the measured LSR velocities are plotted over the time as shown in Figure 8.

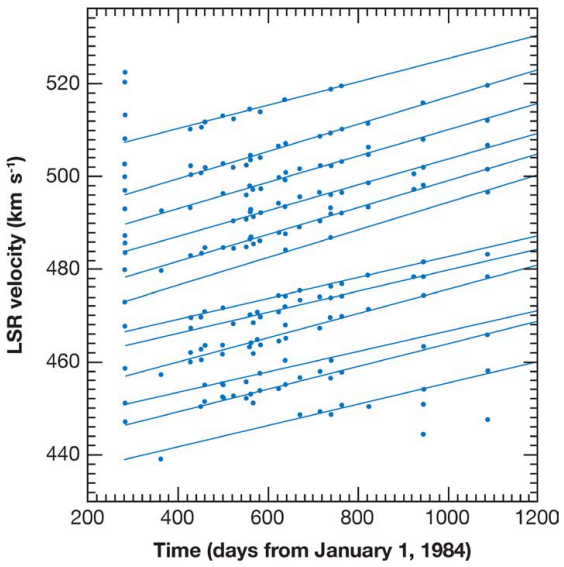

Fig. 8.— LSR velocity of maser spots plotted over time for the prototype AGN disk maser galaxy NGC 4258. (Greenhill et al. 1995, revised by Lo (2005))

Each line in Figure 8 represents the motion of one particular maser spot (Greenhill et al. 1995; Herrnstein et al. 1999; Braatz et al. 2010). At a fixed time, masers which are closer to the black hole have a lower rotational velocity than masers far away. Therefore, the lines can be separated and identified well. Since the recessional velocity is approximately constant over the observed timescales, it means just a constant shift on the y-axis for all points. In Figure 8 masers on

their way from systemic to redshift regions have been plotted, so the rotational velocity and hence the LSR velocity is constantly growing. The gradient of the line of each maser is therefore due to the gradient of v_{rot}, which means it is due to the centripetal acceleration a. Thus, it can be read out of this kind of diagram directly, similar to Θ and v_{rot} in the previous section.

Consequently, all the three parameters a, Θ and v_{rot} can be determined directly and one can use equations (7) and (2) to derive the approximate distance of the galaxy's center from earth as well as its mass.

2.5.6. Determination of the Hubble parameter

As we have seen, masers can be used to determine the redshift as well as the distance of the studied galaxy. Both values are often used as kind of synonyms, since they are strongly correlated (Weigert et al. 2009). They are in first order even linear dependent on each other, connected by the Hubble parameter H_0. It was proposed by Edwin Hubble to describe the expansion of the universe. As it is not a linear expansion as we know nowadays, the Hubble parameter does not have a constant value, but is dependent on the expansion model. Nevertheless, it can be used as a constant for the purposes of this thesis, because it is not changing on human time scales. With known values for the redshift or the recession velocity and the distance from earth, one can determine the Hubble parameter in first order as

$$H = \frac{v_{rec}}{D}. \tag{8}$$

The most recent measured value of the Hubble parameter is $73.8 \pm 2.4\,\mathrm{km\ s^{-1}\ Mpc^{-1}}$ (Riess et al. 2011), provided by observations with the Hubble Space Telescope. However, values differ strongly in dependence of which technique is used for the measurement. Hence, astronomers try to shrink the error bars and obviously AGN disk masers offer very good conditions, as they allow to measure the necessary values for the determination of the Hubble parameter. This is the aim of the Megamaser Cosmology Project (MCP) (Reid et al. 2009; Braatz et al. 2010; Kuo et al. 2011). By determining the Hubble parameter for the galaxy UGC 3789 using the above described maser techniques, they were able to find a value of $69 \pm 11\,\mathrm{km\ s^{-1}\ Mpc^{-1}}$ and want to shrink the error to $< 3\%$ in the following years. Therefore, it is necessary to find at least ten more sources with stable and non-warped disk masers at large distances. The farer the galaxy is away, the more accurate values of the redshift and the distance can be found. The reason is, that the recession velocity is superposed by the proper motion of the galaxy, if the distance is too small. As Hubble's law supposes, objects which are farer away from earth have higher recession velocities. These exceed the proper motions of

the galaxy, if the distance is large enough. A rule of thumb is that the distance from earth has to be at least 30 Mpc for usable results at the determination of the Hubble parameter. Hence, it is necessary for the improvement of the Hubble parameter errors to find a lot of masers with a large enough distance to be able to eliminate the influences of surrounding objects and the proper motion of the galaxy by using statistical approaches. A connection between the X-ray and radio emission, which could be used to increase the detection rates, would in this context be a leap for cosmological research.

2.6. Combination of AGN X-ray and maser radio analysis

There are many good reasons for a combination of an AGN's X-ray information with the radio data of its AGN masers. Each of them can be used for multiple purposes and offers new possibilities for astronomers. The main points are shortly listed in the following in order to get a quick overview.

- Combined results of X-ray and maser analyses complement one another (Castangia et al. 2010).
- A correlation of maser luminosity and X-ray luminosity has been theoretically expected (Neufeld et al. 1994), but not measured yet (Kandalyan and Al-Zyout 2010).
- A correlation of maser luminosity and the hydrogen column density has been found (Zhang et al. 2006).

These relationships are the elementary motivation for this bachelor's thesis and shall therefore be discussed in more detail in the following.

2.6.1. Achieving an entire impression of the AGN

We have seen in section 2.5 what new perspectives AGN disk masers offer for astronomy. Focused on the direct information they offer for AGN research, they can be used to proof the existence of black holes and to estimate their size and masses. They can furthermore be used to map the accretion disks, estimate Eddington luminosities and study accretion efficiencies (Greenhill 2007). X-ray analyses on the other hand offer possibilities to estimate the densities of absorbing molecular gas in the line of sight. This allows a direct determination of intrinsic luminosities which are strongly related to the nuclear activity of the AGN (Castangia et al. 2010). A combination of all those informations offers a completed

impression of the AGN, since X-ray and disk maser analyses complement each another. Moreover, these different properties can be used for further studies and conclusions, as it is discussed in the following.

2.6.2. Relationship of AGN X-ray and maser luminosity

Neufeld et al. (1994) have studied the influence of X-ray emission from an AGN on circumnuclear gas clouds. They found out that the X-ray radiation is the energy source for collisionally pumped maser emission. Indeed Kondratko et al. (2006) reported a possible relationship between unabsorbed X-ray luminosity and H_2O maser luminosity, based on a sample of 30 AGN masers covered with X-ray data in the range of $2-10\,\mathrm{keV}$. However, this relationship could not be confirmed by Kandalyan and Al-Zyout (2010), who used a larger sample of 81 AGN masers.

These results are consistent with the study of the luminosity relations with the nuclear mass (Kandalyan and Al-Zyout 2010). Theory expects a correlation of the mass of the nucleus with maser luminosity (Neufeld et al. 1994) on the one hand and with X-ray luminosity on the other hand. This would lead to a direct correlation of both luminosities. Their analyses showed indeed the dependence $L_{\mathrm{H_2O}} \sim M^{0.6}$, though it has not been quadratic, as the theory predicted. In contrast, a correlation of X-ray luminosity and the mass of the nucleus could not be found, so no link of the luminosities can be provided via the mass of the nucleus yet. Therefore, they proposed further studies in theory as well in practice, best with a bigger sample.

2.6.3. Relationship of AGN column density and maser luminosity

It is plausible that a large density of hydrogen in the line of sight amplifies the maser emission, since the effective cross sections for stimulated emission processes increases. Consequently, hydrogen column densities N_{H}, which can be determined with X-ray spectral analyses, are a solid guide for H_2O megamasers[1] as recent analyses proofed. Zhang et al. (2006) studied the correlation of maser appearance and absorbing hydrogen column densities first. They separated their sample of 64 H_2O masers into 13 kilo- and 51 megamasers, but did not distinguish between AGN and SF masers. With these two sub-samples they performed a Kolmogorov-Smirnov test to study whether their column densities are statistically distinguishable. The result was that the column density distributions differ with a minimum confidence

[1] the most luminous masers, mainly appearing in AGNs (see section 2.4)

level of 99.4%. It is therefore as good as certain that they are linked with different parent populations. Nearly all kilomasers were Compton-thin ($N_{\rm H} < 10^{24}\,{\rm cm}^{-2}$), while of the H_2O megamasers 85% are heavily obscured ($N_{\rm H} > 10^{23}\,{\rm cm}^{-2}$) and 50% are even Compton-thick ($N_{\rm H} \geq 10^{24}\,{\rm cm}^{-2}$) (see Figure 9).

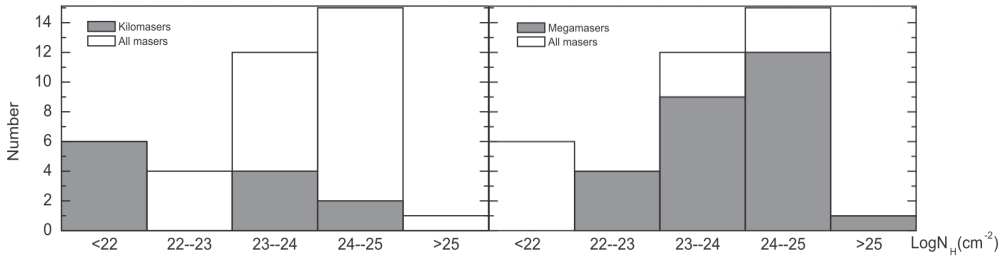

Fig. 9.— Numbers of H_2O kilo- and megamasers as a function of hydrogen column density, adapted from Zhang et al. (2006).

From this point of view column densities can be used as an indicator for masers. With regard to the upcoming eROSITA (Predehl et al. 2010) all-sky X-ray survey this will be an incomparable possibility. eROSITA will launch in 2013 and is expected to discover around 100.000 new X-ray emitting galaxies. Spectral analyses can easily provide estimations for their column densities. It is obvious that a solid guide for megamasers provided by those will help to identify hundreds to thousands of new megamaser galaxies. That would be a giant leap in all matters discussed in the previous sections.

However, the correlation of X-ray and maser luminosity figured out by Zhang et al. (2006) was only weak. They presumed three reasons for this. A clumpy cloud structure of the maser gas, variable positions of masers and nuclear sources as well as different amplifications of background sources could all be influencing factors which decorrelate the dependence. It is commonly known that a weak correlation only can gain significance by increasing the size of the sample.

In 2008 already 104 AGN masers were identified, 42 of them covered with column density data. Therefore, Greenhill et al. (2008) used the bigger sample for a further study. Based on the work of Madejski et al. (2006)[2], they distinguished three more homogeneous sub-samples, AGN masers, AGN disk masers and general megamasers. They found out that 95% of AGN masers, all disk masers and 87% of general megamasers were heavily obscured. Moreover, 60% of AGN masers, 76% of disk masers and 58% of megamasers were even Compton-thick (see Table 1).

Current research showed also another point, why estimations of column den-

[2]Madejski et al. (2006) studied the correlation of column densities and maser luminosity at the same time as Zhang et al. (2006), but focused on a sub-sample of solely AGN disk masers. They found out that eight of eleven disk masers were Compton-thick.

Table 1: Reults of Greenhill et al. (2008)

Sample	$> 10^{23}\,\mathrm{cm}^{-2}$	$\geq 10^{24}\,\mathrm{cm}^{-2}$	No.
Disk masers	100%	76%	21
All AGN masers	95%	60%	42
Megamasers	87%	58%	31

sities can get important. Presumably the accretion disk gets unstable, if the AGN is Compton-thick (Wardle and Yusef-Zadeh 2012). Analyses of masers setted on such a disk could produce a lot of errors. In return, this would mean that according to the statistics of Greenhill et al. (2008) one fourth of all AGN disk masers could be used for reliable analyses. It is therefore even more important to find out about the column densities and study their relationship with the stability of the AGNs accretion disk, in order to make predictions which disk masers give access to reliable data.

As Elitzur (1982) has discussed, maser emission needs large reservoirs of molecular gas along the line of sight. A consequence is therefore that maser hosting AGNs might mainly be type 2 AGNs, such as for example Seyfert 2 galaxies. If one looks on top of the accretion disk, there is only a thin gas disk for maser amplification in the direction perpendicular to the disk. If one looks from the side at the disk, there can be amplification by a deeper structure of gas and stimulated emission can process over longer ways. Furthermore, with the obscuring gas torus in the line of sight, a large reservoir of molecular gas is additionally available. Consequently, one might use the corellation of maser luminosity and column density the other way around. Megamaser emission in AGNs might be seen as an indicator for the AGN type. This is also a point which would be worth further studies.

2.6.4. Outlook of a combined analyses and motivation of this thesis

As mentioned above, the sample size is crucial for significant correlations. Meanwhile, 136 AGN masers have been clearly identified as such. As we will discuss in detail in section 3.2, many of them are still not covered with X-ray information. It is therefore indispensable to complete the X-ray data for AGN masers, which is the basic motivation of this work. However, it is unfortunately beyond the scope of a bachelor's thesis to do so for all of them and hence the focus lies on the ones for which *Swift*/XRT data has been available.

3. Data, analysis and results

3.1. X-ray Telescopes

In this thesis X-ray data for the not previously studied maser hosting AGNs has been used for spectral model fitting with the purpose of finding the photo indices, fluxes and absorbing hydrogen column densities of the AGNs. The first step was to look up for which of them X-ray data was available. This research was done for the currently most important X-ray satellites *Swift*, *XMM-Newton*, *RXTE*, *Chandra* and *Suzaku*. Therefore, these five are shortly introduced in the following, whereat the focus lies on *Swift*, since the analysis of its data is the main point of this bachelor thesis.

3.1.1. Swift

The satellite *Swift* (Gehrels et al. 2004) was launched in 2004 and planned for an orbital life of seven years. However, it will probably be in work until 2016, according to the last review of the NASA (Boggs et al. 2012). Its main task is the study of Gamma Ray Bursts (GRBs), so it has to react very fast in order to observe the GRBs as long as possible. That is where its name comes from. Since *Swift* data is used for the analyses in this bachelor's thesis, its three telescopes are discussed in more detail in the following[3].

- Burst Alert Telescope (BAT)
  BAT can detect X-rays from $15-150\,\mathrm{keV}$ with his Photon Counting detector. Since its field of view is $2.0\,\mathrm{sr}$, which is around a sixth of the sky, it can be used for all sky surveys and detects more than 100 GRBs per year with an location accuracy of $1-4\,\mathrm{arcmin}$. When BAT has recognised a GRB, the other two telescopes will automatically aim that point and take more precise observations.

- X-ray Telescope (XRT)
  XRT has an energy range from $0.2-10\,\mathrm{keV}$. In contrast to BAT, its field of view is $23.6 \times 23.6\,\mathrm{arcmin}$, what therefore leads to a position accuracy of $3-5\,\mathrm{arcsec}$. Its aim is to observe the fluxes, spectra and lightcurves of a GRB and its afterglow, wherefore XRT has a sensitivity limit down to $2 \cdot 10^{-14}\,\mathrm{erg\ cm^{-2}\ s^{-1}}$. XRT can automatically switch between three detector modes, which makes it very adjustable (see also Godet et al. 2007). The

[3]additional data has for the following been taken from NASA's Swift Fact Sheet, online at `http://swift.gsfc.nasa.gov/docs/swift/about_swift/Sci_Fact_Sheet.pdf`

Photon Counting mode works for lower count rates and offers 2-D spatial information by a time resolution of 2.5 s. Windowed Timing can be used at moderate count rates and gives 1-D spatial information by 1.8 ms time resolution. The Photo-diode mode is best at highest count rates, as it offers a 0.14 ms time resolution, but no spatial information. For the analyses performed in this work only the Photon Counting observations have been used.

- Ultraviolet/Optical Telescope (UVOT)
  UVOT takes data in the wavelength range from $170 - 650$ nm. It has a Photon Counting detector, which offers a field of view of 17×17 arcmin with an location accuracy of 0.3 arcsec.

3.1.2. XMM-Newton

The *X-ray Multi-Mirror* satellite (Jansen et al. 2001), referred to as *XMM* or *XMM-Newton*, was launched in 1999 by the European Space Agency (ESA). Its X-ray instrument is constructed for observations in an energy range of $0.1 - 10$ keV and takes pictures with its set of three telescopes, each of them adjusted with 58 Mirrors and a CCD camera. Their combined collection area is $0.4\,\mathrm{m}^2$ and they cover a field of view of 30 arcmin in spectral resolution of around 5 arcsec. In addition, *XMM-Newton* is equipped with the Optical Monitor for observations in the range of $180 - 600$ nm and the Reflection Grating Spectrometer.

3.1.3. Chandra

Named after the astronomer Subrahmanyan Chandrasekhar already before the start, the *Chandra X-ray Observatory* (Weisskopf et al. 2000) was launched in 1999 by the NASA. Its telescopes cover an energy range of $0.08 - 10$ keV and have a way smaller collective area than for example *XMM-Newton*. However, they can reach a spatial resolutions of below 0.5 arcsec, which makes it the best X-ray observatory nowadays.

3.1.4. Suzaku

The japanese satellite *Suzaku* (Mitsuda et al. 2007) was launched in 2005 under the name ASTRO-E2. It is equipped with three telescope types and can cover a total energy range of $0.2 - 600$ keV. At first, there is the Hard X-ray Detector (HXD) and furthermore five sets of the X-ray Telescope (XRT). Thirdly,

four of those sets are also used for the X-ray Imaging Spectrometer (XIS), which operate similar to the photon-counting mode of *Swift*/XRT. In comparison with it, *Suzaku*/XIS covers an slightly wider energy range of $0.2-12\,\mathrm{keV}$ with a smaller field of view of $17.8 \times 17.8\,\mathrm{arcmin}$.

3.1.5. RXTE

The *Rossi X-ray Timing Explorer* (Jahoda et al. 1996), commonly known as *RXTE*, was launched in 1995 and thus is the oldest of the discussed satellites. It took X-ray data for 16 years before it was deactivated by the NASA in January 2012. It was equipped with three instruments, the All-Sky Monitor (ASM), the Proportional Counter Array (PCA) and the High Energy X-ray Timing Experiment (HEXTE). Compared with *Swift*/XRT, the ASM operated in an energy range of $2-10\,\mathrm{keV}$ with a field of view of only $3 \times 5\,\mathrm{arcmin}$.

3.2. Current X-ray information for AGN masers

3.2.1. Overview of all so far identified AGN masers

The original Swift/XRT maser fill-in list contained 93 sources. It was merged with the catalogue published in Zhang et al. (2012) and the online list of Braatz (2012)[4]. Thereby, 43 additional sources have been found which have not been contained in the original fill-in list. That is why these 43 are referred to as "not previously X-ray observed maser sources" in the following. All in all, there are 136 AGN maser sources in the recent completed catalogue, which is shown in Table 2. Since the 93 fill-in list sources were already analysed in the X-ray band, this work wants to focus on the 43 not previously observed sources to contribute to the completion of the X-ray information for AGN masers.

In other works a different sample segmentation is used that shall be introduced in this thesis as well. The 93 fill-in list sources as well as two additional sources published in Zhang et al. (2012) were identified in or before 2008. Hence they are referred to as "old sources". In contrast, additional masers which are solely listed in the online maser list of Jim Braatz (2012) and were discovered mainly after 2008 are accordingly referred to as "new sources". This cataloguing is given in the last column of Table 2. It should be noted that the 43 not previously observed masers consist of 41 new sources and the two old sources from Zhang et al. (2012).

[4]Courtesy Jürgen Walther

Table 2. All 136 currently known AGN masers

Masername	Name	RA	Dec	AGN Type	Dist.	Sub
MASER 000953.6+2555	NGC 23	00 09 53.6	+25 55 23	LINER	60.9	old
MASER 001106.5-1206	NGC 17	00 11 06.5	-12 06 26	Sy2	79.1	old
MASER 001145.2-0054	2MASX J00114518-0054303	00 11 45.2	-00 54 31	Sy2 [a]	191.8	old
MASER 002725.3+4544	2MASX J00272528+4544279	00 27 25.3	+45 44 27		160	new
MASER 004252.8-2332	NGC 235A	00 42 52.8	-23 32 28	Sy1	88.9	old
MASER 004847.1+3157	Mrk 348	00 48 47.1	+31 57 25	Sy2	60.1	old
MASER 005329.9-0846	NGC 291	00 53 29.9	-08 46 04	Sy2 [b]	76.1	old
MASER 010702.2-8018	ESO 013-G012	01 07 02.2	-80 18 28		67.3	old
MASER 011607.2+3305	Mrk 1	01 16 07.2	+33 05 22	Sy2	63.7	old
MASER 012435.1+0347	NGC 520	01 24 35.1	+03 47 33	SBG	30.4	old
MASER 012601.7-0417	2MASX J01260163-0417564	01 26 01.66	-04 17 56.2		75.2	new
MASER 013331.2+3540	NGC 591	01 33 31.2	+35 40 06	Sy2	60.6	old
MASER 013418.2-2925	NGC 613	01 34 18.2	-29 25 07	Sy2	19.7	old
MASER 015951.2-0650	IC 0184	01 59 51.2	-06 50 25	Sy2	70.5	old
MASER 021405.9-0016	2MASX J02140591-0016371	02 14 05.9	-00 16 37	Sy2 [a]	149.4	old
MASER 021703.6 +0517	Mrk 1029	02 17 03.57	+05 17 31.4		121	new
MASER 024104.8-0815	NGC 1052	02 41 04.8	-08 15 21	Sy2,LINER	19.6	old
MASER 024240.7-0000	NGC 1068	02 42 40.7	-00 00 48	Sy2,Sy1	15.2	old
MASER 025040.5+4140	NGC 1106	02 50 40.5	+41 40 17	Sy2	57.8	old
MASER 025329.6-0014	2MASX J02532956-0014052	02 53 29.6	-00 14 06	Sy2 [a]	115	old
MASER 025958.6+3649	Mrk 1066	02 59 58.6	+36 49 14	Sy2	48.1	old
MASER 030349.1-0106	NGC 1194	03 03 49.1	-01 06 13	Sy1.9 [b]	54.3	old
MASER 032448.7-0302	NGC 1320	03 24 48.7	-03 02 32	Sy2	35.5	old
MASER 033646.2 -0750	2MASX J03364614-0750236	03 36 46.16	-07 50 23.6		156.3	new
MASER 033646.4-3600	NGC 1386	03 36 46.4	-36 00 02	Sy2	11.6	old
MASER 033810.4+0114	2MASX J03381036+0114178	03 38 10.4	+01 14 18	Sy2 [a]	159	old
MASER 035000.4 -0127	2MASX J03500035-0127578	03 50 00.35	-01 27 57.7		165	new
MASER 041437.8+0534	MG J0414+0534	04 14 37.8	+05 34 42	QSO1	10836	old
MASER 043703.7 +2456	2MASX J04370366+2456067	04 37 03.67	+24 56 06.8		64.5	new
MASER 043708.3+6637	2MASX J04370825+6637424	04 37 08.26	+66 37 42.3		50.3	new
MASER 044055.0 -0822	IRAS 04385-0828	04 40 54.97	-08 22 22.2	Sy2 [a]	60.4	new
MASER 045252.7+0303	UGC 3193	04 52 52.7	+03 03 24		59.4	old
MASER 050137.8 -0415	Mrk 1089	05 01 37.76	-04 15 28.4	SBG [c]	53.6	new
MASER 050819.7 +1721	CGCG468-002 Ned01	05 08 19.69	+17 21 48.1	Sy2 [b]	70	new
MASER 050950.2+0729	UGC 3255	05 09 50.2	+07 29 00	Sy2	75.6	old
MASER 055542.6 +0323	UGCA 116	05 55 42.63	+03 23 31.8	HII [a]	10.5	new
MASER 061536.3+7102	Mrk 3	06 15 36.3	+71 02 15	Sy2	54	old
MASER 063025.6+6340	VII Zw 073	06 30 25.6	+63 40 41	Sy2	158.7	old
MASER 065008.7+6050	NGC 2273	06 50 08.7	+60 50 45	Sy2	24.5	old
MASER 070421.0 -2135	ESO558-G009	07 04 21.02	-21 35 19.2		102.3	new
MASER 071930.9+5921	UGC 3789	07 19 30.9	+59 21 18	Sy2	43.2	old
MASER 073502.2+3249	NGC 2410	07 35 02.2	+32 49 20	Sy2 [b]	62.4	old
MASER 074241.7+6510	Mrk 78	07 42 41.7	+65 10 37	Sy2	148.5	old
MASER 080019.8+2642	IC 485	08 00 19.8	+26 42 05		111.2	old
MASER 080405.8+0506	Mrk 1210	08 04 05.8	+05 06 50	Sy2,Sy1	53.9	old
MASER 080431.0+3607	SDSS J0804+3607	08 04 31.0	+36 07 18	Sy2	2640	old
MASER 083622.8+3327	2MASX J08362280+3327383	08 36 22.8	+33 27 39	Sy2 [b]	197.5	old
MASER 084338.1+5012	NGC 2639	08 43 38.1	+50 12 20	LINER	44.5	old
MASER 091127.5 -1449	NGC 2781	09 11 27.52	-14 49 00.6		27.4	new
MASER 091246.4 +2304	2MASX J09124641+2304273	09 12 46.38	+23 04 27.3		145.2	new
MASER 091405.1+4006	NGC 2782	09 14 05.1	+40 06 49	Sy1,SBG	34.2	old
MASER 091902.2+2616	NGC 2824	09 19 02.2	+26 16 12	Sy?	36.8	old
MASER 093106.7+4904	SBS0927+493	09 31 06.7	+49 04 47	LINER	136.5	old
MASER 093551.6+6121	UGC 5101	09 35 51.6	+61 21 11	LINER,Sy1.5	157.5	old
MASER 094036.4+0334	Mrk 1419	09 40 36.4	+03 34 37	LINER [b]	65.8	old
MASER 094308.6-1023	NGC 2979	09 43 08.6	-10 23 00	Sy2	36.3	old
MASER 094525.8-1822	NGC 2989	09 45 25.8	-18 22 36	H II	55.6	old
MASER 095929.5-2249	NGC 3081	09 59 29.5	-22 49 35	Sy2 [a], Sy1h [b]	31.9	old
MASER 100157.8+5540	NGC 3079	10 01 57.8	+55 40 47	Sy2,LINER	15	old
MASER 101150.6 -1926	2MASX J10115058-1926436	10 11 50.58	-19 26 43.9		107.4	new
MASER 101355.1+3850	NGC 3160	10 13 55.1	+38 50 34		92.3	old
MASER 101618.7-3333	IC 2560	10 16 18.7	-33 33 50	Sy2	39	old
MASER 102751.3 -4354	NGC 3256	10 27 51.3	-43 54 14		37.4	new
MASER 103138.9 +2559	UGC 5713	10 31 38.87	+25 59 02.3		84.2	new
MASER 103408.6+6001	Mrk 34	10 34 08.6	+60 01 52	Sy2 [b]	201.9	old
MASER 104823.4-2509	NGC 3393	10 48 23.4	-25 09 43	Sy2	50	old
MASER 110048.0+1043	UGC 6093	11 00 48.0	+10 43 41		144.4	old
MASER 110338.4 -0052	2MASX J11033836-0052081	11 03 38.36	-00 52 08.5	Sy2 [b]	114.5	new
MASER 110933.2 +2837	2MASX J11093314+2837393	11 09 33.15	+28 37 39.5		152.3	new
MASER 111131.0 +5540	NGC 3556	11 11 31.0	+55 40 27	H II	9.3	old
MASER 111604.7 -7612	NGC 3620	11 16 04.7	-76 12 59		22.4	new
MASER 111700.1 +3235	CGCG 185-028	11 17 00.12	+32 35 50.6		139.4	new
MASER 111821.3 +4544	NGC 3614	11 18 21.32	+45 44 53.6		31.1	new

Table 2—Continued

Masername	Name	RA	Dec	AGN Type	Dist.	Sub
MASER 112831.9+5833	Arp 299	11 28 31.9	+58 33 45	SBG	41.6	old
MASER 113557.3+7032	NGC 3735	11 35 57.3	+70 32 09	Sy2	35.9	old
MASER 113808.0+1111	CGCG 068-013	11 38 08.0	+11 11 47		142.8	old
MASER 113901.7-3744	NGC 3783	11 39 01.7	-37 44 19	Sy1.5 [b]	38.9	old
MASER 114945.7+5031	CGCG 268-089	11 49 45.7	+50 31 37		105.7	old
MASER 120204.6 +3519	2MASX J12020465+3519173	12 02 04.62	+35 19 18.1		136	new
MASER 120224.0 +1450	UGC 7016	12 02 23.98	+14 50 37.1		96.9	new
MASER 120309.6+4431	NGC 4051	12 03 09.6	+44 31 53	Sy1.5	9.3	old
MASER 121032.6+3924	NGC 4151	12 10 32.6	+39 24 21	Sy1.5	13.3	old
MASER 121409.5 +5431	NGC 4194	12 14 09.5	+54 31 37	H II [a]	33.3	new
MASER 121826.5 +2948	NGC 4253	12 18 26.51	+29 48 46.3	Sy1 [d]	51.7	new
MASER 121857.5+4718	NGC 4258	12 18 57.5	+47 18 14	Sy1.9,LINER	6	old
MASER 122024.0+1450		12 20 24.0	+14 50 37			old
MASER 122112.9+1822	NGC 4293	12 21 12.9	+18 22 57	LINER	11.9	old
MASER 122546.7+1239	NGC 4388	12 25 46.7	+12 39 44	Sy2	33.7	old
MASER 123408.5+0239	NGC 4527	12 34 08.5	+02 39 14	LINER	23.1	old
MASER 124237.4 +1421	NGC 4633	12 42 37.4	+14 21 26		3.9	new
MASER 125559.9 -0804	2MASX J12555984-0804329	12 55 59.86	-08 04 33.6		53.4	new
MASER 125640.5-4655	ESO 269-G012	12 56 40.5	-46 55 34	Sy2	66	old
MASER 130125.2+2918	NGC 4922	13 01 25.2	+29 18 50	Sy2,LINER	94.1	old
MASER 130527.5-4928	NGC 4945	13 05 27.5	-49 28 06	Sy2	7.5	old
MASER 130706.0 -2340	NGC 4968	13 07 05.98	-23 40 37.3	Sy2 [b]	39.4	new
MASER 132952.7+4711	M 51	13 29 52.7	+47 11 43	Sy2	6.2	old
MASER 133817.2+4816	NGC 5256	13 38 17.2	+48 16 32	Sy2,SBG	112.3	old
MASER 134640.8+5228	SBS 1344+527	13 46 40.8	+52 28 37	Sy2 [b]	116.8	old
MASER 135317.8+3329	NGC 5347	13 53 17.8	+33 29 27	Sy2	31.1	old
MASER 135535.9 +0553	2MASX J13553592+0553050	13 55 35.91	+05 53 04.7		156.8	new
MASER 135628.7+6437	MCG+11-17-010	13 56 28.7	+64 37 43	Sy2	126.1	old
MASER 140838.3 -2934	ESO 446-G018	14 08 38.28	-29 34 19.3		63.6	new
MASER 141223.3-2706	NGC 5495	14 12 23.3	-27 06 29	Sy2	89.8	old
MASER 141309.3-6520	Circinus	14 13 09.3	-65 20 21	Sy2	6	old
MASER 141314.8-0312	NGC 5506	14 13 14.8	-03 12 27	Sy1.9	24.7	old
MASER 143240.8-4410	NGC 5643	14 32 40.8	-44 10 29	Sy2	16	old
MASER 143753.3 -0023	NGC 5691	14 37 53.3	-00 23 56	H II [a]	24.9	new
MASER 144223.9-1715	NGC 5728	14 42 23.9	-17 15 11	Sy2	37.2	old
MASER 144536.8 +2702	CGCG 164-019	14 45 36.8	+27 02 05	Sy1.9 [b]	119.5	new
MASER 145700.7+2437	UGC 9618B	14 57 00.7	+24 37 03	LINER	134.6	old
MASER 145835.5+4453	UGC 9639	14 58 35.5	+44 53 06		144	old
MASER 145924.7-1641	NGC 5793	14 59 24.7	-16 41 36	Sy2	46.5	old
MASER 152019.6+5253	2MASX J15201964+5253560	15 20 19.6	+52 53 56		148.9	old
MASER 153916.7 +2427	UGC 9954	15 39 16.7	+24 27 18		137.5	new
MASER 160703.9+0106	2MASX J16070391+0106296	16 07 03.9	+01 06 29		109.5	old
MASER 163032.6+3923	2MASX J16303265+3923031	16 30 32.6	+39 23 03	Sy2 [b]	122.1	old
MASER 163040.9+3029	CGCG 168-018	16 30 40.92	+30 29 19.6		146.9	new
MASER 165258.9+0224	NGC 6240	16 52 58.9	+02 24 03	Sy2	99.5	old
MASER 165716.1+2750	NGC 6264	16 57 16.1	+27 50 59	Sy2	135.7	old
MASER 165815.5+3923	2MFGC 13581	16 58 15.5	+39 23 29	Sy2 [b]	137.2	old
MASER 171018.1 +1344	2MASX J17101815+1344058	17 10 18.1	+13 44 06		126	new
MASER 171318.0+4346	NGC 6323	17 13 18.0	+43 46 56	Sy2	103.6	old
MASER 171659.5-6249	NGC 6300	17 16 59.5	-62 49 14	Sy2	14.8	old
MASER 183820.3-6525	ESO 103-G35	18 38 20.3	-65 25 42	Sy2	53.1	old
MASER 193938.9-0124	2MASX J19393889-0124328	19 39 38.9	-01 24 33		82.5	old
MASER 195215.8+0230	3C403	19 52 15.8	+02 30 24	FR II	235.9	old
MASER 203306.1-0201	NGC 6926	20 33 06.1	-02 01 39	Sy2	79.6	old
MASER 210911.4 -0147	UGC 11685	21 09 11.4	-01 47 54.9		78.3	new
MASER 211129.1 +0503	IC 1361	21 11 29.1	+05 03 15.6		52.8	new
MASER 214457.3 1534	2MASX J21445731+1534503	21 44 57.29	+15 34 50.0		121.8	new
MASER 220117.1-3746	AM 2158-380 NED02	22 01 17.1	-37 46 24	Sy2	128.8	old
MASER 222912.5-1810	TXS 2226-184	22 29 12.5	-18 10 47	LINER	99.9	old
MASER 230456.7+1219	NGC 7479	23 04 56.7	+12 19 22	Sy2	31.7	old
MASER 231925.1+0554	IC 1481	23 19 25.1	+05 54 22	Sy2	81.6	old
MASER 233716.5 +3148	MCG+05-55-041	23 37 16.45	+31 48 02.6		124.7	new
MASER 235544.2 +3012	CGCG498-038	23 55 44.2	+30 12 44	Sy2 [b]	123.2	new

Note. — **Column 1**: maser nomenclature. **Column 2**: name of the object. **Column 3**: right accession in h, m, s. **Column 4**: declination in $deg, arcm, arcs$. **Column 5**: Type of nuclear activity. SBG: starburst galaxy; Sy1, Sy1h, Sy1.5, Sy1.9, Sy2: Seyfert types; LINER: low-ionization nuclear emission line region; ULIRG: ultra luminous infrared galaxy; FR: Fanaroff-Riley Types; H II: Dwarf galaxy with a large number of starforming regions. **Column 6**: The galaxy's distance from earth in Mpc. Therefore the redshift z was taken from the NED. The distance was then derived by $D = cz/H_0$ with $H_0 = 75\,\mathrm{kms}^{-1}\mathrm{Mpc}^{-1}$ and $c = 299792458\,\mathrm{ms}^{-1}$. **Column 7**: Classification according to its sub-sample.

References. — Old sources: Zhang et al. (2012). New sources: Braatz (2012). Galaxy types which were not already given in these references: a) SIMBAD; b) Véron-Cetty and Véron (2006); c) Balzano (1983); d) Contini et al. (1998).

3.2.2. Available Xray-data for the 43 not previously observed sources

The above-mentioned 43 not previously observed sources are separately listed in Table 3. In addition to their catalogued names our specific maser nomenclature, which is based on their coordinates, is listed. Table 3 also gives an overview of the five main X-ray telescopes and shows which one has collected data for which AGN maser galaxy so far, including the total exposure time. This overview of available X-ray data was composed on the basis of NASA's High Energy Astrophysics Science Archive Research Center (HEASARC). In addition to the X-ray observations for each of the new sources the signal-to-noise ratio (SNR) of the available *Swift*/BAT observations[5] is listed. This column is also due to the following combined analysis of soft and hard X-ray data (see section 3.6).

The penultimate line of Table 3 sums up the total number of observations and exposure time that were made for any of the new sources by the particular instrument. In the bottom line it is shown which telescope observed how many of the 43 AGN maser sources. The results can be taken from Table 3 as well. Obviously *Swift*/XRT has seemed to cover the most sources in contrast to the other telescopes, which has made an analysis of its sample promising. However, further studies of the detectors sky images (see section 3.3.2) have shown that for six of these observations *Swift*/XRT's field of view has been overestimated by the default HEASARC search offset. Accordingly, these have been crossed out in Table 3 since they have to be rated as not detected.

All in all there is X-ray data for 17 out of these 43 AGN masers currently listed in HEASARC, already considering the crossed out *Swift*/XRT values. Anyway, some of it has furthermore not been observed long enough for an usable analysis or has not been in the field of view of the other telescopes either, since the HEASARC search offset may be larger than the radii the respective telescopes could cover. In section 3.3.2 it is discussed in detail which of the listed *Swift*/XRT observations have been analysable. Such a discussion will be necessary for further studies of the other telescopes' data as well.

[5]Courtesy Jack Tuller

Table 3. X-ray data for the 43 not previously observed sources

Masername	Name	Search coordinates	#XRT[1]	T_{XRT}[2]	#XMM[3]	T_{XMM}[4]	#RXT[5]	T_{RXT}[6]	#Cha[7]	T_{Cha}[8]	#Suz[9]	T_{Suz}[10]	BAT SNR[11]
new sources[a]													
MASER 002725.3+4544	J0027+4544	00 27 25.3 +45 44 27	0	0	0	0	3	0+?	0	0	0	0	-0.76
MASER 012601.7-0417	J0126-0417	01 26 01.66 -04 17 56.2	0	0	0	0	0	0	0	0	0	0	-1.3
MASER 021703.6+0517	Mrk 1029	02 17 03.57 +05 17 31.4	~~1~~	~~5463.135~~	0	0	0	0	0	0	0	0	-0.33
MASER 033646.4-3600	J0336-0750	03 36 46.16 -07 50 23.6	0	0	0	0	0	0	0	0	0	0	0.48
MASER 035000.4-0127	J0350-0127	03 50 00.35 -01 27 57.7	0	0	0	0	0	0	0	0	0	0	3
MASER 043703.7+2456	J0437+2456	04 37 03.67 +24 56 06.8	0	0	0	0	0	0	0	0	0	0	0.03
MASER 043708.3+6637	J0437+6637	04 37 08.26 +66 37 42.3	0	0	0	0	0	0	0	0	0	0	0.69
MASER 044055.0-0822	IRAS 04385-0828	04 40 54.97 -08 22 22.2	~~1~~	~~10756.1~~	0	0	2	2160	0	0	0	0	1.78
MASER 050137.8-0415	Mrk 1089	05 01 37.76 -04 15 28.4	6	28001.709	0	0	0	0	1	36040	0	0	1.46
MASER 050819.7+1721	CGCG 468-002 NED01	05 08 19.69 +17 21 48.1	4	13759.92	0	0	0	0	0	0	0	0	9.25
MASER 055542.6+0323	UGCA 116	05 55 42.63 +03 23 31.8	2	5275.058	0	0	0	0	0	0	0	0	-0.43
MASER 070421.0-2135	ESO558-G009	07 04 21.02 -21 35 19.2	~~1~~	~~603.706~~	0	0	0	0	0	0	0	0	-0.11
MASER 091127.5-1449	NGC 2781	09 11 27.52 -14 49 00.6	3	10929.21	0	0	0	0	0	0	0	0	-1.2
MASER 091246.4+2304	J0912+2304	09 12 46.38 +23 04 27.3	0	0	0	0	0	0	0	0	0	0	-0.45
MASER 101150.6-1926	J1011-1926	10 11 50.58 -19 26 43.9	0	0	0	0	0	0	0	0	0	0	-0.64
MASER 102751.3-4354	NGC 3256	10 27 51.3 -43 54 14	0	0	3	156277	0	0	2	55730	0	0	0.73
MASER 103138.9+2559	UGC 5713	10 31 38.87 +25 59 02.3	~~4~~	~~3705.877~~	0	0	0	0	0	0	0	0	2.2
MASER 110338.4-0052	J1103-0052	11 03 38.36 -00 52 08.5	0	0	0	0	0	0	0	0	0	0	-0.76
MASER 110933.2+2837	J1109+2837	11 09 33.15 +28 37 39.5	0	0	0	0	0	0	1	27680	0	0	2.9
MASER 111604.7-7612	NGC 3620	11 16 04.7 -76 12 59	0	0	0	0	0	0	0	0	0	0	0.07
MASER 111700.1+3235	CGCG 185-028	11 17 00.12 +32 35 50.6	0	0	0	0	0	0	0	0	0	0	0.16
MASER 111821.3+4544	NGC 3614	11 18 21.32 +45 44 53.6	~~2~~	~~10178.501~~	0	0	0	0	0	0	0	0	-0.69
MASER 120204.6+3519	J1202+3519	12 02 04.62 +35 19 18.1	0	0	0	0	0	0	0	0	0	0	0.96
MASER 120224.0+1450	UGC 7016	12 02 23.98 +14 50 37.1	4	12148.975	0	0	0	0	0	0	0	0	-0.5
MASER 121409.5+5431	NGC 4194	12 14 09.5 +54 31 37	0	0	0	0	0	0	1	35960	0	0	0.35
MASER 121826.5+2948	Mrk 766 / NGC 4253	12 18 26.51 +29 48 46.3	56	148557.21	15	754492	773	843437+?	3	102730	2	157232.8	15.32
MASER 124237.4+1421	NGC 4633	12 42 37.4 +14 21 26	0	0	3	135858	0	0	0	0	0	0	-0.07
MASER 125559.9-0804	J1255-0804	12 55 59.86 -08 04 33.6	0	0	0	0	0	0	0	0	0	0	2.3
MASER 130706.0-2340	NGC 4968	13 07 05.98 -23 40 37.3	0	0	2	26176	0	0	0	0	1	39050.8	2.72
MASER 135535.9+0553	J1355+0553	13 55 35.91 +05 53 04.7	0	0	0	0	0	0	0	0	0	0	1.29

Table 3—Continued

Masername	Name	Search coordinates	#XRT[1]	$T_{\rm XRT}$[2]	#XMM[3]	$T_{\rm XMM}$[4]	#RXT[5]	$T_{\rm RXT}$[6]	#Cha[7]	$T_{\rm Cha}$[8]	#Suz[9]	$T_{\rm Suz}$[10]	BAT SNR[11]
MASER 140838.3-2934	ESO 446-G018	14 08 38.28 -29 34 19.3	0	0	0	0	0	0	0	0	0	0	-0.1
MASER 143753.3-0023	NGC 5691	14 37 53.3 -00 23 56	0	0	0	0	0	0	1	15050	0	0	0.07
MASER 144536.8+2702	CGCG 164-019	14 45 36.8 +27 02 05	1	9513.128	0	0	0	0	0	0	0	0	5.07
MASER 153916.7+2427	UGC 9954	15 39 16.7 +24 27 18	0	0	0	0	0	0	0	0	0	0	0.41
MASER 163040.9+3029	CGCG 168-018	16 30 40.92 +30 29 19.6	~~11~~	~~11468.732~~	0	0	0	0	0	0	0	0	0.08
MASER 171018.1+1344	J1710+1344	17 10 18.1 +13 44 06	0	0	0	0	0	0	0	0	0	0	1.19
MASER 210911.4-0147	UGC 11685	21 09 11.4 -01 47 54.9	0	0	0	0	0	0	0	0	0	0	-0.17
MASER 211129.1+0503	IC 1361	21 11 29.1 +05 03 15.6	0	0	0	0	0	0	0	0	0	0	0.15
MASER 214457.3+1534	J2144+1534	21 44 57.29 15 34 50.0	0	0	0	0	0	0	0	0	0	0	2.74
MASER 233716.5+3148	MCG+05-55-041	23 37 16.45 +31 48 02.6	0	0	0	0	0	0	0	0	0	0	-1.33
MASER 235544.2+3012	CGCG498-038	23 55 44.2 +30 12 44	0	0	0	0	0	0	0	0	0	0	0.49
old sources[b]													
MASER 041437.8+0534	MG J0414+0534	04 14 37.8 +05 34 42	0	0	0	0	0	0	7 [+1]	164990 [+30050]	0	0	0.29
MASER 111131.0+5540	NGC 3556	11 11 31.0 +55 40 27	0	0	0	0	0	0	1	60120	1	84164.2	0.56
summarized			**~~96~~ 76**	**~~270361~~ 228182.21**	**23**	**1072803**	**778**	**845597**	**17 [+1]**	**498300 [+30050]**	**4**	**280448**	-
# observed sources			**~~13~~ 7**	-	**4**	-	**3**	-	**8**	-	**4**	-	**9**

Note. — Results of the data search for currently available X-ray observations of the 43 newly identified maser hosting AGNs performed with HEASARC. This table gives a compilation of the total number of epochs for each sources and the corresponding total exposure time. The information was extracted from the different satellite master files provided by HEASARC. Column one shows the maser nomenclature, column two the catalogued name and column three the exact coordinates of the maser source used for the database search. The other columns are explained in the following. (1) # *Swift*/XRT observations (crossed out values have been outside of the actual field of view and therefore have been rejected), taken from *swiftmastr*, (2) *Swift*/XRT total exposure, taken from *swiftmastr* (3) # XMM observations, taken from *xmmmaster* (4) XMM total duration, taken from *xmmmaster* (5) # RXTE observations, taken from *xtemaster* (6) RXTE total exposure ('?' means that no expsoure data was given), taken from *xtemaster* (7) # Chandra observations (numbers given in []-brakets are listed as observed), taken from *chanmaster* (8) Chandra total exposure, taken from *chanmaster* (9) # Suzaku observations, taken from *suzamaster* (10) Suzaku total exposure, taken from *suzamaster* (11) signal-to-noise ratio of *Swift*/BAT for this object, only sources with a SNR > 2 are counted as observed sources in the bottom row

References. — (a) Braatz (2012); (b) Zhang et al. (2012); data search performed with NASA's High Energy Astrophysics Science Archive Research Center (HEASARC)

3.2.3. X-ray and Swift/BAT data overlap for the 43 not previously observed sources

Using Table 3 a comparison of available X-ray data and *Swift*/BAT γ-ray detections was created. Thereby, only *Swift*/BAT observations with a minimum signal-to-noise ratio of two were considered as usable detections. One can draw the following conclusion from Table 3, always considering that not all the listed data may be analysable.

- Three out of the 43 not previously observed sources seem to have *Swift*/XRT observations and a *Swift*/BAT SNR > 2 (MASER 055542.6+0323, MASER 121826.5+2948, MASER 144536.8+2702), one of them seems also to be observed with *XMM-Newton*, *RXTE*, *Chandra* and *Suzaku* (MASER 121826.5 +2948).
- One source seems to have *XMM-Newton* and *Suzaku* observations and a *Swift*/BAT SNR > 2 (MASER 130706.0-2340).
- One source seems to have *Chandra* observations and a *Swift*/BAT SNR > 2 (MASER 110933.2+2837).
- One source seems to have *RXTE* observations, but only a *Swift*/BAT SNR $=$ 1.78 (MASER 044055.0-0822).
- Four sources have no X-ray observations with any of the above named telescopes, but a *Swift*/BAT SNR > 2 (MASER 035000.4-0127, MASER 103138.9 +2559, MASER 125559.9-0804, MASER 214457.3+1534).

All in all there seems to be an overlap of X-ray and BAT data for five or six out of the 43 sources, whether or not the *Swift*/BAT observation with SNR $= 1.78$ is counted. That means that at least five out of the 22 sources observed in the soft X-ray band were also observed with *Swift*/BAT, whereby three of those four have an overlap with *Swift*/XRT data. These circumstances have suggested a *Swift* data analysis even more.

3.3. *Swift*/XRT data

As mentioned and explained in the foregoing sections, this work focuses on the X-ray data collected by *Swift*/XRT for the 43 not previously observed AGN maser sources. Reasons for this were among others the relatively good data coverage for seven of the 43 sources and the largest overlap with *Swift*/BAT detections, namely for three of the 43 sources. Hence, the possibility to combine the analysis with the hard X-ray data taken by *Swift*/BAT has been given.

3.3.1. Preparation and extraction of the raw data

All *Swift*/XRT observations listed in Table 5 were downloaded on the servers of the Dr. Remeis Observatory Bamberg of the Astronomical Institute of the University of Erlangen-Nuremberg. Afterwards, the data was prepared and extracted. Therefore, automatized scripts of Felicia Krauss were rewritten and adapted for this particular sample, since there are different maser sources with each of them having a different number of epochs. The preparation with these scripts covered the loading and converting of the raw data. For the further analysis only the photon counting mode of *Swift*/XRT was used. The script for the automatized extraction of the raw data uses the given search coordinates to determine the center of a circle with a default radius of 20 pixel in the detectors sky image, which should contain all source counts. The background data has been extracted as a ring around that center with a default inner radius of 35 pixel and outer radius of 47 pixel. Thereby, the detector's source counts in the circle and the background counts in the ring are summed up by the extraction script.

Subsequently, the detector's sky images have been reviewed manually in order to appraise for which of them an spectral analysis was possible and reasonable. Some observations given by the HEASARC search have been out of *Swift*/XRT's field of view or not observed long enough. Figure 10 shows a source which is out of the field of view using the example of observation 00039245001 of MASER021703.6+0517. A typical example of a source with a too low SNR is shown in Figure 11 with observation 00036685001 of MASER050137.8-0415. Thirdly, Figure 12 shows a good detected X-ray source exemplified by observation 00030846001 of MASER121826.5+2948.

For all analysable detections, the aim has furthermore been to control the automatized extraction. In particular cases, the extraction parameters like the center of the source or the respective radii may have had to be adjusted. However, it has appeared that the default values have been appropriate for all of the usable observations, which are listed with "ok" in the column "Sky Image" in Table 5.

Fig. 10.— *Swift*/XRT sky image of observation 00039245001 of MASER021703.6+0517 as an example which is out of the detectors field of view.

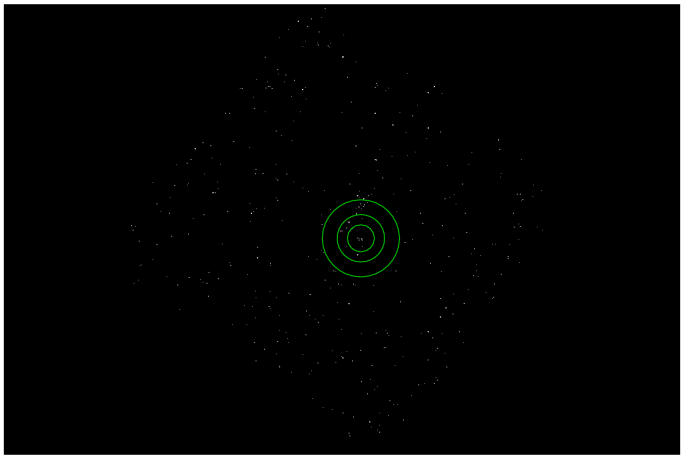

Fig. 11.— *Swift*/XRT sky image of observation 00036685001 of MASER050137.8-0415 as an example of an observation with a too low SNR.

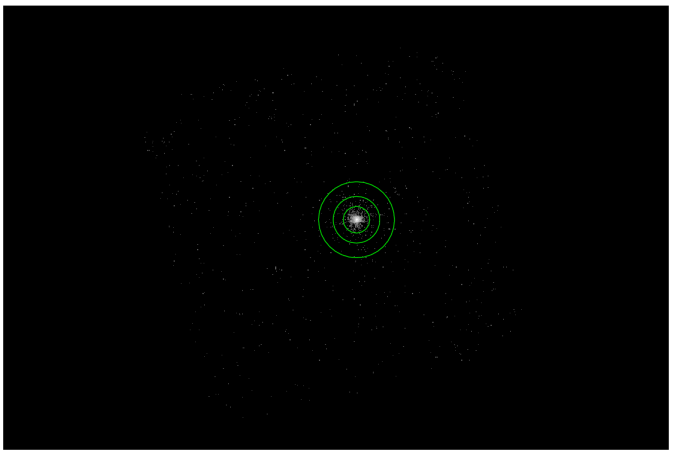

Fig. 12.— *Swift*/XRT sky image of observation 00030846001 of MASER121826.5+2948 as an example of an analysable observation.

3.3.2. Quantifying of the available Swift/XRT data

On the basis of this manual review of the detector's sky images it turned out that only seven of the presumably 13 *Swift*/XRT observed sources were analysable, as already mentioned in the foregoing sections and illustrated by the crossed out values in Table 3. These seven sources are separately listed with their summarized exposure time in Table 4 in order to gain a good and quick overview. The galactic line of sight hydrogen column densities and redshifts of the objects are listed as well. Both values have been used for the spectral model fitting.

Additionally, the following more detailed Table 5 has been created. It summarizes the expressions of the respective sky image as well as the data listed in HEASARC for all available *Swift*/XRT observations of the new sources. The respective targets of *Swift*/XRT, the observation numbers and dates as well as the exposure are given. According to the sky images and the listed HEASARC search offsets some observations were not usable, since the maser coordinates lay out of the line of sight. These as well as masers with a very low intensity are accordingly marked.

Table 4: The seven analysable *Swift*/XRT observed sources

Masername	Total exposure (in ks)	nH (in $10^{22}\,\mathrm{cm}^{-2}$)	z
MASER050137.8-0415	2.80E+04	0.0569	0.01340594
MASER050819.7+1721	1.38E+04	0.184	0.01750544
MASER055542.6+0323	5.28E+03	0.221	0.00263182
MASER091127.5-1449	1.09E+04	0.043	0.00684807
MASER120224.0+1450	1.21E+04	0.0257	0.02425345
MASER121826.5+2948	1.49E+05	0.0178	0.01292894
MASER144536.8+2702	9.51E+03	0.025	0.02989735

Table 5. *Swift*/XRT data for the 43 new sources

Masername	Target of *Swift*	ObsID	Sky image	Observation date	XRT exposure	HEASARC search offset (maser coordinates)
MASER021703.6+0517	CRATESJ0215+0524	39245001	out of FoV	2010-03-05	5463.135	19.881 (02 17 03.57 +05 17 31.4)
MASER044055.0-0822	SwiftJ0441.8-0823	41155001	out of FoV	2010-04-18	10756.1	13.138 (04 40 54.97 -08 22 22.2)
MASER050137.8-0415	HCG031	35911001	ok	2006-08-20	10685.592	3.374 (05 01 37.76 -04 15 28.4)
MASER050137.8-0415	PGC0016574	36685001	low int.	2007-07-22	1474.76	1.239 (05 01 37.76 -04 15 28.4)
MASER050137.8-0415	PGC0016574	36685002	low int.	2007-08-08	2560.74	0.855 (05 01 37.76 -04 15 28.4)
MASER050137.8-0415	PGC0016574	36685004	low int.	2007-12-23	5048.605	1.518 (05 01 37.76 -04 15 28.4)
MASER050137.8-0415	PGC0016574	36685005	low int.	2008-01-11	4330.254	1.970 (05 01 37.76 -04 15 28.4)
MASER050137.8-0415	PGC0016574	36685006	low int.	2008-01-13	3901.758	1.920 (05 01 37.76 -04 15 28.4)
MASER050819.7+1721	SwiftJ0508.1+1727	37118001	ok	2007-10-17	2271.59	6.565 (05 08 19.69 +17 21 48.1)
MASER050819.7+1721	SwiftJ0508.1+1727	37118002	ok	2007-11-07	4763.04	2.690 (05 08 19.69 +17 21 48.1)
MASER050819.7+1721	SwiftJ0508.1+1727	37118003	ok	2007-11-21	1770.49	2.447 (05 08 19.69 +17 21 48.1)
MASER050819.7+1721	SwiftJ0508.1+1727	37118004	ok	2007-12-13	4954.8	5.914 (05 08 19.69 +17 21 48.1)
MASER055542.6+0323	iizw40	40761001	low int.	2010-05-03	2961.979	2.188 (05 55 42.63 +03 23 31.8)
MASER055542.6+0323	iizw40	40761002	low int.	2010-08-06	2313.079	2.234 (05 55 42.63 +03 23 31.8)
MASER070421.0-2135	Automatic Target	360495000	out of FoV	2009-08-20	603.706	12.394 (07 04 21.02 -21 35 19.2)
MASER091127.5-1449	NGC2781	31196001	low int.	2008-04-19	2788.09	2.092 (09 11 27.52 -14 49 00.6)
MASER091127.5-1449	NGC2781	31196002	low int.	2008-04-21	5739.13	1.844 (09 11 27.52 -14 49 00.6)
MASER091127.5-1449	NGC2781	31196003	low int.	2008-04-25	2401.99	3.518 (09 11 27.52 -14 49 00.6)
MASER103138.9+2559	87GB1027+2610	90139001	out of FoV	2009-11-30	396.148	11.238 (10 31 38.87 +25 59 02.3)
MASER103138.9+2559	87GB1027+2610	90139002	out of FoV	2009-12-27	1028.028	14.277 (10 31 38.87 +25 59 02.3)
MASER103138.9+2559	87GB1027+2610	90139003	out of FoV	2009-12-29	1449.208	11.586 (10 31 38.87 +25 59 02.3)
MASER103138.9+2559	87GB1027+2610	90139004	out of FoV	2010-01-06	832.493	11.175 (10 31 38.87 +25 59 02.3)
MASER111821.3+4544	IGRJ11203+4531	31513001	out of FoV	2009-10-10	8044.691	24.488 (11 18 21.32 +45 44 53.6)
MASER111821.3+4544	SDSSJ111913.27+453654.0	39647001	out of FoV	2011-04-25	2133.81	12.725 (11 18 21.32 +45 44 53.6)
MASER120224.0+1450	MASER120224.0+1450	31536001	low int.	2009-11-13	1100.648	1.613 (12 02 23.98 +14 50 37.1)
MASER120224.0+1450	MASER120224.0+1450	31536002	low int.	2009-11-14	2514.83	1.993 (12 02 23.98 +14 50 37.1)
MASER120224.0+1450	MASER120224.0+1450	31536003	low int.	2009-11-17	1995.648	1.599 (12 02 23.98 +14 50 37.1)
MASER120224.0+1450	MASER120224.0+1450	31536004	low int.	2009-11-18	6537.849	0.833 (12 02 23.98 +14 50 37.1)
MASER121826.5+2948	Mkn766	30846001	ok	2006-12-21	3902.321	1.291 (12 18 26.51 +29 48 46.3)
MASER121826.5+2948	Mkn766	30846003	ok	2006-12-24	2452.789	0.589 (12 18 26.51 +29 48 46.3)
MASER121826.5+2948	Mkn766	30846004	ok	2006-12-25	3446.581	3.251 (12 18 26.51 +29 48 46.3)

Table 5—Continued

Masername	Target of *Swift*	ObsID	Sky image	Observation date	XRT exposure	HEASARC search offset (maser coordinates)
MASER121826.5+2948	Mkn766	30846005	ok	2006-12-27	3624.52	3.254 (12 18 26.51 +29 48 46.3)
MASER121826.5+2948	Mkn766	30846006	ok	2006-12-28	3126.538	0.385 (12 18 26.51 +29 48 46.3)
MASER121826.5+2948	Mkn766	30846007	ok	2006-12-28	2642.368	0.655 (12 18 26.51 +29 48 46.3)
MASER121826.5+2948	Mkn766	30846008	ok	2006-12-30	2718.02	2.528 (12 18 26.51 +29 48 46.3)
MASER121826.5+2948	Mkn766	30846009	ok	2006-12-31	2938.41	0.852 (12 18 26.51 +29 48 46.3)
MASER121826.5+2948	Mkn766	30846010	ok	2007-01-01	2567.057	1.332 (12 18 26.51 +29 48 46.3)
MASER121826.5+2948	Mkn766	30846011	ok	2007-01-02	2683.27	0.934 (12 18 26.51 +29 48 46.3)
MASER121826.5+2948	Mkn766	30846012	ok	2007-01-06	2669.781	2.875 (12 18 26.51 +29 48 46.3)
MASER121826.5+2948	Mkn766	30846013	ok	2007-01-14	3186.306	3.796 (12 18 26.51 +29 48 46.3)
MASER121826.5+2948	Mkn766	30846014	ok	2007-01-20	2923.132	2.396 (12 18 26.51 +29 48 46.3)
MASER121826.5+2948	Mkn766	30846015	ok	2007-01-28	3031.317	0.450 (12 18 26.51 +29 48 46.3)
MASER121826.5+2948	Mkn766	30846016	ok	2007-02-04	2705.949	2.662 (12 18 26.51 +29 48 46.3)
MASER121826.5+2948	Mkn766	30846017	ok	2007-02-10	2605.342	0.450 (12 18 26.51 +29 48 46.3)
MASER121826.5+2948	Mkn766	30846018	ok	2007-02-16	2308.291	0.987 (12 18 26.51 +29 48 46.3)
MASER121826.5+2948	Mkn766	30846019	ok	2007-02-23	1892.523	0.545 (12 18 26.51 +29 48 46.3)
MASER121826.5+2948	Mkn766	30846020	ok	2007-03-04	2838.989	1.194 (12 18 26.51 +29 48 46.3)
MASER121826.5+2948	Mkn766	30846021	ok	2007-03-10	3561.717	3.045 (12 18 26.51 +29 48 46.3)
MASER121826.5+2948	Mkn766	30846022	ok	2007-03-14	2659.829	1.386 (12 18 26.51 +29 48 46.3)
MASER121826.5+2948	Mkn766	30846023	ok	2007-03-19	2404.427	2.426 (12 18 26.51 +29 48 46.3)
MASER121826.5+2948	Mkn766	30846024	ok	2007-03-21	3155.739	1.800 (12 18 26.51 +29 48 46.3)
MASER121826.5+2948	Mkn766	30846025	ok	2007-03-26	2513.393	0.900 (12 18 26.51 +29 48 46.3)
MASER121826.5+2948	Mkn766	30846026	ok	2007-04-01	1587.609	1.812 (12 18 26.51 +29 48 46.3)
MASER121826.5+2948	Mkn766	30846028	ok	2007-04-12	160	2.936 (12 18 26.51 +29 48 46.3)
MASER121826.5+2948	Mkn766	30846029	ok	2007-04-16	2753.891	6.470 (12 18 26.51 +29 48 46.3)
MASER121826.5+2948	Mkn766	30846030	ok	2007-04-23	3008.468	0.879 (12 18 26.51 +29 48 46.3)
MASER121826.5+2948	Mkn766	30846031	ok	2007-04-29	1330.761	0.259 (12 18 26.51 +29 48 46.3)
MASER121826.5+2948	Mkn766	30846032	ok	2007-05-01	1785.067	1.343 (12 18 26.51 +29 48 46.3)
MASER121826.5+2948	Mkn766	30846034	ok	2007-05-09	2668.199	0.649 (12 18 26.51 +29 48 46.3)
MASER121826.5+2948	Mkn766	30846035	ok	2007-05-13	3327.597	1.422 (12 18 26.51 +29 48 46.3)
MASER121826.5+2948	Mkn766	30846036	ok	2007-05-18	2680.233	0.543 (12 18 26.51 +29 48 46.3)
MASER121826.5+2948	Mkn766	30846037	ok	2007-05-25	2926.43	2.501 (12 18 26.51 +29 48 46.3)

Table 5—Continued

Masername	Target of *Swift*	ObsID	Sky image	Observation date	XRT exposure	HEASARC search offset (maser coordinates)
MASER121826.5+2948	Mkn766	30846038	ok	2007-06-01	3263.5	1.803 (12 18 26.51 +29 48 46.3)
MASER121826.5+2948	Mkn766	30846039	ok	2007-06-08	4067.26	1.088 (12 18 26.51 +29 48 46.3)
MASER121826.5+2948	Mkn766	30846040	ok	2007-06-15	3775.97	1.265 (12 18 26.51 +29 48 46.3)
MASER121826.5+2948	Mkn766	30846041	ok	2007-06-22	3046.78	2.054 (12 18 26.51 +29 48 46.3)
MASER121826.5+2948	ON325	31536004	out of FoV	2009-12-03	4995.22	20.383 (12 18 26.51 +29 48 46.3)
MASER121826.5+2948	RBS1093	31906001	out of FoV	2011-01-04	4386.077	19.570 (12 18 26.51 +29 48 46.3)
MASER121826.5+2948	RBS1093	31906002	out of FoV	2011-01-08	2377.268	19.497 (12 18 26.51 +29 48 46.3)
MASER121826.5+2948	RBS1093	31906004	out of FoV	2011-01-10	4071.173	20.343 (12 18 26.51 +29 48 46.3)
MASER121826.5+2948	RBS1093	31906005	out of FoV	2011-01-11	4275.028	20.852 (12 18 26.51 +29 48 46.3)
MASER121826.5+2948	RBS1093	31906006	out of FoV	2011-01-12	2986.171	19.372 (12 18 26.51 +29 48 46.3)
MASER121826.5+2948	RBS1093	31906007	out of FoV	2011-12-08	2712.409	20.184 (12 18 26.51 +29 48 46.3)
MASER121826.5+2948	RBS1093	31972001	out of FoV	2011-04-22	1292.782	18.531 (12 18 26.51 +29 48 46.3)
MASER121826.5+2948	RBS1093	31972002	out of FoV	2011-04-23	2344.526	19.372 (12 18 26.51 +29 48 46.3)
MASER121826.5+2948	RBS1093	31972003	out of FoV	2011-04-24	2136.299	19.392 (12 18 26.51 +29 48 46.3)
MASER121826.5+2948	RBS1093	31972004	out of FoV	2011-04-25	2250.104	20.713 (12 18 26.51 +29 48 46.3)
MASER121826.5+2948	RBS1093	31972005	out of FoV	2011-04-27	85.056	17.938 (12 18 26.51 +29 48 46.3)
MASER121826.5+2948	RBS1093	31972006	out of FoV	2011-04-29	1970.729	18.884 (12 18 26.51 +29 48 46.3)
MASER121826.5+2948	RBS1093	31972007	out of FoV	2011-05-01	2242.22	20.302 (12 18 26.51 +29 48 46.3)
MASER121826.5+2948	RBS1093	31972008	out of FoV	2011-05-02	1883.769	19.555 (12 18 26.51 +29 48 46.3)
MASER121826.5+2948	RBS1093	31972010	out of FoV	2011-05-05	1658.387	19.910 (12 18 26.51 +29 48 46.3)
MASER121826.5+2948	RBS1093	31972011	out of FoV	2011-05-06	1578.673	21.249 (12 18 26.51 +29 48 46.3)
MASER121826.5+2948	saa-cold-204-7	67748001	out of FoV	2005-07-23	370.944	12.718 (12 18 26.51 +29 48 46.3)
MASER144536.8+2702	SwiftJ1445.6+2702	37385001	ok	2010-11-26	9513.128	2.201 (14 45 36.8 +27 02 05)
MASER163040.9+3029	P330E	56770008	out of FoV	2006-03-19	221.79	23.904 (16 30 40.92 +30 29 19.6)
MASER163040.9+3029	P330E	56770013	out of FoV	2006-03-23	196.465	23.526 (16 30 40.92 +30 29 19.6)
MASER163040.9+3029	P330E	56770014	out of FoV	2006-03-23	402.065	24.154 (16 30 40.92 +30 29 19.6)
MASER163040.9+3029	P330E	56770015	out of FoV	2006-03-23	439.675	24.187 (16 30 40.92 +30 29 19.6)
MASER163040.9+3029	P330E	56770016	out of FoV	2006-03-23	995.925	23.523 (16 30 40.92 +30 29 19.6)
MASER163040.9+3029	P330E	56770017	out of FoV	2007-05-13	517.774	23.594 (16 30 40.92 +30 29 19.6)
MASER163040.9+3029	P330E	56770018	out of FoV	2007-05-13	2295.294	23.620 (16 30 40.92 +30 29 19.6)
MASER163040.9+3029	P330E	56770019	out of FoV	2007-05-13	1528.146	23.775 (16 30 40.92 +30 29 19.6)

Table 5—Continued

Masername	Target of *Swift*	ObsID	Sky image	Observation date	XRT exposure	HEASARC search offset (maser coordinates)
MASER163040.9+3029	P330E	56770023	out of FoV	2007-05-18	457.178	22.313 (16 30 40.92 +30 29 19.6)
MASER163040.9+3029	P330E	56770024	out of FoV	2008-10-24	1088.16	22.699 (16 30 40.92 +30 29 19.6)
MASER163040.9+3029	P330E	56770025	out of FoV	2010-07-07	3326.26	23.621 (16 30 40.92 +30 29 19.6)

Note. — Results of the X-ray data search for the newly detected masers. The listed data is an extraction of the *swiftmastr* file created with HEASARC. It is complemented by the corresponding maser nomenclature in column one and a short note which data appeared to be analysable in column four. Therefore, the sky images of the *Swift*/XRT detector were studied after the extraction of the raw data (see section 3.3.1).

References. — NASA's High Energy Astrophysics Science Archive Research Center (HEASARC)

3.4. Formal analysis of X-ray data

The main task for an X-ray astrophysicist is to find out the spectrum of the source. It contains all the necessary information of the object. Hence, the question is how to get the real spectral energy distribution $S(E)$ out of the satellite's data (Nowak 2009; Hanke 2007).

The first point to consider is the effective area of the telescope, described by the "ancillary response function" (ARF), in formulae written as $A(E)$ (Nowak 2009; Hanke 2007). It is influenced by filters, windows, shields, mirrors and collimators of the telescope. Furthermore, it has to consider the detector's efficiency, defect chips and contamination as well as dithering effects. In addition, it is strongly energy dependent. The ARF files are adapted by the respective calibration team of the spacecraft, for example by using Monte Carlo simulations.

In the first step, one has used the ARF to consider the statistical influences until the photon is actually detected. However, what one then measures with a X-ray satellite are not single photons from a source, but counts per integration time and energy channel (Nowak 2009; Hanke 2007). These counts are measured as voltage signals in a semiconductor chip for example. Its "pulse height amplitude" (PHA) is thereby integrated over a time period and has to be binned in discrete energy channels. This is due to technical constraints of the photon detector, but also intended in order to get a better signal to noise ratio (SNR) per bin and to reduce the telemetry data. All the physical and statistical effects happening there have to be covered by the "redistribution matrix function" (RMF), given as $R(E)$. Although it is also often referred to as "response matrix function" in literature, the term "response function" (RSP) is correctly used for a RMF that already includes the respective ARF.

As a third point, one has to consider that not all counts are source counts, but some counts are also due to background radiation, particles or detector noise (Nowak 2009; Hanke 2007). To take account of this, it is important to set reference areas in the sky image of the detector, as it is described in section 3.3.1. Thereby, it is distinguished between source counts C and background counts B.

Now one has all influencing factors for a spectral analysis of X-ray data. According to Davis (2001) a formal equation for the connection of all those parameters is

$$C_i = B_i + \iint dE\ dt\ K\big(R_i(E)A(E)S(E)\big), \tag{9}$$

where K is the kernel connecting the different functions and i is the Index of the energy bin. In order to gather all desired information about the observed object, one would need to solve this equation for the source spectra $S(E)$.

3.5. Spectral model fitting in theory and practice

Unfortunately, it is impossible to calculate $S(E)$ directly from solving equation (9), because the formal solution gets unstable as Dolan (1972) showed. That is the point where spectral model fitting becomes important (Hanke 2007; Nowak 2009). By setting different parameters one can create model spectra $\tilde{S}(E)$ for the source. Out of these, model count rates $M_i = \iint dEdt\, K\big(R_i(E)A(E)\tilde{S}(E)\big)$ can be calculated. Therefore, it is the aim to find the best spectral model where the model count rate M_i is most close to the real detected count rate $C_i^0 := C_i - B_i$. For this reason, fitting statistics are needed to compare M_i with C_i^0, while an algorithm searches for the minimum of the statistic by trying different parameters.

3.5.1. Fitting statistics

In this work two different kinds of fitting statistics were applied. The first one is the χ^2 statistic, which is commonly used in X-ray astronomy. It is defined as

$$\chi^2 := \sum_i (C_i^0 - M_i)^2/\sigma_i^2, \tag{10}$$

where σ_i are the errors of the detected count rates C_i^0 (Houck 2012; Hanke 2007). Usually these are derived as $\sigma_i = \sqrt{C_i + B_i}$, at which a Gaussian distribution needs to be assumed. This leads to the equation

$$\chi^2 = \sum_i \left(\frac{C_i - B_i - M_i}{C_i + B_i}\right)^2. \tag{11}$$

Given a number of bins n, a number of parameters $m < n$ may be fixed due to physical reasons (Hanke 2007). This leaves a number of degrees of freedom $f = n - m$ for the fitting process. As mentioned above, the fitting algorithm tries to find the minimum of the statistic, in this case the minimal χ^2. For a better comparability it is common to publish the reduced statistics, in this case $\chi^2_{\mathrm{red}} = \chi^2/f$. For a statistical measurement of Gaussian distributed data $\tilde{S}(E) \approx S(E)$, it follows that M_i is the expected value. Thus, the measured data points C_i^0 are expected to scatter around M_i with an error $\sigma_i \approx C_i^0 - M_i$. Considering equation (10) and the fixed parameters, this leads directly to $\chi^2 \approx f$. Therefore, the criteria for a good fit is $\chi^2_{\mathrm{red}} \approx 1$ at the end of the calculations. However, a result of $\chi^2_{\mathrm{red}} < 1$ suggests that the errors σ_i were overestimated or calculated wrongly. This can be due to the assumption of Gaussian distributed data. If one has too few counts per bin this approach is wrong and instead one has to assume a Poisson distribution.

Exactly this is the approach of the Cash statistic, which was introduced by Webster Cash (1979). It is defined to be

$$S_{\text{Cash}} := 2 \sum_i (M_i - C_i) + C_i \ln(C_i/M_i). \tag{12}$$

As Schmahl (2005) showed the χ^2 and Cash statistic are basically the same for more than ten counts/bin, like it could be expected from the Gaussian approximation. But for values below that level and especially for less than one count/bin the χ^2 Statistic gets remarkably bad. Since X-ray data can have quite short exposure time, it might often not provide more than ten counts/bin. Hence, in these cases the χ^2 statistic should not be used in the common way[6]. Otherwise, one should prefer to use the Cash rather than the χ^2 statistic. For this bachelor's thesis both types of statistics have been used for all plots in order to compare the results in section 4.

3.5.2. Fitting functions

The physical process behind the observed X-ray spectra is presumably Comptonization of seed photons (Wilms 2010; Titarchuk 1994). This term describes the effect of inverse Compton scattering. In the standard case of Compton scattering a photon hits a resting electron and transfers parts of its momentum and energy. However, when the electron is in motion the photon can gain momentum and energy from the electron. This effect is described by the quantum mechanical Kompaneets equation (Kompaneets 1957), which is absolutely non-trivial to solve[7]. Approximations as well as numerical solutions with Monte Carlo simulations show that it results in a powerlaw dependence of the X-ray spectra. It is of the form $I(\nu) \propto \nu^{-\alpha}$ with the spectral slope α. In X-ray astronomy, however, it is usual to refer to the photon index $\Gamma := \alpha + 1$. The calculation of the photon index is therefore one of the main tasks.

Depending on additional absorption and reflection processes this can also result in more complex models. While spectra from $0.5 - 10\,\text{keV}$ usually can be described by a pure powerlaw, the hard X-ray range can show a Compton reflection hump at $30\,\text{keV}$ and a high-energy exponential cutoff in the range of a few $100\,\text{keV}$. These features then have to be modelled with a composition of

[6]However, there is also a more complicated error estimation provided by Gehrels (1986) which can be used without assuming a Gaussian distribution. A more detailed discussion of this topic would go beyond the scope of this bachelor's thesis. For further study see the stated literature.

[7]For an analytical solution see e.g. Titarchuk and Lyubarskij (1995)

two powerlaws, called broken powerlaw fit, or a cutoff powerlaw fit. An overview of these three fitting functions is given with the following equations. A simple powerlaw is defined as

$$f(E) = A \left(\frac{E}{1\,\mathrm{keV}} \right)^{-\Gamma}, \tag{13}$$

where A is the norm of the fit and Γ is the above described photon index, so there are two free parameters reducing the degrees of freedom by two. The broken powerlaw is defined as

$$\begin{aligned} f(E) &= A \left(\frac{E}{1\,\mathrm{keV}} \right)^{-\Gamma_1} \quad \mathrm{for} E \leq E_{\mathrm{break}}, \\ f(E) &= A \left(\frac{E_{\mathrm{break}}}{1\,\mathrm{keV}} \right)^{\Gamma_2 - \Gamma_1} \left(\frac{E}{1\,\mathrm{keV}} \right)^{-\Gamma_2} \quad \mathrm{for} E \geq E_{\mathrm{break}}. \end{aligned} \tag{14}$$

Thereby A is again the norm of the fit, Γ_1 and Γ_2 are the two photon indices and E_{break} is the so called break energy. Therefore, this method leaves another two degrees of freedom less than a simple powerlaw. The definition of the cutoff powerlaw is

$$f(E) = A \left(\frac{E}{1\,\mathrm{keV}} \right)^{-\Gamma} \exp\left(-\frac{E}{E_{\mathrm{cut}}} \right). \tag{15}$$

In addition to the two parameters of the pure powerlaw the exponential high energy cutoff at E_{cut} costs a third degree of freedom. In this bachelor's thesis all three models have been performed for all analyses so that the results can be compared in section 4.

3.5.3. Absorption models

Soft X-ray radiation can easily be absorbed by hydrogen gas clouds. Depending on the type of AGN and hence the viewing angle the torus can lay in the line of sight and absorb a lot of radiation. Therefore, it is thereby necessary to use absorption models in combination with the different fitting functions. Furthermore, another main task of this work was to determine the hydrogen column densities of the maser hosting AGNs, since they offer a direct link between X-ray and maser luminosities (see section 2.6).

For this bachelor's thesis the need for absorption models has been proved for all analysed masers. Therefore, the χ^2 statistic has been used in combination with a powerlaw fit. At first, fits without any absorption were performed. Secondly, fits with pure galactic absorption have been made, at which the redshift parameter was set to $z = 0$ and the galactic hydrogen column density was set to the respective value from Table 4. Thirdly, fits with free hydrogen absorption parameters have

been performed. Thereby, the redshift parameter for the absorption has been fixed on the known redshift of the respective object, which is listed in Table 4. This third method then determines the hydrogen column densities which fits best to the data. The results of these three different absorption model fits are compared in terms of their adequacy in section 4.

3.5.4. Summarizing of weaker sources and fitting

A lot of the *Swift*/XRT data studied for this work have a quite short exposure time for their single observations. Nevertheless, many objects have been observed in several of those short epochs spread over a few months as it can be seen from the observation IDs and dates in Table 5. For this data it is applicable to summarize the single PHA files (see section 3.5) and handle the result as one observation. For this procedure only ongoing observation numbers have been used and the combined files are in the following referred to as an observation ID marked with an "X" as last letter. The summarizing of PHA files has been performed for MASER050137.8-0415, MASER050819.7+1721, MASER091127.5-1449 and MASER120224.0+1450. The PHAs of MASER121826.5+2948 have been good enough for single analyses and did not need to be combined. For these a mean value of the single fitting parameters could be derived instead.

3.5.5. Estimation of significances for X-ray detections

Only the Photon Counting mode of *Swift*/XRT is used for this bachelor's thesis. It works a bit different than the γ-ray instruments Li and Ma (1983) described in their work, but their statistical model can be adapted for the purposes of this work. Therefore, their idea shall be discussed first. In the beginning, their telescope points directly at the source coordinates. It detects N_{on} counts in total over a time t_{on}. Afterwards it points to the background and measures N_{off} counts over a time t_{off} that can differ from t_{on} by the factor α with $t_{\mathrm{on}} = \alpha t_{\mathrm{off}}$. One can now estimate the mean number of counts which are just due to the source by $N_{\mathrm{source}} = N_{\mathrm{on}} - \alpha N_{\mathrm{off}}$. As Li and Ma (1983) stated a statistical fluctuation of the background counts could therefore cause something that looks like a positive detection of a source, too. Consequently, it is important to estimate the statistical reliability of the measurement. For this reason, they provided several mathematical approaches by using Poisson and likelihood methods. They could estimate the significance of an observation out of the source counts N_{source} and their standard deviation.

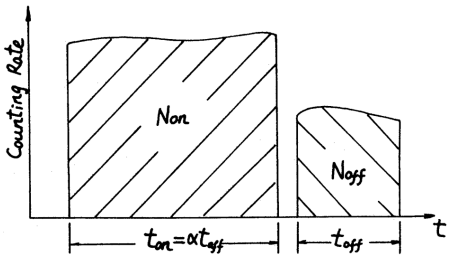

Fig. 13.— A typical observation in γ-ray astronomy according to Li and Ma (1983)

For our purposes the situation is mathematically the same, but α is due to another reason. *Swift*/XRT has a field of view that covers the source as well as the background with a single observation. Therefore, $t_{\rm on} = t_{\rm off}$. Instead α is needed to describe the ratio of the two regions that are chosen for the summarizing of source and background counts.

Gillessen and Harney (2005) have developed the work of Li and Ma (1983) by using Bayesian statistics. They were able to improve the model and wrote a Mathematica script that gives the significance of a detection in terms of *sigma*. A reliable observation is thereby given by a factor $> 3\sigma$, lower values are an indicator for statistical background fluctuation.

3.5.6. Estimation of upper limits for the weakest sources

For the estimation of upper limits it is necessary to have a bright model source. One has to assume that its spectra is typical for the type of sources that shall be analysed. We have chosen MASER121826.5+2948 for this purpose, because it is the brightest source analysed in this work. As we will discuss in section 4 in more detail, it has a very variable soft excess. Nevertheless, observation 00030846041 could be chosen, since it does not show this feature and can be described by a simple powerlaw, which is the expected spectral distribution for all sources.

With the chosen reference source a "typical" spectra is simulated with the values $T_{\rm sim}$ for the simulated exposure, $N_{\rm sim}$ for the simulated source counts and $F_{\rm sim}$ for the simulated flux. Now one can derive the estimated flux of the observed source by using its source counts $N_{\rm obs}$ and its exposure $T_{\rm obs}$ and the equation

$$F_{\rm obs} = \frac{N_{\rm obs}}{T_{\rm obs}} \left(\frac{T_{\rm sim}}{N_{\rm sim}} F_{\rm sim} \right). \tag{16}$$

3.6. Combined *Swift*/XRT and *Swift*/BAT fitting

For two of the three sources which could be analysed by spectral model fitting, namely MASER050819.7+1721 and MASER121826.5+2948, also *Swift*/BAT data with a SNR > 2 has been available. Consequently, their data could be used for a combined analysis of the spectra. Analogue to the single analysis of the *Swift*/XRT data the methods discussed in section 3.5 have been used and compared.

3.7. Results

Whenever possible spectral model fitting has been applied for single or summarized PHAs. However, this has only been possible for three of the seven presumably analysable sources, namely MASER050137.8-0415, MASER050819.7+1721 and MASER121826.5+2948. In the following just the plots and results which are discussed in detail in section 4 are given. The remaining relevant fits can be found in the appendix. The abbreviations used in the following and in the plots in the appendix are shown in Table 6.

Table 6: Abbreviations used for the *Swift*/XRT spectral model fitting

P.L.	powerlaw fit
B.P.L.	broken powerlaw fit
C.P.L.	cutoff powerlaw fit
una.	unabsorbed / fit without absorption model
gal. abs.	fit with galactic absorption model
abs.	fit with free hydrogen parameter absorption model
d.o.f.	degrees of freedom
BreakE	break energy of the broken powerlaw fit
HighECut	cutoff energy of the cutoff powerlaw fit

During the analyses it has come clear, that the other four sources may have be observed too short or are to quite in the X-ray band to allow spectral model fitting with *Swift*/XRT data. Consequently, for MASER055542.6+0323, MASER091127.5 -1449, MASER120224.0+1450 and MASER144536.8+2702 upper limits and standard deviations have been derived.

3.7.1. MASER121826.5+2948

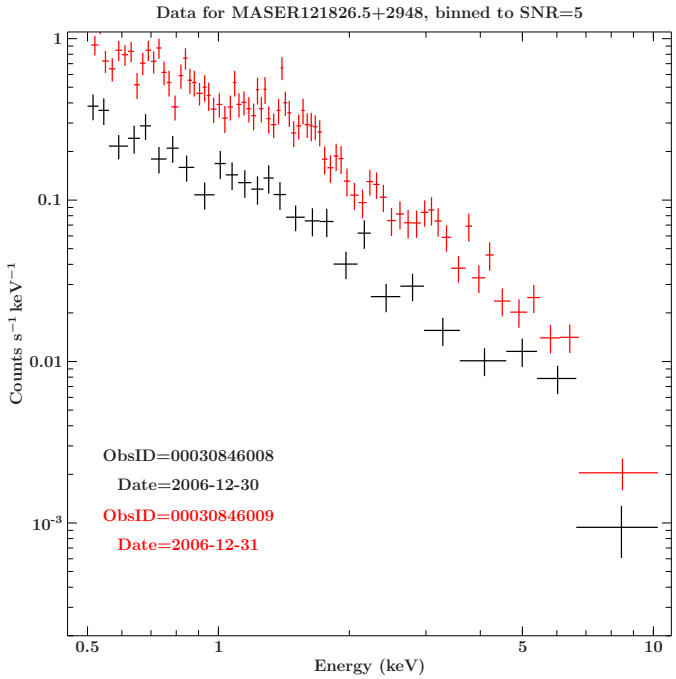

Fig. 14.— Study of the source with *Swift*/XRT. Illustration of the amplitude variability over daily timescales.

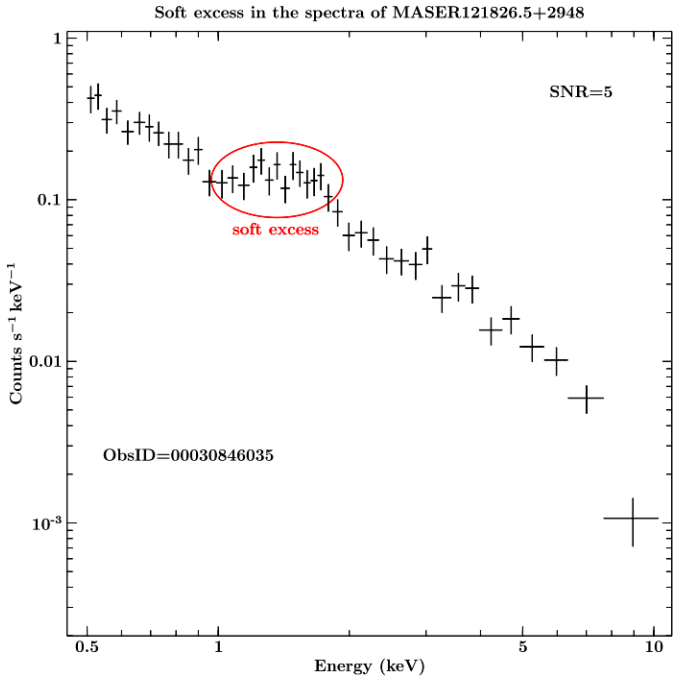

Fig. 15.— Study of the source with *Swift*/XRT. Illustration of the appearing soft excess exemplified by observation 00030846035.

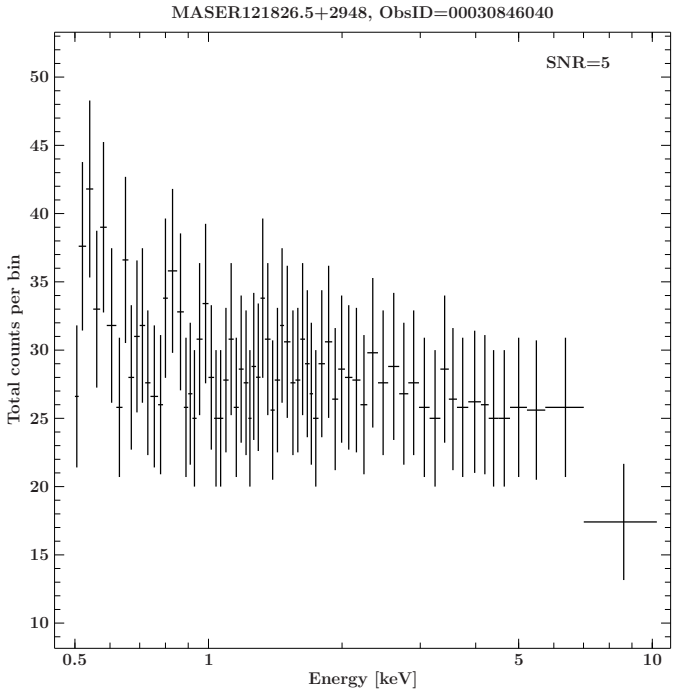

Fig. 16.— *Swift*/XRT data for observation 00030846040. For the comparison of χ^2 and Cash statistic the counts/bin are plotted.

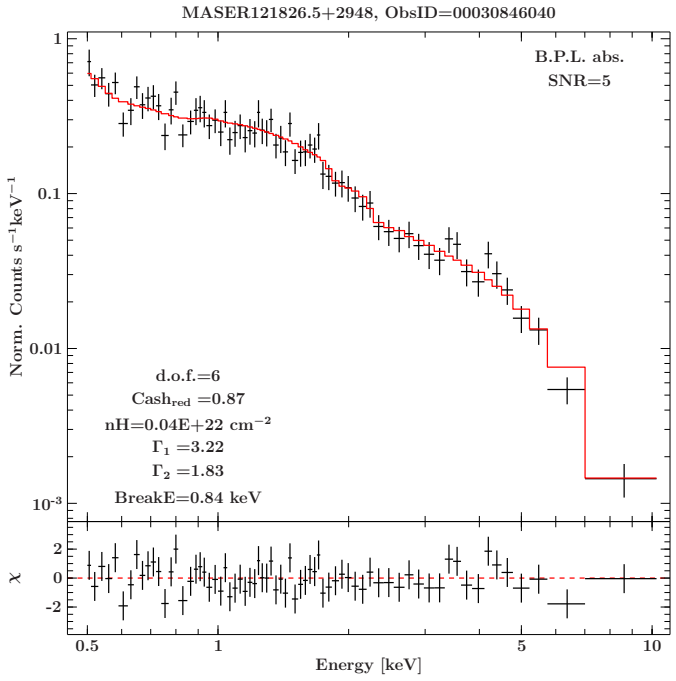

Fig. 17.— *Swift*/XRT analysis statistic exemplified on observation 00030846040. Broken powerlaw fit with Cash statistic for data binned to SNR ≥ 5 with free hydrogen absorption.

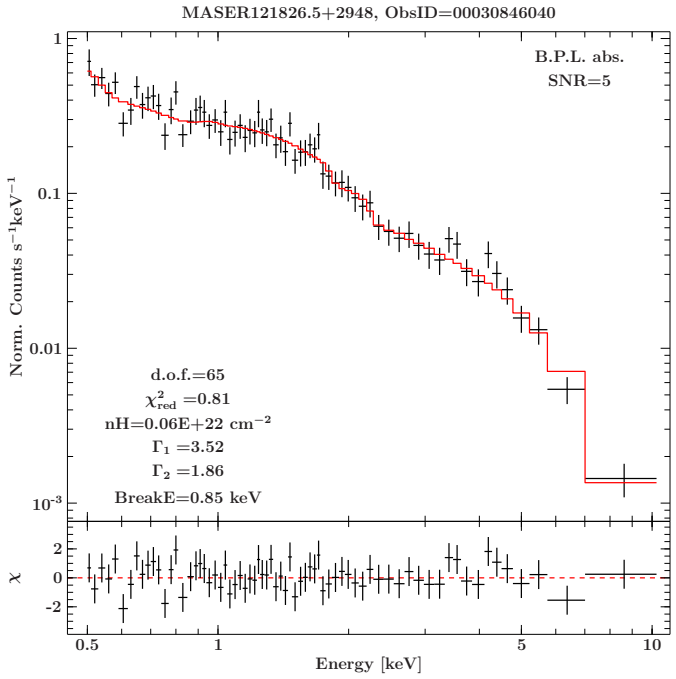

Fig. 18.— *Swift*/XRT analysis exemplified on observation 00030846040. Broken powerlaw fits with χ^2 statistic for data binned to SNR ≥ 5 with free hydrogen absorption.

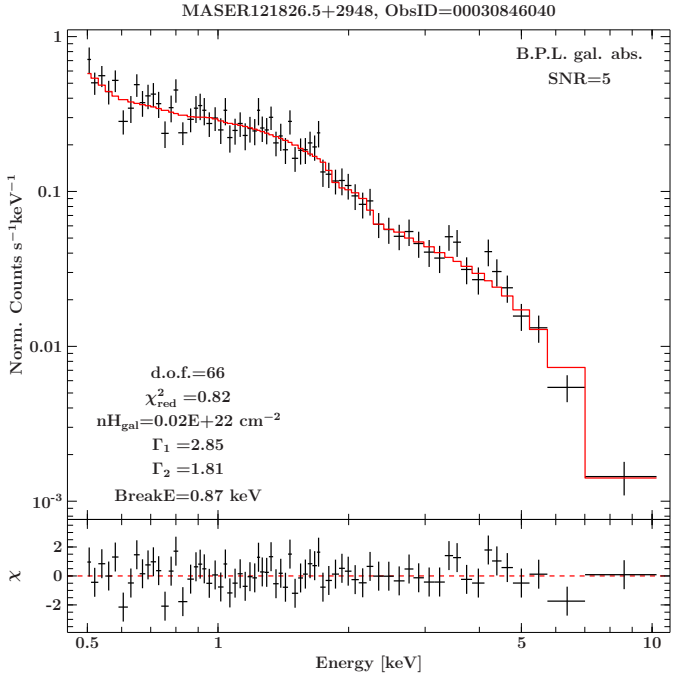

Fig. 19.— *Swift*/XRT analysis exemplified on observation 00030846040. Broken powerlaw fits with χ^2 statistic for data binned to SNR ≥ 5 with galactic absorption.

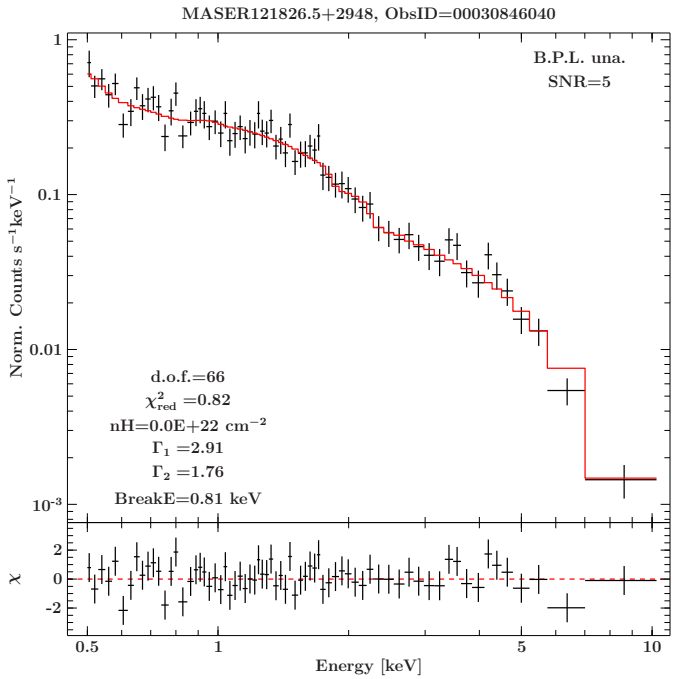

Fig. 20.— *Swift*/XRT analysis exemplified on observation 00030846040. Broken powerlaw fits with χ^2 statistic for data binned to SNR ≥ 5 without absorption.

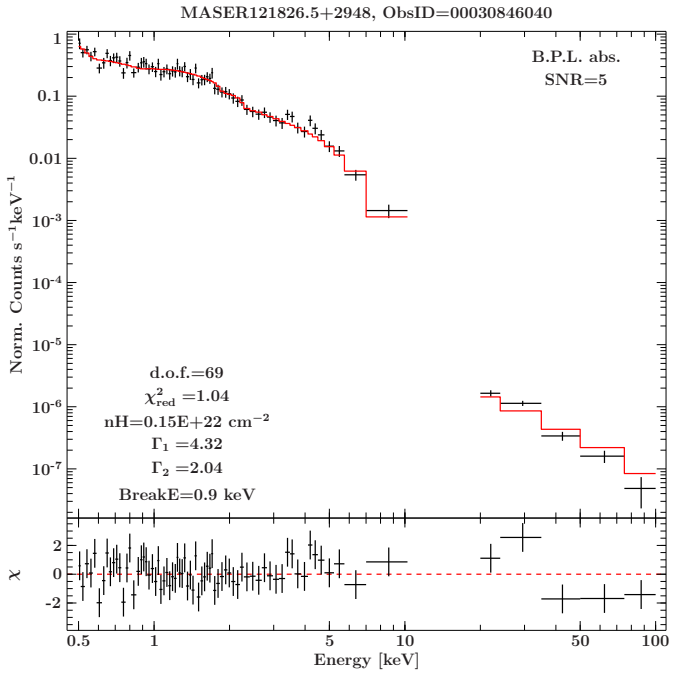

Fig. 21.— Combined *Swift*/XRT and *Swift*/BAT analysis exemplified on observation 00030846040. Broken powerlaw with χ^2 statistic for data binned to SNR ≥ 5 with free hydrogen absorption.

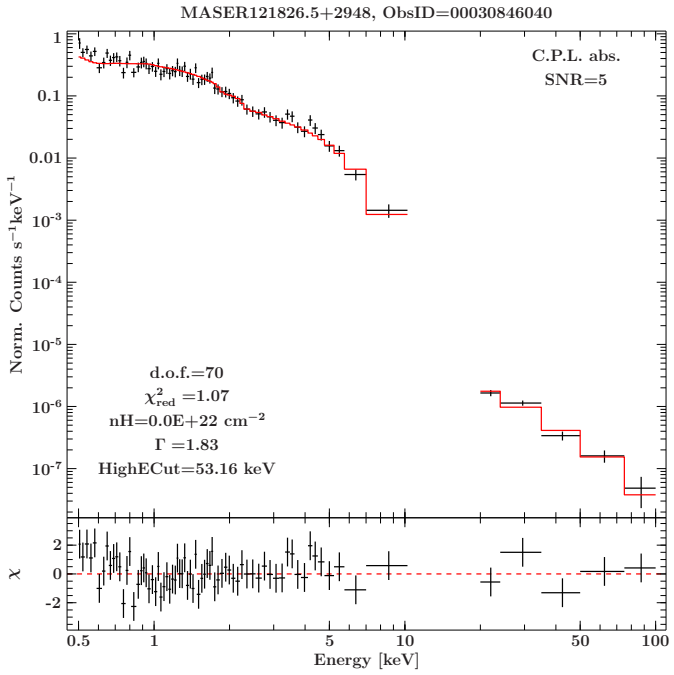

Fig. 22.— Combined *Swift*/XRT and *Swift*/BAT analysis exemplified on observation 00030846040. Cutoff powerlaw with χ^2 statistic for data binned to SNR ≥ 5 with free hydrogen absorption.

Table 7. Results of the spectral model fitting for MASER121826.5+2948 (B.P.L. abs., SNR=5, χ^2)

ObsID	Exposure [a]	γ_1 [b]	γ_2 [b]	BreakE [c]	$Flux_{0.5-2\,keV}$ [d] measured	intrinsic	$Flux_{2-10\,keV}$ [d] measured	intrinsic	N_H [e]	χ^2_{red}	d.o.f.
00030846001	3.82E+03	$3.66^{+0.85}_{-1.01}$	$1.84^{+0.14}_{-0.15}$	$0.81^{+0.08}_{-0.12}$	8.67E-12$^{+3.35E-13}_{-3.35E-13}$	1.07E-11$^{+4.14E-13}_{-4.14E-13}$	1.32E-11$^{+5.10E-13}_{-5.10E-13}$	1.33E-11$^{+5.13E-13}_{-5.13E-13}$	5.92E+20	1.28	62
00030846003	2.39E+03	$2.70^{+1.23}_{-0.52}$	$1.91^{+0.10}_{-0.04}$	$0.81^{+0.29}_{-0.19}$	1.09E-11$^{+5.09E-13}_{-5.09E-13}$	1.09E-11$^{+5.09E-13}_{-5.09E-13}$	1.36E-11$^{+6.33E-13}_{-6.33E-13}$	1.36E-11$^{+6.33E-13}_{-6.33E-13}$	4.24E+14	1.27	42
00030846004	3.30E+03	$3.00^{+1.06}_{-0.62}$	$1.77^{+0.12}_{-0.07}$	$0.72^{+0.11}_{-0.09}$	1.16E-11$^{+4.16E-13}_{-4.16E-13}$	1.16E-11$^{+4.16E-13}_{-4.16E-13}$	1.79E-11$^{+6.40E-13}_{-6.40E-13}$	1.79E-11$^{+6.40E-13}_{-6.40E-13}$	0.00E+00	1.15	70
00030846005	3.59E+03	$3.93^{+0.67}_{-0.95}$	$1.91^{+0.12}_{-0.15}$	$0.89^{+0.08}_{-0.09}$	1.18E-11$^{+3.95E-13}_{-3.95E-13}$	1.98E-11$^{+6.62E-13}_{-6.62E-13}$	1.92E-11$^{+6.42E-13}_{-6.42E-13}$	1.95E-11$^{+6.50E-13}_{-6.50E-13}$	1.42E+21	1.15	80
00030846006	3.07E+03	$2.93^{+1.01}_{-0.53}$	$1.85^{+0.16}_{-0.11}$	$0.92^{+0.23}_{-0.15}$	1.29E-11$^{+4.86E-13}_{-4.86E-13}$	1.36E-11$^{+5.15E-13}_{-5.15E-13}$	1.69E-11$^{+6.37E-13}_{-6.37E-13}$	1.69E-11$^{+6.38E-13}_{-6.38E-13}$	1.53E+20	0.97	62
00030846008	2.67E+03	$3.25^{+0.59}_{-0.51}$	$1.75^{+0.15}_{-0.15}$	$0.92^{+0.21}_{-0.12}$	5.20E-12$^{+3.27E-13}_{-3.27E-13}$	5.20E-12$^{+3.27E-13}_{-3.27E-13}$	7.08E-12$^{+4.45E-13}_{-4.45E-13}$	7.08E-12$^{+4.45E-13}_{-4.45E-13}$	3.13E+12	1.25	22
00030846009	2.88E+03	$3.56^{+0.89}_{-0.87}$	$1.94^{+0.15}_{-0.13}$	$1.00^{+0.08}_{-0.08}$	1.56E-11$^{+5.37E-13}_{-5.37E-13}$	2.11E-11$^{+7.25E-13}_{-7.25E-13}$	1.90E-11$^{+6.52E-13}_{-6.52E-13}$	1.91E-11$^{+6.57E-13}_{-6.57E-13}$	7.59E+20	1.38	71
00030846012	2.64E+03	$2.98^{+1.00}_{-0.34}$	$1.48^{+0.16}_{-0.15}$	$1.11^{+0.19}_{-0.14}$	6.62E-12$^{+3.50E-13}_{-3.50E-13}$	6.62E-12$^{+3.50E-13}_{-3.50E-13}$	1.19E-11$^{+6.31E-13}_{-6.31E-13}$	1.19E-11$^{+6.31E-13}_{-6.31E-13}$	0.00E+00	0.93	32
00030846013	3.12E+03	$3.05^{+0.93}_{-0.49}$	$0.96^{+0.23}_{-0.31}$	$1.41^{+0.49}_{-0.26}$	3.46E-12$^{+2.27E-13}_{-2.27E-13}$	3.46E-12$^{+2.27E-13}_{-2.27E-13}$	9.10E-12$^{+5.98E-13}_{-5.98E-13}$	9.10E-12$^{+5.98E-13}_{-5.98E-13}$	3.97E+15	1.52	21
00030846014	2.86E+03	$3.27^{+0.89}_{-0.83}$	$1.85^{+0.12}_{-0.11}$	$0.95^{+0.16}_{-0.11}$	1.97E-11$^{+5.81E-13}_{-5.81E-13}$	2.54E-11$^{+7.50E-13}_{-7.50E-13}$	2.88E-11$^{+8.50E-13}_{-8.50E-13}$	2.90E-11$^{+8.56E-13}_{-8.56E-13}$	6.94E+20	1.25	98
00030846015	3.00E+03	$3.83^{+1.38}_{-0.86}$	$1.68^{+0.21}_{-0.16}$	$0.95^{+0.11}_{-0.10}$	7.06E-12$^{+3.86E-13}_{-3.86E-13}$	8.43E-12$^{+4.61E-13}_{-4.61E-13}$	1.09E-11$^{+5.93E-13}_{-5.93E-13}$	1.09E-11$^{+5.95E-13}_{-5.95E-13}$	4.34E+20	1.30	30
00030846016	2.63E+03	$3.99^{+1.21}_{-0.76}$	$1.90^{+0.20}_{-0.12}$	$0.91^{+0.10}_{-0.08}$	1.53E-11$^{+5.46E-13}_{-5.46E-13}$	2.34E-11$^{+8.32E-13}_{-8.32E-13}$	2.24E-11$^{+7.96E-13}_{-7.96E-13}$	2.26E-11$^{+8.05E-13}_{-8.05E-13}$	1.09E+21	0.86	69
00030846017	2.55E+03	$2.19^{+1.27}_{-0.23}$	$1.87^{+0.00}_{-0.33}$	$1.10^{+3.02}_{-0.60}$	1.36E-11$^{+5.33E-13}_{-5.33E-13}$	1.36E-11$^{+5.33E-13}_{-5.33E-13}$	1.79E-11$^{+7.01E-13}_{-7.01E-13}$	1.79E-11$^{+7.01E-13}_{-7.01E-13}$	1.80E+18	0.88	58
00030846018	2.29E+03	$2.80^{+1.45}_{-0.64}$	$1.58^{+0.22}_{-0.13}$	$0.91^{+0.25}_{-0.18}$	6.05E-12$^{+3.51E-13}_{-3.51E-13}$	6.29E-12$^{+3.64E-13}_{-3.64E-13}$	1.19E-11$^{+6.90E-13}_{-6.90E-13}$	1.19E-11$^{+6.91E-13}_{-6.91E-13}$	1.11E+20	0.60	27
00030846019	1.87E+03	$2.95^{+1.64}_{-1.04}$	$1.74^{+0.23}_{-0.31}$	$1.08^{+1.07}_{-0.38}$	1.21E-11$^{+6.22E-13}_{-6.22E-13}$	1.55E-11$^{+7.96E-13}_{-7.96E-13}$	2.01E-11$^{+1.03E-12}_{-1.03E-12}$	2.02E-11$^{+1.04E-12}_{-1.04E-12}$	6.80E+20	1.08	35
00030846020	2.78E+03	$3.47^{+1.12}_{-1.08}$	$1.94^{+0.18}_{-0.15}$	$0.81^{+0.13}_{-0.13}$	1.43E-11$^{+5.79E-13}_{-5.79E-13}$	1.79E-11$^{+7.26E-13}_{-7.26E-13}$	1.94E-11$^{+7.89E-13}_{-7.89E-13}$	1.96E-11$^{+7.94E-13}_{-7.94E-13}$	6.29E+20	0.95	55
00030846021	3.42E+03	$3.25^{+2.74}_{-0.64}$	$1.35^{+0.36}_{-0.47}$	$1.29^{+0.67}_{-0.30}$	1.88E-12$^{+1.83E-13}_{-1.83E-13}$	1.88E-12$^{+1.83E-13}_{-1.83E-13}$	3.03E-12$^{+2.96E-13}_{-2.96E-13}$	3.03E-12$^{+2.96E-13}_{-2.96E-13}$	0.00E+00	0.74	7
00030846022	2.63E+03	$4.70^{+2.09}_{-1.63}$	$1.86^{+0.32}_{-0.23}$	$1.00^{+0.09}_{-0.11}$	8.61E-12$^{+4.67E-13}_{-4.67E-13}$	1.76E-11$^{+9.56E-13}_{-9.56E-13}$	1.25E-11$^{+6.80E-13}_{-6.80E-13}$	1.27E-11$^{+6.90E-13}_{-6.90E-13}$	1.66E+21	0.85	30
00030846023	2.37E+03	$4.37^{+1.58}_{-1.94}$	$1.85^{+0.27}_{-0.27}$	$0.84^{+0.15}_{-0.17}$	4.41E-12$^{+3.09E-13}_{-3.09E-13}$	6.65E-12$^{+4.66E-13}_{-4.66E-13}$	7.00E-12$^{+4.91E-13}_{-4.91E-13}$	7.07E-12$^{+4.96E-13}_{-4.96E-13}$	1.08E+21	0.85	17
00030846024	3.11E+03	$2.93^{+1.53}_{-0.76}$	$1.75^{+0.19}_{-0.13}$	$1.07^{+0.26}_{-0.14}$	1.15E-11$^{+4.26E-13}_{-4.26E-13}$	1.42E-11$^{+5.23E-13}_{-5.23E-13}$	1.83E-11$^{+6.74E-13}_{-6.74E-13}$	1.84E-11$^{+6.78E-13}_{-6.78E-13}$	5.65E+20	1.16	67
00030846025	2.48E+03	$3.50^{+1.18}_{-1.20}$	$1.92^{+0.19}_{-0.14}$	$0.86^{+0.12}_{-0.16}$	1.01E-11$^{+4.52E-13}_{-4.52E-13}$	1.31E-11$^{+5.90E-13}_{-5.90E-13}$	1.41E-11$^{+6.33E-13}_{-6.33E-13}$	1.42E-11$^{+6.38E-13}_{-6.38E-13}$	7.31E+20	0.77	44
00030846029	2.72E+03	$4.00^{+1.62}_{-1.27}$	$1.81^{+0.25}_{-0.19}$	$1.01^{+0.10}_{-0.10}$	8.22E-12$^{+4.00E-13}_{-4.00E-13}$	1.48E-11$^{+7.19E-13}_{-7.19E-13}$	1.38E-11$^{+6.70E-13}_{-6.70E-13}$	1.40E-11$^{+6.80E-13}_{-6.80E-13}$	1.50E+21	1.74	40
00030846030	2.98E+03	$4.46^{+1.57}_{-1.20}$	$1.53^{+0.21}_{-0.13}$	$0.77^{+0.12}_{-0.09}$	5.85E-12$^{+3.21E-13}_{-3.21E-13}$	6.32E-12$^{+3.48E-13}_{-3.48E-13}$	1.21E-11$^{+6.64E-13}_{-6.64E-13}$	1.21E-11$^{+6.66E-13}_{-6.66E-13}$	2.11E+20	1.02	30
00030846034	2.61E+03	$3.35^{+1.16}_{-1.19}$	$1.46^{+0.21}_{-0.49}$	$0.96^{+1.12}_{-0.16}$	3.37E-12$^{+2.65E-13}_{-2.65E-13}$	3.37E-12$^{+2.65E-13}_{-2.65E-13}$	6.65E-12$^{+5.22E-13}_{-5.22E-13}$	6.65E-12$^{+5.22E-13}_{-5.22E-13}$	0.00E+00	1.15	13
00030846035	3.28E+03	$4.61^{+1.99}_{-1.17}$	$1.63^{+0.29}_{-0.17}$	$1.00^{+0.08}_{-0.07}$	6.36E-12$^{+3.06E-13}_{-3.06E-13}$	1.19E-11$^{+5.70E-13}_{-5.70E-13}$	1.21E-11$^{+5.83E-13}_{-5.83E-13}$	1.23E-11$^{+5.91E-13}_{-5.91E-13}$	1.47E+21	0.70	39
00030846036	2.63E+03	$4.63^{+1.23}_{-1.21}$	$1.76^{+0.20}_{-0.16}$	$0.86^{+0.10}_{-0.08}$	9.27E-12$^{+4.30E-13}_{-4.30E-13}$	1.34E-11$^{+6.22E-13}_{-6.22E-13}$	1.50E-11$^{+6.99E-13}_{-6.99E-13}$	1.52E-11$^{+7.04E-13}_{-7.04E-13}$	9.11E+20	0.90	41
00030846037	2.90E+03	$2.33^{+0.64}_{-0.31}$	$1.69^{+0.08}_{-0.08}$	$0.96^{+0.29}_{-0.23}$	1.26E-11$^{+4.80E-13}_{-4.80E-13}$	1.26E-11$^{+4.80E-13}_{-4.80E-13}$	2.14E-11$^{+8.13E-13}_{-8.13E-13}$	2.14E-11$^{+8.13E-13}_{-8.13E-13}$	6.87E+13	1.34	63
00030846038	3.23E+03	$3.77^{+0.99}_{-0.66}$	$1.95^{+0.16}_{-0.10}$	$0.85^{+0.08}_{-0.08}$	1.79E-11$^{+5.29E-13}_{-5.29E-13}$	2.64E-11$^{+7.80E-13}_{-7.80E-13}$	2.58E-11$^{+7.61E-13}_{-7.61E-13}$	2.60E-11$^{+7.69E-13}_{-7.69E-13}$	1.06E+21	1.08	98
00030846039	4.05E+03	$3.78^{+1.39}_{-0.90}$	$1.68^{+0.20}_{-0.11}$	$0.78^{+0.11}_{-0.11}$	5.63E-12$^{+2.76E-13}_{-2.76E-13}$	5.82E-12$^{+2.86E-13}_{-2.86E-13}$	9.40E-12$^{+4.61E-13}_{-4.61E-13}$	9.41E-12$^{+4.62E-13}_{-4.62E-13}$	9.43E+19	0.77	37
00030846040	3.74E+03	$3.52^{+1.12}_{-1.03}$	$1.86^{+0.18}_{-0.14}$	$0.85^{+0.18}_{-0.14}$	9.78E-12$^{+3.67E-13}_{-3.67E-13}$	1.21E-11$^{+4.53E-13}_{-4.53E-13}$	1.41E-11$^{+5.29E-13}_{-5.29E-13}$	1.42E-11$^{+5.32E-13}_{-5.32E-13}$	5.74E+20	0.81	65
total/mean	8.76E+04	3.49 ± 0.66	1.73 ± 0.22	0.95 ± 0.15	9.68E-12 $\pm$ 4.45E-12	1.25E-11 $\pm$ 6.51E-12	1.48E-11 $\pm$ 5.82E-12	1.49E-11 $\pm$ 5.88E-12	5.47E+20 $\pm$5.32E+20	1.06 $\pm$0.26	47.50 $\pm$23.75

Note. — (a) Exposure time in s; (b) photon index that fits below/above the break energy; (c) break energy of the broken powerlaw fit in keV; (d) fluxes in $ergcm^{-2}s^{-1}$; (e) hydrogen column density in cm^{-2}; (1) the last row shows the total exposure time respective the mean values of the parameters with sample standard deviations.

3.7.2. MASER050819.7+1721

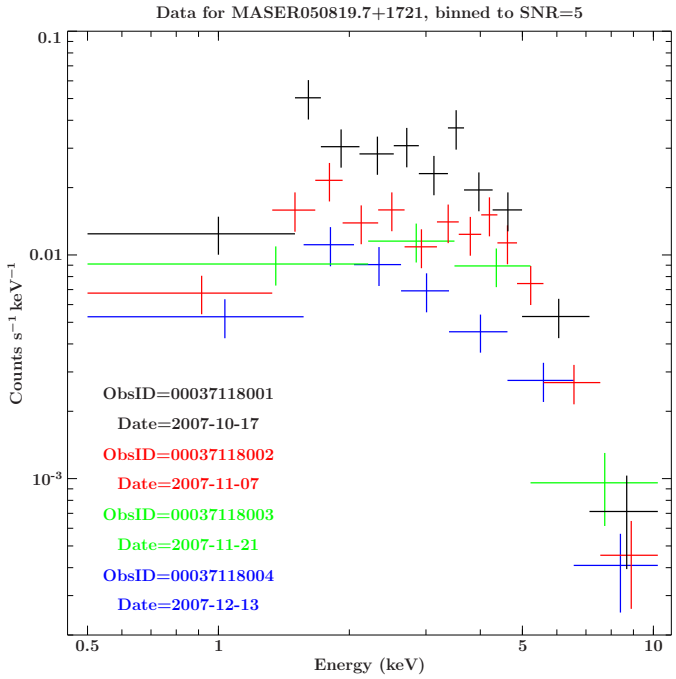

Fig. 23.— Study of the source with *Swift*/XRT. Illustration of the amplitude variability over timescales of months. For the start times and exposure of the respective observation number see Table 5

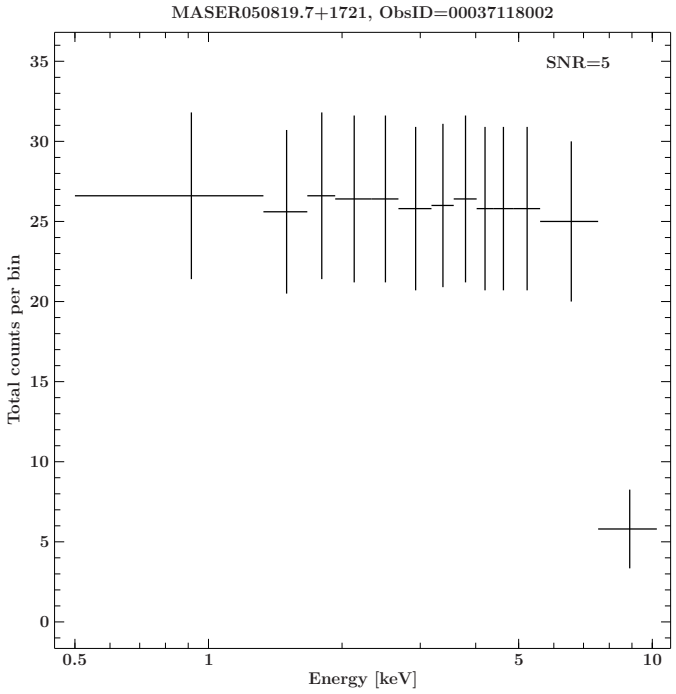

Fig. 24.— *Swift*/XRT data for observation 000037118002. For the comparison of χ^2 and Cash statistic the counts/bin are plotted.

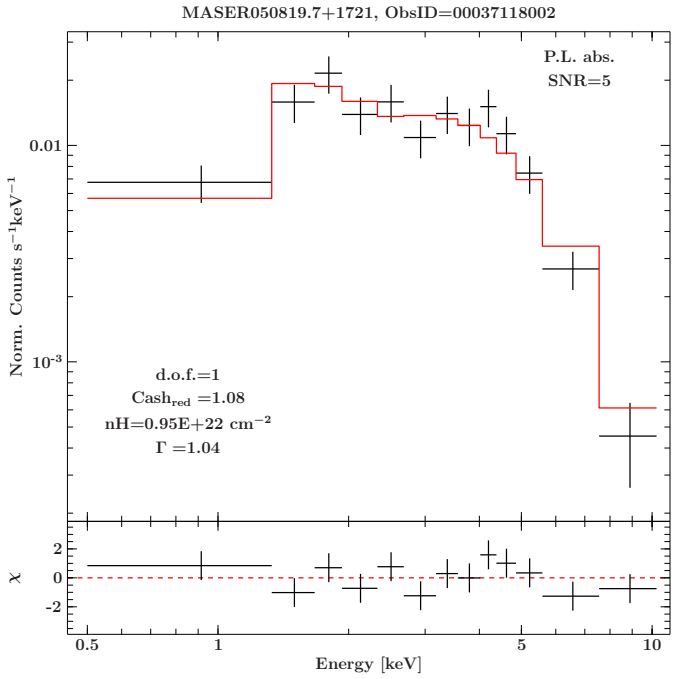

Fig. 25.— *Swift*/XRT analysis exemplified on observation 00037118002. Powerlaw fit with Cash statistic for data binned to SNR ≥ 5 with free hydrogen absorption.

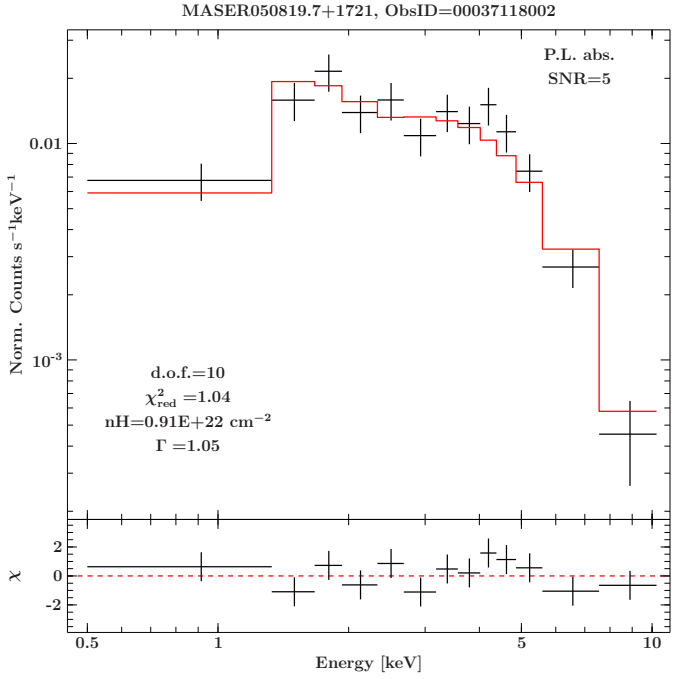

Fig. 26.— *Swift*/XRT analysis exemplified on observation 00037118002. Powerlaw fit with χ^2 statistic for data binned to SNR ≥ 5 with free hydrogen absorption.

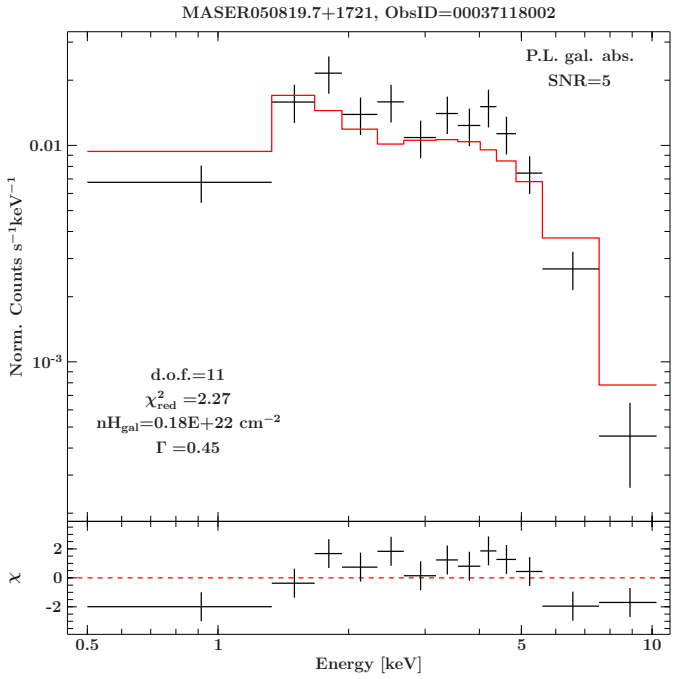

Fig. 27.— *Swift*/XRT analysis exemplified on observation 00037118002. Powerlaw fit with χ^2 statistic for data binned to SNR ≥ 5 with galactic absorption.

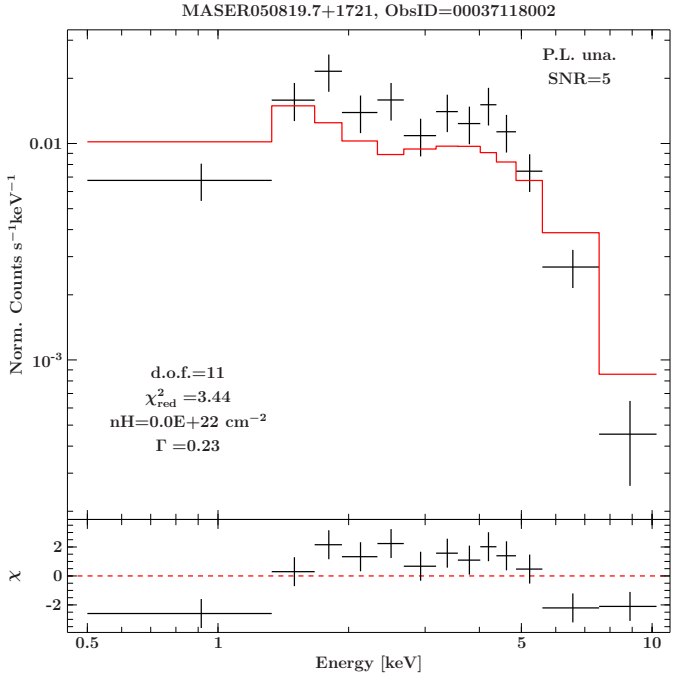

Fig. 28.— *Swift*/XRT analysis exemplified on observation 00037118002. Powerlaw fit with χ^2 statistic for data binned to SNR ≥ 5 without absorption.

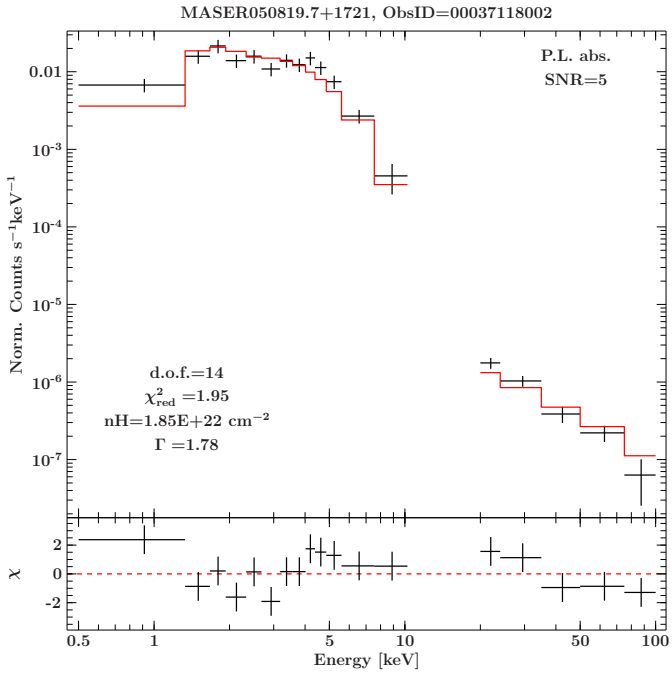

Fig. 29.— Combined *Swift*/XRT and *Swift*/BAT analysis exemplified on observation 00037118002. Powerlaw with χ^2 statistic for data binned to SNR ≥ 5 with free hydrogen absorption.

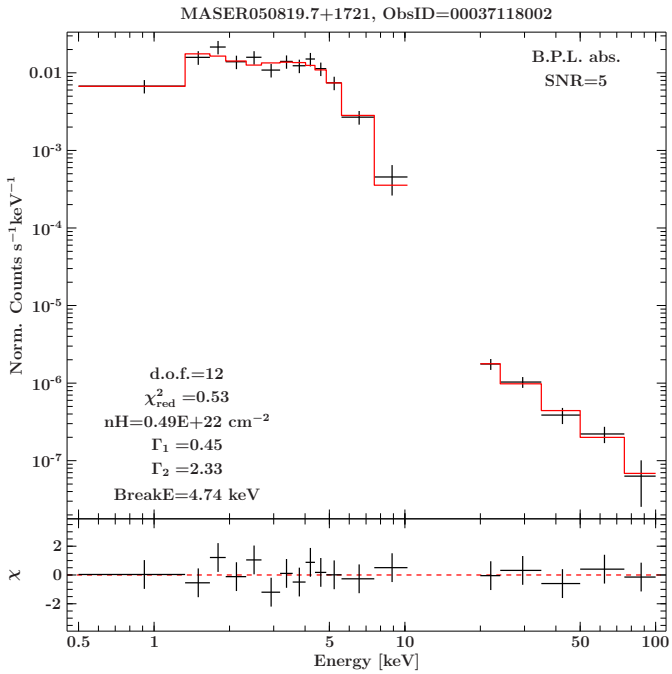

Fig. 30.— Combined *Swift*/XRT and *Swift*/BAT analysis exemplified on observation 00037118002. Broken powerlaw with χ^2 statistic for data binned to SNR ≥ 5 with free hydrogen absorption.

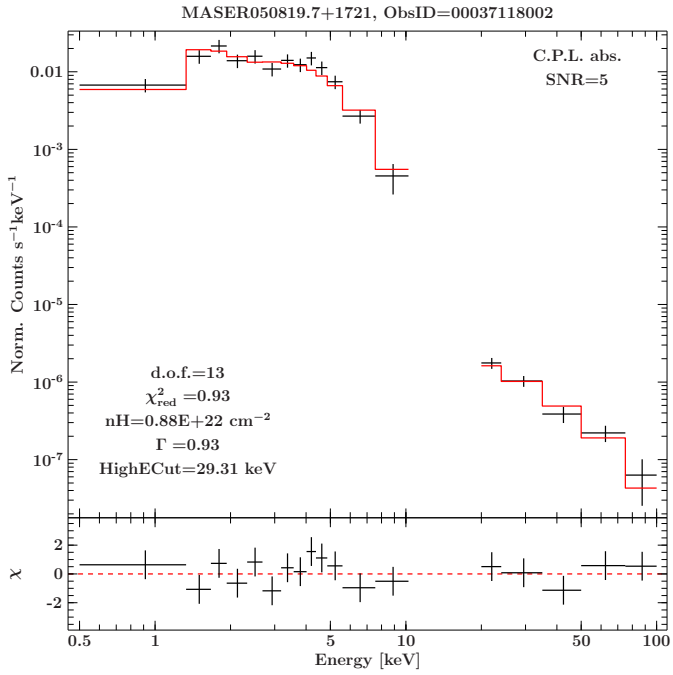

Fig. 31.— Combined *Swift*/XRT and *Swift*/BAT analysis exemplified on observation 00037118002. Cutoff powerlaw with χ^2 statistic for data binned to SNR ≥ 5 with free hydrogen absorption.

Table 8. Results of the *Swift*/XRT spectral model fitting for MASER050819.7+1721 (P.L. abs., SNR=5, χ^2 and Cash)

ObsID	Exposure [a]	Γ [b]	$\mathrm{Flux}_{0.5-2\,\mathrm{keV}}$ [c] measured	intrinsic	$\mathrm{Flux}_{2-10\,\mathrm{keV}}$ [c] measured	intrinsic	N_{H} [d]	$\mathrm{Stat}_{\mathrm{red}}$	d.o.f.
χ^2 statistic									
00037118001	2.26E+03	$1.68^{+0.46}_{-0.40}$	$8.10\text{E-}13^{+8.36\text{E-}14}_{-8.36\text{E-}14}$	$6.18\text{E-}12^{+6.38\text{E-}13}_{-6.38\text{E-}13}$	$1.02\text{E-}11^{+1.05\text{E-}12}_{-1.05\text{E-}12}$	$1.15\text{E-}11^{+1.19\text{E-}12}_{-1.19\text{E-}12}$	1.60E+22	0.86	8
00037118002	4.75E+03	$1.05^{+0.35}_{-0.31}$	$4.11\text{E-}13^{+3.88\text{E-}14}_{-3.88\text{E-}14}$	$1.39\text{E-}12^{+1.32\text{E-}13}_{-1.32\text{E-}13}$	$6.45\text{E-}12^{+6.10\text{E-}13}_{-6.10\text{E-}13}$	$6.82\text{E-}12^{+6.45\text{E-}13}_{-6.45\text{E-}13}$	9.07E+21	1.04	10
00037118003	1.75E+03	$1.99^{+1.12}_{-0.91}$	$2.96\text{E-}13^{+5.34\text{E-}14}_{-5.34\text{E-}14}$	$4.23\text{E-}12^{+7.62\text{E-}13}_{-7.62\text{E-}13}$	$4.11\text{E-}12^{+7.41\text{E-}13}_{-7.41\text{E-}13}$	$5.01\text{E-}12^{+9.03\text{E-}13}_{-9.03\text{E-}13}$	2.24E+22	1.10	1
00037118004	4.91E+03	$1.36^{+0.63}_{-0.54}$	$2.43\text{E-}13^{+3.17\text{E-}14}_{-3.17\text{E-}14}$	$9.83\text{E-}13^{+1.28\text{E-}13}_{-1.28\text{E-}13}$	$2.81\text{E-}12^{+3.66\text{E-}13}_{-3.66\text{E-}13}$	$3.01\text{E-}12^{+3.93\text{E-}13}_{-3.93\text{E-}13}$	9.95E+21	0.38	4
total/mean	1.37E+04	1.52 ± 0.40	$4.40\text{E-}13 \pm 2.56\text{E-}13$	$3.19\text{E-}12 \pm 2.46\text{E-}12$	$5.88\text{E-}12 \pm 3.23\text{E-}12$	$6.59\text{E-}12 \pm 3.64\text{E-}12$	$1.43\text{E+}22 \pm 6.18\text{E+}21$	0.85 ± 0.32	5.75 ± 4.03
Cash statistic									
00037118001	2.26E+03	$1.77^{+0.48}_{-0.55}$	$7.89\text{E-}13^{+5.76\text{E-}14}_{-1.07\text{E-}13}$	$7.86\text{E-}12^{+5.73\text{E-}13}_{-1.06\text{E-}12}$	$1.10\text{E-}11^{+8.05\text{E-}13}_{-1.49\text{E-}12}$	$1.29\text{E-}11^{+9.39\text{E-}13}_{-1.74\text{E-}12}$	1.89E+22	1.14	8
00037118002	4.75E+03	$1.04^{+0.35}_{-0.30}$	$4.09\text{E-}13^{+4.12\text{E-}14}_{-3.52\text{E-}14}$	$1.43\text{E-}12^{+1.44\text{E-}13}_{-1.24\text{E-}13}$	$6.78\text{E-}12^{+6.83\text{E-}13}_{-5.84\text{E-}13}$	$7.18\text{E-}12^{+7.23\text{E-}13}_{-6.18\text{E-}13}$	9.49E+21	1.08	10
00037118003	1.75E+03	$2.00^{+1.10}_{-0.97}$	$2.79\text{E-}13^{+5.29\text{E-}14}_{-4.69\text{E-}14}$	$4.54\text{E-}12^{+8.61\text{E-}13}_{-7.63\text{E-}13}$	$4.28\text{E-}12^{+8.12\text{E-}13}_{-7.19\text{E-}13}$	$5.29\text{E-}12^{+1.00\text{E-}12}_{-8.89\text{E-}13}$	2.42E+22	1.21	1
00037118004	4.91E+03	$1.35^{+0.55}_{-0.51}$	$2.49\text{E-}13^{+3.66\text{E-}14}_{-2.87\text{E-}14}$	$9.50\text{E-}13^{+1.40\text{E-}13}_{-1.10\text{E-}13}$	$2.77\text{E-}12^{+4.08\text{E-}13}_{-3.20\text{E-}13}$	$2.96\text{E-}12^{+4.36\text{E-}13}_{-3.41\text{E-}13}$	9.37E+21	0.41	4
total/mean	1.37E+04	1.54 ± 0.43	$4.31\text{E-}13 \pm 2.49\text{E-}13$	$3.69\text{E-}12 \pm 3.20\text{E-}12$	$6.21\text{E-}12 \pm 3.61\text{E-}12$	$7.07\text{E-}12 \pm 4.23\text{E-}12$	$1.55\text{E+}22 \pm 7.32\text{E+}21$	0.96 ± 0.37	5.75 ± 4.03

Note. — (a) Exposure time in s; (b) photon index (c) fluxes in erg cm^{-2} s^{-1}; (d) hydrogen column density in cm^{-2}; (1) the last row shows the total exposure time respective the mean values of the parameters with sample standard deviations.

Table 9. Results of the combined *Swift*/XRT and *Swift*/BAT spectral model fitting for MASER050819.7+1721 (B.P.L. abs., SNR=5, χ^2)

ObsID	Γ_1 [a]	Γ_2 [a]	BreakE [b]	$\mathrm{Flux}_{0.5-2\,\mathrm{keV}}$ [c] measured	intrinsic	$\mathrm{Flux}_{2-10\,\mathrm{keV}}$ [c] measured	intrinsic	$\mathrm{Flux}_{20-100\,\mathrm{keV}}$ [c] measured	intrinsic	N_H [d]	χ^2_red	d.o.f.
00037118001	$7.02^{+1.98}_{-3.40}$	$2.00^{+0.26}_{-0.32}$	$7.02^{+1.98}_{-3.40}$	$8.20\text{E-}13^{+8.42\text{E-}14}_{-8.42\text{E-}14}$	$2.27\text{E-}09^{+2.33\text{E-}10}_{-2.33\text{E-}10}$	$9.42\text{E-}12^{+9.67\text{E-}13}_{-9.67\text{E-}13}$	$1.36\text{E-}11^{+1.39\text{E-}12}_{-1.39\text{E-}12}$	$1.64\text{E-}11^{+2.51\text{E-}12}_{-2.51\text{E-}12}$	$1.64\text{E-}11^{+2.51\text{E-}12}_{-2.51\text{E-}12}$	3.91E+22	0.53	10
00037118002	$0.45^{+0.03}_{-0.60}$	$4.74^{+1.29}_{-0.67}$	$0.45^{+0.03}_{-0.60}$	$3.94\text{E-}13^{+3.70\text{E-}14}_{-3.70\text{E-}14}$	$7.69\text{E-}13^{+7.21\text{E-}14}_{-7.21\text{E-}14}$	$5.66\text{E-}12^{+5.31\text{E-}13}_{-5.31\text{E-}13}$	$5.84\text{E-}12^{+5.48\text{E-}13}_{-5.48\text{E-}13}$	$1.64\text{E-}11^{+2.50\text{E-}12}_{-2.50\text{E-}12}$	$1.64\text{E-}11^{+2.50\text{E-}12}_{-2.50\text{E-}12}$	4.87E+21	0.53	12
00037118003	$-0.44^{+9.44}_{-0.90}$	$3.59^{+\mathrm{inf}}_{-3.58}$	$-0.44^{+9.44}_{-0.90}$	$3.18\text{E-}13^{+5.70\text{E-}14}_{-5.70\text{E-}14}$	$3.18\text{E-}13^{+5.70\text{E-}14}_{-5.70\text{E-}14}$	$3.92\text{E-}12^{+7.02\text{E-}13}_{-7.02\text{E-}13}$	$3.92\text{E-}12^{+7.02\text{E-}13}_{-7.02\text{E-}13}$	$1.63\text{E-}11^{+2.49\text{E-}12}_{-2.49\text{E-}12}$	$1.63\text{E-}11^{+2.49\text{E-}12}_{-2.49\text{E-}12}$	0.00E+00	0.24	3
00037118004	$1.36^{+0.63}_{-0.54}$	$21.76^{+16.02}_{-17.46}$	$1.36^{+0.63}_{-0.54}$	$2.43\text{E-}13^{+3.17\text{E-}14}_{-3.17\text{E-}14}$	$9.83\text{E-}13^{+1.28\text{E-}13}_{-1.28\text{E-}13}$	$2.81\text{E-}12^{+3.66\text{E-}13}_{-3.66\text{E-}13}$	$3.01\text{E-}12^{+3.93\text{E-}13}_{-3.93\text{E-}13}$	$1.64\text{E-}11^{+2.50\text{E-}12}_{-2.50\text{E-}12}$	$1.64\text{E-}11^{+2.50\text{E-}12}_{-2.50\text{E-}12}$	9.95E+21	0.36	6
total/mean	2.10 ± 3.36	8.02 ± 9.23	2.10 ± 3.36	$4.44\text{E-}13 \pm 2.58\text{E-}13$	$5.67\text{E-}10 \pm 1.13\text{E-}09$	$5.45\text{E-}12 \pm 2.89\text{E-}12$	$6.59\text{E-}12 \pm 4.81\text{E-}12$	$1.63\text{E-}11 \pm 5.64\text{E-}14$	$1.64\text{E-}11 \pm 6.51\text{E-}14$	1.35E+22	0.41 $\pm$0.14	7.75 $\pm$4.03

Note. — (a) photon index that fits below/above the break energy; (b) break energy of the broken powerlaw fit in keV; (c) fluxes in erg cm^{-2} s^{-1}; (d) hydrogen column density in cm^{-2}; (1) the last row shows the total exposure time respective the mean values of the parameters with sample standard deviations.

3.7.3. MASER050137.8-0415

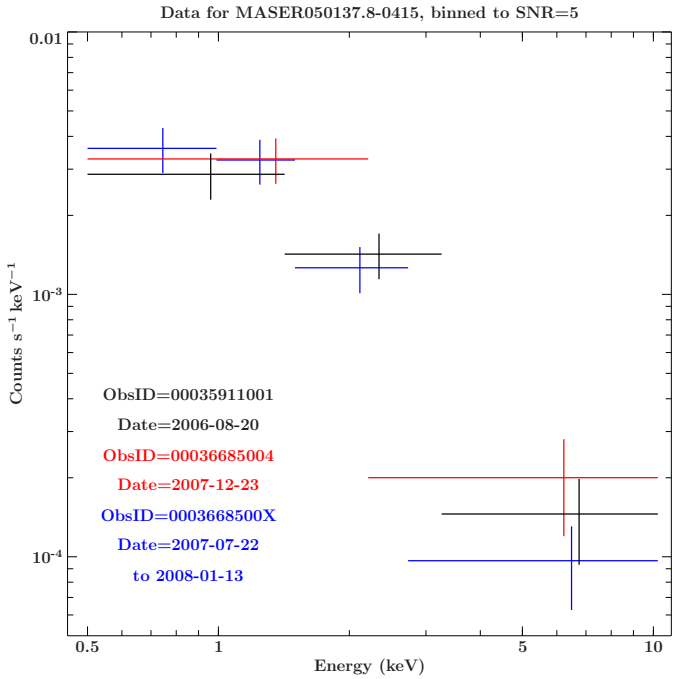

Fig. 32.— Study of the source with *Swift*/XRT, binned to a SNR ≥ 5. No significant amplitude variability can be seen, so a summarizing of PHAs is possible even over longer timescales.

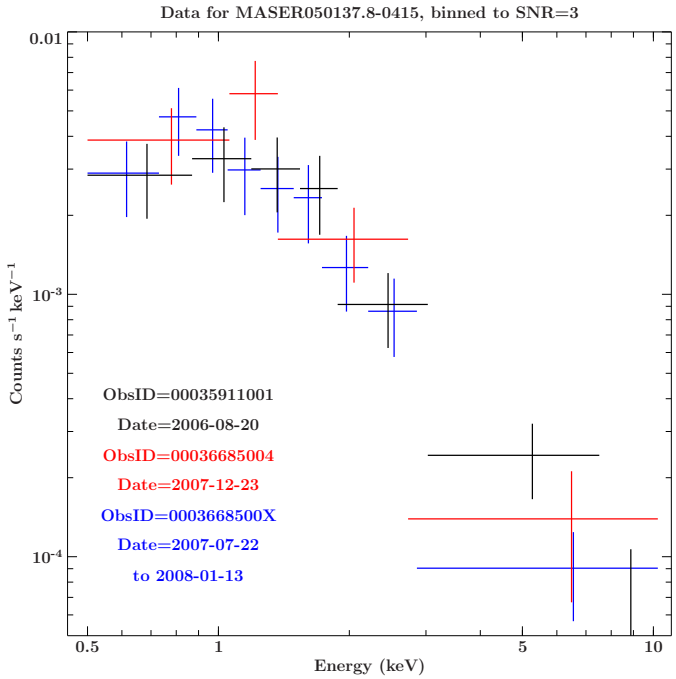

Fig. 33.— Study of the source with *Swift*/XRT, binned to a SNR ≥ 3. No significant amplitude variability can be seen, so a summarizing of PHAs is possible even over longer timescales.

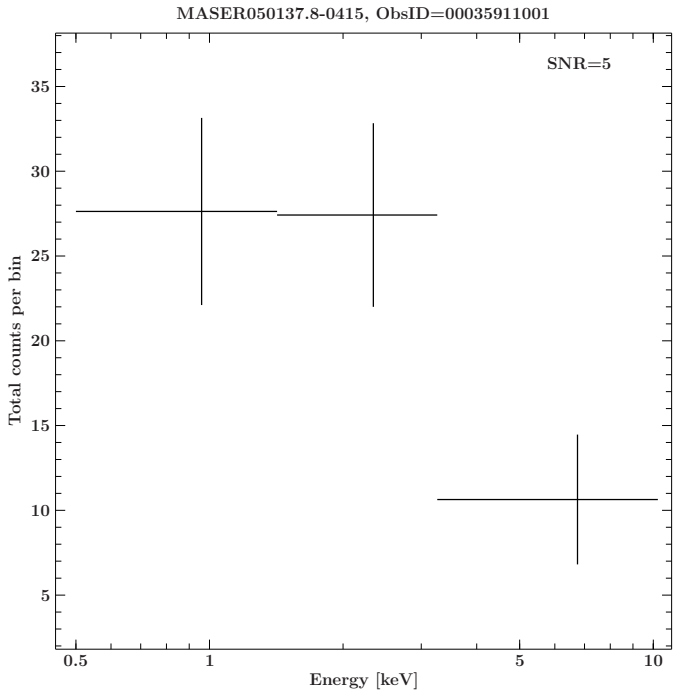

Fig. 34.— *Swift*/XRT data for observation 000037118002, binned to a SNR $\geq$ 5. For the comparison of χ^2 and Cash statistic the counts/bin are plotted.

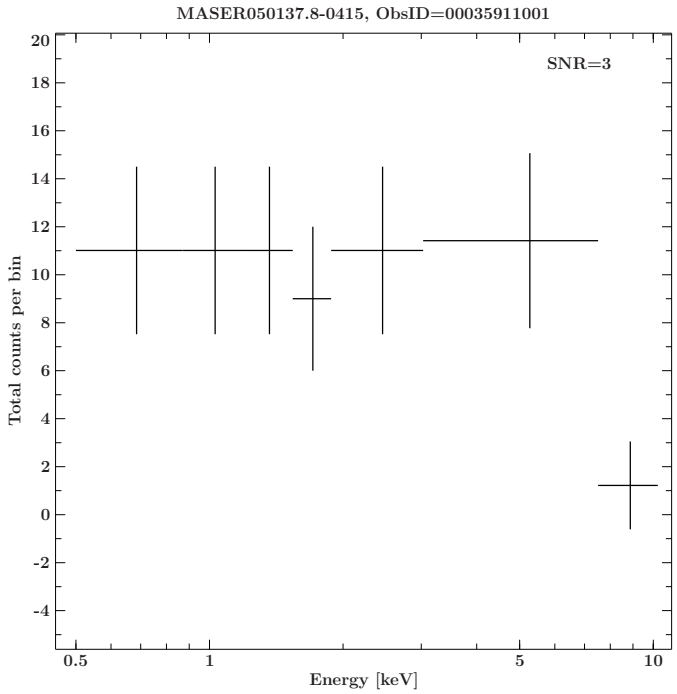

Fig. 35.— *Swift*/XRT data for observation 000037118002, binned to a SNR $\geq$ 3. For the comparance of χ^2 and Cash statistic the counts/bin are plotted.

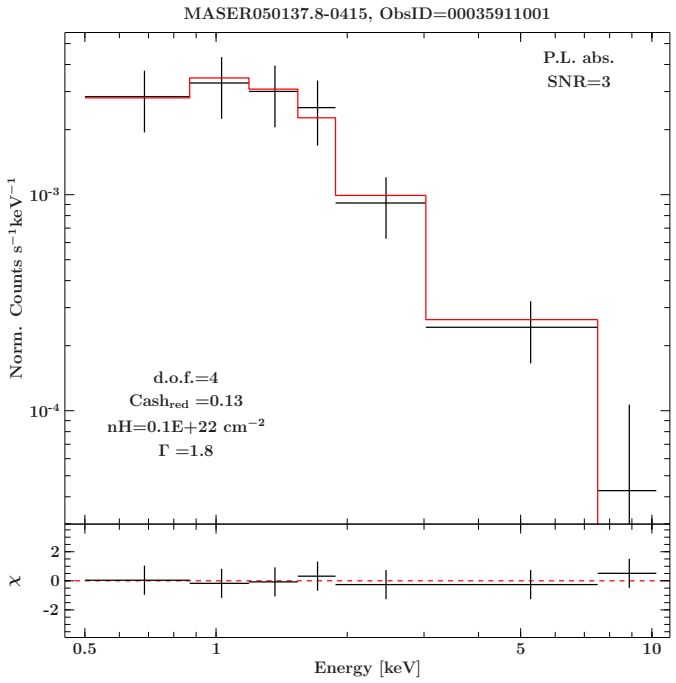

Fig. 36.— *Swift*/XRT analysis of observation 00035911001. Powerlaw fit with Cash statistic for data binned to SNR ≥ 3 with free hydrogen absorption.

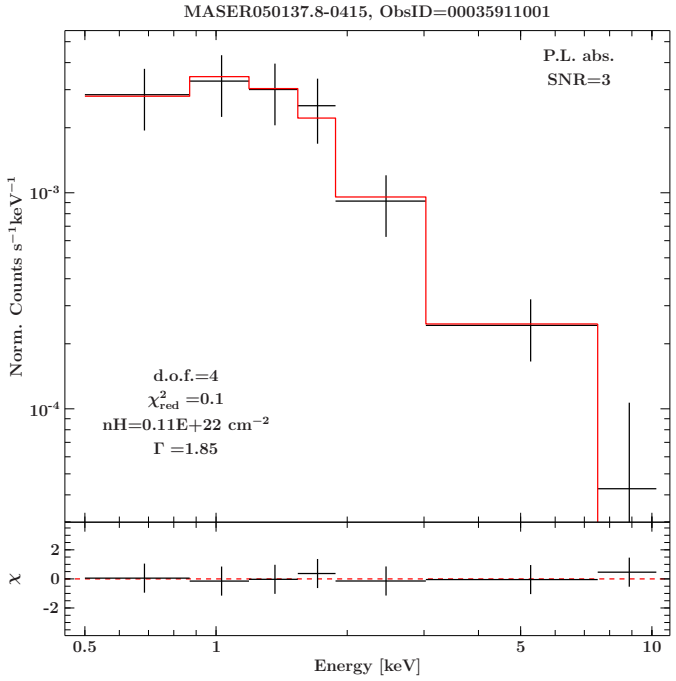

Fig. 37.— *Swift*/XRT analysis of observation 00035911001. Powerlaw fit with χ^2 statistic for data binned to SNR ≥ 3 with free hydrogen absorption.

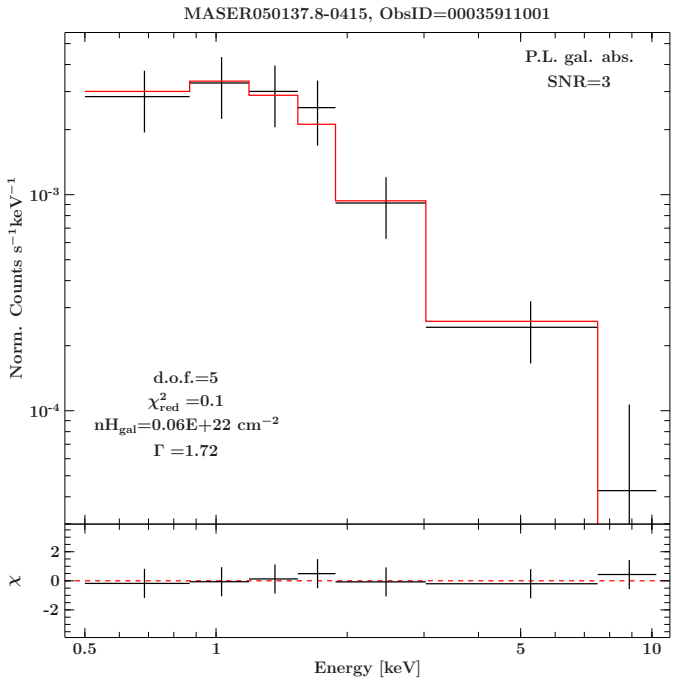

Fig. 38.— *Swift*/XRT analysis of observation 00035911001. Powerlaw fit with χ^2 statistic for data binned to SNR ≥ 3 with galactic absorption.

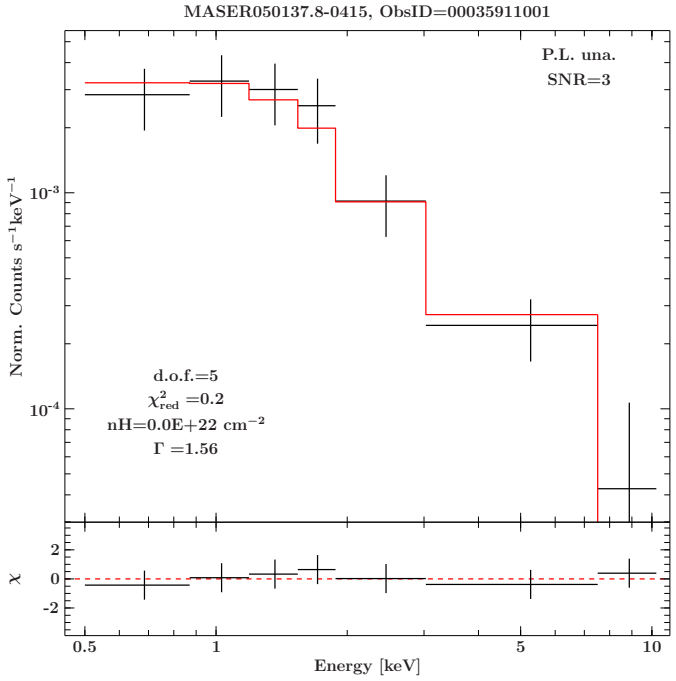

Fig. 39.— *Swift*/XRT analysis of observation 00035911001. Powerlaw fit with χ^2 statistic for data binned to SNR ≥ 3 without absorption.

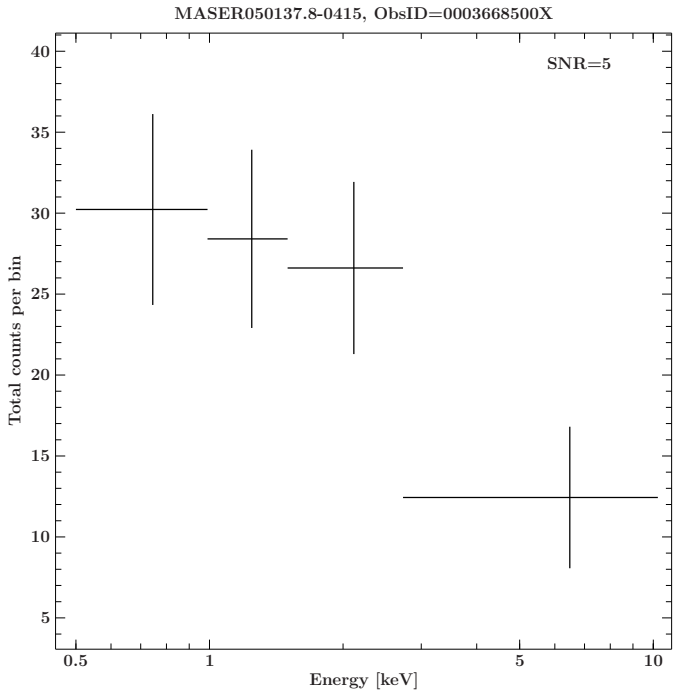

Fig. 40.— *Swift*/XRT data for observation 000037118002. For the comparison of χ^2 and Cash statistic the counts/bin are plotted.

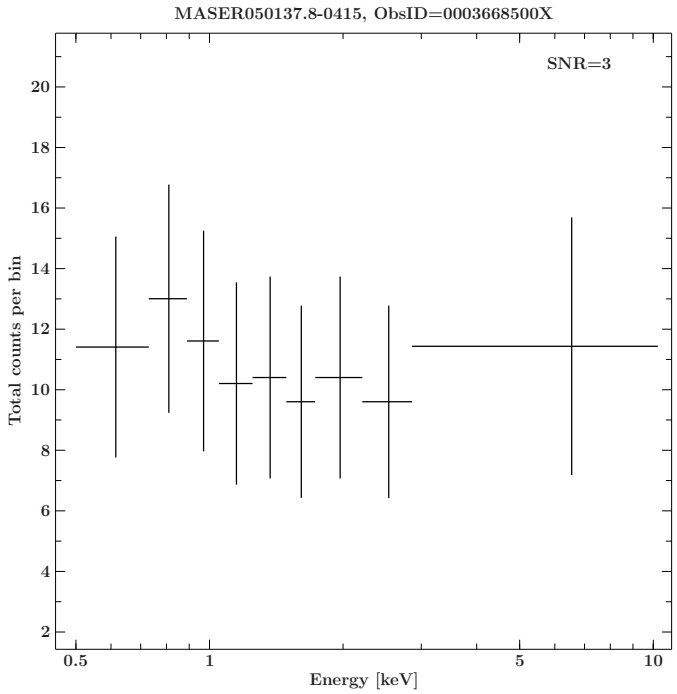

Fig. 41.— *Swift*/XRT data for observation 000037118002. For the comparison of χ^2 and Cash statistic the counts/bin are plotted.

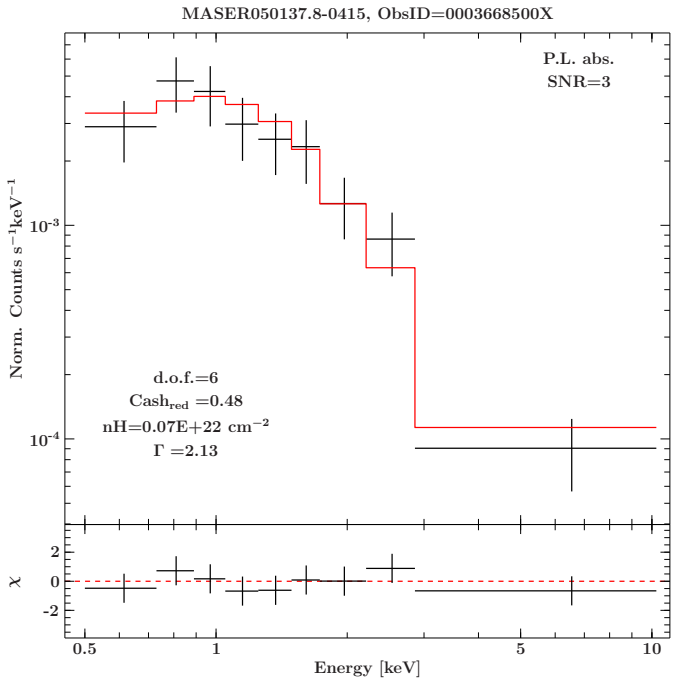

Fig. 42.— *Swift*/XRT analysis of the summarized PHAs of observation 00036685001 to 00036685004. Powerlaw fit with Cash statistic for data binned to SNR ≥ 3 with free hydrogen absorption.

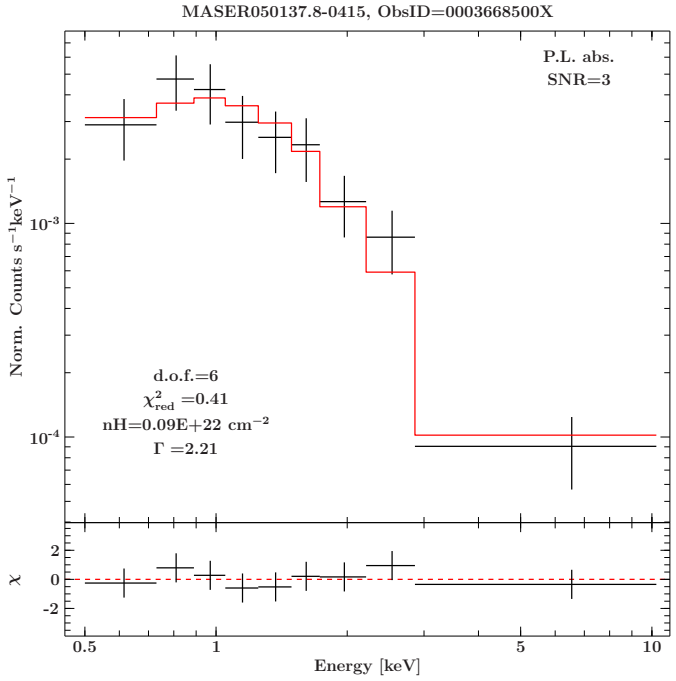

Fig. 43.— *Swift*/XRT analysis of the summarized PHAs of observation 00036685001 to 00036685004. Powerlaw fit with χ^2 statistic for data binned to SNR ≥ 3 with free hydrogen absorption.

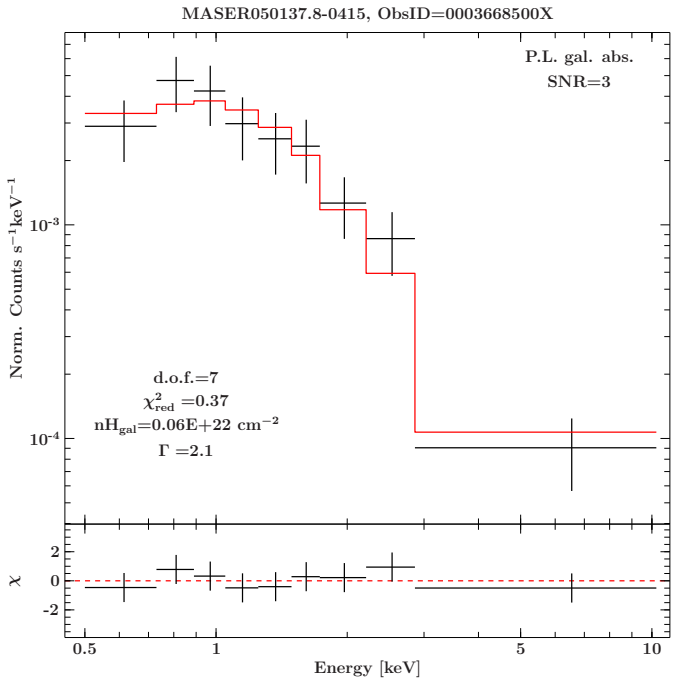

Fig. 44.— *Swift*/XRT analysis of the summarized PHAs of observation 00036685001 to 00036685004. Powerlaw fit with χ^2 statistic for data binned to SNR ≥ 3 with galactic absorption.

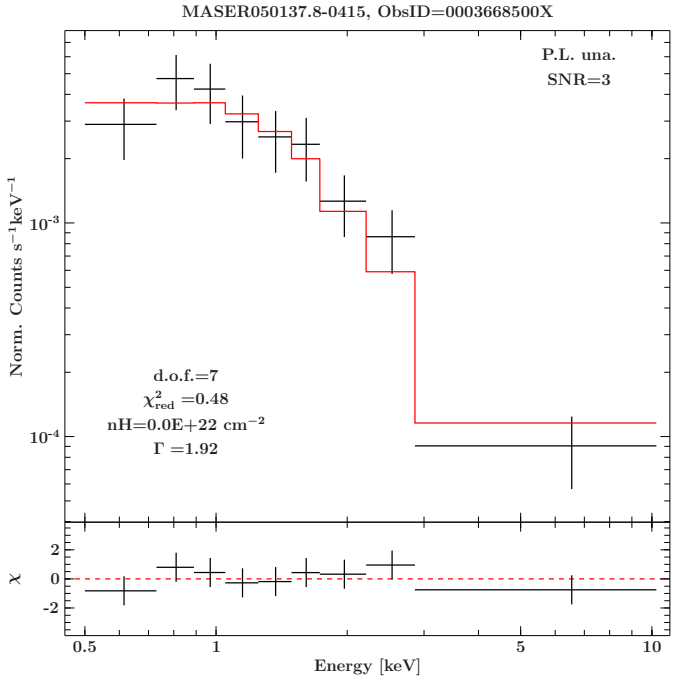

Fig. 45.— *Swift*/XRT analysis of the summarized PHAs of observation 00036685001 to 00036685004. Powerlaw fit with χ^2 statistic for data binned to SNR ≥ 3 without absorption.

Table 10. Results of the *Swift*/XRT spectral model fitting for MASER050137.8-0415 (P.L. abs., SNR=3, χ^2 and Cash)

ObsID	Exposure [a]	Γ [b]	$\mathrm{Flux}_{0.5-2\,\mathrm{keV}}$ [c] measured	intrinsic	$\mathrm{Flux}_{2-10\,\mathrm{keV}}$ [c] measured	intrinsic	N_{H} [d]	$\mathrm{Stat}_{\mathrm{red}}$	d.o.f.
χ^2 statistic									
00035911001	1.05E+04	$1.80^{+0.80}_{-0.52}$	$1.06\text{E-}13^{+2.15\text{E-}14}_{-2.31\text{E-}14}$	$1.41\text{E-}13^{+2.86\text{E-}14}_{-3.07\text{E-}14}$	$2.18\text{E-}13^{+4.41\text{E-}14}_{-4.74\text{E-}14}$	$2.20\text{E-}13^{+4.46\text{E-}14}_{-4.79\text{E-}14}$	1.03E+21	0.13	4
0003668500X	1.71E+04	$2.13^{+0.76}_{-0.44}$	$1.05\text{E-}13^{+1.63\text{E-}14}_{-2.01\text{E-}14}$	$1.33\text{E-}13^{+2.05\text{E-}14}_{-2.53\text{E-}14}$	$1.26\text{E-}13^{+1.94\text{E-}14}_{-2.39\text{E-}14}$	$1.27\text{E-}13^{+1.96\text{E-}14}_{-2.41\text{E-}14}$	7.27E+20	0.48	6
total/mean	2.76E+04	1.97 ± 0.23	1.06E-13 ± 6.86E-16	1.37E-13 ± 6.18E-15	1.72E-13 ± 6.56E-14	1.74E-13 ± 6.63E-14	8.77E+20 ± 2.13E+20	0.31 ± 0.24	5.00 ± 1.41
Cash statistic									
00035911001	1.05E+04	$1.85^{+0.85}_{-0.57}$	$1.05\text{E-}13^{+2.26\text{E-}14}_{-2.26\text{E-}14}$	$1.42\text{E-}13^{+3.06\text{E-}14}_{-3.06\text{E-}14}$	$2.04\text{E-}13^{+4.38\text{E-}14}_{-4.38\text{E-}14}$	$2.06\text{E-}13^{+4.43\text{E-}14}_{-4.43\text{E-}14}$	1.08E+21	0.10	4
0003668500X	1.71E+04	$2.21^{+0.74}_{-0.51}$	$1.00\text{E-}13^{+1.81\text{E-}14}_{-1.81\text{E-}14}$	$1.34\text{E-}13^{+2.41\text{E-}14}_{-2.41\text{E-}14}$	$1.13\text{E-}13^{+2.03\text{E-}14}_{-2.03\text{E-}14}$	$1.14\text{E-}13^{+2.05\text{E-}14}_{-2.05\text{E-}14}$	9.09E+20	0.41	6
total/mean	2.76E+04	2.03 ± 0.25	1.03E-13 ± 3.31E-15	1.38E-13 ± 5.72E-15	1.58E-13 ± 6.43E-14	1.60E-13 ± 6.49E-14	9.94E+20 ± 1.20E+20	0.26 ± 0.22	5.00 ± 1.41

Note. — (a) Exposure time in s; (b) photon index (c) fluxes in erg cm^{-2} s^{-1}; (d) hydrogen column density in cm^{-2}; (1) the last row shows the total exposure time respective the mean values of the parameters with sample standard deviations.

3.7.4. Upper limits and standard deviations

For the calculation of the significances in the following Table 11 the parameter α, which was discussed in section 3.5.5, was needed. As explained, it can be derived as the quotient of the source region to the background region. With the general used sky image source radius of 20 pixel, the inner radius of the background ring of 35 pixel and the outer radius of 57 pixel one gets the value $\alpha = 0.1976284585$.

Table 11: Upper limits and standard deviations

Masername	ObsID	Flux1[a]	Flux2[a]	σ[b]	Src.[c]	Bkg.[c]	Exp.[e]
MASER050137.8-0415	00035911001	6.54E-13	3.56E-13	0.0523094	78	45	1.05E+04
MASER050137.8-0415	00036685001	6.59E-13	4.40E-13	0.092362	11	12	1.46E+03
MASER050137.8-0415	00036685002	5.82E-13	3.55E-13	0.0740112	17	16	2.54E+03
MASER050137.8-0415	00036685004	7.73E-13	3.55E-13	0.185222	42	25	4.99E+03
MASER050137.8-0415	00036685005	4.96E-13	2.78E-13	0.391009	25	15	4.28E+03
MASER050137.8-0415	00036685006	6.33E-13	4.21E-14	0.0284023	20	20	3.86E+03
MASER050137.8-0415	0003668500X	6.34E-13	2.72E-13	2.33204E-05	115	88	1.71E+04
MASER055542.6+0323	00040761001	not possible	9.00E-14	0.0057128	3	11	2.88E+03
MASER055542.6+0323	00040761002	5.62E-14	not possible	0.0242554	2	7	2.29E+03
MASER055542.6+0323	0004076100X	6.44E-15	3.16E-14	0.000536944	5	18	5.17E+03
MASER091127.5-1449	00031196001	1.86E-13	1.17E-13	0.0213388	8	13	2.77E+03
MASER091127.5-1449	00031196002	1.30E-13	4.01E-14	5.49313E-05	9	26	5.68E+03
MASER091127.5-1449	00031196003	1.62E-13	not possible	0.0057128	3	11	2.38E+03
MASER091127.5-1449	0003119600X	1.52E-13	3.33E-14	2.72045E-8	20	50	1.08E+04
MASER120224.0+1450	00031536001	2.64E-13	5.95E-14	0.19055	3	5	1.10E+03
MASER120224.0+1450	00031536002	2.19E-13	2.61E-14	0.051636	5	9	2.50E+03
MASER120224.0+1450	00031536003	1.46E-13	1.46E-13	0.438372	5	5	1.99E+03
MASER120224.0+1450	00031536004	7.47E-14	5.44E-15	0.000046271	7	25	6.49E+03
MASER120224.0+1450	0003153600X	1.33E-13	3.77E-14	1.68004E-6	17	39	1.21E+04
MASER144536.8+2702	00037385001	1.62E-13	6.40E-13	0.156748	60	33	9.38E+03

Note. — (a) upper limit of the flux in erg cm^{-2} s^{-1}; Flux1 = Flux$_{0.5-2\,\mathrm{keV}}$; Flux2 = Flux$_{2-10\,\mathrm{keV}}$. (b) significance of a positive detection in terms of the standard deviation σ. (c) source counts. (d) background counts. (e) exposure time in ks.

3.7.5. Overview of the final results

All results of the spectral model fitting and upper limit estimation are listed summarized in the following Table 12. This table contains the results of the best fitting methods and observations, which are named in detail in the table notes. For sources with several observations the mean values of the foregoing tables are listed. For sources where only upper limits could be estimated no photon indices and hydrogen column densities could be given.

Table 12: Overview of the final results

Masername	#Obs[a]	Tot. exp.[b] (ks)	Γ[c]	Flux$^{d}_{0.5-2\,\mathrm{keV}}$ (erg cm^{-2} s^{-1})	Flux$^{d}_{2-10\,\mathrm{keV}}$ (erg cm^{-2} s^{-1})	nH[e] (cm^{-2})
MASER050137.8-0415[1]	6	2.76E+04	1.97	1.37E-13	1.74E-13	8.77E+20
			±0.23	±6.81E-16	±6.63E-14	±2.13E+20
MASER050819.7+1721[2]	4	1.37E+04	1.54	3.69E-12	7.07E-12	1.55E+22
			±0.43	±3.20E-12	±4.23E-12	±7.32E+21
MASER055542.6+0323[3]	2	2.88E+03	–	< 6.44E-15	< 3.16E-14	–
MASER091127.5-1449[4]	3	1.08E+04	–	< 1.52E-13	< 3.33E-14	–
MASER120224.0+1450[5]	4	1.21E+04	–	< 1.33E-13	< 3.77E-14	–
MASER121826.5+2948[6]	38	8.76E+04	1.73	1.25E-11	1.49E-11	5.47E+20
			±0.22	±6.51E-12	±5.88E-12	±5.32E+20
MASER144536.8+2702[7]	1	9.38E+03	–	< 1.62E-13	< 6.40E-13	–

Note. — (a) number of analysable observations. (b) total exposure time of all analysable observations that were used for a summarized PHA or calculations of mean values. (c) mean value of the photon index. (d) intrinsic X-ray fluxes of the sources in the given energy ranges. (e) hydrogen column density. (1) mean value of observations 00035911001 and the summarized PHAs 0003668500X with Cash statistic, P.L. abs., SNR=3. (2) mean value of observations 00037118001 to 00037118004 with Cash statistic, P.L. abs., SNR=5. (3) result of the calculation for the summarized PHAs of observations 00040761001 and 00040761002. (4) result of the calculation for the summarized PHAs of observations 00031196001 to 00031196003. (5) result of the calculation for the summarized PHAs of observations 00031536001 to 00031536004. (6) mean value of observations 00030846001 to 00030846041 (whenever they were analysable) with χ^2 statistic, B.P.L. abs., SNR=5; the given photon index is the one above the break energy of the broken powerlaw. (7) results of the calculation for observation 00037385001.

4. Discussion

4.1. Discussion of MASER121826.5+2948

For MASER121826.5+2948, better known as Mkn766, a lot of good single observations are available, because it is used as a reference source in astronomy. Therefore it has already been studied well in the past. The recent data from 2007 is thus used for a comparison with the results of Molendi and Maccacaro (1994). They found out that there are great amplitude variations over timescales of a few days. Therefore, they suggested that the spectra origins in emission from an accretion disk and based their assumption on the fact that no variations in absorbing column densities could be figured out. Moreover, they discussed the apparent soft excess, which also varies from day to day.

This findings can be supported by the analyses done in this bachelor's thesis. According to the different spectral plots and calculated fluxes that were performed the 2007 data shows remarkable flux variations on timescales of a few days (see Figure 14), just as they were reported from Molendi and Maccacaro (1994). Due to the soft excess a powerlaw fit is a too strongly simplified model, even though the reduced statistic values are close to 1. This can be seen directly from the residues at around 1 keV in the powerlaw plots in appendix A.1 and is illustrated in Figure 15. Therefore, a more complex model had to be chosen. Although it is still to simplified to represent the physical aspects of the soft excess, a broken powerlaw with a break energy at $\sim 1\,\mathrm{keV}$ can fit the spectra well (see Figures 20 to 18 and appendix A.1). A cutoff powerlaw model instead has not been reasonable considering the residues (see appendix A.1). One has to note that the reduced statistics reach values below 1 for these both models. This is a hint that the errors are overestimated, even though enough data bins and counts/bin are reached.

In addition, there is just small difference between unabsorbed, galactic absorbed and free-hydrogen absorbed model fits for any of the observations (see Figures 18 to 20 and appendix A.1 for the other observations). The free hydrogen absorption fits result in a mean column density of $\sim 5 \cdot 10^{20}\,\mathrm{cm}^{-2}$ (see Table 7), which is five times the galactic absorption. These results are consistent with the AGN type. As given in Table 2, MASER121826.5+2948 is a Seyfert 1 galaxy and consequently there is no dust torus in the line of sight. An unabsorbed spectra is therefore reasonable. Nevertheless, from March to April 2007[8] the amplitudes of the spectra were constantly on a lower level. This is probably due to the emission process Molendi and Maccacaro (1994) described. Moreover, in this time the soft excess becomes very obvious, as it can be seen clearly in Figure 15.

[8] Observations 00030846021 to 00030846035

Furthermore, fits have also been performed with Cash statistic for a comparison with the results of the χ^2 statistic. As it can be seen from Figure 16 the counts/bin are > 20 except the last bin and hence high enough for using χ^2 statistics. Theory states that the results for both statistics are the same for that case. This can be confirmed by the performed analyses, exemplified by the comparison of Figure 17 and 18 (see also the other plots in appendix A.1).

As a powerlaw model is to simple for the *Swift*/XRT spectra, it does not make sense for the combined analysis with *Swift*/BAT data at all. This gets obvious by considering the residues of the plots (see appendix A.1). Also the broken powerlaw and the cutoff powerlaw are too simplified assumptions in this case, considering the residues in Figures 21 and 22. Moreover, by studying all the other observations given in appendix A.1 it is conspicuous that the break energies of the broken powerlaw and the cutoff energies of the cutoff powerlaw differ from observation to observation. The reason is that now the soft excess as well as the connection to the data bins from $20 - 100\,\mathrm{keV}$ has to be contained in the plot model. Therefore more complicated ones would have to be designed for an ongoing analysis. Furthermore, the differences lead to the conclusion that the strong variability of this source may be another cause. As it is, the BAT data that was provided for this analysis was summarized over months and hence is not simultaneous to the XRT data. Therefore, no final deduction can be drawn from the given data for the *Swift*/XRT and *Swift*/BAT combination, except that a more complex analysis has to be done. Consequently, an additional combined analysis with Cash statistics is not necessary, also seen against the background of the above discussed similarity of the χ^2 and Cash statistic for these observations.

4.2. Discussion of MASER050819.7+1721

An analysis for the summarized PHAs seemed promising in the beginning. However, by reviewing the plot results it got obvious, that the data scatters strongly around the best fit (see appendix A.2). Furthermore, the lowest energy bin does not fit to the rest. At first view, this could be seen as an indicator for a soft excess, but the key is to study the single observations. Figure 23 points out, that there are large amplitude variation periods for this source over time scales of months. Unfortunately, the single observations were separated in time for several weeks, so that a summarizing of PHAs could lead to fitting errors. Therefore, the single observations had to be analysed, even though they offer few degrees of freedom. That is why the errors are probably overestimated and hence the statistic values for all observations except 00037118002 are smaller than 1. For that reason observation 00037118002 was chosen to exemplify the plotting results, since it offers most degrees of freedom, the best fitting statistics and represents kind of a

mean amplitude of the four observations according to Figure 23. The other plots can be seen in appendix A.2.

The counts/bin ratio (see Figure 24) for this observation implies that χ^2 and Cash statistic are theoretically expected to deliver the same results. Consequently, the search for the best absorption model could be performed with the usual χ^2 statistic. Figures 28 to 26 clearly point out, that the source is intrinsic absorbed with a hydrogen column density of $\sim 1 \cdot 10^{22}\,\mathrm{cm}^2$. The unabsorbed model does not fit to the data at all, as it can be seen from the residues and the χ^2 values. Things get better for fits with the galactic absorption model, but obviously just the free hydrogen absorption can explain the data well. This fact gets plausible if one considers the AGN type of this source, which is given in Table 2. MASER050819.7+1721 is a Seyfert 2 galaxy, so there is the X-ray obscuring dust torus in the line of sight. Thereby, also the low count rate can be explained. Consequently, no more complicated fitting models need to be chosen, because the simple absorbed powerlaw can explain the spectra. The amplitude variability of the source is reflected in the estimated fluxes, but a mean value has been calculated. Moreover, a comparison of the results listed in Table 8 shows that theory was right, since χ^2 and Cash give basically the same parameter values.

The combined analysis of *Swift*/XRT and *Swift*/BAT data could therefore be performed for χ^2 statistics and the free hydrogen absorption model according to the previous results. As it can be seen in Figure 29, a simple absorbed powerlaw results in large residues for the *Swift*/BAT data bins. Consequently, a more complicated model has to be chosen to explain the combined spectra from $0.5 - 100\,\mathrm{kev}$. For observation 00037118002 it can be fitted well by a broken powerlaw with a break energy of $\sim 20\,\mathrm{kev}$ or a high energy cutoff at $\sim 30\,\mathrm{kev}$. A close look at the residues of the respective plots (see appendix A.2) shows furthermore that the broken powerlaw is slightly better for all observations. For this reason the broken powerlaw is decided to be the best of the three models for this data range and hence its results are listed in Table 9. However, these show a very strong fluctuation in the photon indices and break energies. No reliable conclusion can therefore be made for that parameters. Nevertheless, the results for the fluxes and the column density are consistent with these of the pure *Swift*/XRT fitting.

4.3. Discussion of MASER050137.8-0415

For data binned to a SNR > 5 an analysis of the formal spectral fit for MASER050137.8-0415 has not been physically reasonable even for the best single observation, number 00035911001, since it did not leave any degrees of freedom (see Figure 34). Also a fit for the summarized PHAs of observation 00036685001 to

00036685004 would not have been meaningful (see Figure 40). In contrast, binned to a SNR > 3 the data has seemed useful at first view. However, if one considers the statistics, whether for χ^2 or Cash, they show values < 1 (see Figures 37 and 43). As discussed in section 3.5, values of this kind are an indicator for overestimated errors, possibly due too few degrees of freedom. That seems surprising if one considers the exposure times of the single observations and the summarized PHA. Observation 00035911001 has an exposure of circa 10.7 ksec, the combined PHAs 0003668500X of 17.3 ksec (see Table 5). Considering the two well shaped spectra for SNR > 3 (see Figures 37 and 43)) this is a sign for a very weak X-ray source. The low emission is consistent with the galaxy type of MASER050137.8-0415, because it is a starburst galaxy (see Table 2). Starburst galaxies are very dense regions with a lot of dust. Consequently, scattering effects cause low X-ray but very high IR luminosities. Furthermore, a comparison of Figure 37 to 39 as well as Figure 43 to 45 indicates that a hydrogen column density of $\sim 10^{23}\,\mathrm{cm}^{-2}$ obscures the source. With regard to the bad statistic values for this object upper limits and standard deviations were calculated, too.

4.4. Discussion of upper limits and standard deviations

A look at the exposure times and the upper limits of the sources listed in Table 11 makes clear that these five sources (MASER055542.6+0323, MASER091127.5 - 1449, MASER120224.0+1450, MASER144536.8+2702 and MASER050137.8-0415) are obviously very weak X-ray emitters. This is also shown by the very low significances that have been calculated for them (see Table 11). Considering the summarized PHAs or the best single observations one can see that the total exposure is in a range of ~ 10 ks. Compared with the observations of MASER121826.5+2948 and MASER050819.7 +1721, which were analysable very well by spectral model fitting, this is even a factor 2 to 3 more in the exposure time. In this context one should take a look at the galaxy types of these five sources.

We have already discussed MASER050137.8-0415 in the previous section and stated that it is a starburst galaxy, which is consistent with the low X-ray emission. Although the standard deviations listed in Table 11 are smaller than 0.4 σ and thus too small to confirm it being a X-ray source, the well fitted spectra is a clear indication for this (see section 4.3). According to the best fitting results[9] in Table 10 the instrinsic flux from $0.5 - 2$ keV has a mean value of $1.38 \cdot 10^{-13} \pm 5.72 \cdot 10^{-15}$ erg cm^{-2} s^{-1}, the one from $2-10$ keV of $1.60 \cdot 10^{-13} \pm 6.49 \cdot 10^{-14}$ erg cm^{-2} s^{-1}. The result of the upper limit calculation is that the flux from $0.5 - 2$ keV is below

[9]here P.L. abs., SNR=3, Cash statistic is considered to be the best model

$4.96{\cdot}10^{-13}$ erg cm^{-2} s^{-1} and the one from 2−10 keV below $2.72{\cdot}10^{-13}$ erg cm^{-2} s^{-1}, considering the weakest measurements from Table 11. Thus, by comparing the results of the upper limit calculations with these of the spectral model fitting one can see that they are consistent with one another. MASER050137.8-0415 is definitely a X-ray source with a typical powerlaw shaped spectra, even though it is a very weak one.

MASER055542.6+0323 is a HII type galaxy, which may explain the low luminosity. Unfortunately there is no information for MASER091127.5-1449 and MASER120224.0+1450 available. However, it is known that MASER144536.8 +2702 is a Sy1.9 type, so the absorbing dust torus of the AGN could give the important information about the hydrogen column density one needs for the statistical connection of X-ray and maser emission.

It is important to have a look at the limits *Swift*/XRT provides. As we have stated in section 3.1 it can measure fluxes down to $2 \cdot 10^{-14}$ erg cm^{-2} s^{-1}. Even though the flux upper limits of the five sources do not undergo this technical limit, they are rather close to it. That may explain why no spectra could be measured with *Swift*/XRT for these sources, although they were mainly exposed over timescales of ~ 10 ks in total. It is therefore necessary to have a closer look with a more sensitive instrument to get more detailed X-ray information for these AGNs, among others the hydrogen column densities needed for the indication of masers. However, meanwhile it is just possible to give upper limits.

5. Conclusion and Perspectives

We have seen that 136 AGN maser sources have been detected with radio interferometry yet, a main part of these by the Megamaser Cosmology Project. As discussed in section 2.6, the connection of X-ray absorbing hydrogen column densities of the AGN and maser appearance can lead to a strongly increased detection rate. Furthermore, the analyses complement one another and give access to detailed information about the AGN. Therefore, in this bachelor's thesis the current X-ray information for maser hosting AGNs has been discussed in detail. We have found out, that from the 43 sources which have not been covered by the original *Swift*/XRT maser fill-in list a total of seven has been detected with *Swift*/XRT meanwhile. These have been analysed in this work. Thereby, it has been possible to study three sources with spectral model fitting, two of these also in combination with *Swift*/BAT data (MASER121826.5+2948 and MASER050819.7+1721). For the other four sources upper limits and standard deviations could be calculated. A closer look at the exposure times of the single sources made clear that five of the seven are very weak X-ray sources, since they have been observed in total over respective timescales of $\sim$ 10 ks. These five sources contain MASER055542.6+0323, MASER091127.5-144, MASER120224.0+1450 and MASER144536.8+2702, for which upper limits could be provided, as well as MASER050137.8-0415, which made a simple spectral model fitting possible, but offered very low counts/bin rates and bad statistics.

It is therefore necessary to take a closer look at these five with a more sensitive telescope, for example *XMM-Newton*. Moreover, ongoing analyses have to be done for the other 17 sources which have already been observed by one of the telescopes *XMM-Newton*, *RXTE*, *Chandra* and *Suzaku* (see table 5). Beyond that it is necessary to study the X-ray emission of the 26 sources which have not been observed at all until now. A good possibility would be another *Swift*/XRT survey for this sample, which could be analysed for a first impression. Afterwards, ongoing analyses could again be figured out with *XMM-Newton* or other more sensitive instruments.

This completing of the X-ray data for the whole 136 AGN masers will help to improve the statistics discussed for example by Zhang et al. (2006) and others. Thus, X-ray information can become a useful and reliable guide for new maser detections. This is even more important if one considers the upcoming X-ray survey eROSITA, the follower of the successful ROSAT survey. With eROSITA hundreds of thousand of unknown X-ray sources are expected to be detected. A solid X-ray guide for masers will thereby increase the number of AGN maser sources dramatically.

A. Appendix

A.1. Remaining spectral model fitting plots for MASER121826.5+2948

ObsID 00030846001

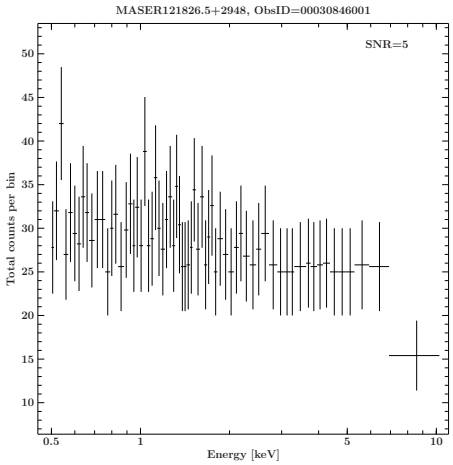

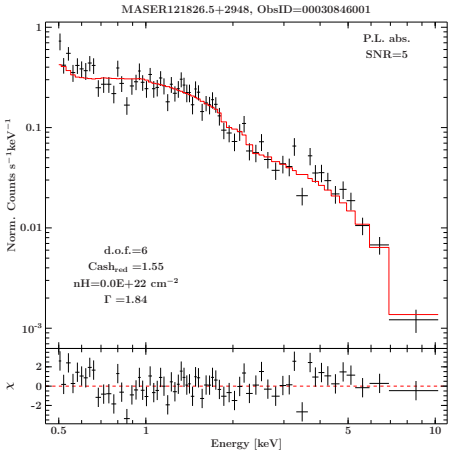

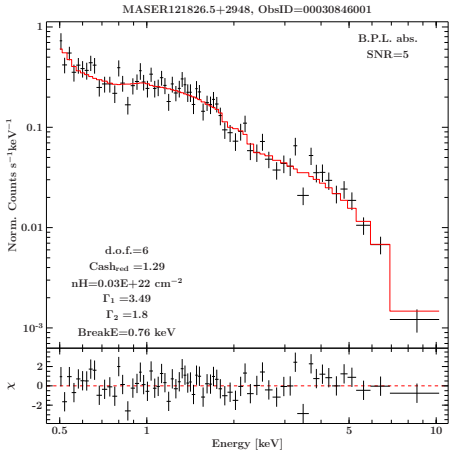

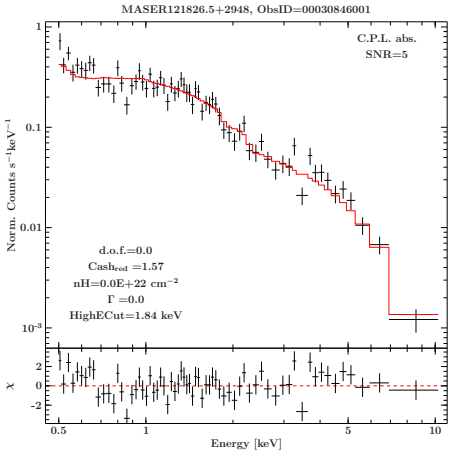

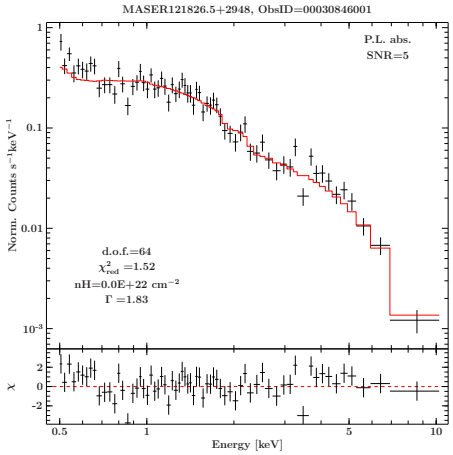

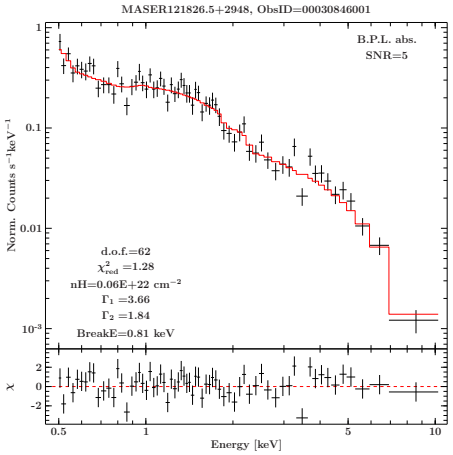

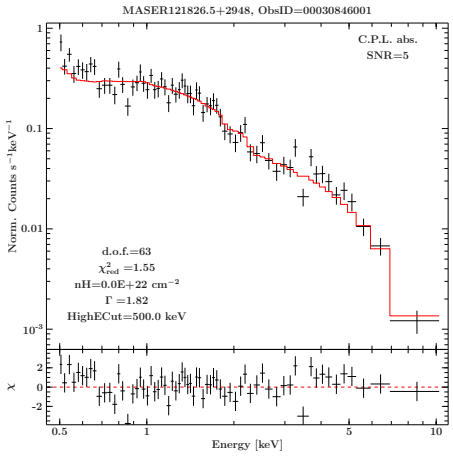
MASER121826.5+2948, ObsID=00030846001
C.P.L. abs.
SNR=5
d.o.f.=63
χ^2_{red} =1.55
nH=0.0E+22 cm^{-2}
Γ =1.82
HighECut=500.0 keV
Norm. Counts s^{-1}keV^{-1}
χ
Energy [keV]

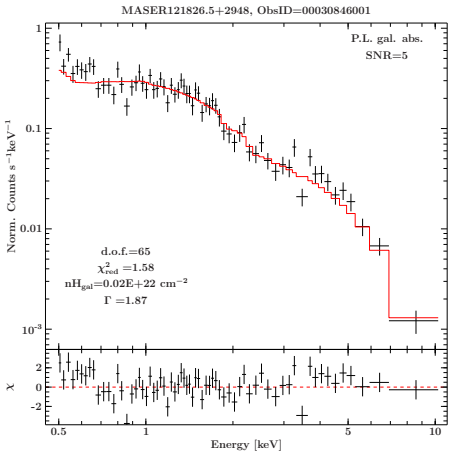
MASER121826.5+2948, ObsID=00030846001
P.L. gal. abs.
SNR=5
d.o.f.=65
χ^2_{red} =1.58
nH$_{gal}$=0.02E+22 cm^{-2}
Γ =1.87
Norm. Counts s^{-1}keV^{-1}
χ
Energy [keV]

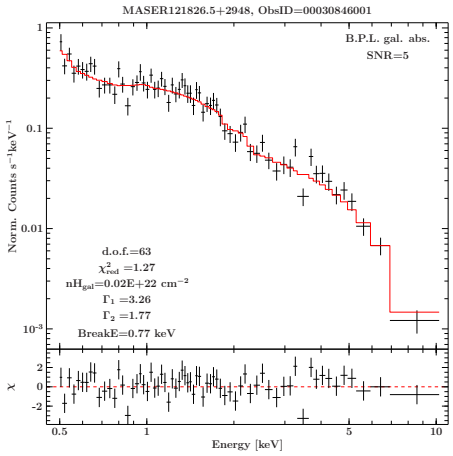
MASER121826.5+2948, ObsID=00030846001
B.P.L. gal. abs.
SNR=5
d.o.f.=63
χ^2_{red} =1.27
nH$_{gal}$=0.02E+22 cm^{-2}
Γ$_1$ =3.26
Γ$_2$ =1.77
BreakE=0.77 keV
Norm. Counts s^{-1}keV^{-1}
χ
Energy [keV]

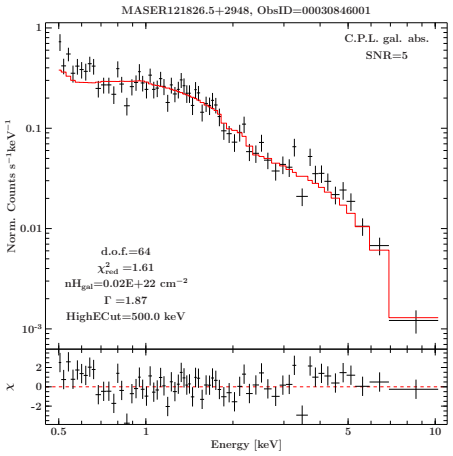
MASER121826.5+2948, ObsID=00030846001
C.P.L. gal. abs.
SNR=5
d.o.f.=64
χ^2_{red} =1.61
nH$_{gal}$=0.02E+22 cm^{-2}
Γ =1.87
HighECut=500.0 keV
Norm. Counts s^{-1}keV^{-1}
χ
Energy [keV]

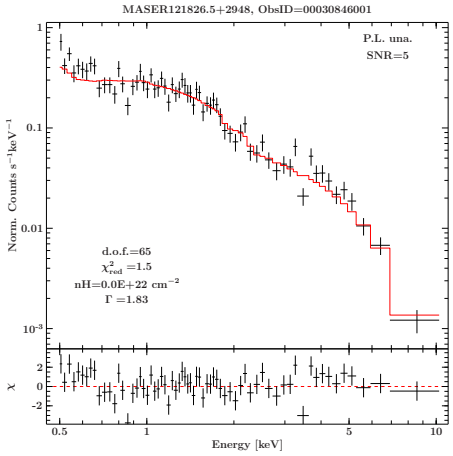
MASER121826.5+2948, ObsID=00030846001
P.L. una.
SNR=5
d.o.f.=65
χ^2_{red} =1.5
nH=0.0E+22 cm^{-2}
Γ =1.83
Norm. Counts s^{-1}keV^{-1}
χ
Energy [keV]

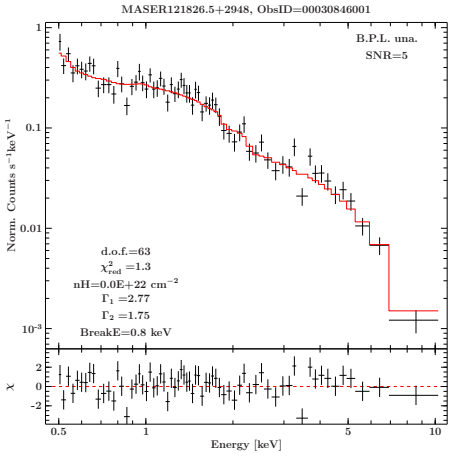
MASER121826.5+2948, ObsID=00030846001
B.P.L. una.
SNR=5
d.o.f.=63
χ^2_{red} =1.3
nH=0.0E+22 cm^{-2}
Γ$_1$ =2.77
Γ$_2$ =1.75
BreakE=0.8 keV
Norm. Counts s^{-1}keV^{-1}
χ
Energy [keV]

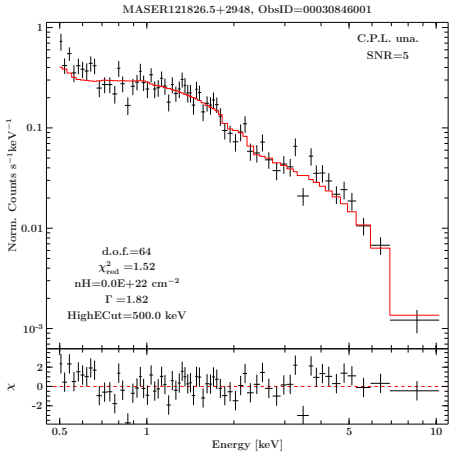
MASER121826.5+2948, ObsID=00030846001
C.P.L. una.
SNR=5
d.o.f.=64
χ^2_{red} =1.52
nH=0.0E+22 cm^{-2}
Γ =1.82
HighECut=500.0 keV
Norm. Counts s^{-1}keV^{-1}
χ
Energy [keV]

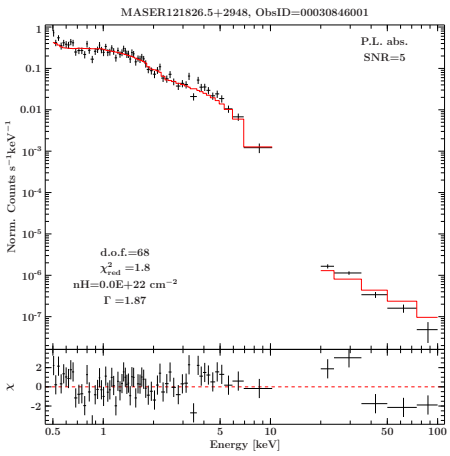
MASER121826.5+2948, ObsID=00030846001
P.L. abs.
SNR=5
d.o.f.=68
χ^2_{red} =1.8
nH=0.0E+22 cm^{-2}
Γ =1.87
Norm. Counts s^{-1}keV^{-1}
χ
Energy [keV]

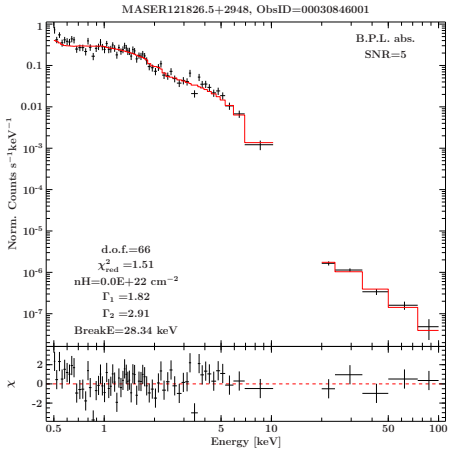
MASER121826.5+2948, ObsID=00030846001
B.P.L. abs.
SNR=5
d.o.f.=66
χ^2_{red} =1.51
nH=0.0E+22 cm^{-2}
Γ_1 =1.82
Γ_2 =2.91
BreakE=28.34 keV
Norm. Counts s^{-1}keV^{-1}
χ
Energy [keV]

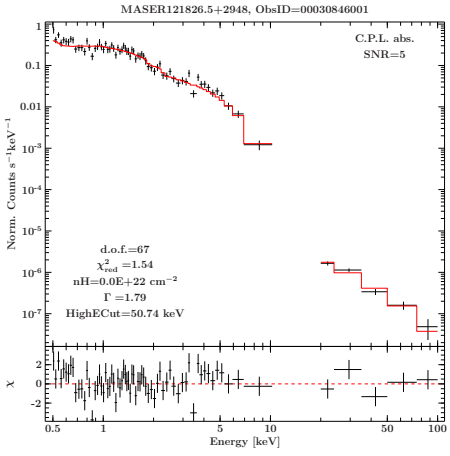
MASER121826.5+2948, ObsID=00030846001
C.P.L. abs.
SNR=5
d.o.f.=67
χ^2_{red} =1.54
nH=0.0E+22 cm^{-2}
Γ =1.79
HighECut=50.74 keV
Norm. Counts s^{-1}keV^{-1}
χ
Energy [keV]

ObsID 00030846003

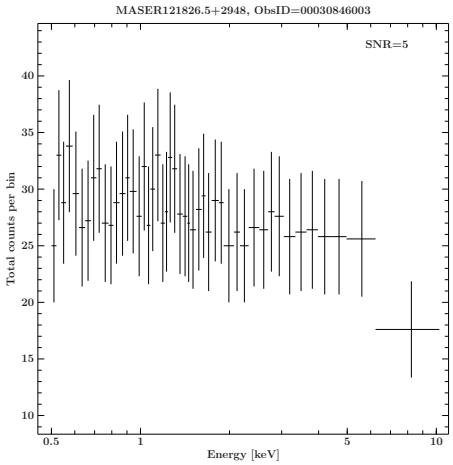

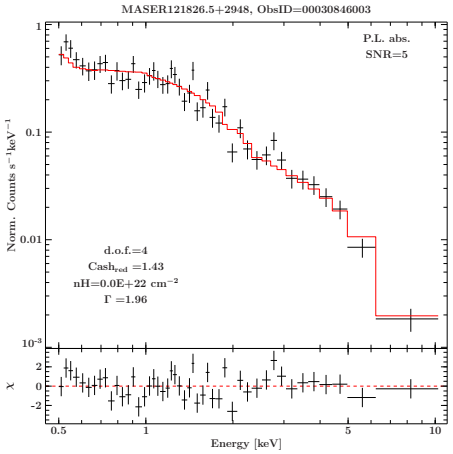

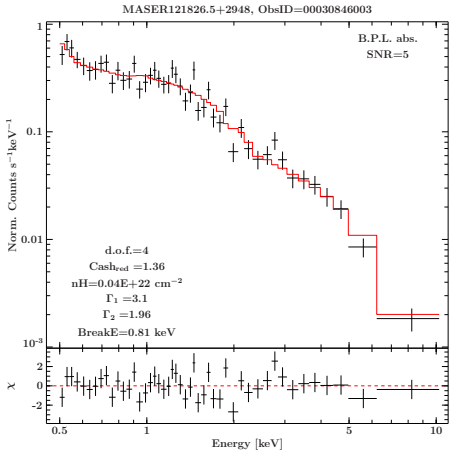

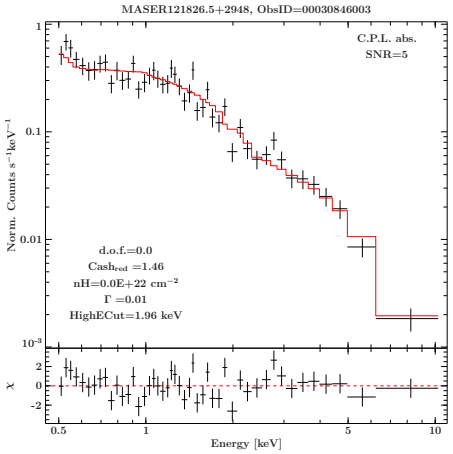

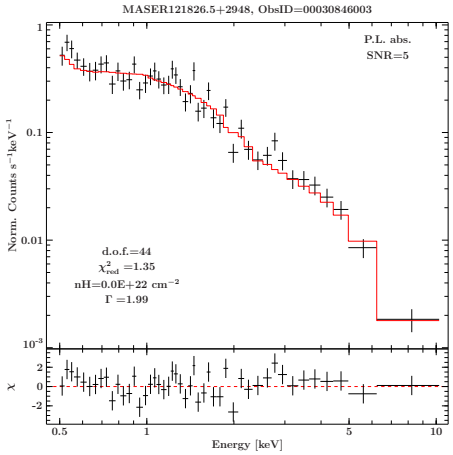

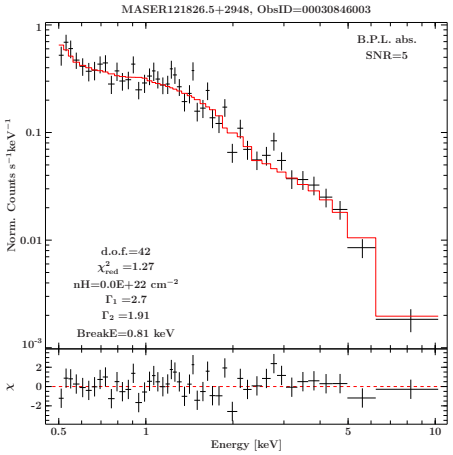

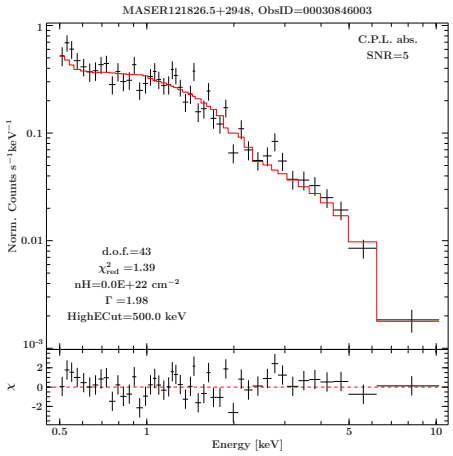
MASER121826.5+2948, ObsID=00030846003
C.P.L. abs.
SNR=5
d.o.f.=43
χ^2_{red} =1.39
nH=0.0E+22 cm^{-2}
Γ =1.98
HighECut=500.0 keV
Norm. Counts s^{-1}keV^{-1}
χ
Energy [keV]

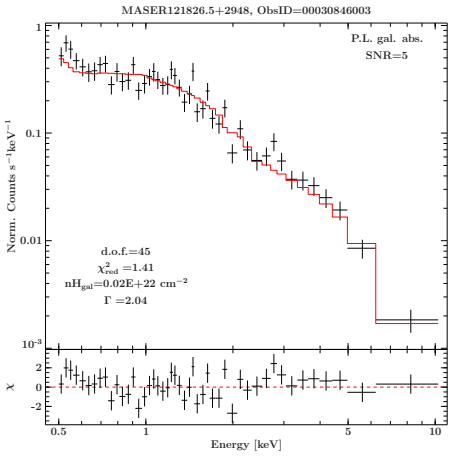
MASER121826.5+2948, ObsID=00030846003
P.L. gal. abs.
SNR=5
d.o.f.=45
χ^2_{red} =1.41
nH_{gal}=0.02E+22 cm^{-2}
Γ =2.04
Norm. Counts s^{-1}keV^{-1}
χ
Energy [keV]

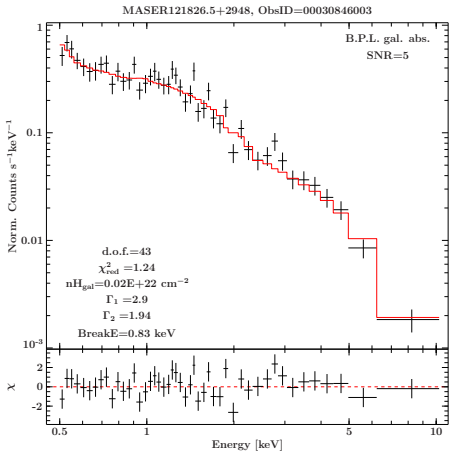
MASER121826.5+2948, ObsID=00030846003
B.P.L. gal. abs.
SNR=5
d.o.f.=43
χ^2_{red} =1.24
nH_{gal}=0.02E+22 cm^{-2}
Γ_1 =2.9
Γ_2 =1.94
BreakE=0.83 keV
Norm. Counts s^{-1}keV^{-1}
χ
Energy [keV]

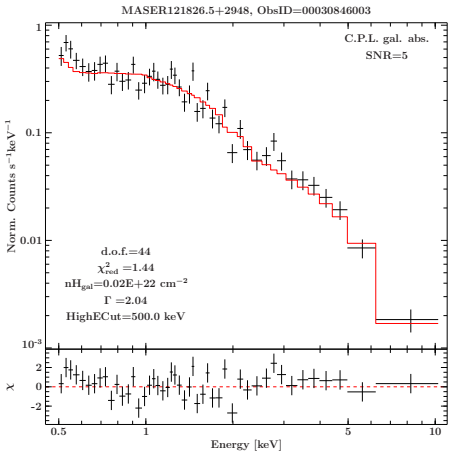
MASER121826.5+2948, ObsID=00030846003
C.P.L. gal. abs.
SNR=5
d.o.f.=44
χ^2_{red} =1.44
nH_{gal}=0.02E+22 cm^{-2}
Γ =2.04
HighECut=500.0 keV
Norm. Counts s^{-1}keV^{-1}
χ
Energy [keV]

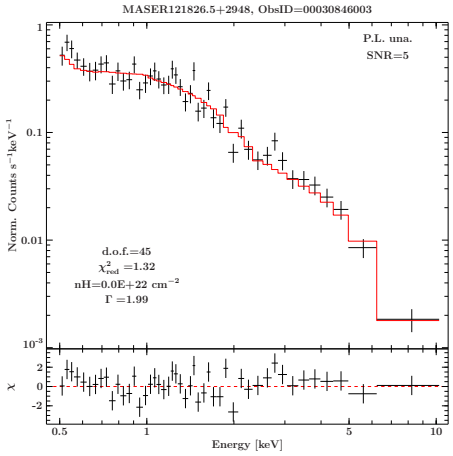
MASER121826.5+2948, ObsID=00030846003
P.L. una.
SNR=5
d.o.f.=45
χ^2_{red} =1.32
nH=0.0E+22 cm^{-2}
Γ =1.99
Norm. Counts s^{-1}keV^{-1}
χ
Energy [keV]

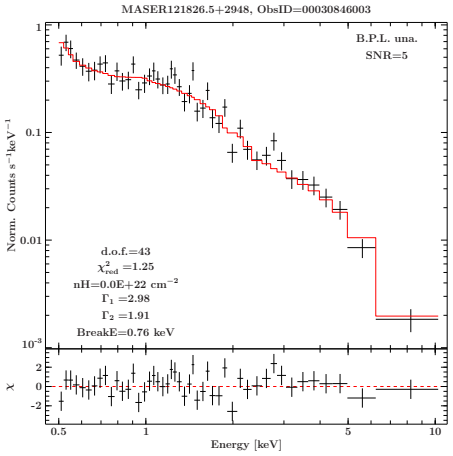
MASER121826.5+2948, ObsID=00030846003
B.P.L. una.
SNR=5
d.o.f.=43
χ^2_{red} =1.25
nH=0.0E+22 cm^{-2}
Γ_1 =2.98
Γ_2 =1.91
BreakE=0.76 keV
Norm. Counts s^{-1}keV^{-1}
χ
Energy [keV]

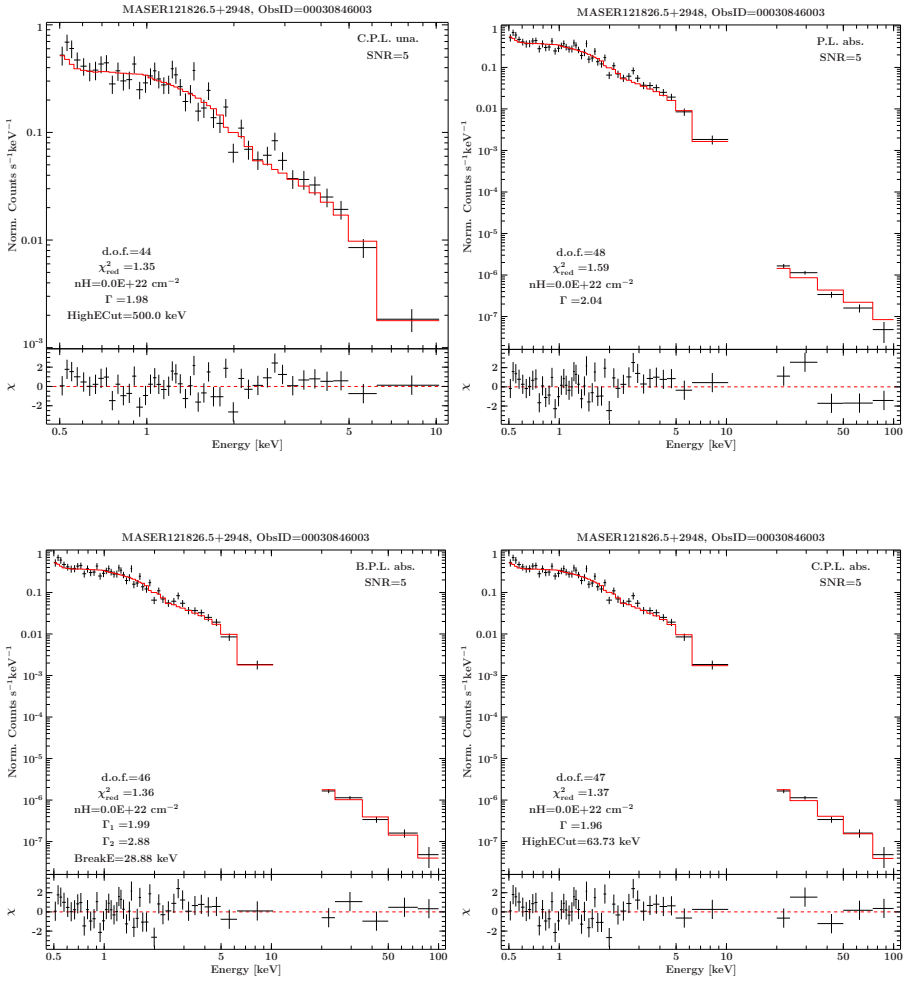
MASER121826.5+2948, ObsID=00030846003
C.P.L. una.
SNR=5
d.o.f.=44
χ^2_{red} =1.35
nH=0.0E+22 cm^{-2}
Γ =1.98
HighECut=500.0 keV
Norm. Counts s^{-1}keV^{-1}
χ
Energy [keV]
MASER121826.5+2948, ObsID=00030846003
P.L. abs.
SNR=5
d.o.f.=48
χ^2_{red} =1.59
nH=0.0E+22 cm^{-2}
Γ =2.04
Norm. Counts s^{-1}keV^{-1}
χ
Energy [keV]
MASER121826.5+2948, ObsID=00030846003
B.P.L. abs.
SNR=5
d.o.f.=46
χ^2_{red} =1.36
nH=0.0E+22 cm^{-2}
Γ$_1$ =1.99
Γ$_2$ =2.88
BreakE=28.88 keV
Norm. Counts s^{-1}keV^{-1}
χ
Energy [keV]
MASER121826.5+2948, ObsID=00030846003
C.P.L. abs.
SNR=5
d.o.f.=47
χ^2_{red} =1.37
nH=0.0E+22 cm^{-2}
Γ =1.96
HighECut=63.73 keV
Norm. Counts s^{-1}keV^{-1}
χ
Energy [keV]

ObsID 00030846004

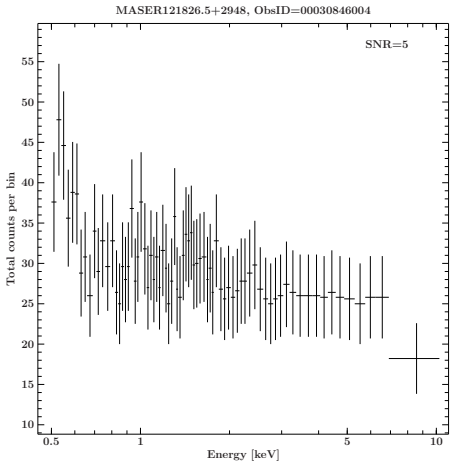

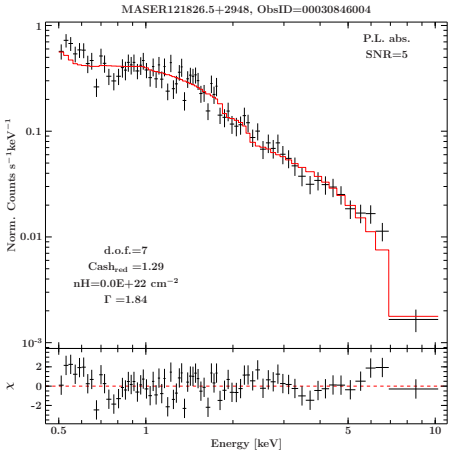

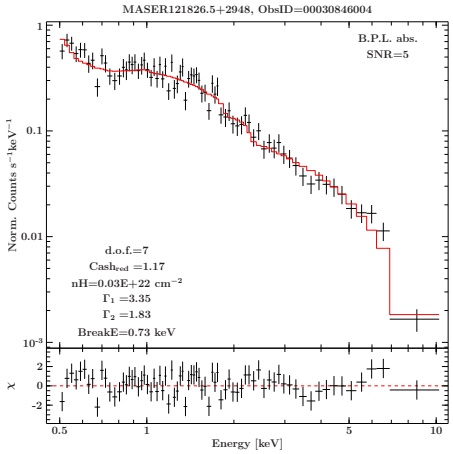

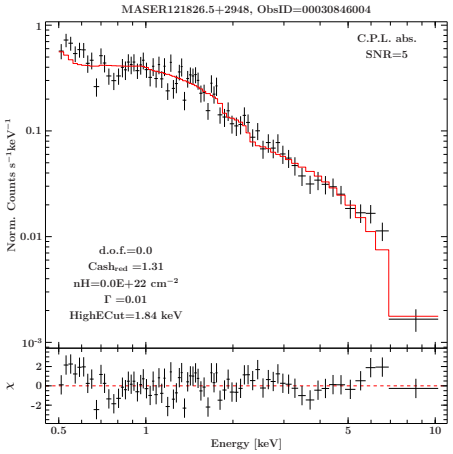

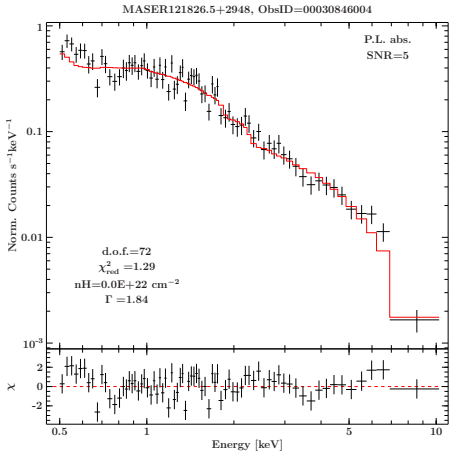

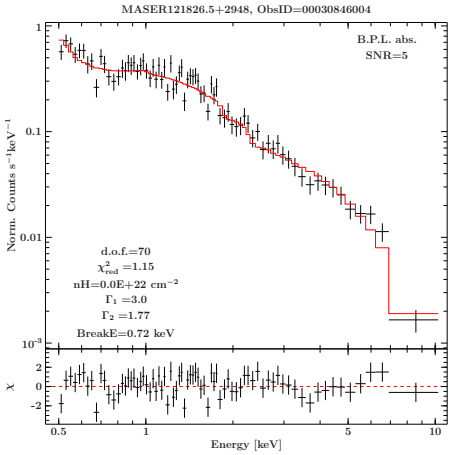

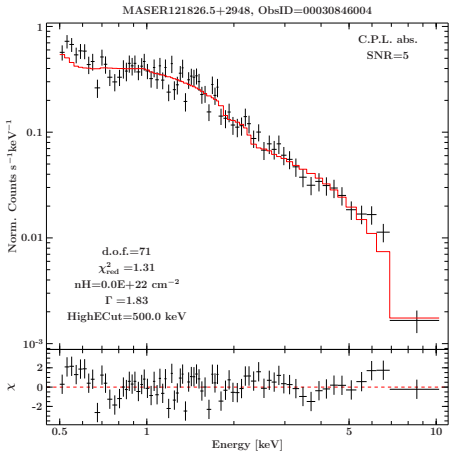
MASER121826.5+2948, ObsID=00030846004
C.P.L. abs.
SNR=5
d.o.f.=71
χ^2_{red} =1.31
nH=0.0E+22 cm^{-2}
Γ =1.83
HighECut=500.0 keV
Norm. Counts s^{-1}keV^{-1}
χ
Energy [keV]

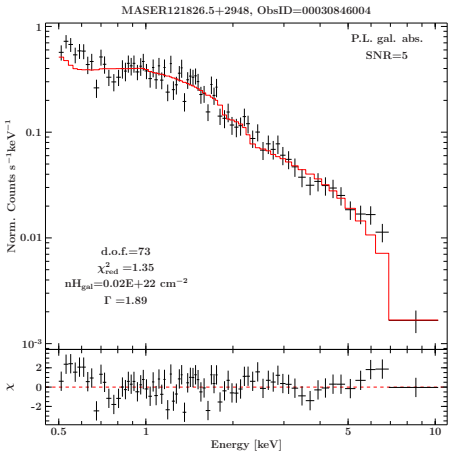
MASER121826.5+2948, ObsID=00030846004
P.L. gal. abs.
SNR=5
d.o.f.=73
χ^2_{red} =1.35
nH_{gal}=0.02E+22 cm^{-2}
Γ =1.89
Norm. Counts s^{-1}keV^{-1}
χ
Energy [keV]

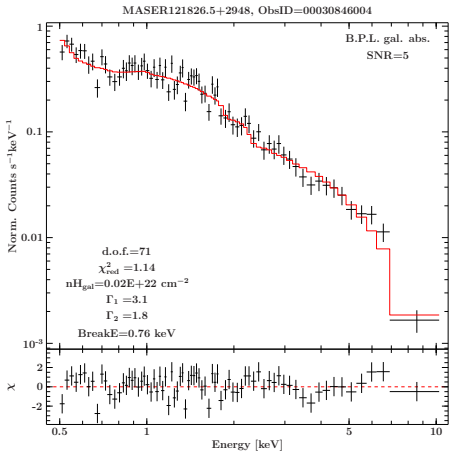
MASER121826.5+2948, ObsID=00030846004
B.P.L. gal. abs.
SNR=5
d.o.f.=71
χ^2_{red} =1.14
nH_{gal}=0.02E+22 cm^{-2}
Γ_1 =3.1
Γ_2 =1.8
BreakE=0.76 keV
Norm. Counts s^{-1}keV^{-1}
χ
Energy [keV]

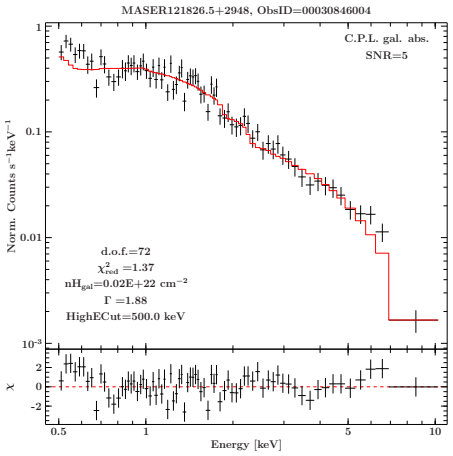
MASER121826.5+2948, ObsID=00030846004
C.P.L. gal. abs.
SNR=5
d.o.f.=72
χ^2_{red} =1.37
nH_{gal}=0.02E+22 cm^{-2}
Γ =1.88
HighECut=500.0 keV
Norm. Counts s^{-1}keV^{-1}
χ
Energy [keV]

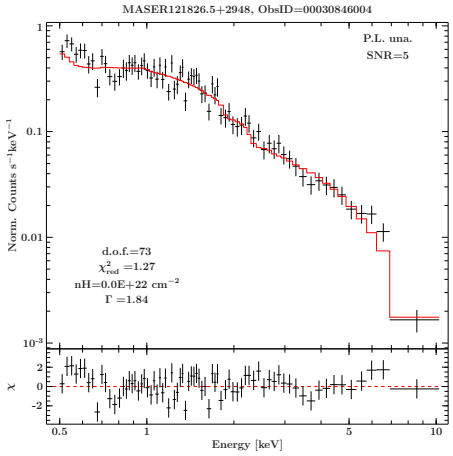
MASER121826.5+2948, ObsID=00030846004
P.L. una.
SNR=5
d.o.f.=73
χ^2_{red} =1.27
nH=0.0E+22 cm^{-2}
Γ =1.84
Norm. Counts s^{-1}keV^{-1}
χ
Energy [keV]

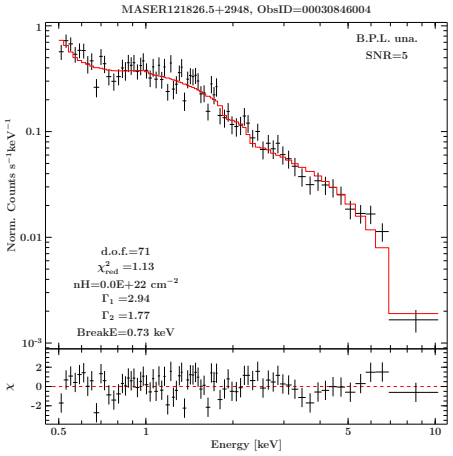
MASER121826.5+2948, ObsID=00030846004
B.P.L. una.
SNR=5
d.o.f.=71
χ^2_{red} =1.13
nH=0.0E+22 cm^{-2}
Γ_1 =2.94
Γ_2 =1.77
BreakE=0.73 keV
Norm. Counts s^{-1}keV^{-1}
χ
Energy [keV]

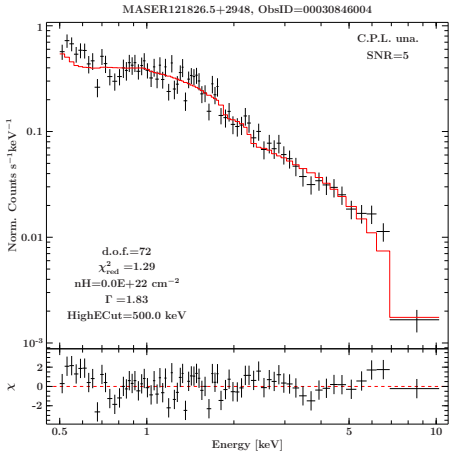
MASER121826.5+2948, ObsID=00030846004
C.P.L. una.
SNR=5
d.o.f.=72
χ^2_{red} =1.29
nH=0.0E+22 cm^{-2}
Γ =1.83
HighECut=500.0 keV
Norm. Counts s^{-1}keV^{-1}
χ
Energy [keV]

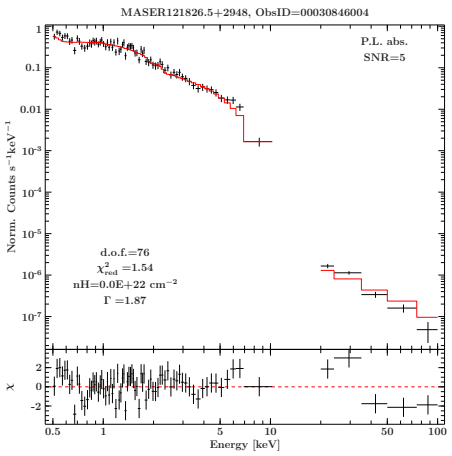
MASER121826.5+2948, ObsID=00030846004
P.L. abs.
SNR=5
d.o.f.=76
χ^2_{red} =1.54
nH=0.0E+22 cm^{-2}
Γ =1.87
Norm. Counts s^{-1}keV^{-1}
χ
Energy [keV]

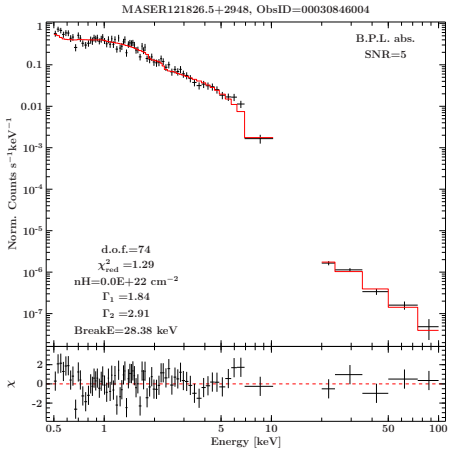
MASER121826.5+2948, ObsID=00030846004
B.P.L. abs.
SNR=5
d.o.f.=74
χ^2_{red} =1.29
nH=0.0E+22 cm^{-2}
Γ_1 =1.84
Γ_2 =2.91
BreakE=28.38 keV
Norm. Counts s^{-1}keV^{-1}
χ
Energy [keV]

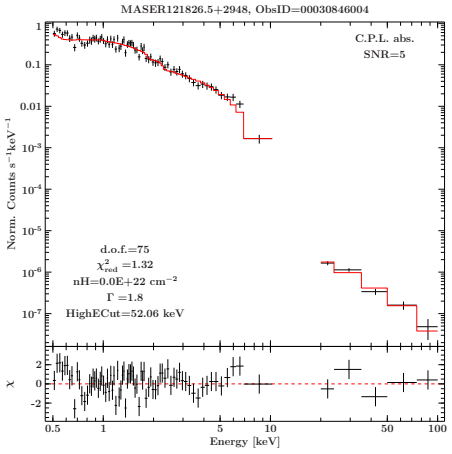
MASER121826.5+2948, ObsID=00030846004
C.P.L. abs.
SNR=5
d.o.f.=75
χ^2_{red} =1.32
nH=0.0E+22 cm^{-2}
Γ =1.8
HighECut=52.06 keV
Norm. Counts s^{-1}keV^{-1}
χ
Energy [keV]

ObsID 00030846005

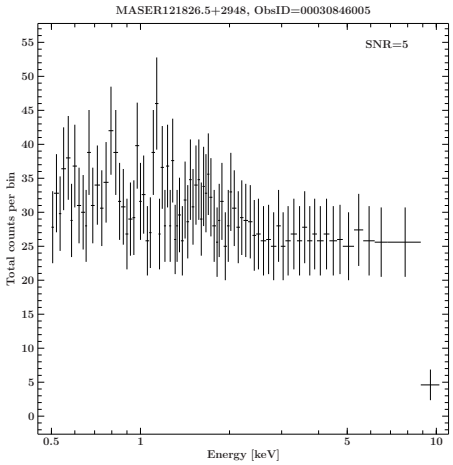

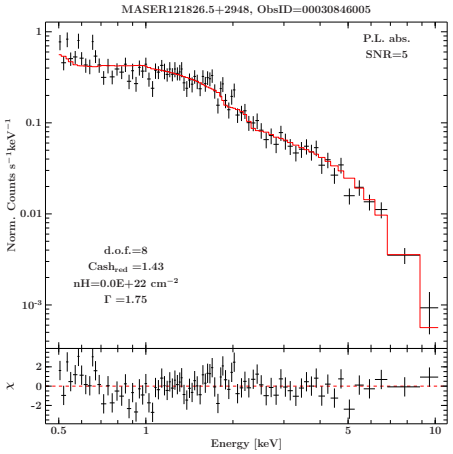

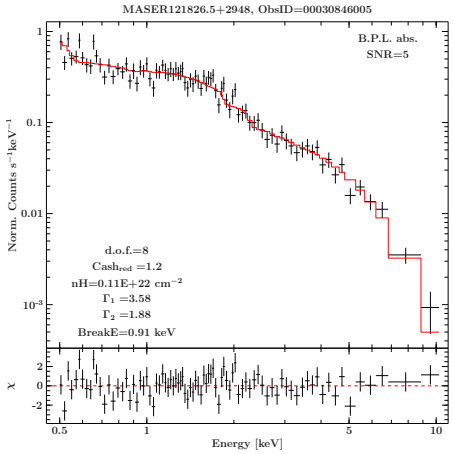

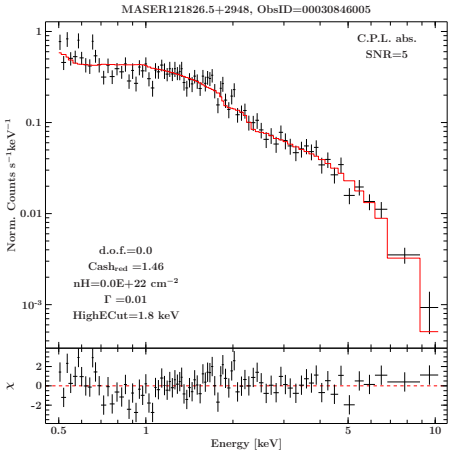

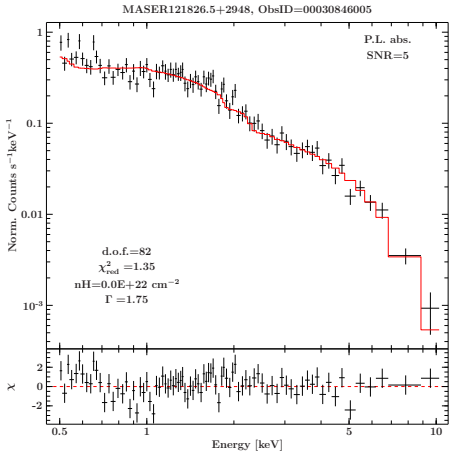

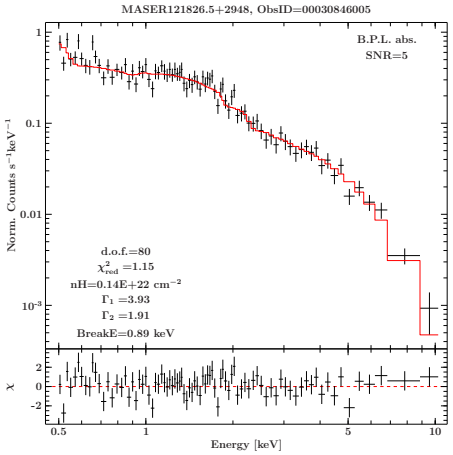

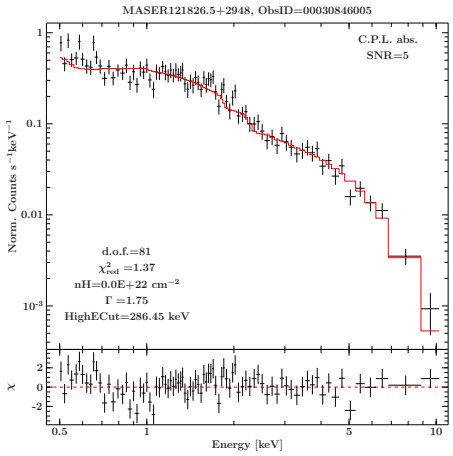
MASER121826.5+2948, ObsID=00030846005
C.P.L. abs.
SNR=5
d.o.f.=81
χ^2_{red} =1.37
nH=0.0E+22 cm^{-2}
Γ =1.75
HighECut=286.45 keV
Norm. Counts s^{-1}keV^{-1}
Energy [keV]

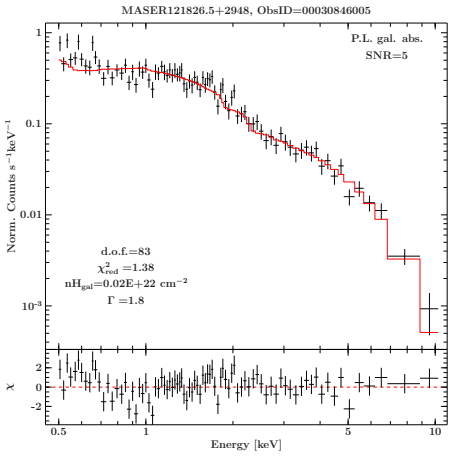
MASER121826.5+2948, ObsID=00030846005
P.L. gal. abs.
SNR=5
d.o.f.=83
χ^2_{red} =1.38
nH$_{gal}$=0.02E+22 cm^{-2}
Γ =1.8
Norm. Counts s^{-1}keV^{-1}
Energy [keV]

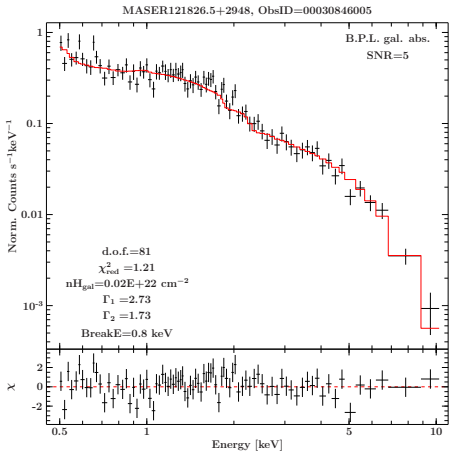
MASER121826.5+2948, ObsID=00030846005
B.P.L. gal. abs.
SNR=5
d.o.f.=81
χ^2_{red} =1.21
nH$_{gal}$=0.02E+22 cm^{-2}
Γ$_1$ =2.73
Γ$_2$ =1.73
BreakE=0.8 keV
Norm. Counts s^{-1}keV^{-1}
Energy [keV]

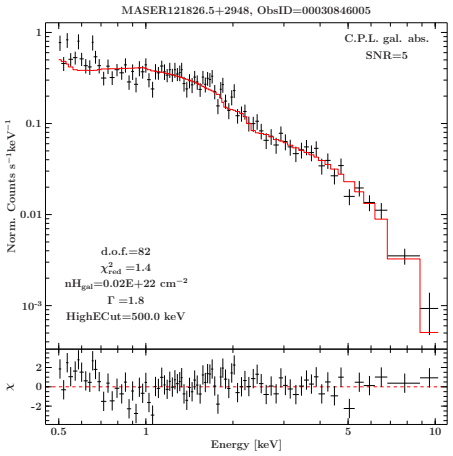
MASER121826.5+2948, ObsID=00030846005
C.P.L. gal. abs.
SNR=5
d.o.f.=82
χ^2_{red} =1.4
nH$_{gal}$=0.02E+22 cm^{-2}
Γ =1.8
HighECut=500.0 keV
Norm. Counts s^{-1}keV^{-1}
Energy [keV]

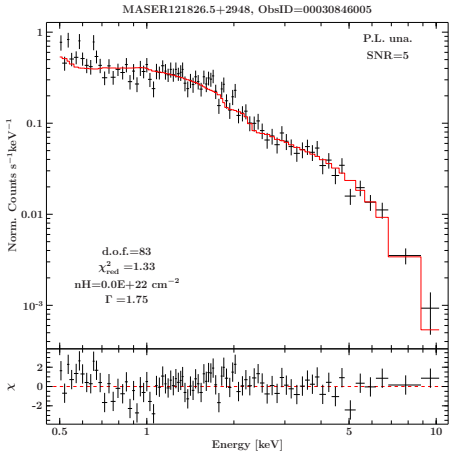
MASER121826.5+2948, ObsID=00030846005
P.L. una.
SNR=5
d.o.f.=83
χ^2_{red} =1.33
nH=0.0E+22 cm^{-2}
Γ =1.75
Norm. Counts s^{-1}keV^{-1}
Energy [keV]

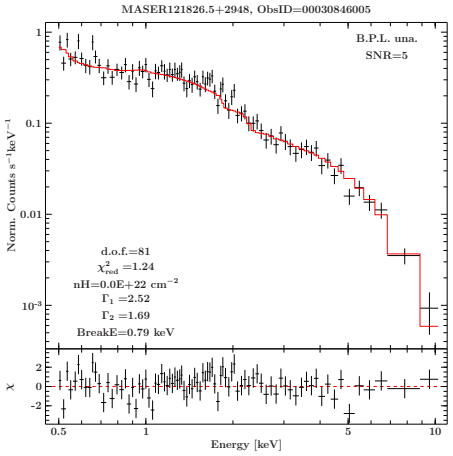
MASER121826.5+2948, ObsID=00030846005
B.P.L. una.
SNR=5
d.o.f.=81
χ^2_{red} =1.24
nH=0.0E+22 cm^{-2}
Γ$_1$ =2.52
Γ$_2$ =1.69
BreakE=0.79 keV
Norm. Counts s^{-1}keV^{-1}
Energy [keV]

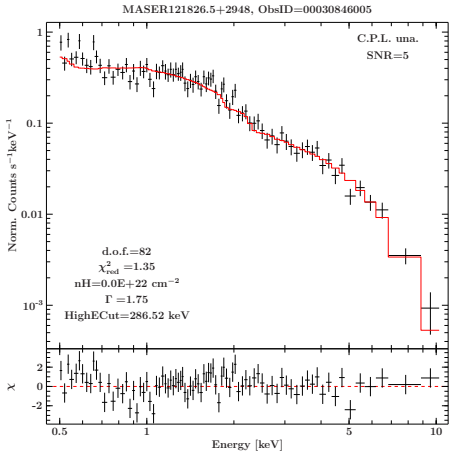
MASER121826.5+2948, ObsID=00030846005
C.P.L. una.
SNR=5
d.o.f.=82
χ^2_{red} =1.35
nH=0.0E+22 cm^{-2}
Γ =1.75
HighECut=286.52 keV
Norm. Counts s^{-1}keV^{-1}
χ
Energy [keV]

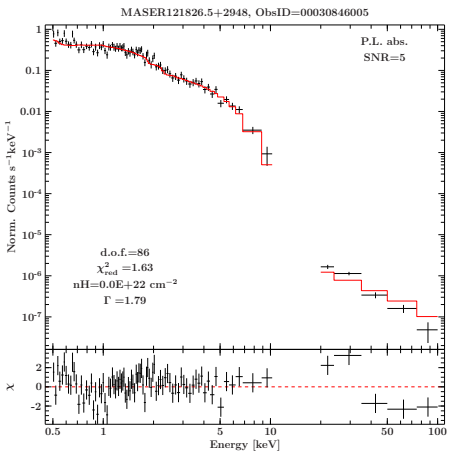
MASER121826.5+2948, ObsID=00030846005
P.L. abs.
SNR=5
d.o.f.=86
χ^2_{red} =1.63
nH=0.0E+22 cm^{-2}
Γ =1.79
Norm. Counts s^{-1}keV^{-1}
χ
Energy [keV]

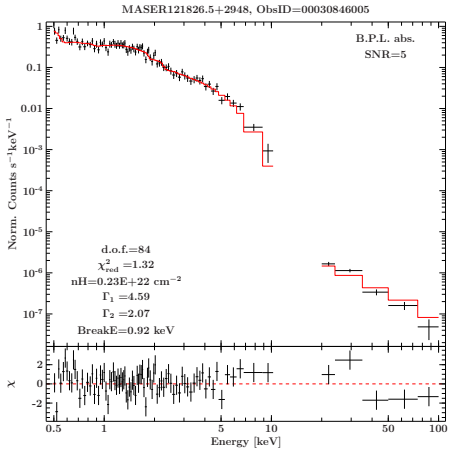
MASER121826.5+2948, ObsID=00030846005
B.P.L. abs.
SNR=5
d.o.f.=84
χ^2_{red} =1.32
nH=0.23E+22 cm^{-2}
Γ_1 =4.59
Γ_2 =2.07
BreakE=0.92 keV
Norm. Counts s^{-1}keV^{-1}
χ
Energy [keV]

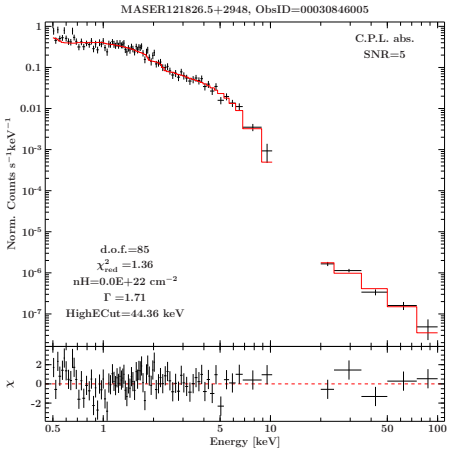
MASER121826.5+2948, ObsID=00030846005
C.P.L. abs.
SNR=5
d.o.f.=85
χ^2_{red} =1.36
nH=0.0E+22 cm^{-2}
Γ =1.71
HighECut=44.36 keV
Norm. Counts s^{-1}keV^{-1}
χ
Energy [keV]

ObsID 00030846006

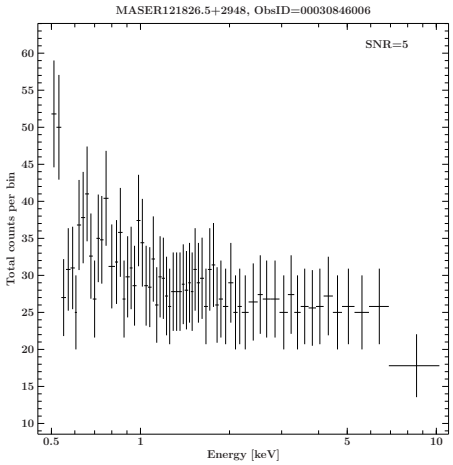

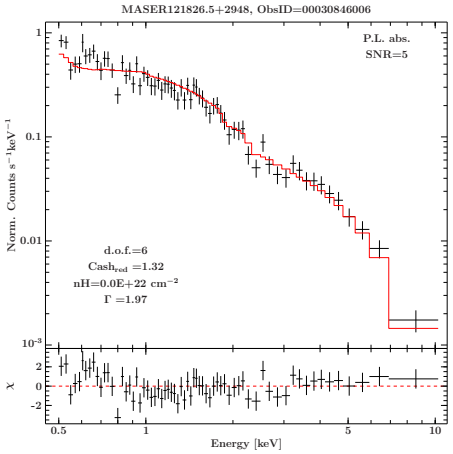

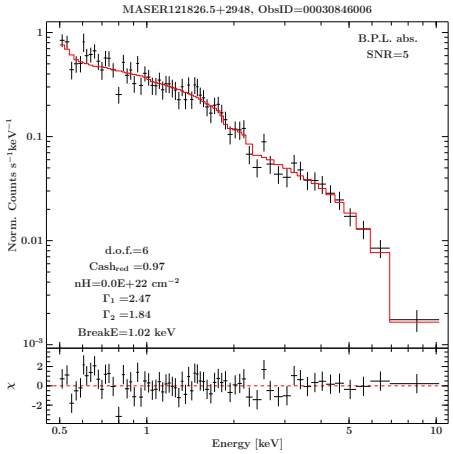

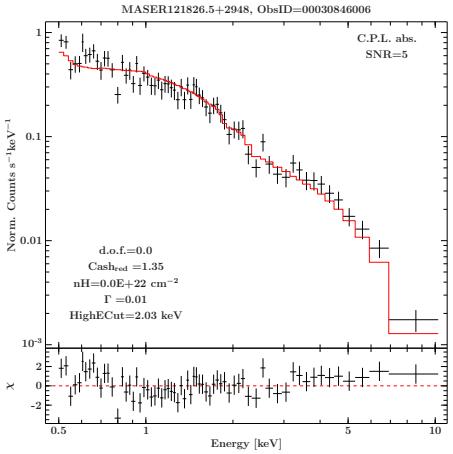

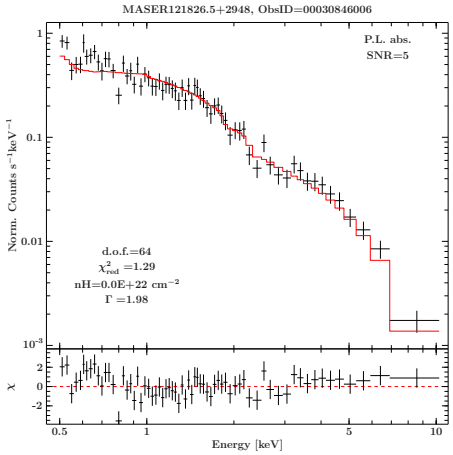

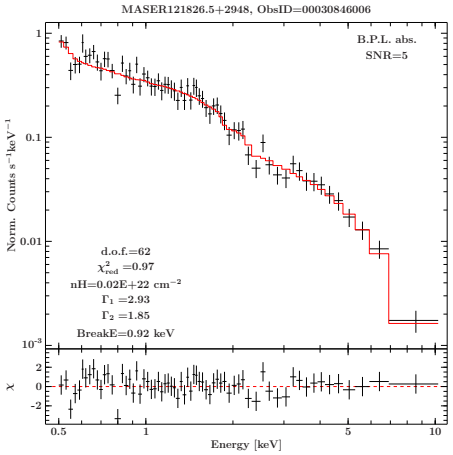

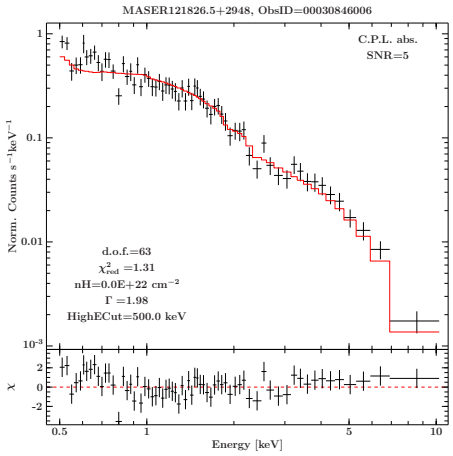
MASER121826.5+2948, ObsID=00030846006
C.P.L. abs.
SNR=5
d.o.f.=63
χ^2_{red} =1.31
nH=0.0E+22 cm^{-2}
Γ =1.98
HighECut=500.0 keV
Norm. Counts s^{-1}keV^{-1}
χ
Energy [keV]

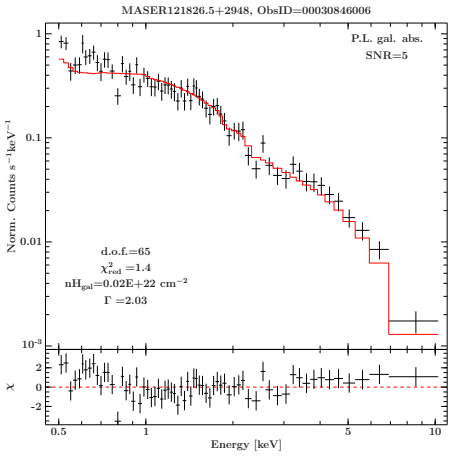
MASER121826.5+2948, ObsID=00030846006
P.L. gal. abs.
SNR=5
d.o.f.=65
χ^2_{red} =1.4
nH$_{gal}$=0.02E+22 cm^{-2}
Γ =2.03
Norm. Counts s^{-1}keV^{-1}
χ
Energy [keV]

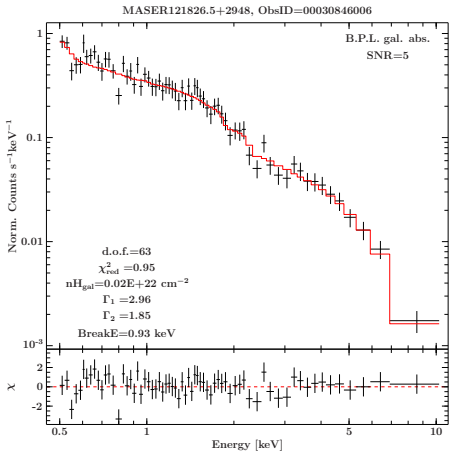
MASER121826.5+2948, ObsID=00030846006
B.P.L. gal. abs.
SNR=5
d.o.f.=63
χ^2_{red} =0.95
nH$_{gal}$=0.02E+22 cm^{-2}
Γ$_1$ =2.96
Γ$_2$ =1.85
BreakE=0.93 keV
Norm. Counts s^{-1}keV^{-1}
χ
Energy [keV]

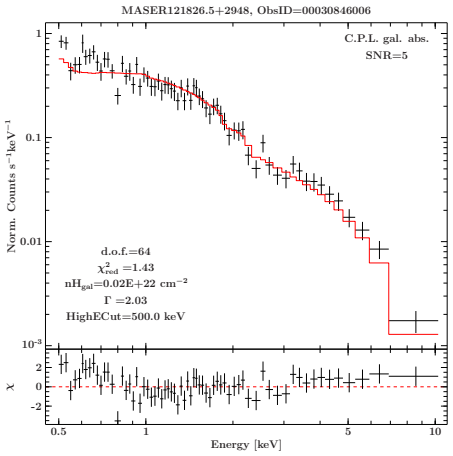
MASER121826.5+2948, ObsID=00030846006
C.P.L. gal. abs.
SNR=5
d.o.f.=64
χ^2_{red} =1.43
nH$_{gal}$=0.02E+22 cm^{-2}
Γ =2.03
HighECut=500.0 keV
Norm. Counts s^{-1}keV^{-1}
χ
Energy [keV]

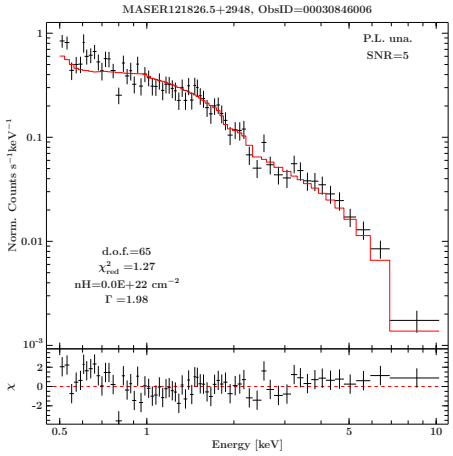
MASER121826.5+2948, ObsID=00030846006
P.L. una.
SNR=5
d.o.f.=65
χ^2_{red} =1.27
nH=0.0E+22 cm^{-2}
Γ =1.98
Norm. Counts s^{-1}keV^{-1}
χ
Energy [keV]

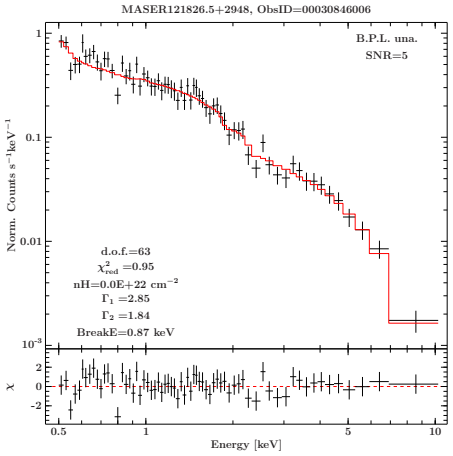
MASER121826.5+2948, ObsID=00030846006
B.P.L. una.
SNR=5
d.o.f.=63
χ^2_{red} =0.95
nH=0.0E+22 cm^{-2}
Γ$_1$ =2.85
Γ$_2$ =1.84
BreakE=0.87 keV
Norm. Counts s^{-1}keV^{-1}
χ
Energy [keV]

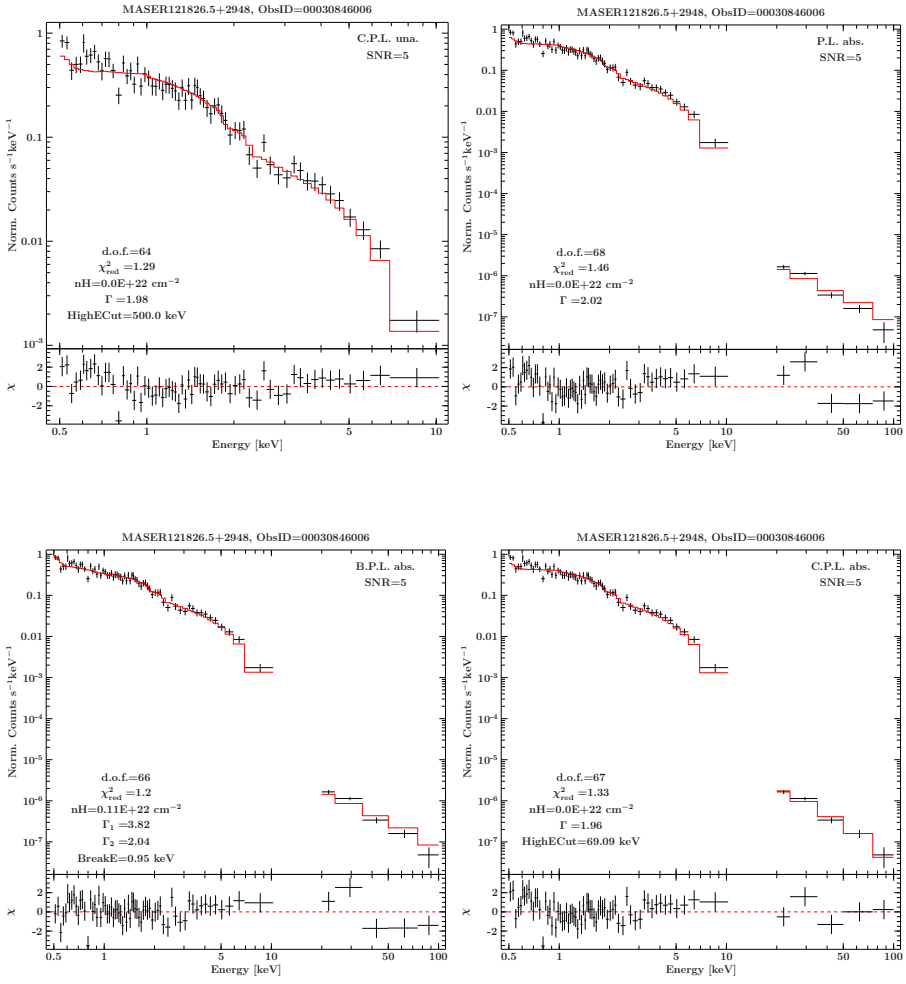
MASER121826.5+2948, ObsID=00030846006
C.P.L. una.
SNR=5
d.o.f.=64
χ^2_{red} =1.29
nH=0.0E+22 cm^{-2}
Γ =1.98
HighECut=500.0 keV
Norm. Counts s^{-1}keV^{-1}
χ
Energy [keV]
MASER121826.5+2948, ObsID=00030846006
P.L. abs.
SNR=5
d.o.f.=68
χ^2_{red} =1.46
nH=0.0E+22 cm^{-2}
Γ =2.02
Norm. Counts s^{-1}keV^{-1}
χ
Energy [keV]
MASER121826.5+2948, ObsID=00030846006
B.P.L. abs.
SNR=5
d.o.f.=66
χ^2_{red} =1.2
nH=0.11E+22 cm^{-2}
Γ_1 =3.82
Γ_2 =2.04
BreakE=0.95 keV
Norm. Counts s^{-1}keV^{-1}
χ
Energy [keV]
MASER121826.5+2948, ObsID=00030846006
C.P.L. abs.
SNR=5
d.o.f.=67
χ^2_{red} =1.33
nH=0.0E+22 cm^{-2}
Γ =1.96
HighECut=69.09 keV
Norm. Counts s^{-1}keV^{-1}
χ
Energy [keV]

ObsID 00030846008

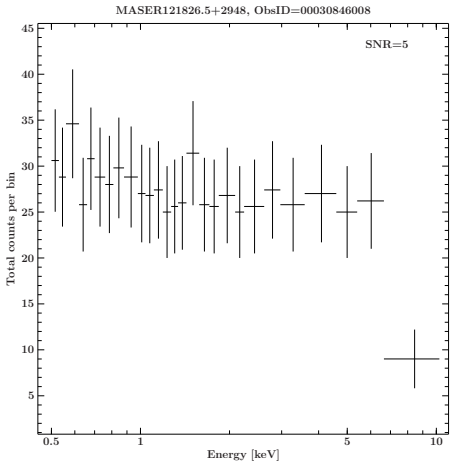

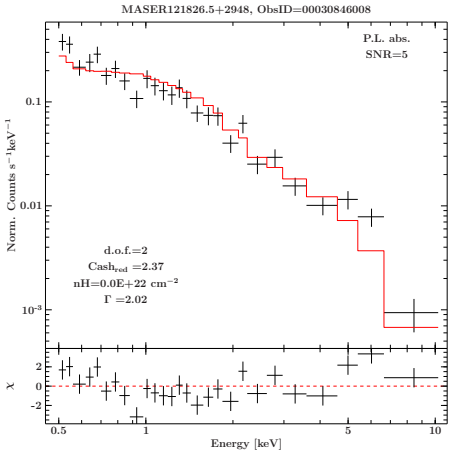

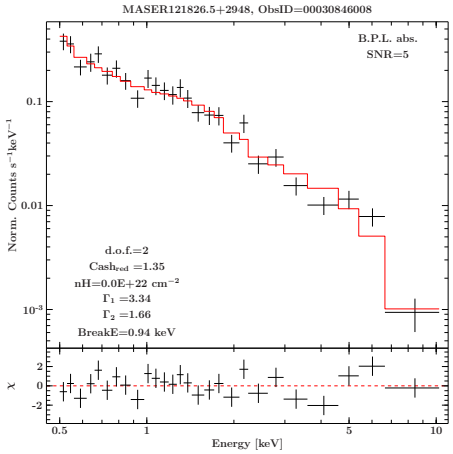

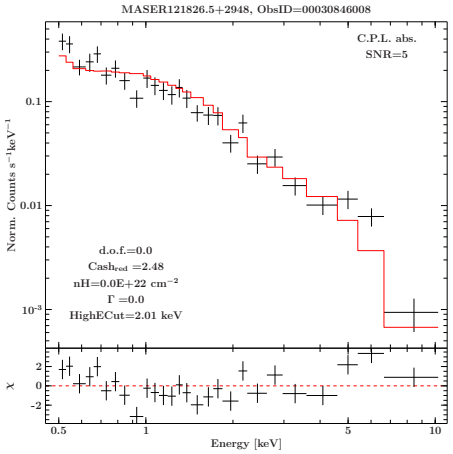

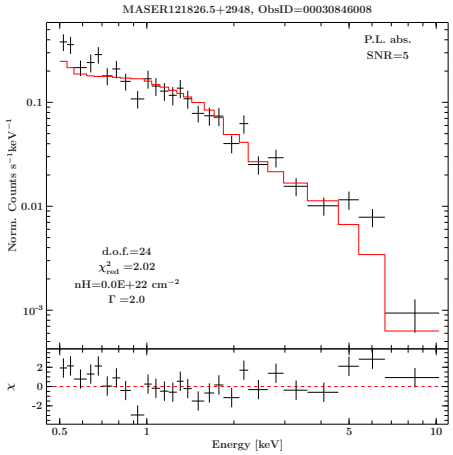

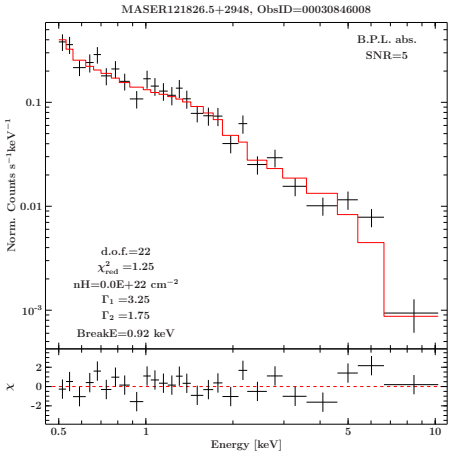

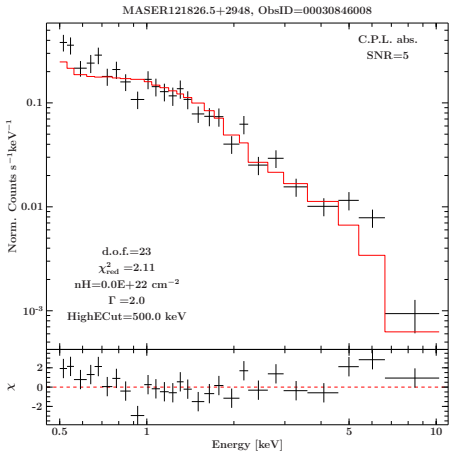
MASER121826.5+2948, ObsID=00030846008
C.P.L. abs.
SNR=5
d.o.f.=23
χ^2_{red} =2.11
nH=0.0E+22 cm^{-2}
Γ =2.0
HighECut=500.0 keV
Norm. Counts s^{-1}keV^{-1}
Energy [keV]

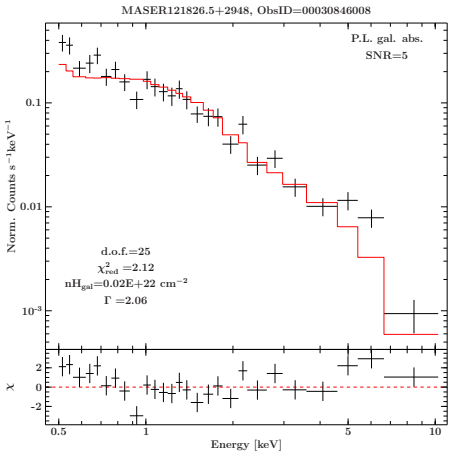
MASER121826.5+2948, ObsID=00030846008
P.L. gal. abs.
SNR=5
d.o.f.=25
χ^2_{red} =2.12
nH$_{gal}$=0.02E+22 cm^{-2}
Γ =2.06
Norm. Counts s^{-1}keV^{-1}
Energy [keV]

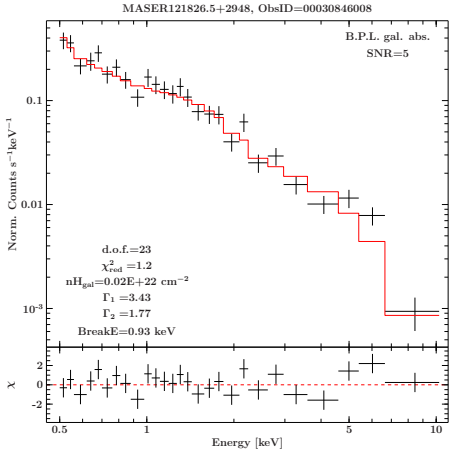
MASER121826.5+2948, ObsID=00030846008
B.P.L. gal. abs.
SNR=5
d.o.f.=23
χ^2_{red} =1.2
nH$_{gal}$=0.02E+22 cm^{-2}
Γ$_1$ =3.43
Γ$_2$ =1.77
BreakE=0.93 keV
Norm. Counts s^{-1}keV^{-1}
Energy [keV]

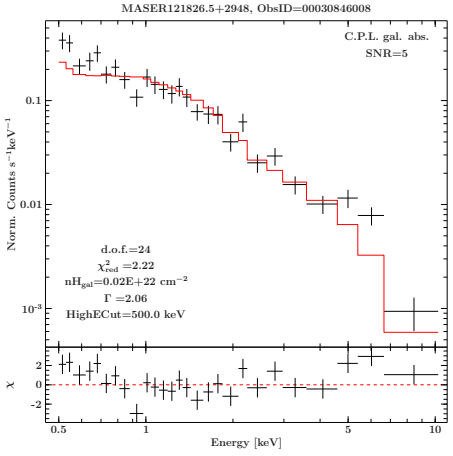
MASER121826.5+2948, ObsID=00030846008
C.P.L. gal. abs.
SNR=5
d.o.f.=24
χ^2_{red} =2.22
nH$_{gal}$=0.02E+22 cm^{-2}
Γ =2.06
HighECut=500.0 keV
Norm. Counts s^{-1}keV^{-1}
Energy [keV]

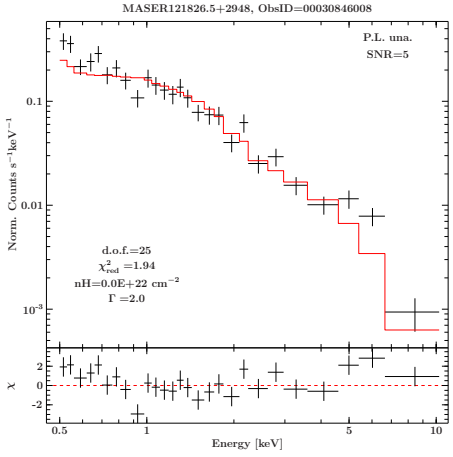
MASER121826.5+2948, ObsID=00030846008
P.L. una.
SNR=5
d.o.f.=25
χ^2_{red} =1.94
nH=0.0E+22 cm^{-2}
Γ =2.0
Norm. Counts s^{-1}keV^{-1}
Energy [keV]

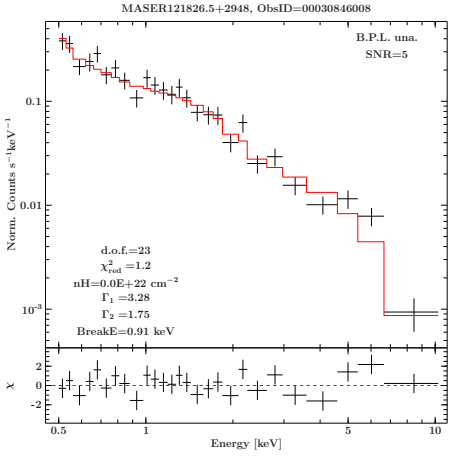
MASER121826.5+2948, ObsID=00030846008
B.P.L. una.
SNR=5
d.o.f.=23
χ^2_{red} =1.2
nH=0.0E+22 cm^{-2}
Γ$_1$ =3.28
Γ$_2$ =1.75
BreakE=0.91 keV
Norm. Counts s^{-1}keV^{-1}
Energy [keV]

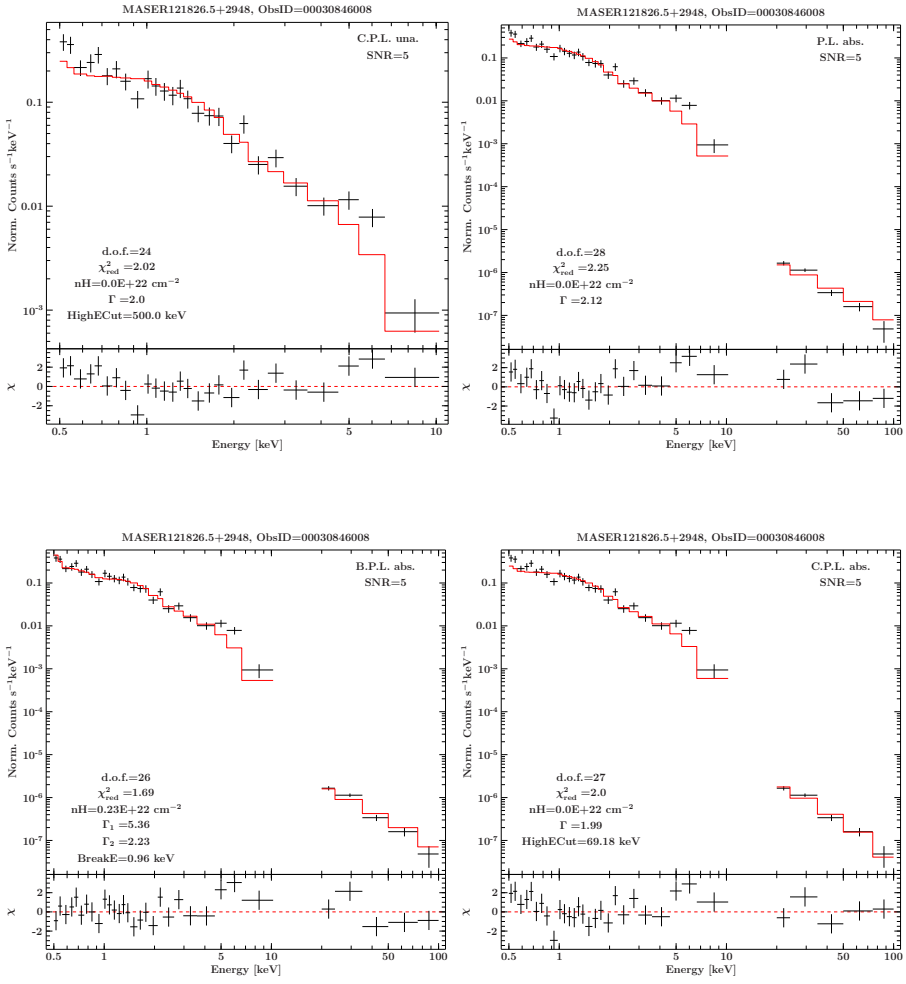
MASER121826.5+2948, ObsID=00030846008
C.P.L. una.
SNR=5
d.o.f.=24
χ^2_{red} =2.02
nH=0.0E+22 cm^{-2}
Γ =2.0
HighECut=500.0 keV
MASER121826.5+2948, ObsID=00030846008
P.L. abs.
SNR=5
d.o.f.=28
χ^2_{red} =2.25
nH=0.0E+22 cm^{-2}
Γ =2.12
MASER121826.5+2948, ObsID=00030846008
B.P.L. abs.
SNR=5
d.o.f.=26
χ^2_{red} =1.69
nH=0.23E+22 cm^{-2}
Γ$_1$ =5.36
Γ$_2$ =2.23
BreakE=0.96 keV
MASER121826.5+2948, ObsID=00030846008
C.P.L. abs.
SNR=5
d.o.f.=27
χ^2_{red} =2.0
nH=0.0E+22 cm^{-2}
Γ =1.99
HighECut=69.18 keV
Norm. Counts s^{-1}keV^{-1}
χ
Energy [keV]

ObsID 00030846009

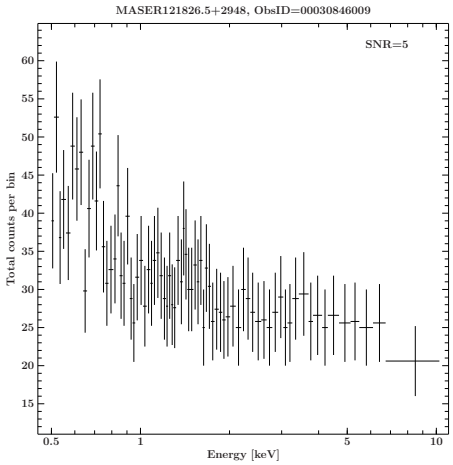

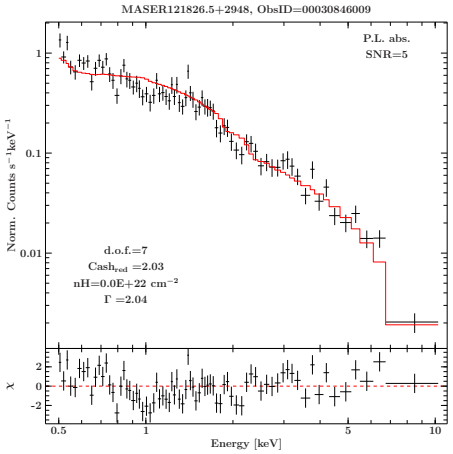

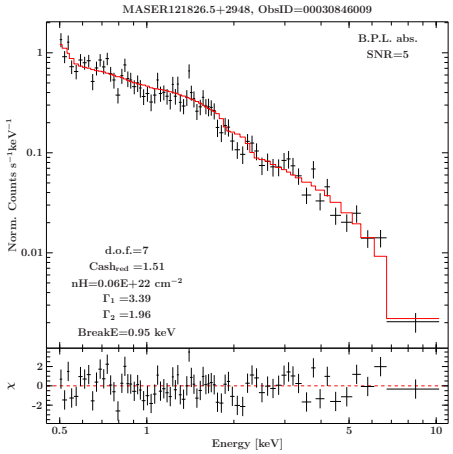

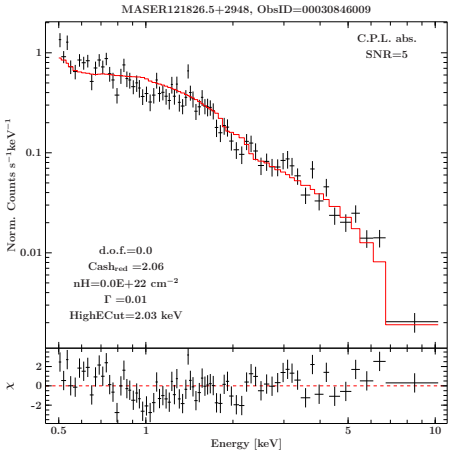

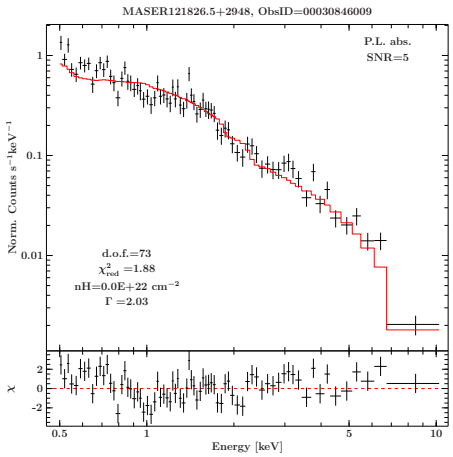

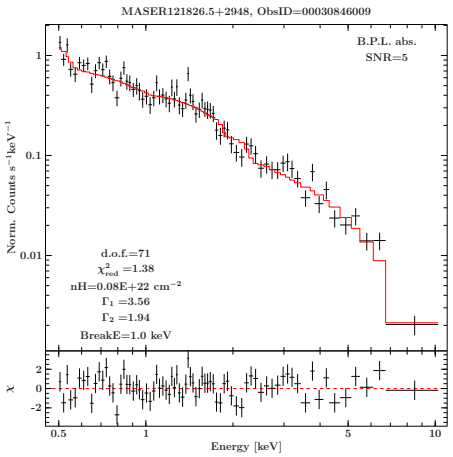

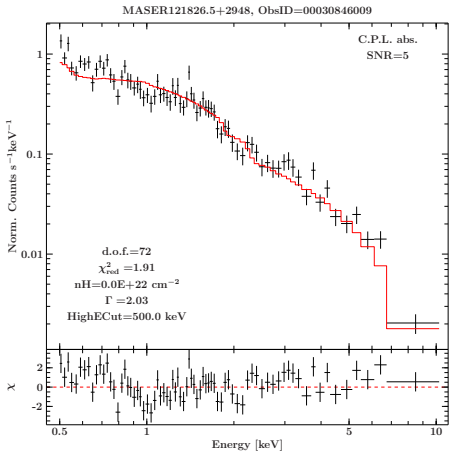
MASER121826.5+2948, ObsID=00030846009
C.P.L. abs.
SNR=5
d.o.f.=72
χ^2_{red} =1.91
nH=0.0E+22 cm^{-2}
Γ =2.03
HighECut=500.0 keV
Norm. Counts s^{-1}keV^{-1}
χ
Energy [keV]

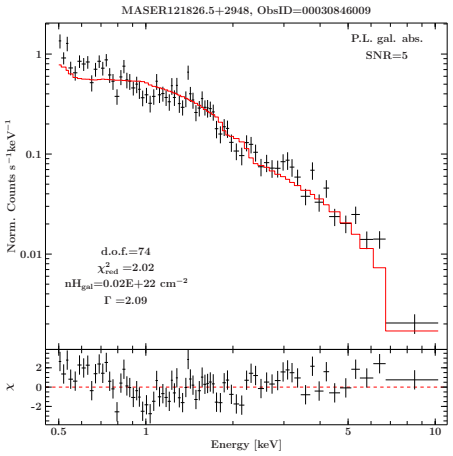
MASER121826.5+2948, ObsID=00030846009
P.L. gal. abs.
SNR=5
d.o.f.=74
χ^2_{red} =2.02
nH_{gal}=0.02E+22 cm^{-2}
Γ =2.09
Norm. Counts s^{-1}keV^{-1}
χ
Energy [keV]

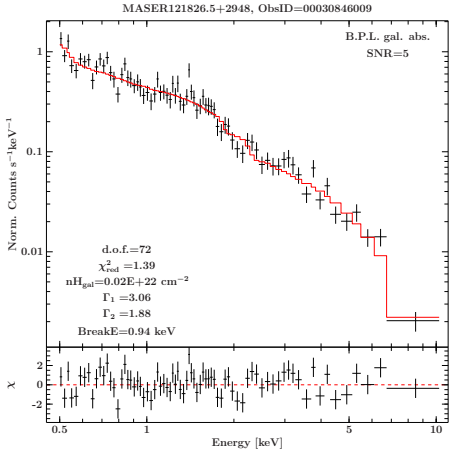
MASER121826.5+2948, ObsID=00030846009
B.P.L. gal. abs.
SNR=5
d.o.f.=72
χ^2_{red} =1.39
nH_{gal}=0.02E+22 cm^{-2}
Γ_1 =3.06
Γ_2 =1.88
BreakE=0.94 keV
Norm. Counts s^{-1}keV^{-1}
χ
Energy [keV]

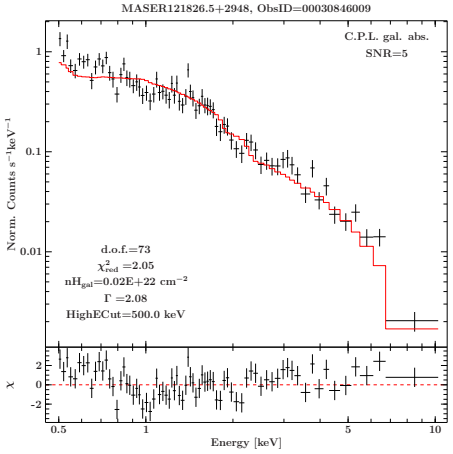
MASER121826.5+2948, ObsID=00030846009
C.P.L. gal. abs.
SNR=5
d.o.f.=73
χ^2_{red} =2.05
nH_{gal}=0.02E+22 cm^{-2}
Γ =2.08
HighECut=500.0 keV
Norm. Counts s^{-1}keV^{-1}
χ
Energy [keV]

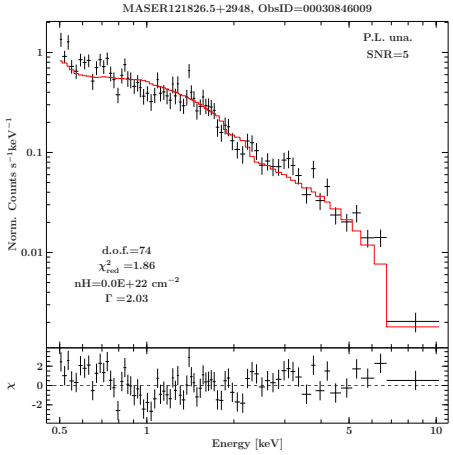
MASER121826.5+2948, ObsID=00030846009
P.L. una.
SNR=5
d.o.f.=74
χ^2_{red} =1.86
nH=0.0E+22 cm^{-2}
Γ =2.03
Norm. Counts s^{-1}keV^{-1}
χ
Energy [keV]

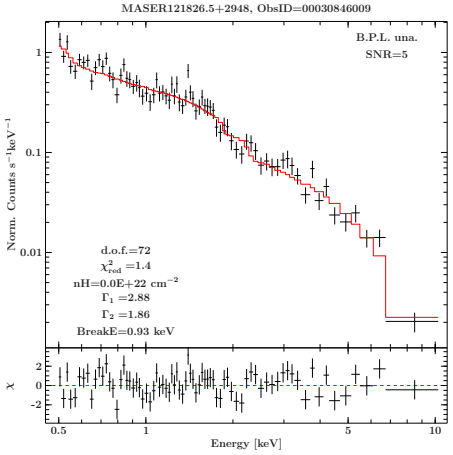
MASER121826.5+2948, ObsID=00030846009
B.P.L. una.
SNR=5
d.o.f.=72
χ^2_{red} =1.4
nH=0.0E+22 cm^{-2}
Γ_1 =2.88
Γ_2 =1.86
BreakE=0.93 keV
Norm. Counts s^{-1}keV^{-1}
χ
Energy [keV]

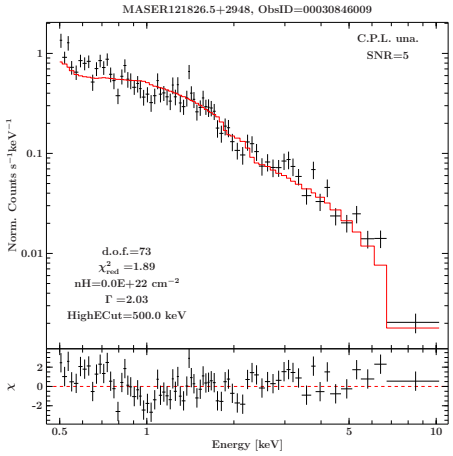
MASER121826.5+2948, ObsID=00030846009
C.P.L. una.
SNR=5
d.o.f.=73
χ^2_{red} =1.89
nH=0.0E+22 cm^{-2}
Γ =2.03
HighECut=500.0 keV
Norm. Counts s^{-1}keV^{-1}
χ
Energy [keV]

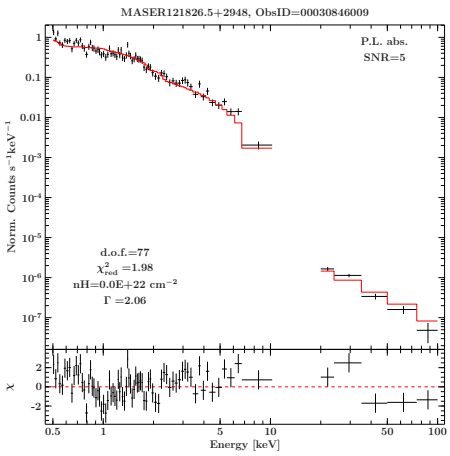
MASER121826.5+2948, ObsID=00030846009
P.L. abs.
SNR=5
d.o.f.=77
χ^2_{red} =1.98
nH=0.0E+22 cm^{-2}
Γ =2.06
Norm. Counts s^{-1}keV^{-1}
χ
Energy [keV]

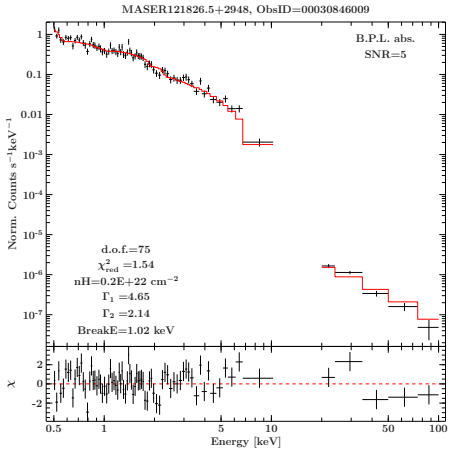
MASER121826.5+2948, ObsID=00030846009
B.P.L. abs.
SNR=5
d.o.f.=75
χ^2_{red} =1.54
nH=0.2E+22 cm^{-2}
Γ$_1$ =4.65
Γ$_2$ =2.14
BreakE=1.02 keV
Norm. Counts s^{-1}keV^{-1}
χ
Energy [keV]

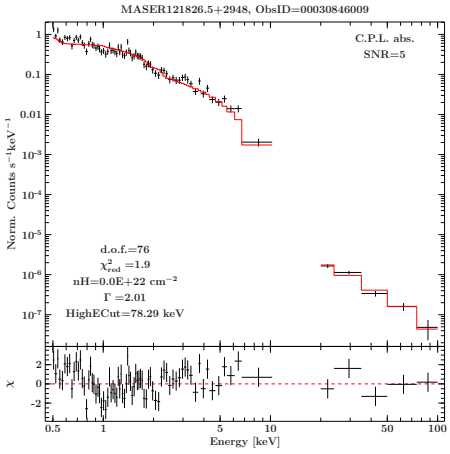
MASER121826.5+2948, ObsID=00030846009
C.P.L. abs.
SNR=5
d.o.f.=76
χ^2_{red} =1.9
nH=0.0E+22 cm^{-2}
Γ =2.01
HighECut=78.29 keV
Norm. Counts s^{-1}keV^{-1}
χ
Energy [keV]

ObsID 00030846012

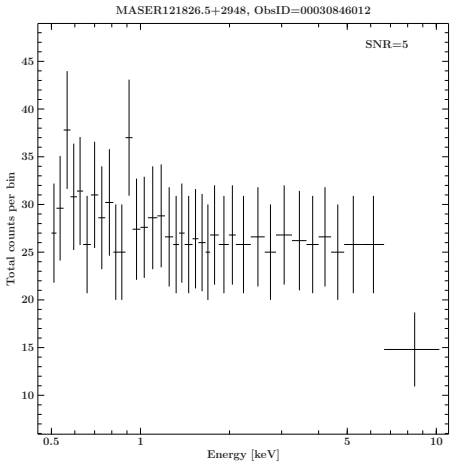

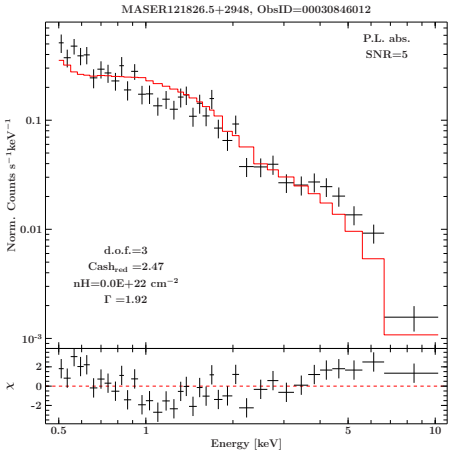

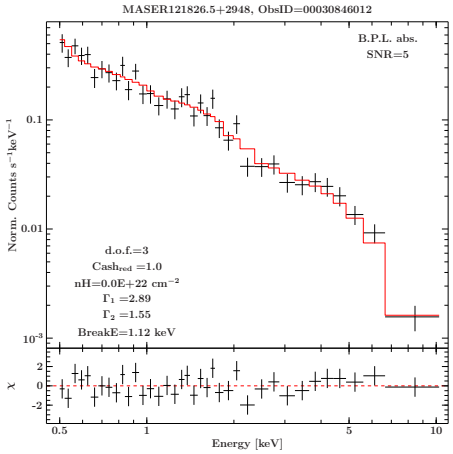

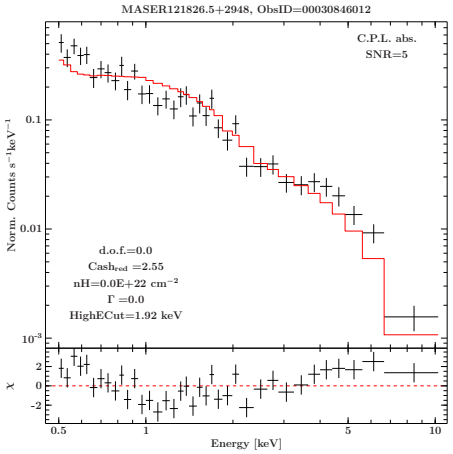

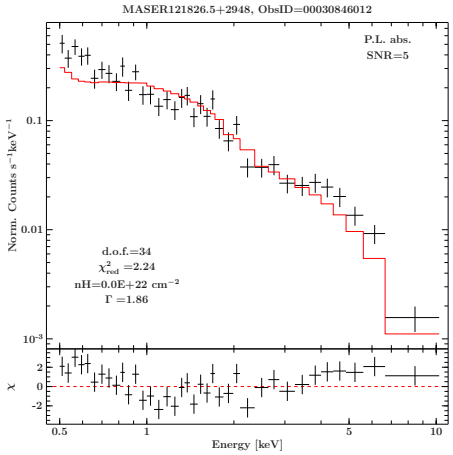

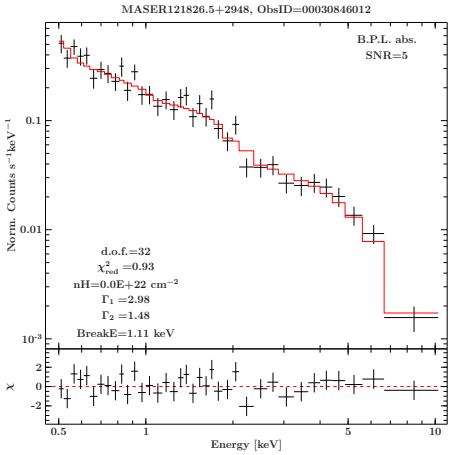

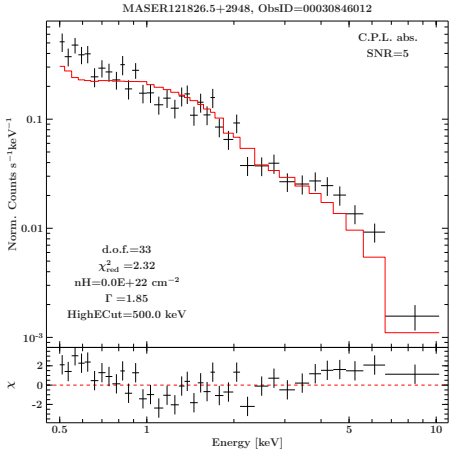
MASER121826.5+2948, ObsID=00030846012
C.P.L. abs.
SNR=5
d.o.f.=33
χ^2_{red} =2.32
nH=0.0E+22 cm^{-2}
Γ =1.85
HighECut=500.0 keV
Norm. Counts s^{-1}keV^{-1}
χ
Energy [keV]

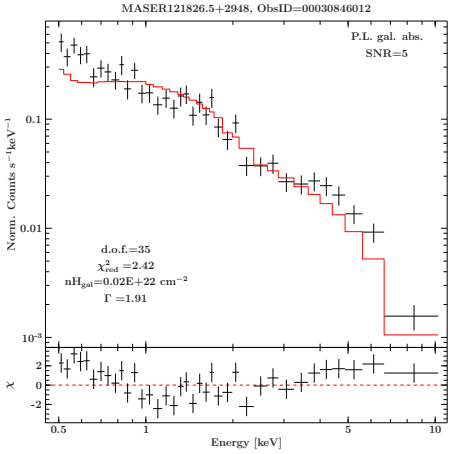
MASER121826.5+2948, ObsID=00030846012
P.L. gal. abs.
SNR=5
d.o.f.=35
χ^2_{red} =2.42
nH$_{gal}$=0.02E+22 cm^{-2}
Γ =1.91
Norm. Counts s^{-1}keV^{-1}
χ
Energy [keV]

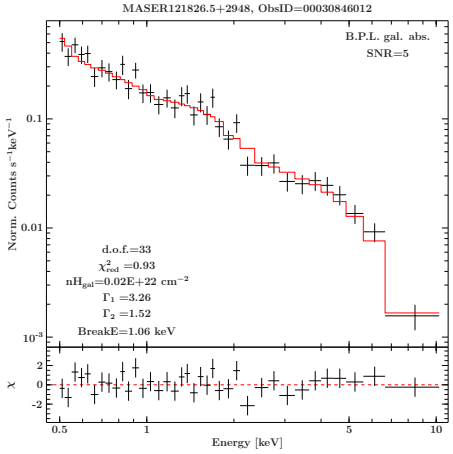
MASER121826.5+2948, ObsID=00030846012
B.P.L. gal. abs.
SNR=5
d.o.f.=33
χ^2_{red} =0.93
nH$_{gal}$=0.02E+22 cm^{-2}
Γ$_1$ =3.26
Γ$_2$ =1.52
BreakE=1.06 keV
Norm. Counts s^{-1}keV^{-1}
χ
Energy [keV]

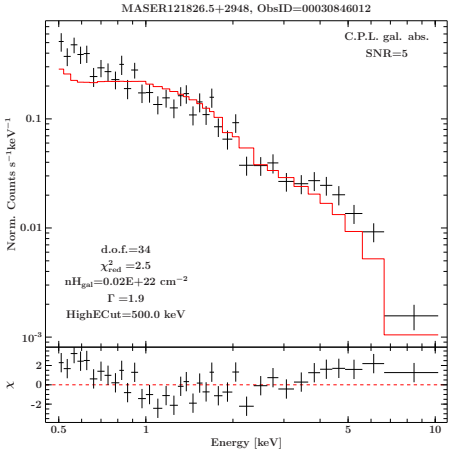
MASER121826.5+2948, ObsID=00030846012
C.P.L. gal. abs.
SNR=5
d.o.f.=34
χ^2_{red} =2.5
nH$_{gal}$=0.02E+22 cm^{-2}
Γ =1.9
HighECut=500.0 keV
Norm. Counts s^{-1}keV^{-1}
χ
Energy [keV]

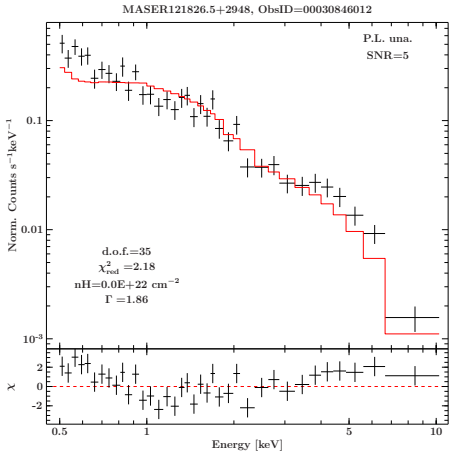
MASER121826.5+2948, ObsID=00030846012
P.L. una.
SNR=5
d.o.f.=35
χ^2_{red} =2.18
nH=0.0E+22 cm^{-2}
Γ =1.86
Norm. Counts s^{-1}keV^{-1}
χ
Energy [keV]

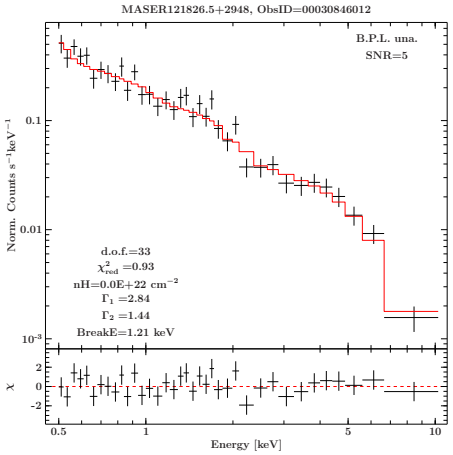
MASER121826.5+2948, ObsID=00030846012
B.P.L. una.
SNR=5
d.o.f.=33
χ^2_{red} =0.93
nH=0.0E+22 cm^{-2}
Γ$_1$ =2.84
Γ$_2$ =1.44
BreakE=1.21 keV
Norm. Counts s^{-1}keV^{-1}
χ
Energy [keV]

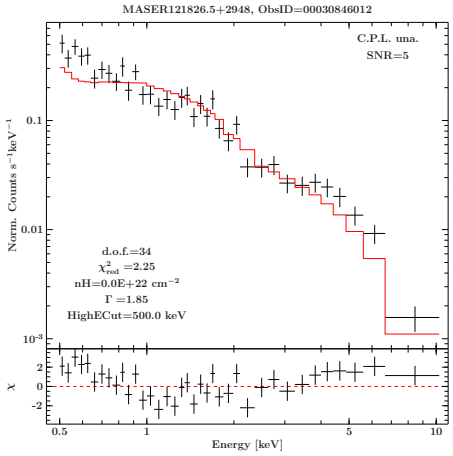
MASER121826.5+2948, ObsID=00030846012
C.P.L. una.
SNR=5
d.o.f.=34
χ^2_{red} =2.25
nH=0.0E+22 cm^{-2}
Γ =1.85
HighECut=500.0 keV
Norm. Counts s^{-1}keV^{-1}
χ
Energy [keV]

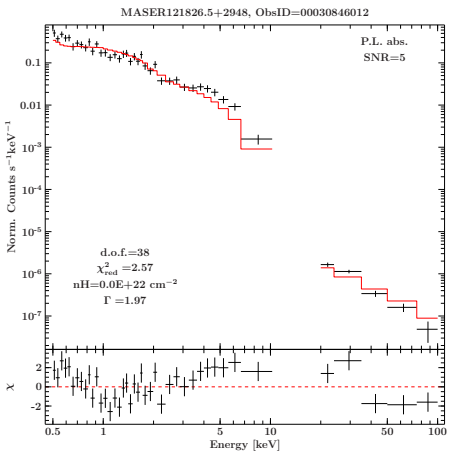
MASER121826.5+2948, ObsID=00030846012
P.L. abs.
SNR=5
d.o.f.=38
χ^2_{red} =2.57
nH=0.0E+22 cm^{-2}
Γ =1.97
Norm. Counts s^{-1}keV^{-1}
χ
Energy [keV]

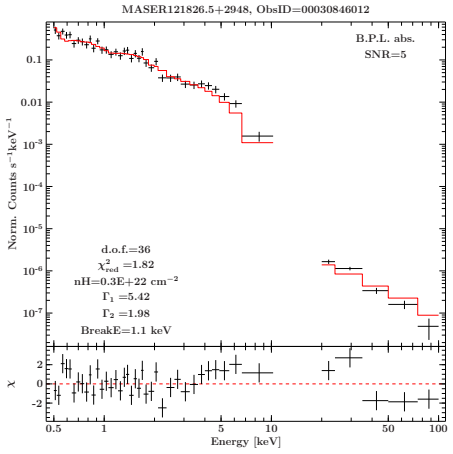
MASER121826.5+2948, ObsID=00030846012
B.P.L. abs.
SNR=5
d.o.f.=36
χ^2_{red} =1.82
nH=0.3E+22 cm^{-2}
Γ_1 =5.42
Γ_2 =1.98
BreakE=1.1 keV
Norm. Counts s^{-1}keV^{-1}
χ
Energy [keV]

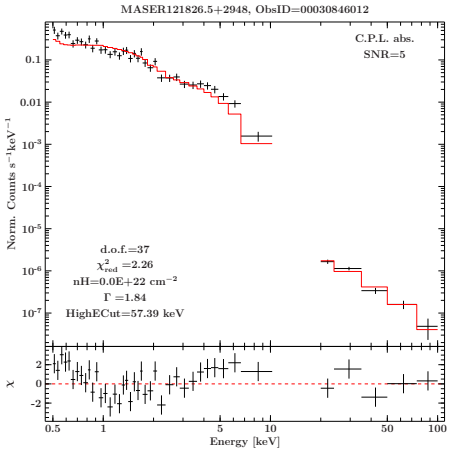
MASER121826.5+2948, ObsID=00030846012
C.P.L. abs.
SNR=5
d.o.f.=37
χ^2_{red} =2.26
nH=0.0E+22 cm^{-2}
Γ =1.84
HighECut=57.39 keV
Norm. Counts s^{-1}keV^{-1}
χ
Energy [keV]

ObsID 00030846013

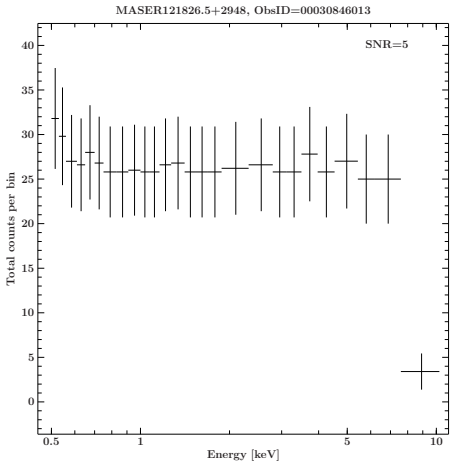

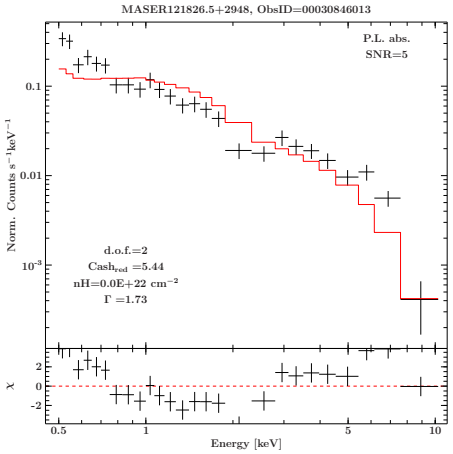

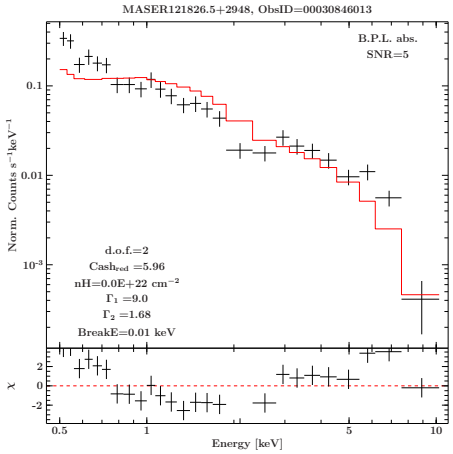

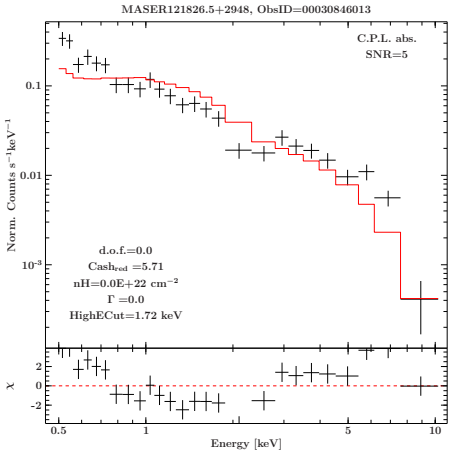

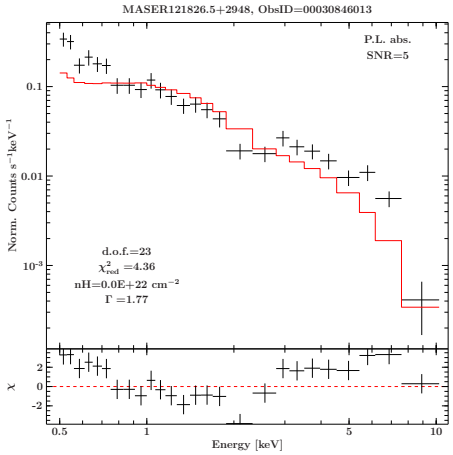

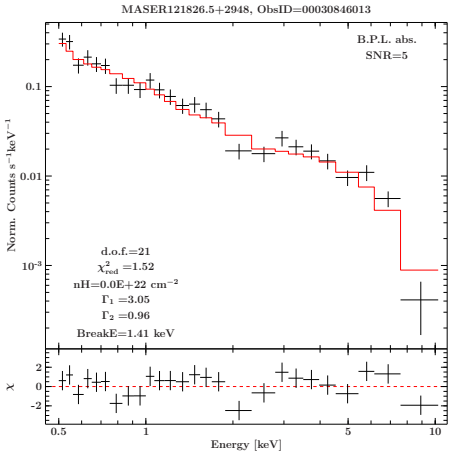

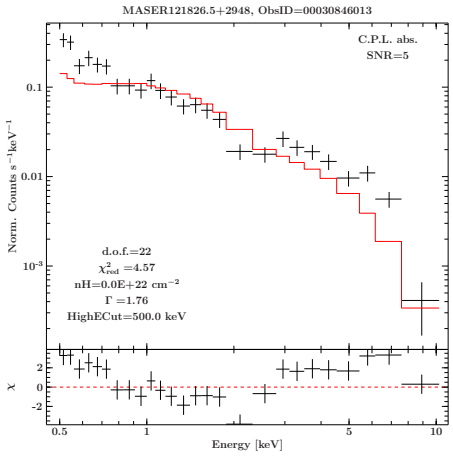
MASER121826.5+2948, ObsID=00030846013
C.P.L. abs.
SNR=5
d.o.f.=22
χ^2_{red} =4.57
nH=0.0E+22 cm^{-2}
Γ =1.76
HighECut=500.0 keV
Norm. Counts s^{-1}keV^{-1}
χ
Energy [keV]

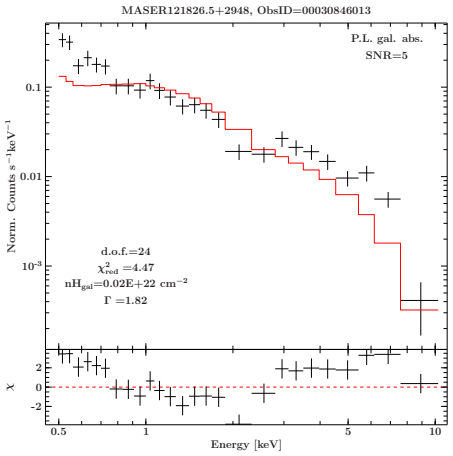
MASER121826.5+2948, ObsID=00030846013
P.L. gal. abs.
SNR=5
d.o.f.=24
χ^2_{red} =4.47
nH_{gal}=0.02E+22 cm^{-2}
Γ =1.82
Norm. Counts s^{-1}keV^{-1}
χ
Energy [keV]

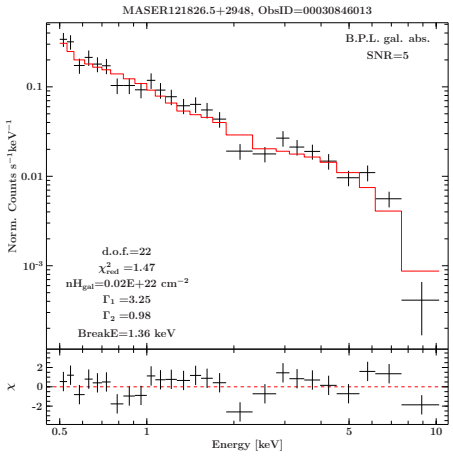
MASER121826.5+2948, ObsID=00030846013
B.P.L. gal. abs.
SNR=5
d.o.f.=22
χ^2_{red} =1.47
nH_{gal}=0.02E+22 cm^{-2}
Γ_1 =3.25
Γ_2 =0.98
BreakE=1.36 keV
Norm. Counts s^{-1}keV^{-1}
χ
Energy [keV]

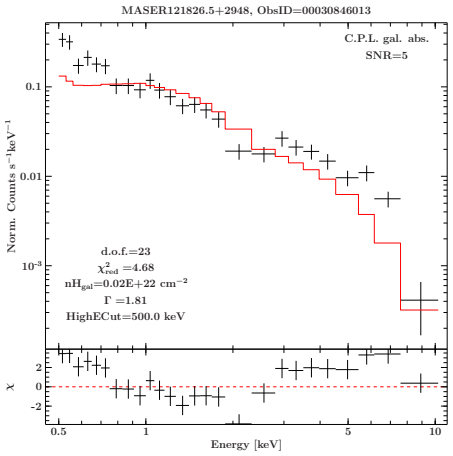
MASER121826.5+2948, ObsID=00030846013
C.P.L. gal. abs.
SNR=5
d.o.f.=23
χ^2_{red} =4.68
nH_{gal}=0.02E+22 cm^{-2}
Γ =1.81
HighECut=500.0 keV
Norm. Counts s^{-1}keV^{-1}
χ
Energy [keV]

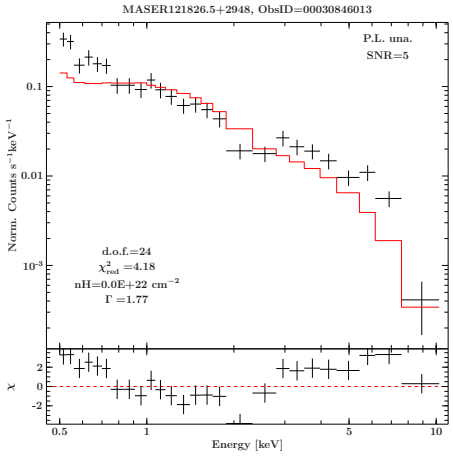
MASER121826.5+2948, ObsID=00030846013
P.L. una.
SNR=5
d.o.f.=24
χ^2_{red} =4.18
nH=0.0E+22 cm^{-2}
Γ =1.77
Norm. Counts s^{-1}keV^{-1}
χ
Energy [keV]

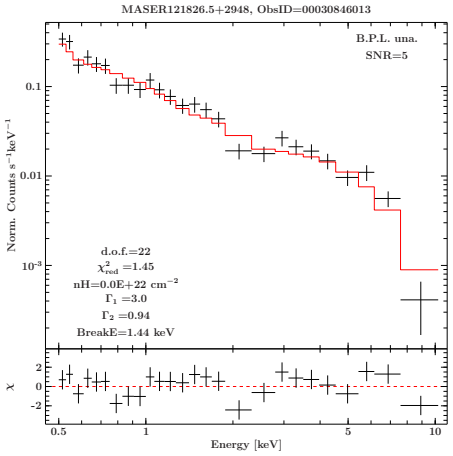
MASER121826.5+2948, ObsID=00030846013
B.P.L. una.
SNR=5
d.o.f.=22
χ^2_{red} =1.45
nH=0.0E+22 cm^{-2}
Γ_1 =3.0
Γ_2 =0.94
BreakE=1.44 keV
Norm. Counts s^{-1}keV^{-1}
χ
Energy [keV]

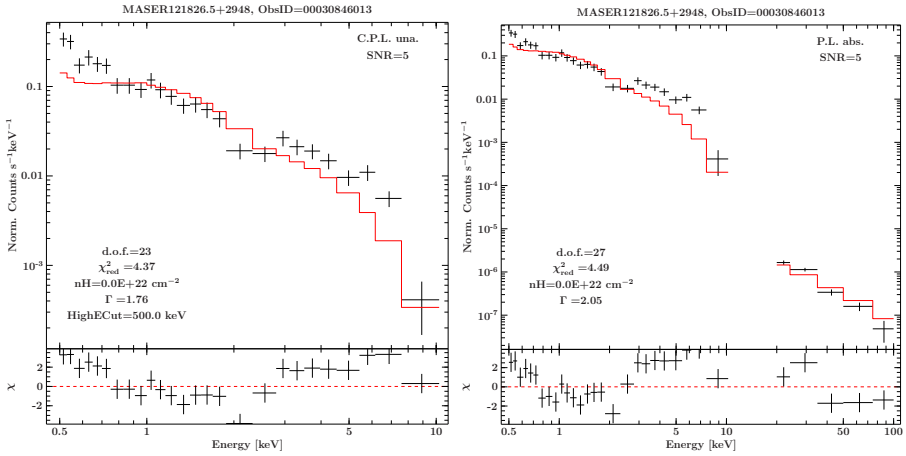
MASER121826.5+2948, ObsID=00030846013
C.P.L. una.
SNR=5
d.o.f.=23
χ^2_{red} =4.37
nH=0.0E+22 cm^{-2}
Γ =1.76
HighECut=500.0 keV
Norm. Counts s^{-1}keV^{-1}
χ
Energy [keV]
MASER121826.5+2948, ObsID=00030846013
P.L. abs.
SNR=5
d.o.f.=27
χ^2_{red} =4.49
nH=0.0E+22 cm^{-2}
Γ =2.05
Norm. Counts s^{-1}keV^{-1}
χ
Energy [keV]

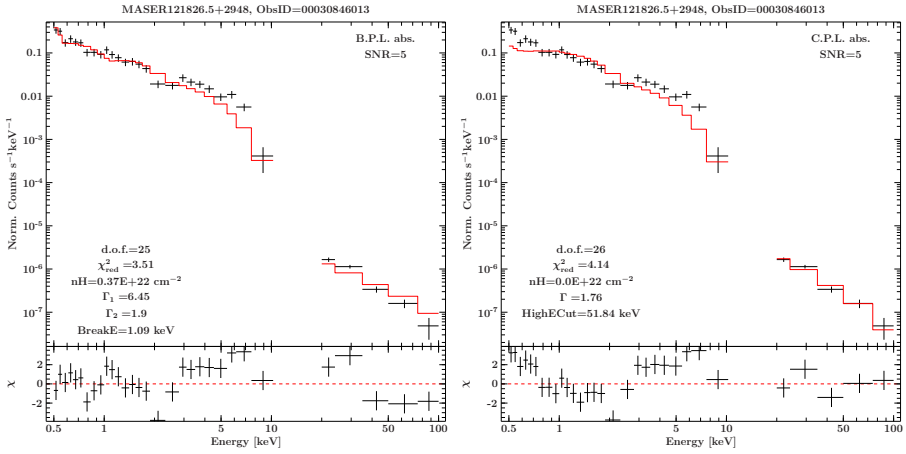
MASER121826.5+2948, ObsID=00030846013
B.P.L. abs.
SNR=5
d.o.f.=25
χ^2_{red} =3.51
nH=0.37E+22 cm^{-2}
Γ_1 =6.45
Γ_2 =1.9
BreakE=1.09 keV
Norm. Counts s^{-1}keV^{-1}
χ
Energy [keV]
MASER121826.5+2948, ObsID=00030846013
C.P.L. abs.
SNR=5
d.o.f.=26
χ^2_{red} =4.14
nH=0.0E+22 cm^{-2}
Γ =1.76
HighECut=51.84 keV
Norm. Counts s^{-1}keV^{-1}
χ
Energy [keV]

ObsID 00030846014

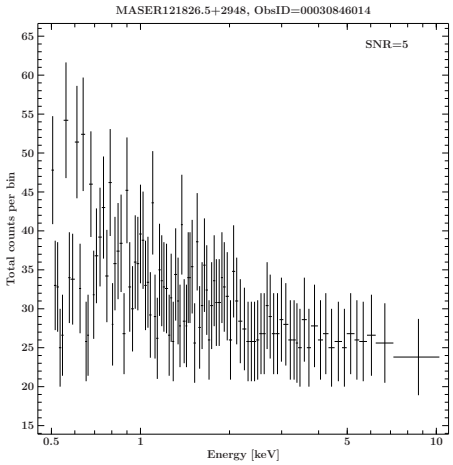

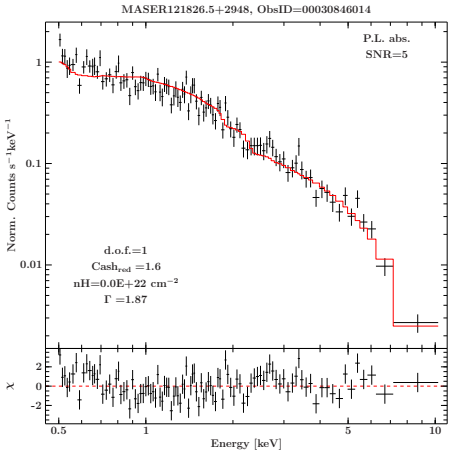

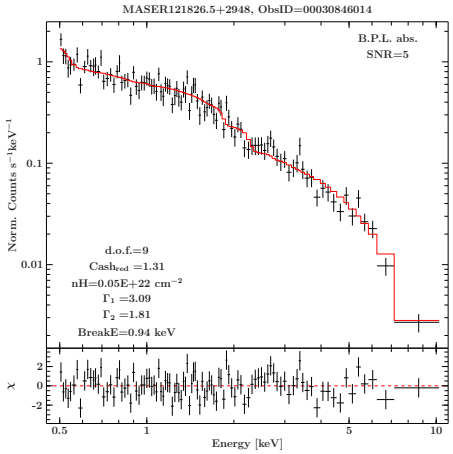

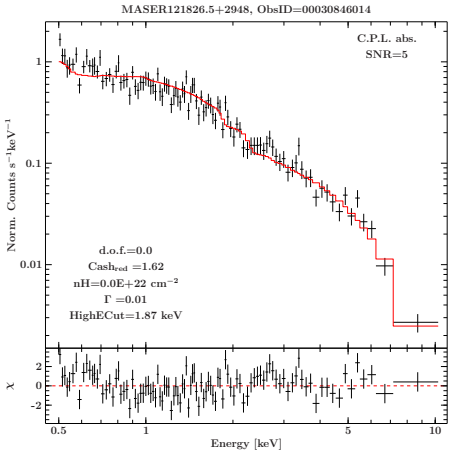

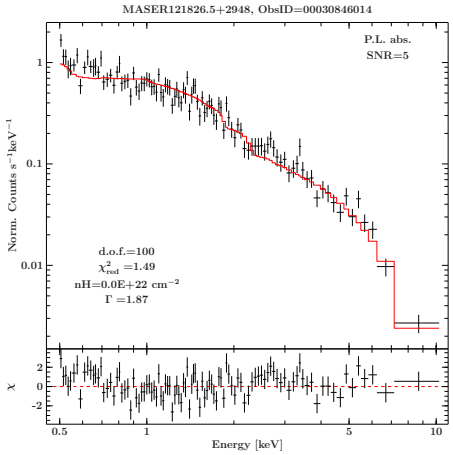

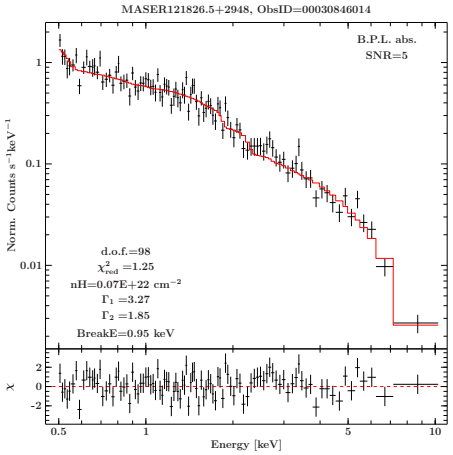

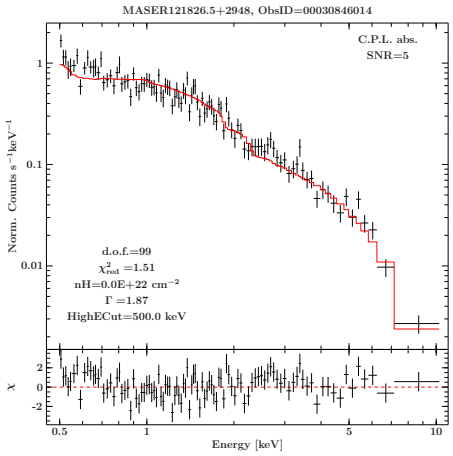
MASER121826.5+2948, ObsID=00030846014
C.P.L. abs.
SNR=5
d.o.f.=99
χ^2_{red} =1.51
nH=0.0E+22 cm^{-2}
Γ =1.87
HighECut=500.0 keV
Norm. Counts s^{-1}keV^{-1}
χ
Energy [keV]

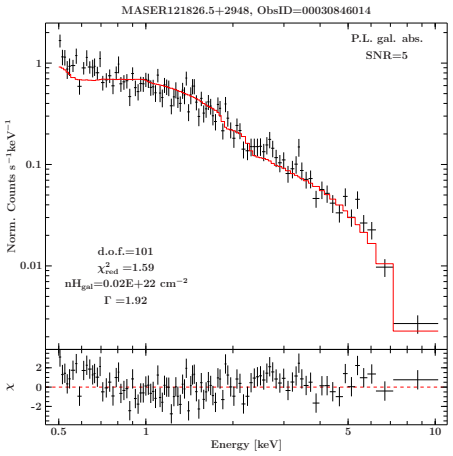
MASER121826.5+2948, ObsID=00030846014
P.L. gal. abs.
SNR=5
d.o.f.=101
χ^2_{red} =1.59
nH$_{gal}$=0.02E+22 cm^{-2}
Γ =1.92
Norm. Counts s^{-1}keV^{-1}
χ
Energy [keV]

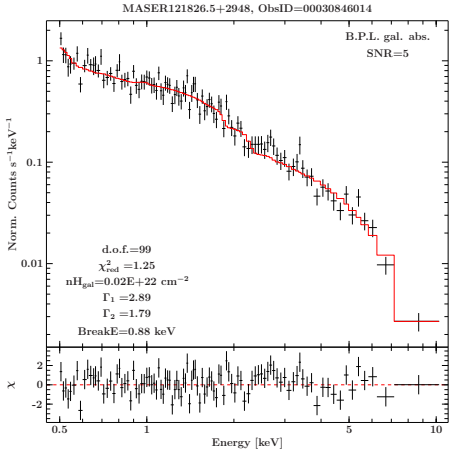
MASER121826.5+2948, ObsID=00030846014
B.P.L. gal. abs.
SNR=5
d.o.f.=99
χ^2_{red} =1.25
nH$_{gal}$=0.02E+22 cm^{-2}
Γ$_1$ =2.89
Γ$_2$ =1.79
BreakE=0.88 keV
Norm. Counts s^{-1}keV^{-1}
χ
Energy [keV]

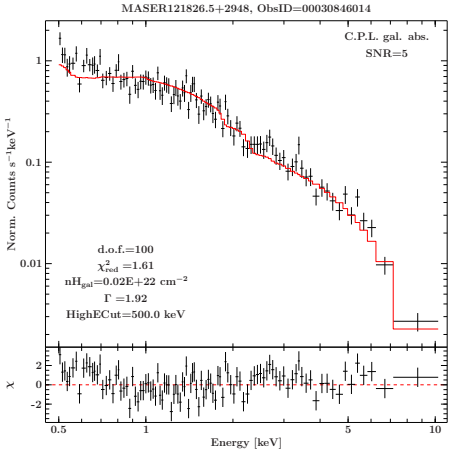
MASER121826.5+2948, ObsID=00030846014
C.P.L. gal. abs.
SNR=5
d.o.f.=100
χ^2_{red} =1.61
nH$_{gal}$=0.02E+22 cm^{-2}
Γ =1.92
HighECut=500.0 keV
Norm. Counts s^{-1}keV^{-1}
χ
Energy [keV]

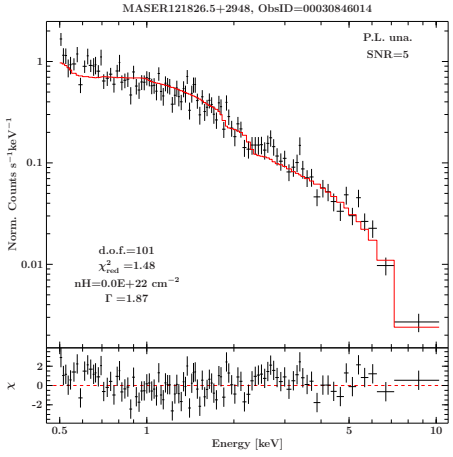
MASER121826.5+2948, ObsID=00030846014
P.L. una.
SNR=5
d.o.f.=101
χ^2_{red} =1.48
nH=0.0E+22 cm^{-2}
Γ =1.87
Norm. Counts s^{-1}keV^{-1}
χ
Energy [keV]

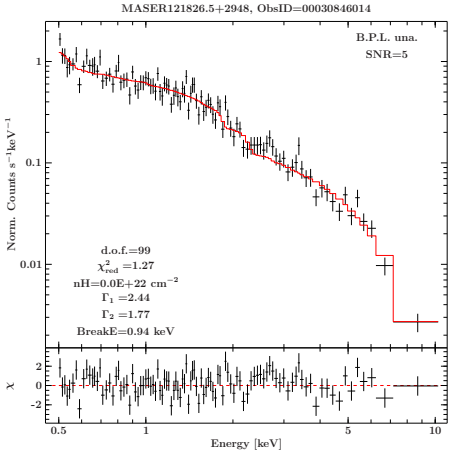
MASER121826.5+2948, ObsID=00030846014
B.P.L. una.
SNR=5
d.o.f.=99
χ^2_{red} =1.27
nH=0.0E+22 cm^{-2}
Γ$_1$ =2.44
Γ$_2$ =1.77
BreakE=0.94 keV
Norm. Counts s^{-1}keV^{-1}
χ
Energy [keV]

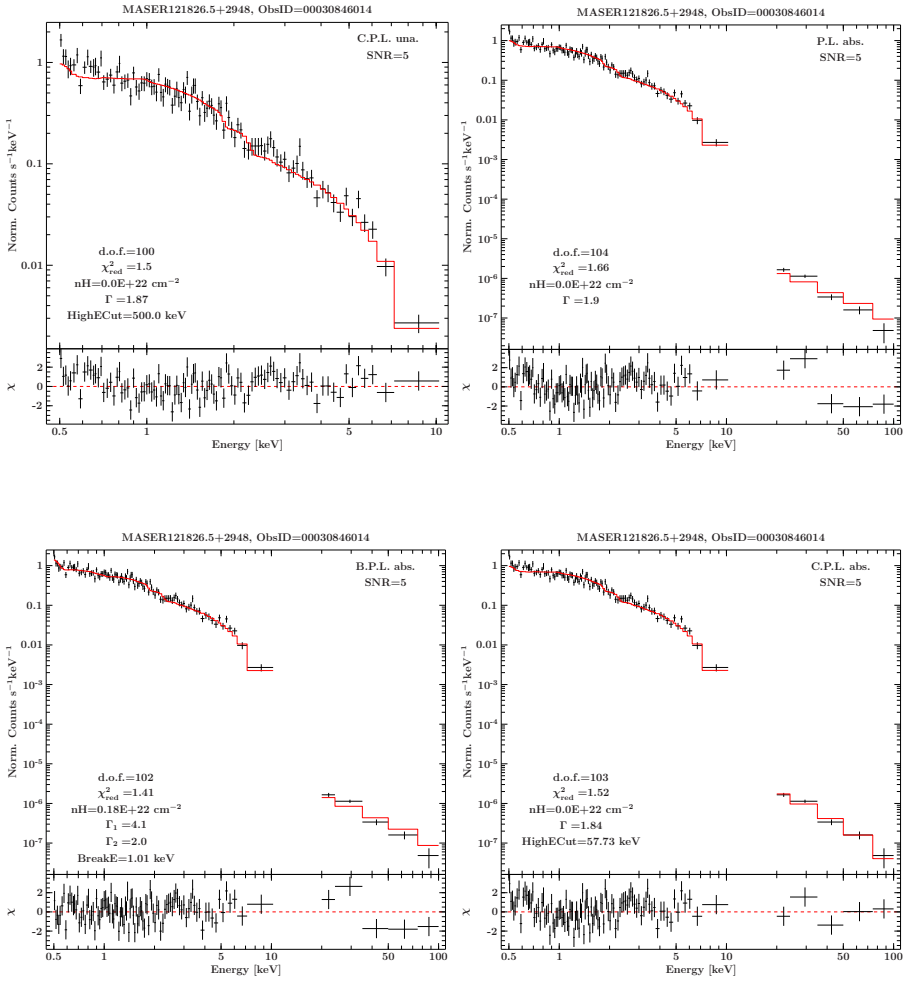
MASER121826.5+2948, ObsID=00030846014
C.P.L. una.
SNR=5
d.o.f.=100
χ^2_{red} =1.5
nH=0.0E+22 cm^{-2}
Γ =1.87
HighECut=500.0 keV
MASER121826.5+2948, ObsID=00030846014
P.L. abs.
SNR=5
d.o.f.=104
χ^2_{red} =1.66
nH=0.0E+22 cm^{-2}
Γ =1.9
MASER121826.5+2948, ObsID=00030846014
B.P.L. abs.
SNR=5
d.o.f.=102
χ^2_{red} =1.41
nH=0.18E+22 cm^{-2}
Γ$_1$ =4.1
Γ$_2$ =2.0
BreakE=1.01 keV
MASER121826.5+2948, ObsID=00030846014
C.P.L. abs.
SNR=5
d.o.f.=103
χ^2_{red} =1.52
nH=0.0E+22 cm^{-2}
Γ =1.84
HighECut=57.73 keV
Norm. Counts s^{-1}keV^{-1}
χ
Energy [keV]

ObsID 00030846015

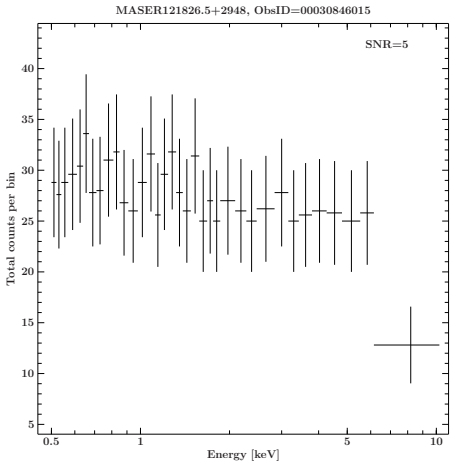

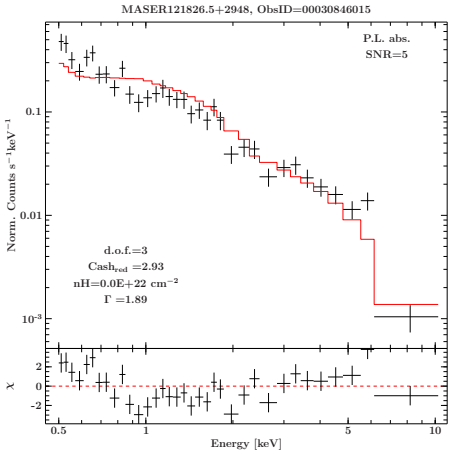

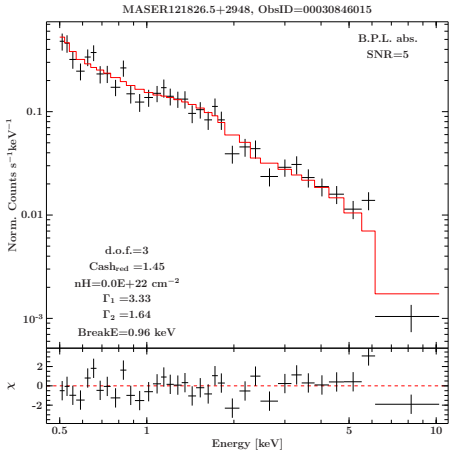

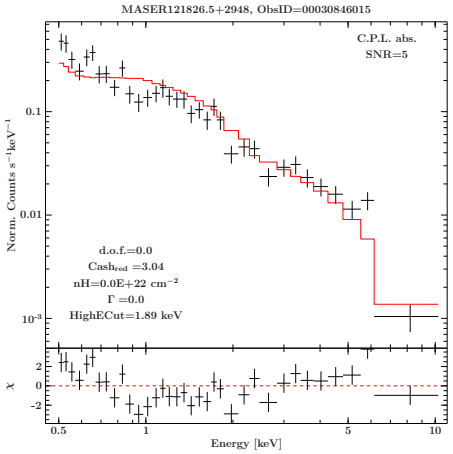

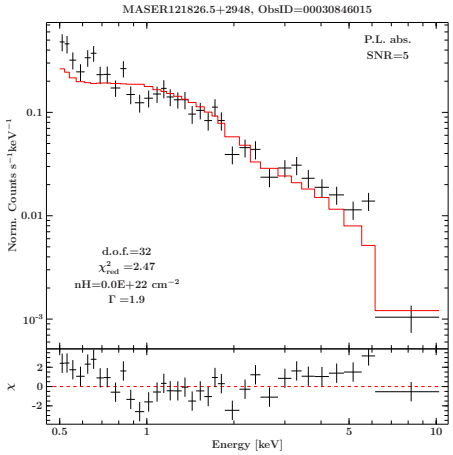

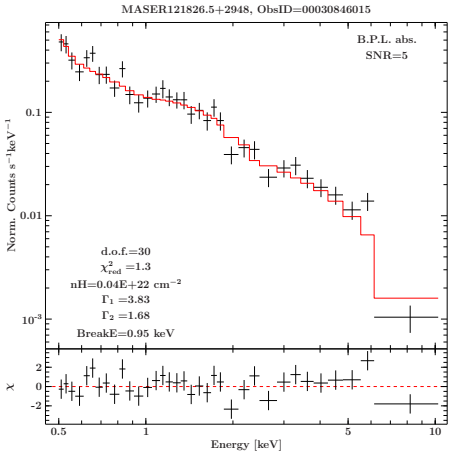

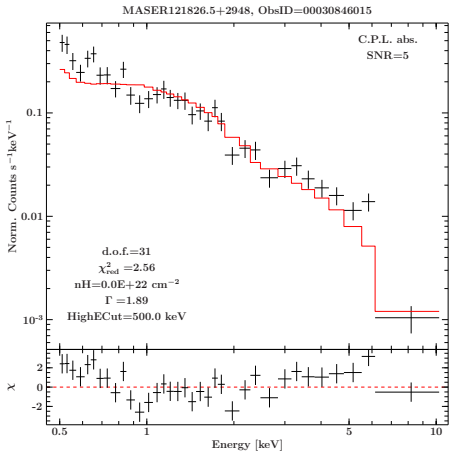
MASER121826.5+2948, ObsID=00030846015
C.P.L. abs.
SNR=5
d.o.f.=31
χ^2_{red} =2.56
nH=0.0E+22 cm^{-2}
Γ =1.89
HighECut=500.0 keV
Norm. Counts s^{-1}keV^{-1}
χ
Energy [keV]

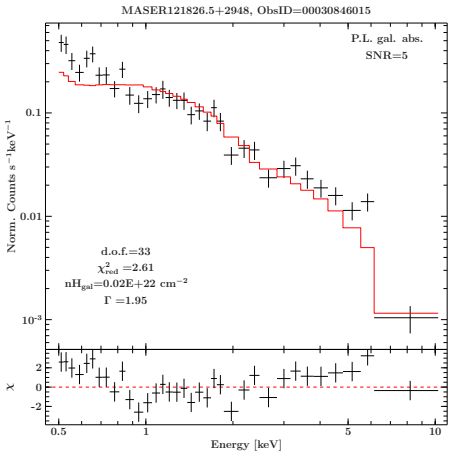
MASER121826.5+2948, ObsID=00030846015
P.L. gal. abs.
SNR=5
d.o.f.=33
χ^2_{red} =2.61
nH$_{gal}$=0.02E+22 cm^{-2}
Γ =1.95
Norm. Counts s^{-1}keV^{-1}
χ
Energy [keV]

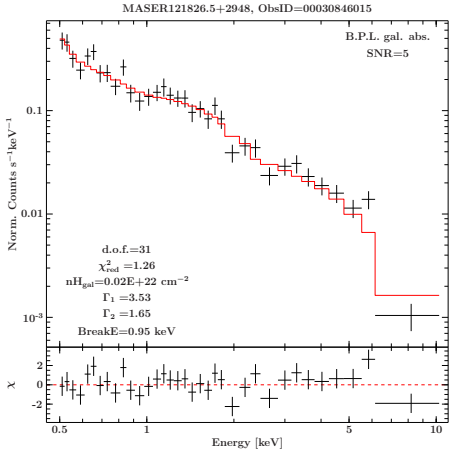
MASER121826.5+2948, ObsID=00030846015
B.P.L. gal. abs.
SNR=5
d.o.f.=31
χ^2_{red} =1.26
nH$_{gal}$=0.02E+22 cm^{-2}
Γ$_1$ =3.53
Γ$_2$ =1.65
BreakE=0.95 keV
Norm. Counts s^{-1}keV^{-1}
χ
Energy [keV]

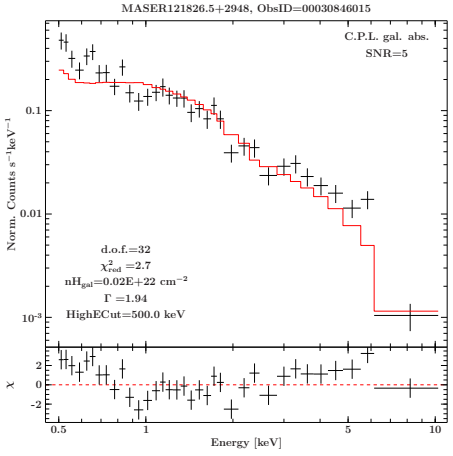
MASER121826.5+2948, ObsID=00030846015
C.P.L. gal. abs.
SNR=5
d.o.f.=32
χ^2_{red} =2.7
nH$_{gal}$=0.02E+22 cm^{-2}
Γ =1.94
HighECut=500.0 keV
Norm. Counts s^{-1}keV^{-1}
χ
Energy [keV]

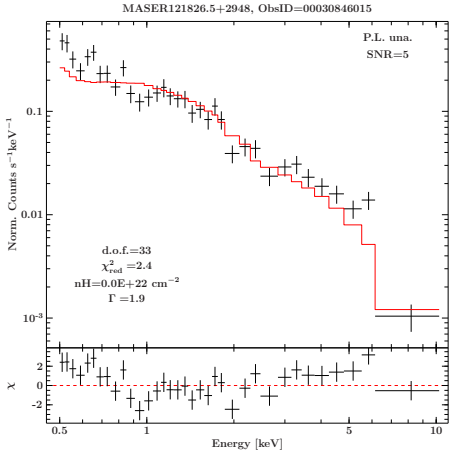
MASER121826.5+2948, ObsID=00030846015
P.L. una.
SNR=5
d.o.f.=33
χ^2_{red} =2.4
nH=0.0E+22 cm^{-2}
Γ =1.9
Norm. Counts s^{-1}keV^{-1}
χ
Energy [keV]

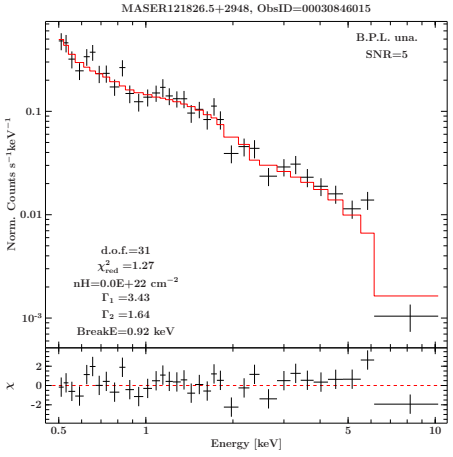
MASER121826.5+2948, ObsID=00030846015
B.P.L. una.
SNR=5
d.o.f.=31
χ^2_{red} =1.27
nH=0.0E+22 cm^{-2}
Γ$_1$ =3.43
Γ$_2$ =1.64
BreakE=0.92 keV
Norm. Counts s^{-1}keV^{-1}
χ
Energy [keV]

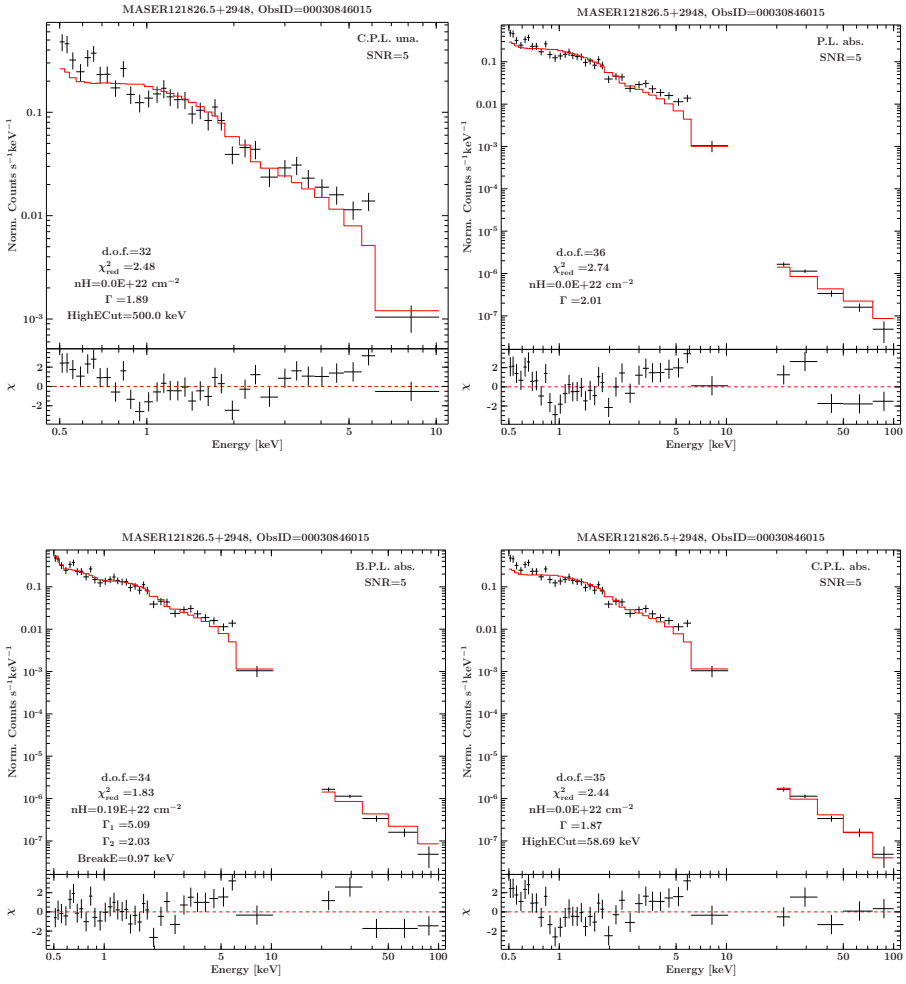
MASER121826.5+2948, ObsID=00030846015
C.P.L. una.
SNR=5
d.o.f.=32
χ^2_{red} =2.48
nH=0.0E+22 cm^{-2}
Γ =1.89
HighECut=500.0 keV
Norm. Counts s^{-1}keV^{-1}
χ
Energy [keV]
MASER121826.5+2948, ObsID=00030846015
P.L. abs.
SNR=5
d.o.f.=36
χ^2_{red} =2.74
nH=0.0E+22 cm^{-2}
Γ =2.01
Norm. Counts s^{-1}keV^{-1}
χ
Energy [keV]
MASER121826.5+2948, ObsID=00030846015
B.P.L. abs.
SNR=5
d.o.f.=34
χ^2_{red} =1.83
nH=0.19E+22 cm^{-2}
Γ$_1$ =5.09
Γ$_2$ =2.03
BreakE=0.97 keV
Norm. Counts s^{-1}keV^{-1}
χ
Energy [keV]
MASER121826.5+2948, ObsID=00030846015
C.P.L. abs.
SNR=5
d.o.f.=35
χ^2_{red} =2.44
nH=0.0E+22 cm^{-2}
Γ =1.87
HighECut=58.69 keV
Norm. Counts s^{-1}keV^{-1}
χ
Energy [keV]

ObsID 00030846016

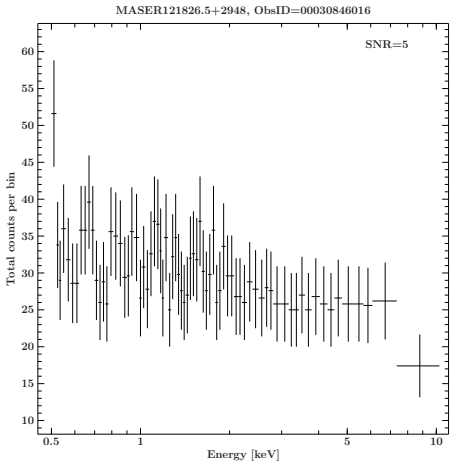

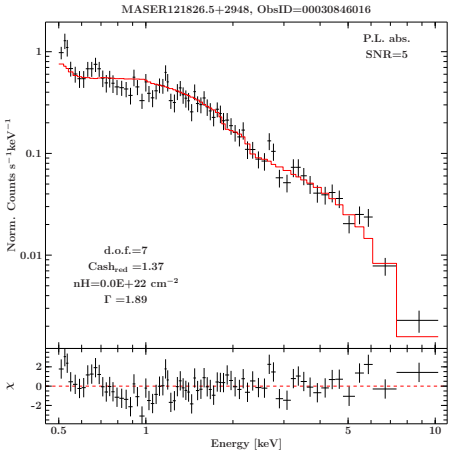

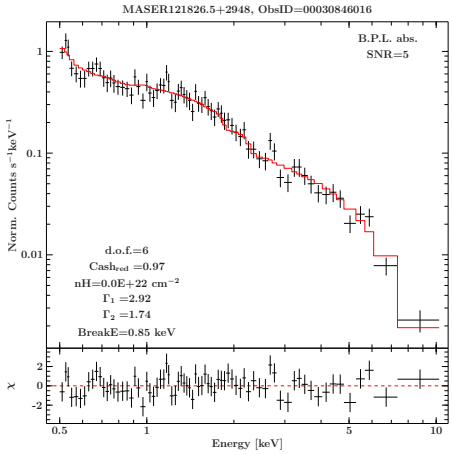

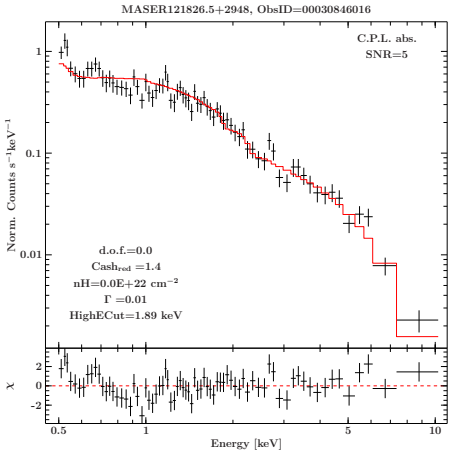

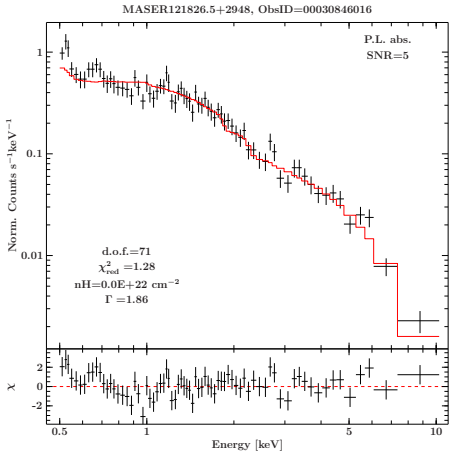

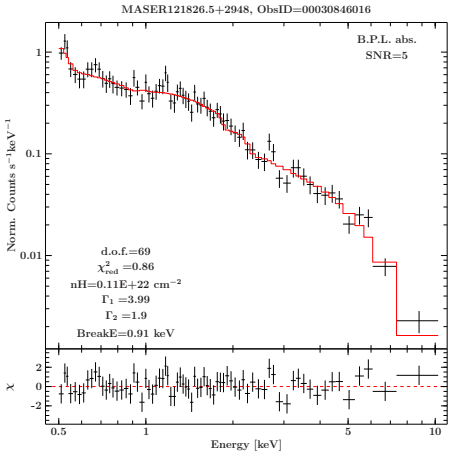

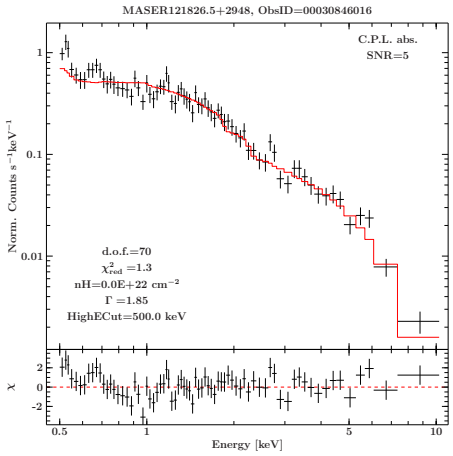
MASER121826.5+2948, ObsID=00030846016
C.P.L. abs.
SNR=5
d.o.f.=70
χ^2_{red} =1.3
nH=0.0E+22 cm^{-2}
Γ =1.85
HighECut=500.0 keV
Norm. Counts s^{-1}keV^{-1}
χ
Energy [keV]

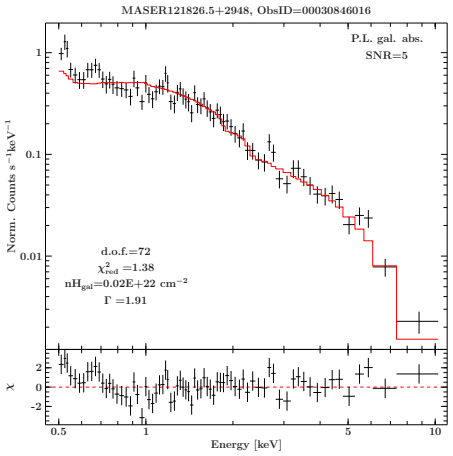
MASER121826.5+2948, ObsID=00030846016
P.L. gal. abs.
SNR=5
d.o.f.=72
χ^2_{red} =1.38
nH$_{gal}$=0.02E+22 cm^{-2}
Γ =1.91
Norm. Counts s^{-1}keV^{-1}
χ
Energy [keV]

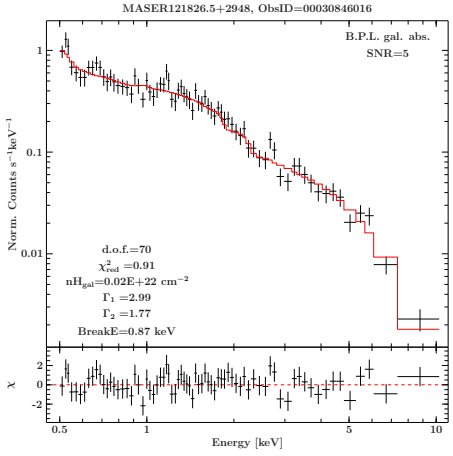
MASER121826.5+2948, ObsID=00030846016
B.P.L. gal. abs.
SNR=5
d.o.f.=70
χ^2_{red} =0.91
nH$_{gal}$=0.02E+22 cm^{-2}
Γ$_1$ =2.99
Γ$_2$ =1.77
BreakE=0.87 keV
Norm. Counts s^{-1}keV^{-1}
χ
Energy [keV]

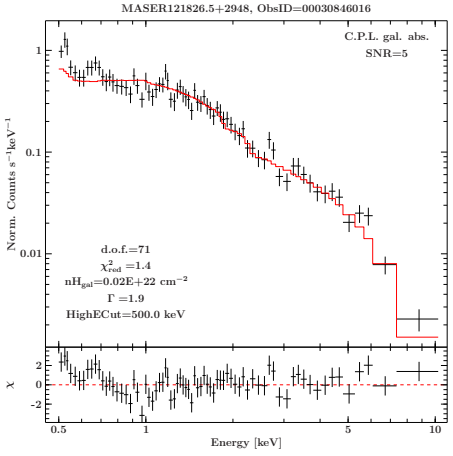
MASER121826.5+2948, ObsID=00030846016
C.P.L. gal. abs.
SNR=5
d.o.f.=71
χ^2_{red} =1.4
nH$_{gal}$=0.02E+22 cm^{-2}
Γ =1.9
HighECut=500.0 keV
Norm. Counts s^{-1}keV^{-1}
χ
Energy [keV]

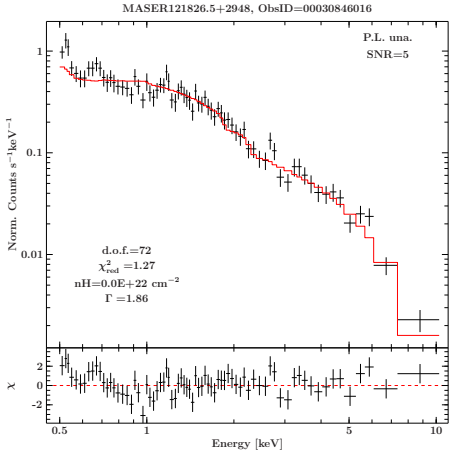
MASER121826.5+2948, ObsID=00030846016
P.L. una.
SNR=5
d.o.f.=72
χ^2_{red} =1.27
nH=0.0E+22 cm^{-2}
Γ =1.86
Norm. Counts s^{-1}keV^{-1}
χ
Energy [keV]

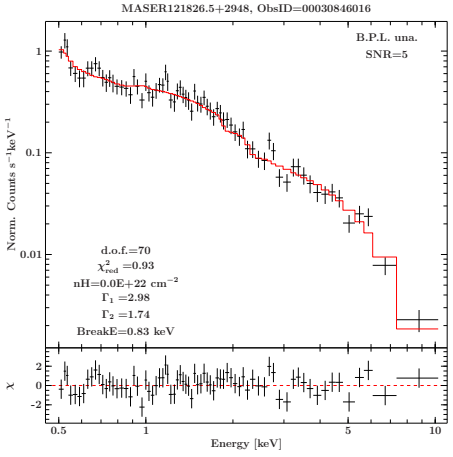
MASER121826.5+2948, ObsID=00030846016
B.P.L. una.
SNR=5
d.o.f.=70
χ^2_{red} =0.93
nH=0.0E+22 cm^{-2}
Γ$_1$ =2.98
Γ$_2$ =1.74
BreakE=0.83 keV
Norm. Counts s^{-1}keV^{-1}
χ
Energy [keV]

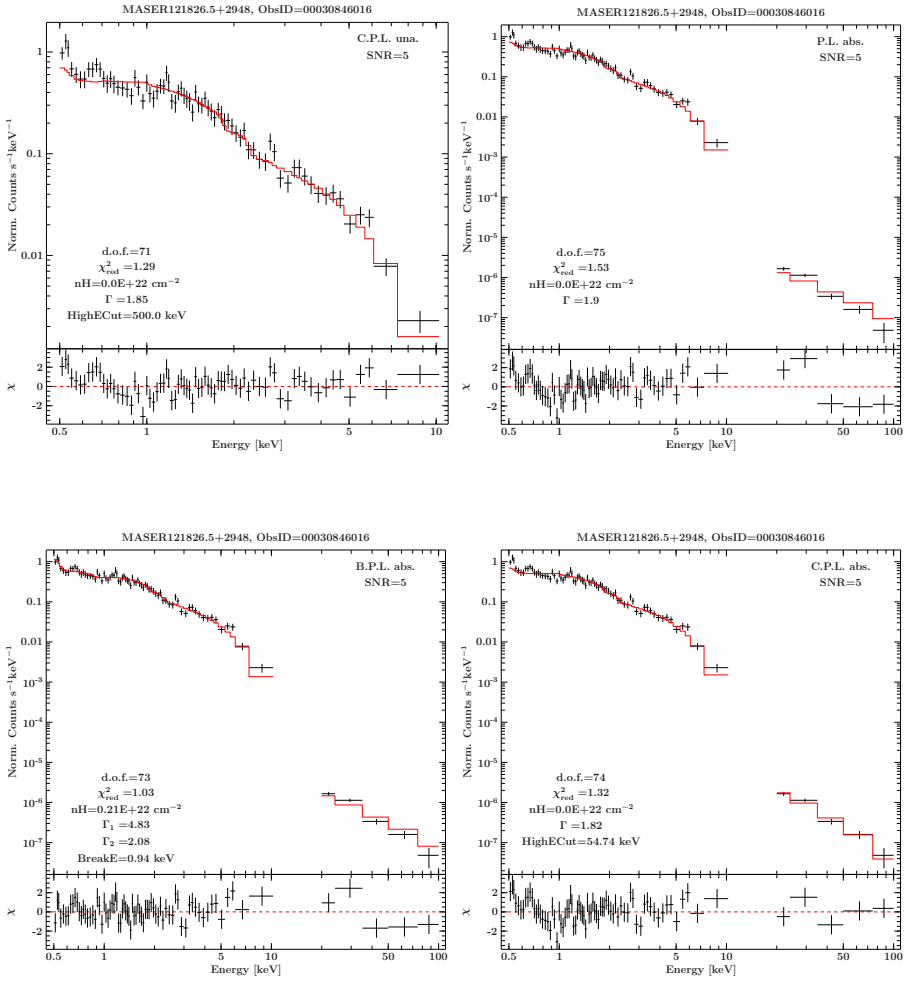
MASER121826.5+2948, ObsID=00030846016
C.P.L. una.
SNR=5
d.o.f.=71
χ^2_{red} =1.29
nH=0.0E+22 cm^{-2}
Γ =1.85
HighECut=500.0 keV
MASER121826.5+2948, ObsID=00030846016
P.L. abs.
SNR=5
d.o.f.=75
χ^2_{red} =1.53
nH=0.0E+22 cm^{-2}
Γ =1.9
MASER121826.5+2948, ObsID=00030846016
B.P.L. abs.
SNR=5
d.o.f.=73
χ^2_{red} =1.03
nH=0.21E+22 cm^{-2}
Γ_1 =4.83
Γ_2 =2.08
BreakE=0.94 keV
MASER121826.5+2948, ObsID=00030846016
C.P.L. abs.
SNR=5
d.o.f.=74
χ^2_{red} =1.32
nH=0.0E+22 cm^{-2}
Γ =1.82
HighECut=54.74 keV
Norm. Counts s^{-1}keV^{-1}
χ
Energy [keV]

ObsID 00030846017

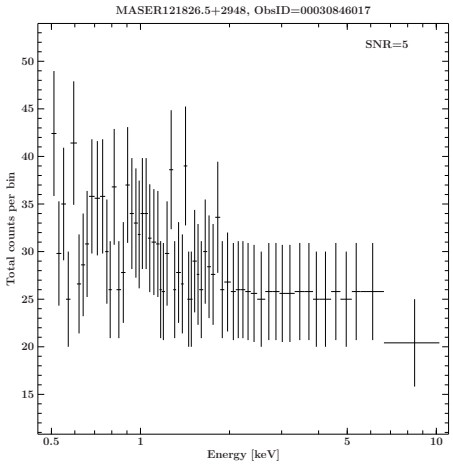

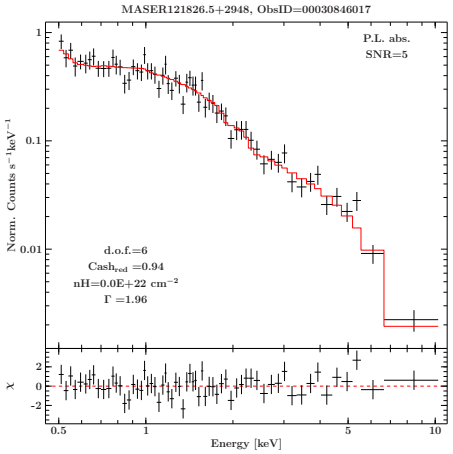

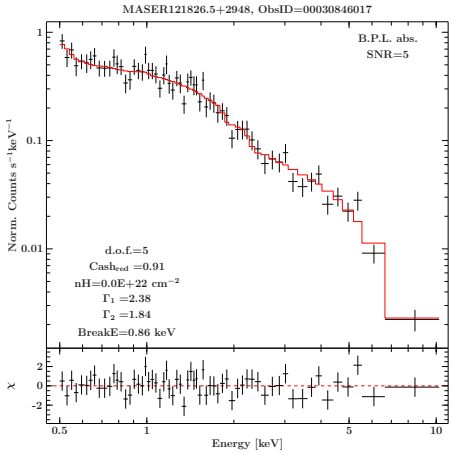

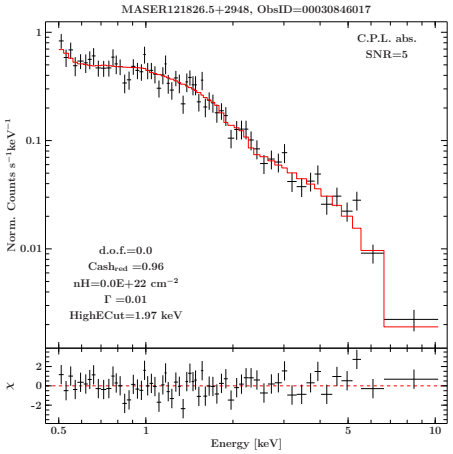

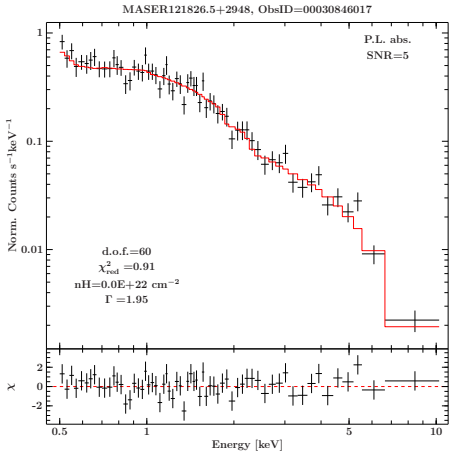

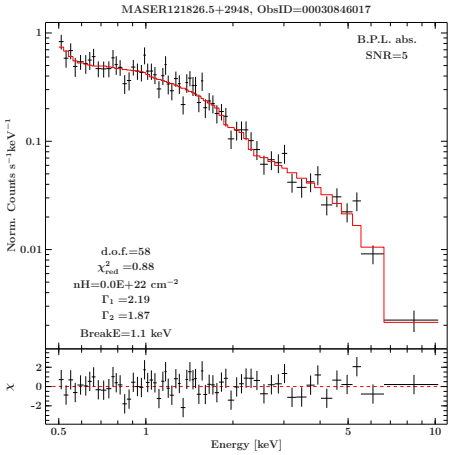

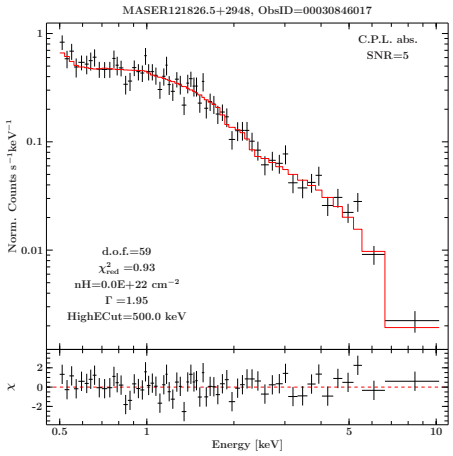
MASER121826.5+2948, ObsID=00030846017
C.P.L. abs.
SNR=5
d.o.f.=59
χ^2_{red} =0.93
nH=0.0E+22 cm^{-2}
Γ =1.95
HighECut=500.0 keV
Norm. Counts s^{-1}keV^{-1}
χ
Energy [keV]

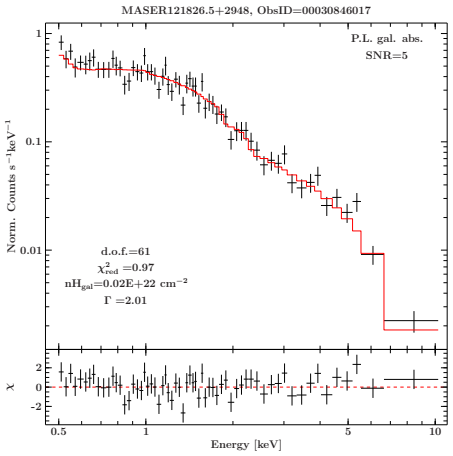
MASER121826.5+2948, ObsID=00030846017
P.L. gal. abs.
SNR=5
d.o.f.=61
χ^2_{red} =0.97
nH$_{gal}$=0.02E+22 cm^{-2}
Γ =2.01
Norm. Counts s^{-1}keV^{-1}
χ
Energy [keV]

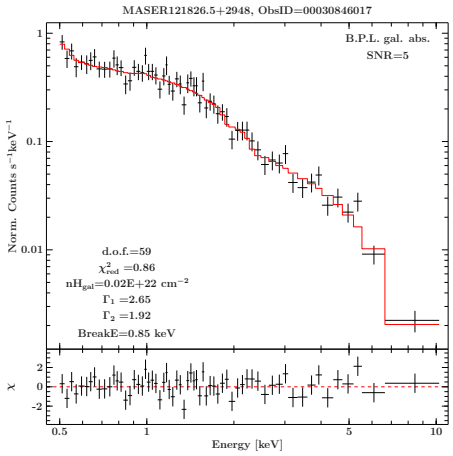
MASER121826.5+2948, ObsID=00030846017
B.P.L. gal. abs.
SNR=5
d.o.f.=59
χ^2_{red} =0.86
nH$_{gal}$=0.02E+22 cm^{-2}
Γ$_1$ =2.65
Γ$_2$ =1.92
BreakE=0.85 keV
Norm. Counts s^{-1}keV^{-1}
χ
Energy [keV]

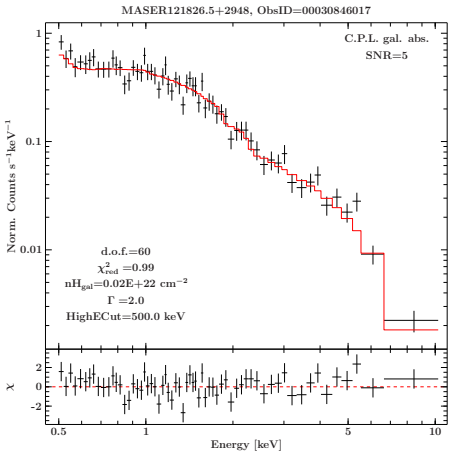
MASER121826.5+2948, ObsID=00030846017
C.P.L. gal. abs.
SNR=5
d.o.f.=60
χ^2_{red} =0.99
nH$_{gal}$=0.02E+22 cm^{-2}
Γ =2.0
HighECut=500.0 keV
Norm. Counts s^{-1}keV^{-1}
χ
Energy [keV]

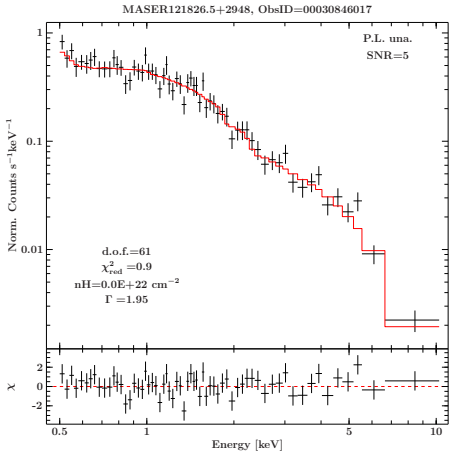
MASER121826.5+2948, ObsID=00030846017
P.L. una.
SNR=5
d.o.f.=61
χ^2_{red} =0.9
nH=0.0E+22 cm^{-2}
Γ =1.95
Norm. Counts s^{-1}keV^{-1}
χ
Energy [keV]

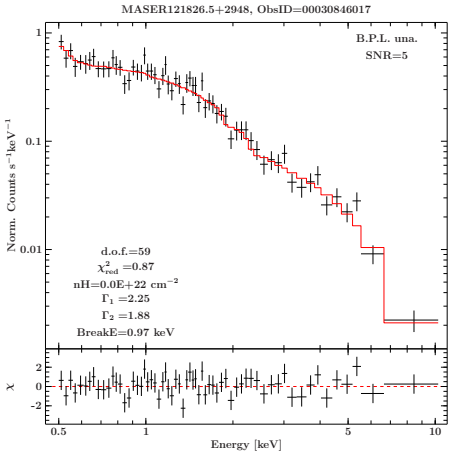
MASER121826.5+2948, ObsID=00030846017
B.P.L. una.
SNR=5
d.o.f.=59
χ^2_{red} =0.87
nH=0.0E+22 cm^{-2}
Γ$_1$ =2.25
Γ$_2$ =1.88
BreakE=0.97 keV
Norm. Counts s^{-1}keV^{-1}
χ
Energy [keV]

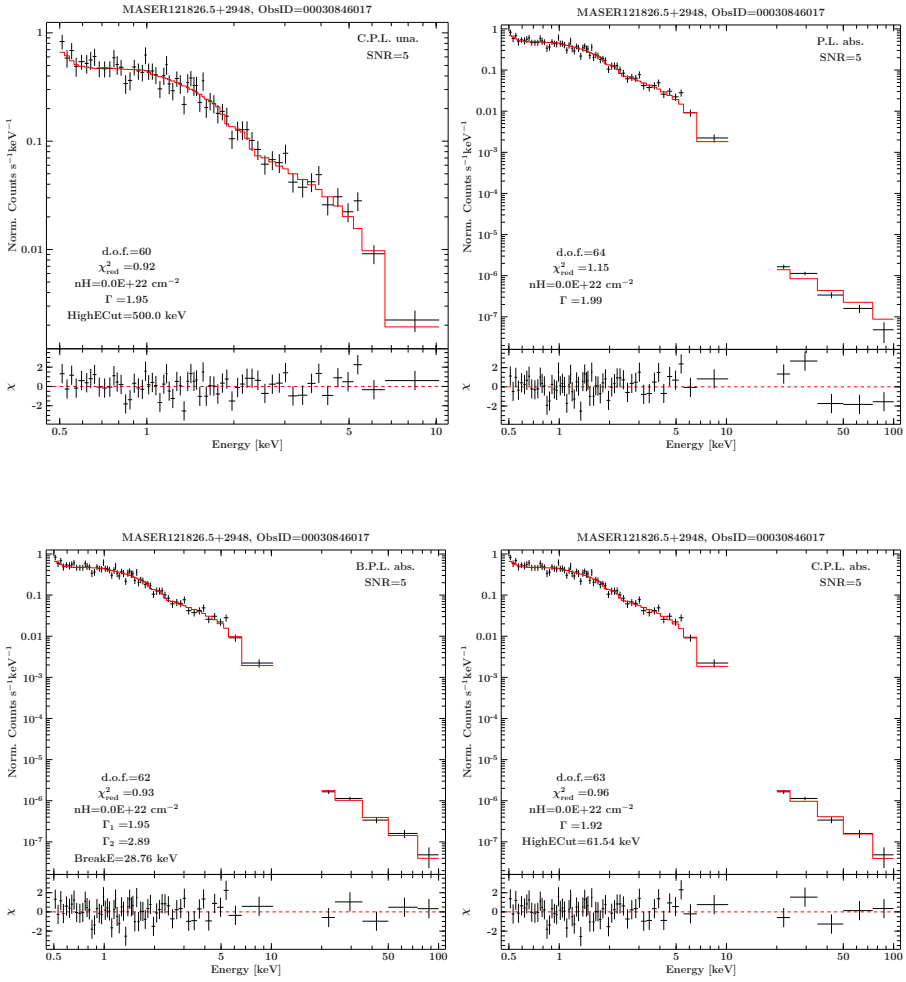
MASER121826.5+2948, ObsID=00030846017
C.P.L. una.
SNR=5
d.o.f.=60
χ^2_{red} =0.92
nH=0.0E+22 cm^{-2}
Γ =1.95
HighECut=500.0 keV
Norm. Counts s^{-1}keV^{-1}
χ
Energy [keV]
MASER121826.5+2948, ObsID=00030846017
P.L. abs.
SNR=5
d.o.f.=64
χ^2_{red} =1.15
nH=0.0E+22 cm^{-2}
Γ =1.99
Norm. Counts s^{-1}keV^{-1}
χ
Energy [keV]
MASER121826.5+2948, ObsID=00030846017
B.P.L. abs.
SNR=5
d.o.f.=62
χ^2_{red} =0.93
nH=0.0E+22 cm^{-2}
Γ$_1$ =1.95
Γ$_2$ =2.89
BreakE=28.76 keV
Norm. Counts s^{-1}keV^{-1}
χ
Energy [keV]
MASER121826.5+2948, ObsID=00030846017
C.P.L. abs.
SNR=5
d.o.f.=63
χ^2_{red} =0.96
nH=0.0E+22 cm^{-2}
Γ =1.92
HighECut=61.54 keV
Norm. Counts s^{-1}keV^{-1}
χ
Energy [keV]

ObsID 00030846018

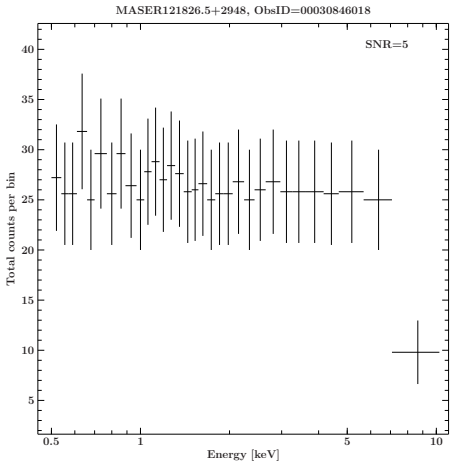

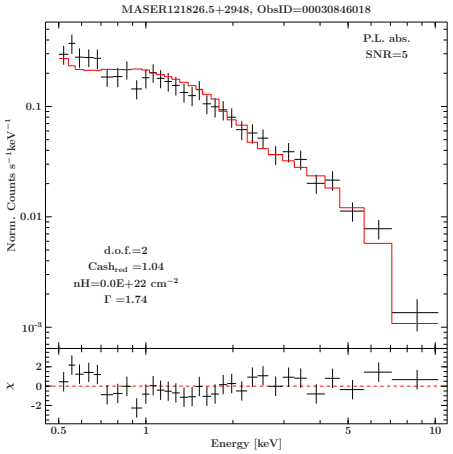

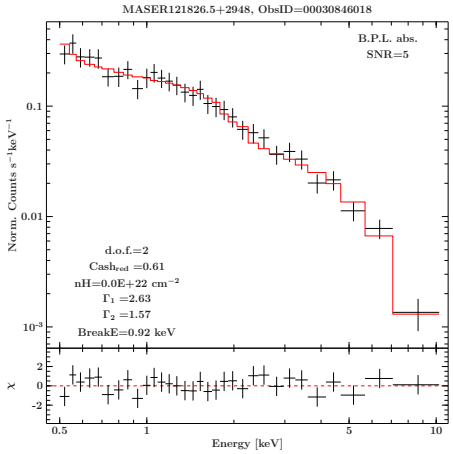

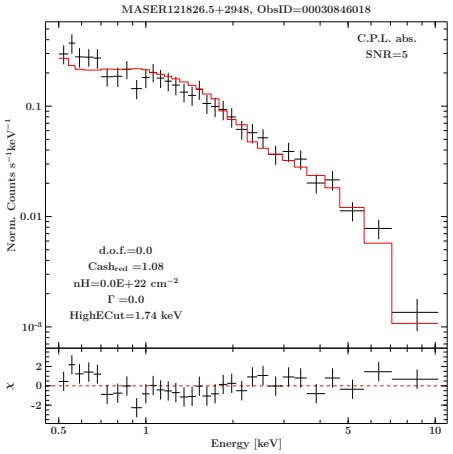

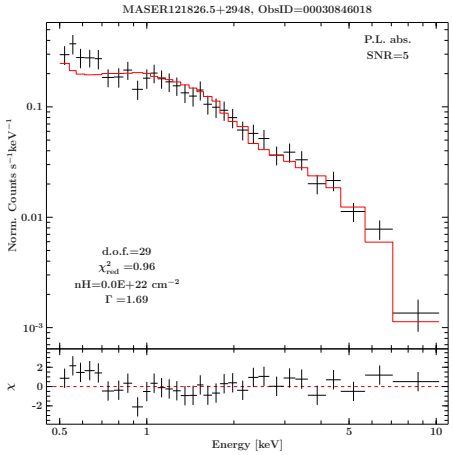

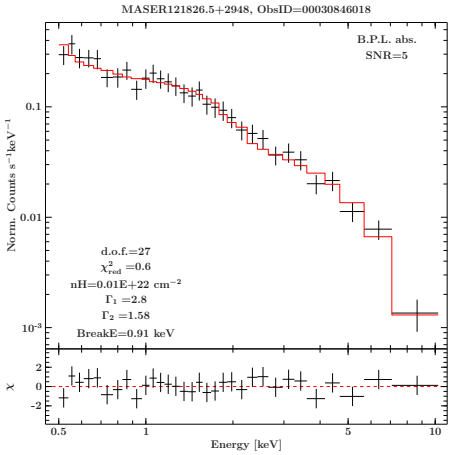

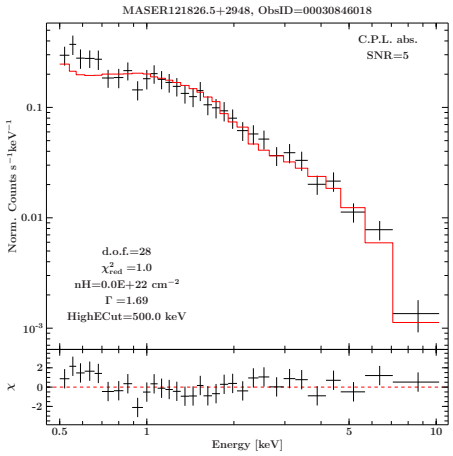
MASER121826.5+2948, ObsID=00030846018
C.P.L. abs.
SNR=5
d.o.f.=28
χ^2_{red} =1.0
nH=0.0E+22 cm^{-2}
Γ =1.69
HighECut=500.0 keV
Norm. Counts s^{-1}keV^{-1}
χ
Energy [keV]

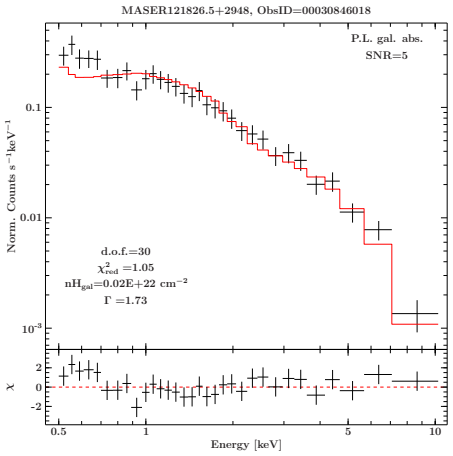
MASER121826.5+2948, ObsID=00030846018
P.L. gal. abs.
SNR=5
d.o.f.=30
χ^2_{red} =1.05
nH$_{gal}$=0.02E+22 cm^{-2}
Γ =1.73
Norm. Counts s^{-1}keV^{-1}
χ
Energy [keV]

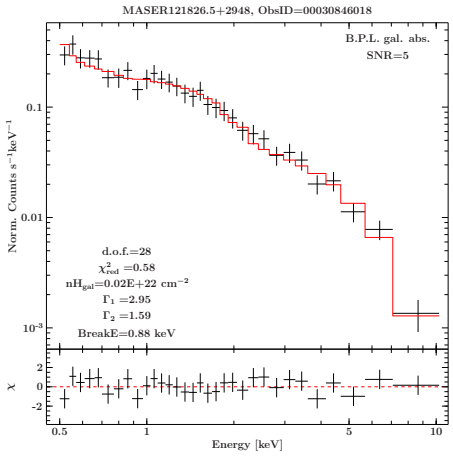
MASER121826.5+2948, ObsID=00030846018
B.P.L. gal. abs.
SNR=5
d.o.f.=28
χ^2_{red} =0.58
nH$_{gal}$=0.02E+22 cm^{-2}
Γ$_1$ =2.95
Γ$_2$ =1.59
BreakE=0.88 keV
Norm. Counts s^{-1}keV^{-1}
χ
Energy [keV]

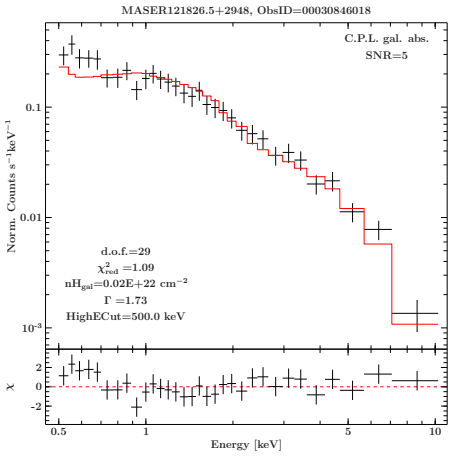
MASER121826.5+2948, ObsID=00030846018
C.P.L. gal. abs.
SNR=5
d.o.f.=29
χ^2_{red} =1.09
nH$_{gal}$=0.02E+22 cm^{-2}
Γ =1.73
HighECut=500.0 keV
Norm. Counts s^{-1}keV^{-1}
χ
Energy [keV]

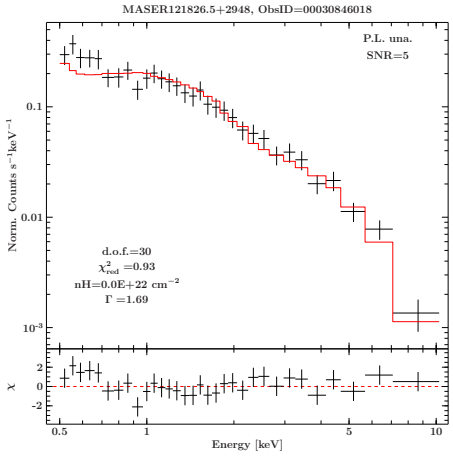
MASER121826.5+2948, ObsID=00030846018
P.L. una.
SNR=5
d.o.f.=30
χ^2_{red} =0.93
nH=0.0E+22 cm^{-2}
Γ =1.69
Norm. Counts s^{-1}keV^{-1}
χ
Energy [keV]

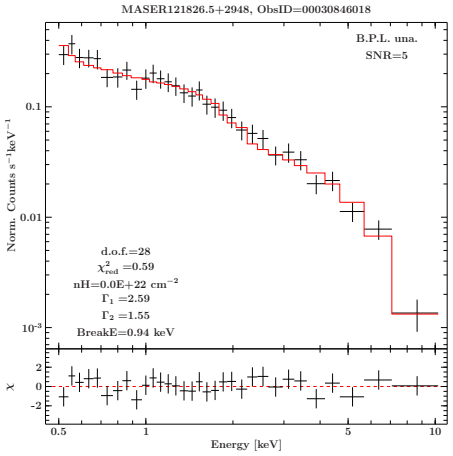
MASER121826.5+2948, ObsID=00030846018
B.P.L. una.
SNR=5
d.o.f.=28
χ^2_{red} =0.59
nH=0.0E+22 cm^{-2}
Γ$_1$ =2.59
Γ$_2$ =1.55
BreakE=0.94 keV
Norm. Counts s^{-1}keV^{-1}
χ
Energy [keV]

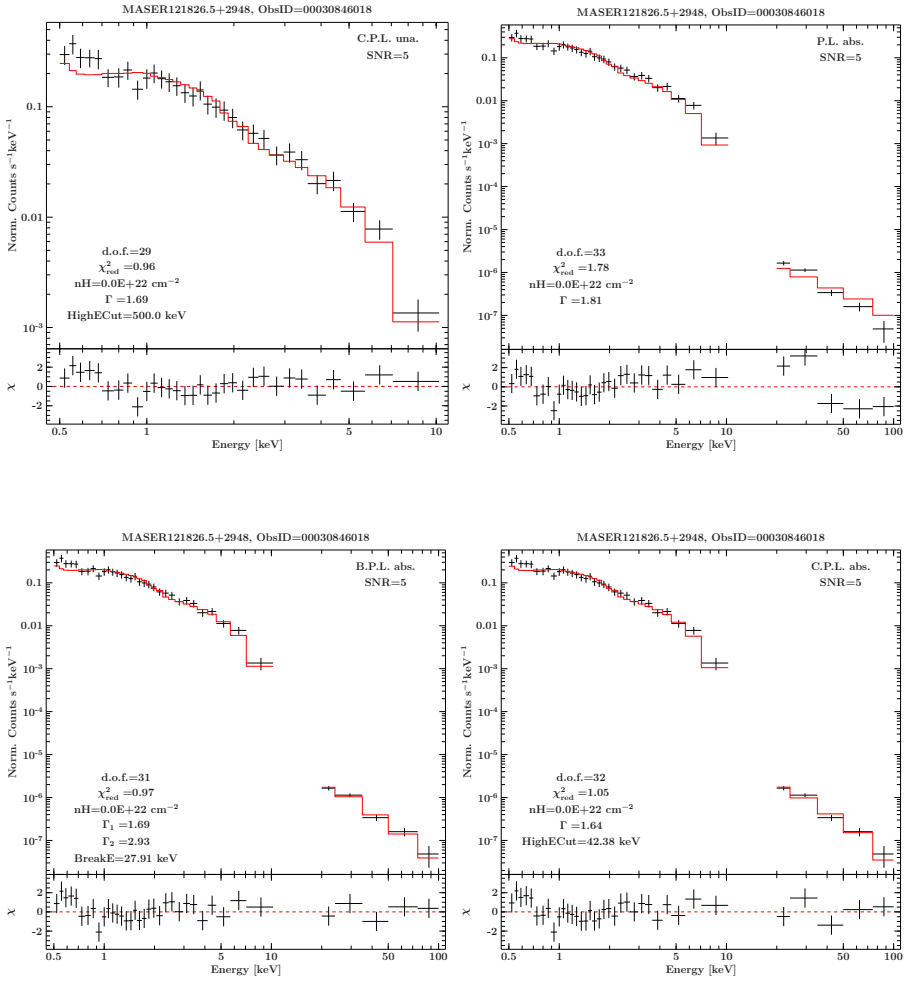
MASER121826.5+2948, ObsID=00030846018
C.P.L. una.
SNR=5
d.o.f.=29
χ^2_{red} =0.96
nH=0.0E+22 cm^{-2}
Γ =1.69
HighECut=500.0 keV
MASER121826.5+2948, ObsID=00030846018
P.L. abs.
SNR=5
d.o.f.=33
χ^2_{red} =1.78
nH=0.0E+22 cm^{-2}
Γ =1.81
MASER121826.5+2948, ObsID=00030846018
B.P.L. abs.
SNR=5
d.o.f.=31
χ^2_{red} =0.97
nH=0.0E+22 cm^{-2}
Γ_1 =1.69
Γ_2 =2.93
BreakE=27.91 keV
MASER121826.5+2948, ObsID=00030846018
C.P.L. abs.
SNR=5
d.o.f.=32
χ^2_{red} =1.05
nH=0.0E+22 cm^{-2}
Γ =1.64
HighECut=42.38 keV
Norm. Counts s^{-1}keV^{-1}
χ
Energy [keV]

ObsID 00030846019

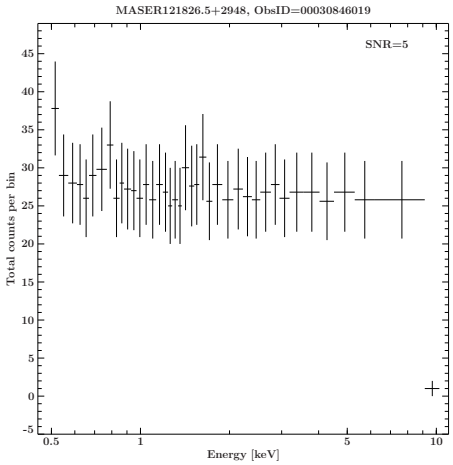

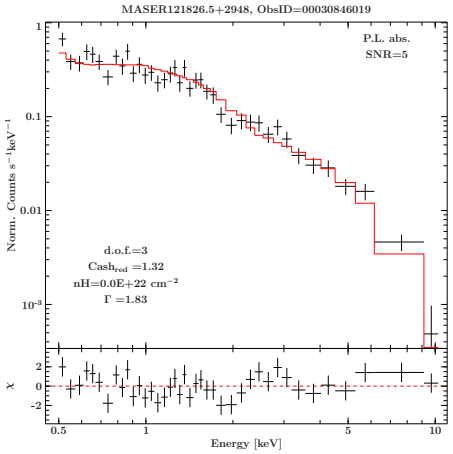

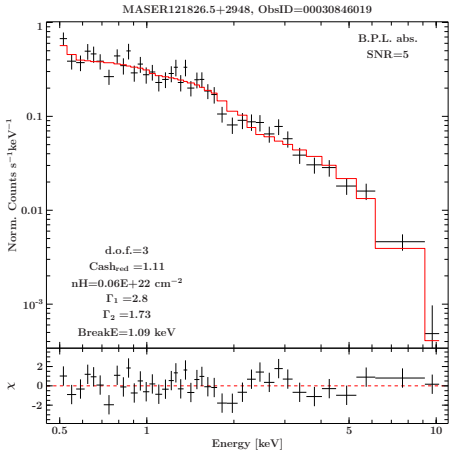

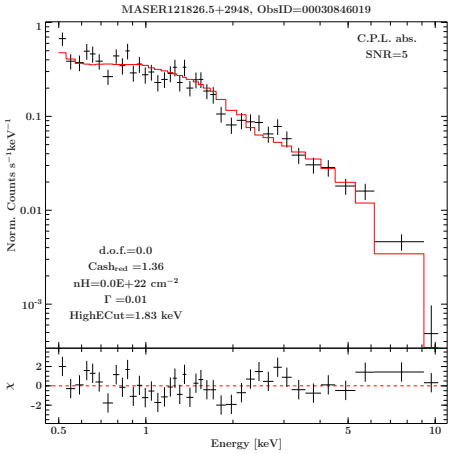

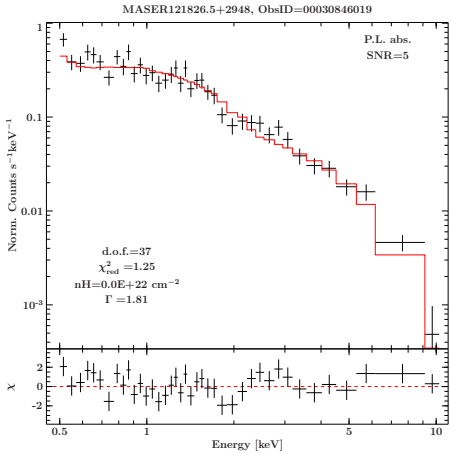

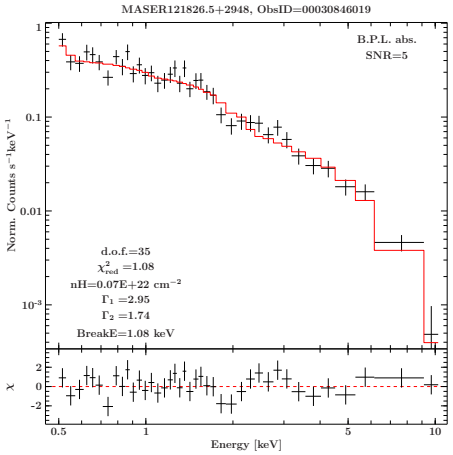

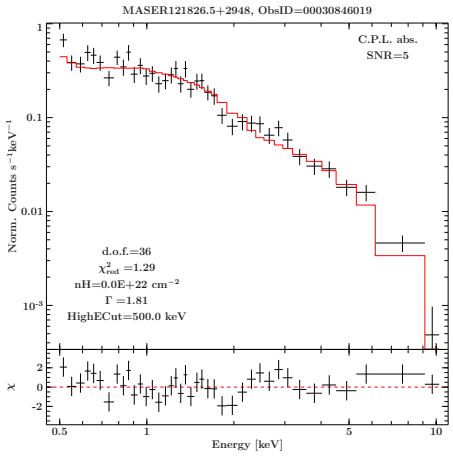
MASER121826.5+2948, ObsID=00030846019
C.P.L. abs.
SNR=5
d.o.f.=36
χ^2_{red} =1.29
nH=0.0E+22 cm^{-2}
Γ =1.81
HighECut=500.0 keV
Norm. Counts s^{-1}keV^{-1}
χ
Energy [keV]

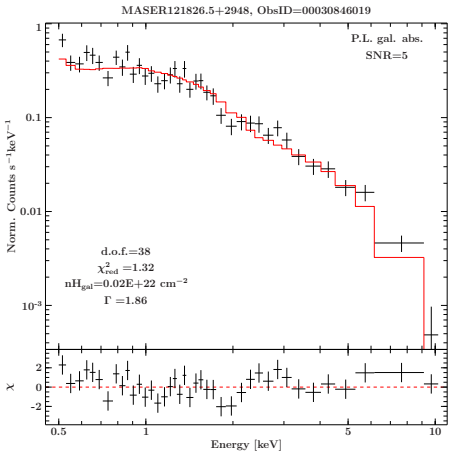
MASER121826.5+2948, ObsID=00030846019
P.L. gal. abs.
SNR=5
d.o.f.=38
χ^2_{red} =1.32
nH$_{gal}$=0.02E+22 cm^{-2}
Γ =1.86
Norm. Counts s^{-1}keV^{-1}
χ
Energy [keV]

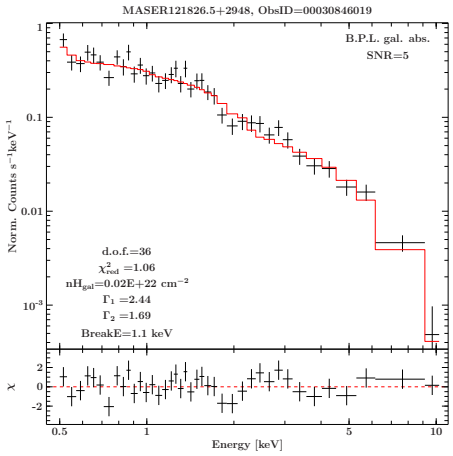
MASER121826.5+2948, ObsID=00030846019
B.P.L. gal. abs.
SNR=5
d.o.f.=36
χ^2_{red} =1.06
nH$_{gal}$=0.02E+22 cm^{-2}
Γ$_1$ =2.44
Γ$_2$ =1.69
BreakE=1.1 keV
Norm. Counts s^{-1}keV^{-1}
χ
Energy [keV]

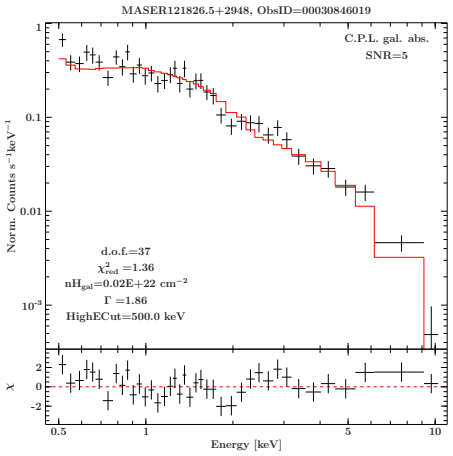
MASER121826.5+2948, ObsID=00030846019
C.P.L. gal. abs.
SNR=5
d.o.f.=37
χ^2_{red} =1.36
nH$_{gal}$=0.02E+22 cm^{-2}
Γ =1.86
HighECut=500.0 keV
Norm. Counts s^{-1}keV^{-1}
χ
Energy [keV]

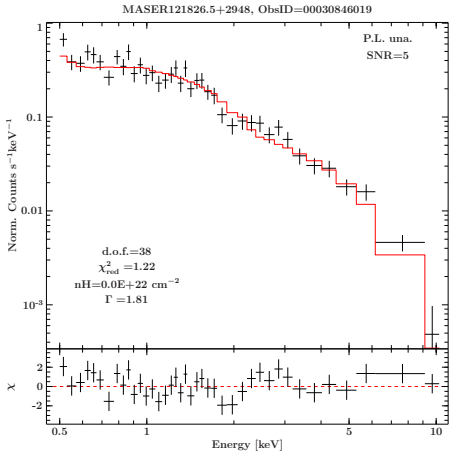
MASER121826.5+2948, ObsID=00030846019
P.L. una.
SNR=5
d.o.f.=38
χ^2_{red} =1.22
nH=0.0E+22 cm^{-2}
Γ =1.81
Norm. Counts s^{-1}keV^{-1}
χ
Energy [keV]

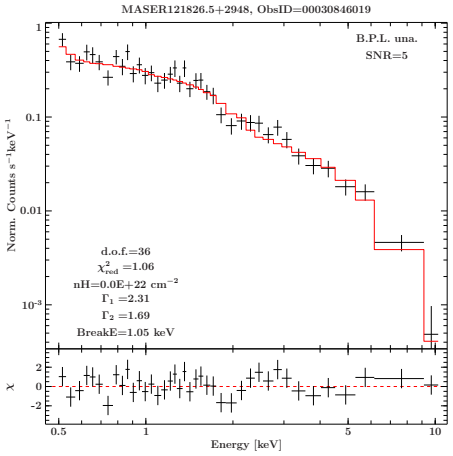
MASER121826.5+2948, ObsID=00030846019
B.P.L. una.
SNR=5
d.o.f.=36
χ^2_{red} =1.06
nH=0.0E+22 cm^{-2}
Γ$_1$ =2.31
Γ$_2$ =1.69
BreakE=1.05 keV
Norm. Counts s^{-1}keV^{-1}
χ
Energy [keV]

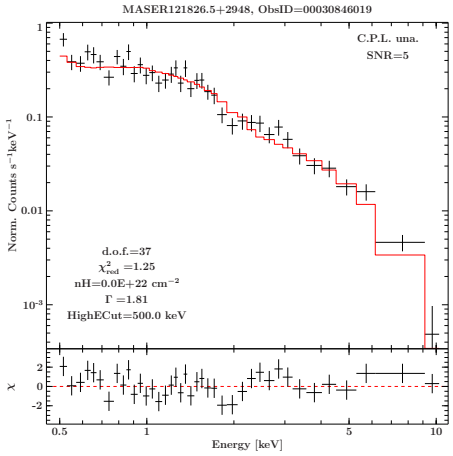
MASER121826.5+2948, ObsID=00030846019
C.P.L. una.
SNR=5
d.o.f.=37
χ^2_{red} =1.25
nH=0.0E+22 cm^{-2}
Γ =1.81
HighECut=500.0 keV
Norm. Counts s^{-1}keV^{-1}
χ
Energy [keV]

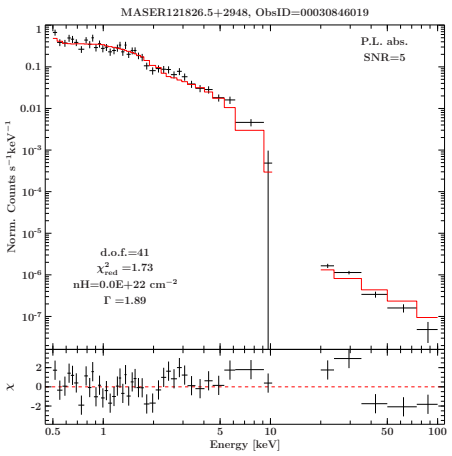
MASER121826.5+2948, ObsID=00030846019
P.L. abs.
SNR=5
d.o.f.=41
χ^2_{red} =1.73
nH=0.0E+22 cm^{-2}
Γ =1.89
Norm. Counts s^{-1}keV^{-1}
χ
Energy [keV]

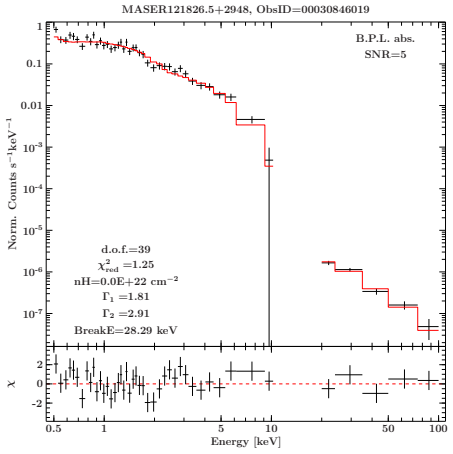
MASER121826.5+2948, ObsID=00030846019
B.P.L. abs.
SNR=5
d.o.f.=39
χ^2_{red} =1.25
nH=0.0E+22 cm^{-2}
Γ_1 =1.81
Γ_2 =2.91
BreakE=28.29 keV
Norm. Counts s^{-1}keV^{-1}
χ
Energy [keV]

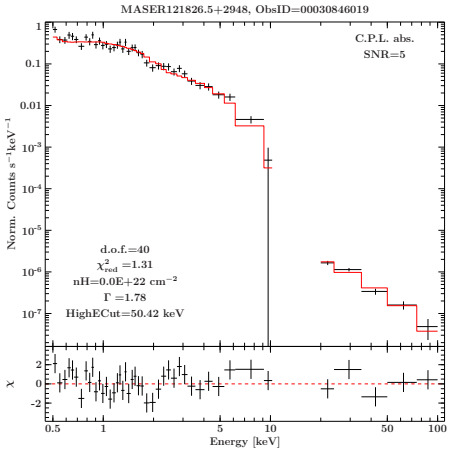
MASER121826.5+2948, ObsID=00030846019
C.P.L. abs.
SNR=5
d.o.f.=40
χ^2_{red} =1.31
nH=0.0E+22 cm^{-2}
Γ =1.78
HighECut=50.42 keV
Norm. Counts s^{-1}keV^{-1}
χ
Energy [keV]

ObsID 00030846020

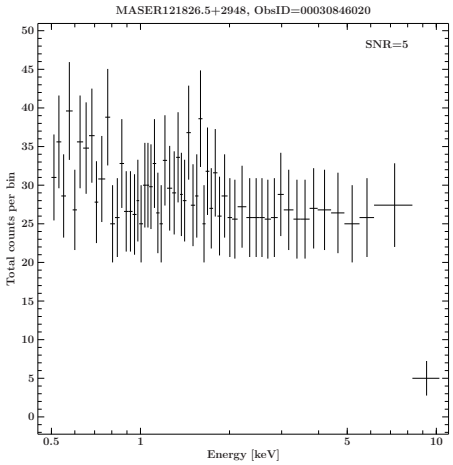

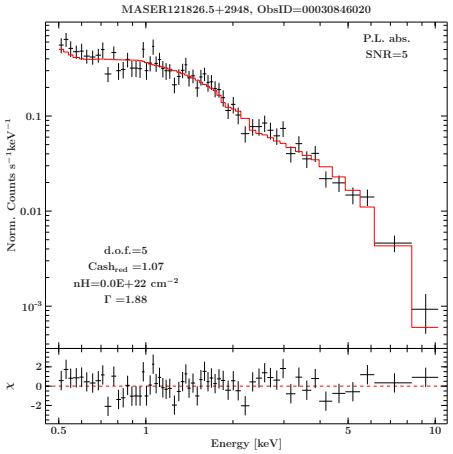

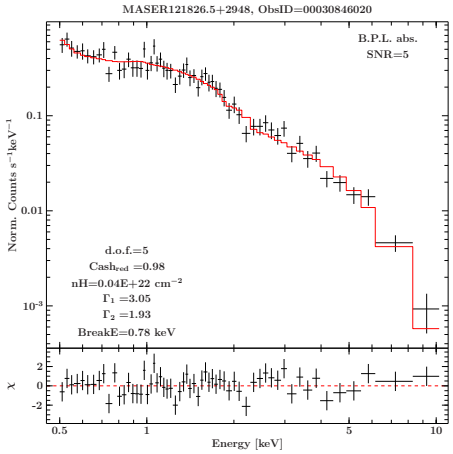

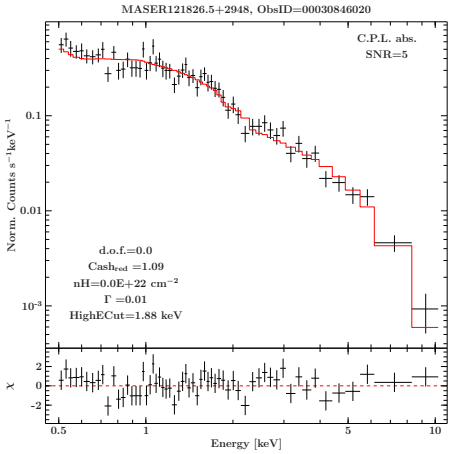

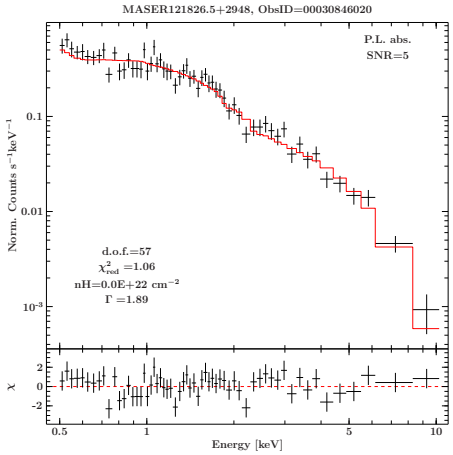

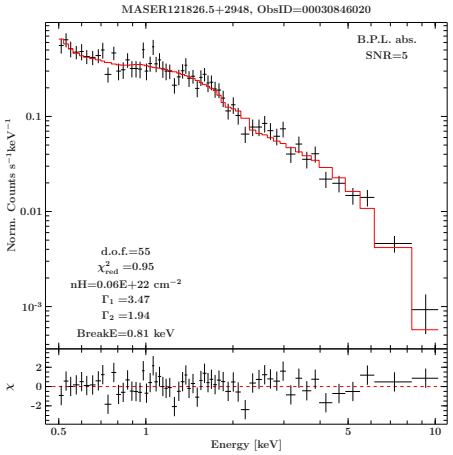

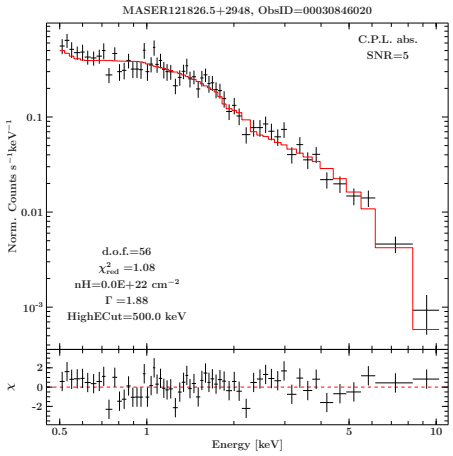
MASER121826.5+2948, ObsID=00030846020
C.P.L. abs.
SNR=5
d.o.f.=56
χ^2_{red} =1.08
nH=0.0E+22 cm^{-2}
Γ =1.88
HighECut=500.0 keV
Norm. Counts s^{-1}keV^{-1}
χ
Energy [keV]

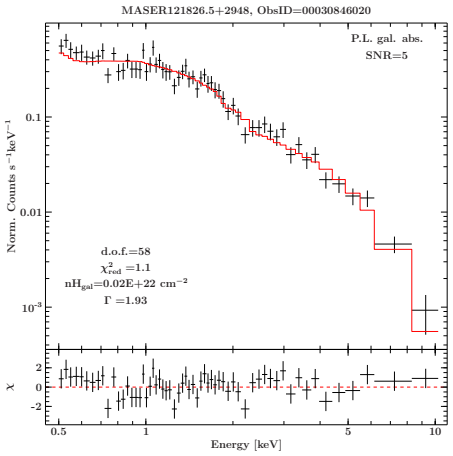
MASER121826.5+2948, ObsID=00030846020
P.L. gal. abs.
SNR=5
d.o.f.=58
χ^2_{red} =1.1
nH$_{gal}$=0.02E+22 cm^{-2}
Γ =1.93
Norm. Counts s^{-1}keV^{-1}
χ
Energy [keV]

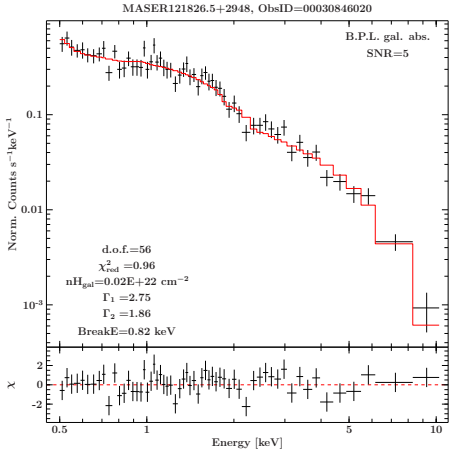
MASER121826.5+2948, ObsID=00030846020
B.P.L. gal. abs.
SNR=5
d.o.f.=56
χ^2_{red} =0.96
nH$_{gal}$=0.02E+22 cm^{-2}
Γ$_1$ =2.75
Γ$_2$ =1.86
BreakE=0.82 keV
Norm. Counts s^{-1}keV^{-1}
χ
Energy [keV]

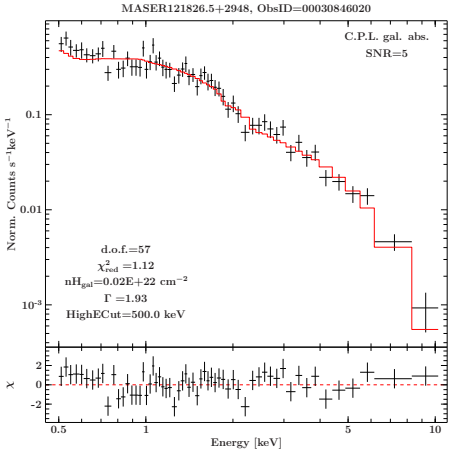
MASER121826.5+2948, ObsID=00030846020
C.P.L. gal. abs.
SNR=5
d.o.f.=57
χ^2_{red} =1.12
nH$_{gal}$=0.02E+22 cm^{-2}
Γ =1.93
HighECut=500.0 keV
Norm. Counts s^{-1}keV^{-1}
χ
Energy [keV]

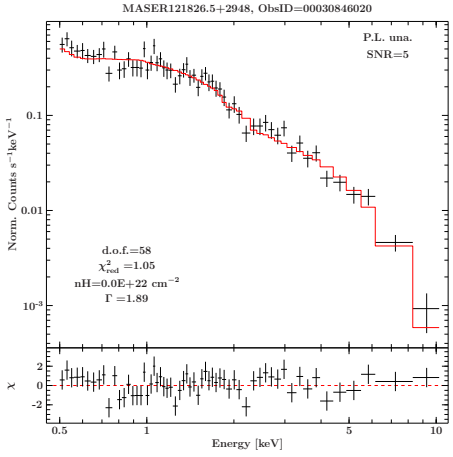
MASER121826.5+2948, ObsID=00030846020
P.L. una.
SNR=5
d.o.f.=58
χ^2_{red} =1.05
nH=0.0E+22 cm^{-2}
Γ =1.89
Norm. Counts s^{-1}keV^{-1}
χ
Energy [keV]

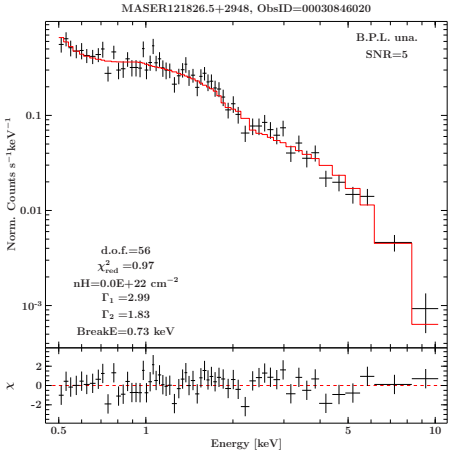
MASER121826.5+2948, ObsID=00030846020
B.P.L. una.
SNR=5
d.o.f.=56
χ^2_{red} =0.97
nH=0.0E+22 cm^{-2}
Γ$_1$ =2.99
Γ$_2$ =1.83
BreakE=0.73 keV
Norm. Counts s^{-1}keV^{-1}
χ
Energy [keV]

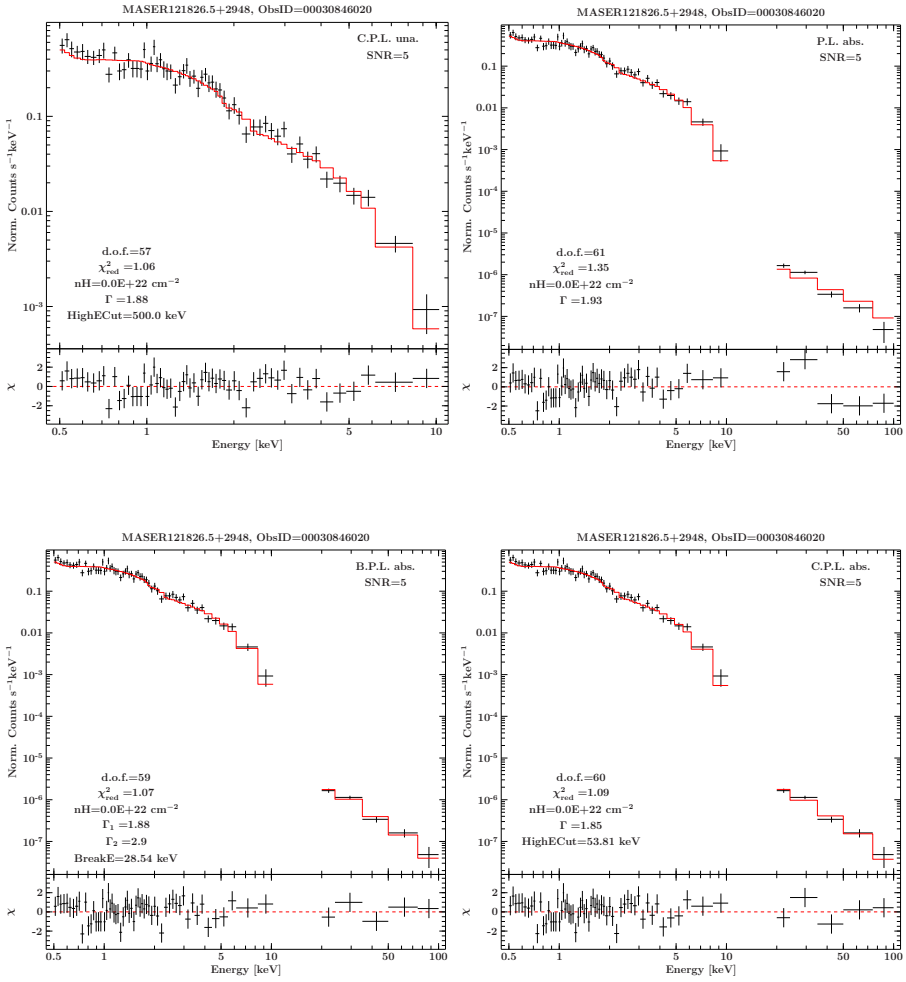
MASER121826.5+2948, ObsID=00030846020
C.P.L. una.
SNR=5
d.o.f.=57
χ^2_{red} =1.06
nH=0.0E+22 cm^{-2}
Γ =1.88
HighECut=500.0 keV
MASER121826.5+2948, ObsID=00030846020
P.L. abs.
SNR=5
d.o.f.=61
χ^2_{red} =1.35
nH=0.0E+22 cm^{-2}
Γ =1.93
MASER121826.5+2948, ObsID=00030846020
B.P.L. abs.
SNR=5
d.o.f.=59
χ^2_{red} =1.07
nH=0.0E+22 cm^{-2}
Γ$_1$ =1.88
Γ$_2$ =2.9
BreakE=28.54 keV
MASER121826.5+2948, ObsID=00030846020
C.P.L. abs.
SNR=5
d.o.f.=60
χ^2_{red} =1.09
nH=0.0E+22 cm^{-2}
Γ =1.85
HighECut=53.81 keV
Norm. Counts s^{-1}keV^{-1}
χ
Energy [keV]

ObsID 00030846021

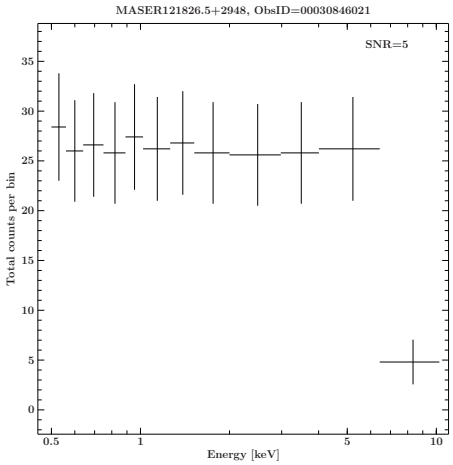

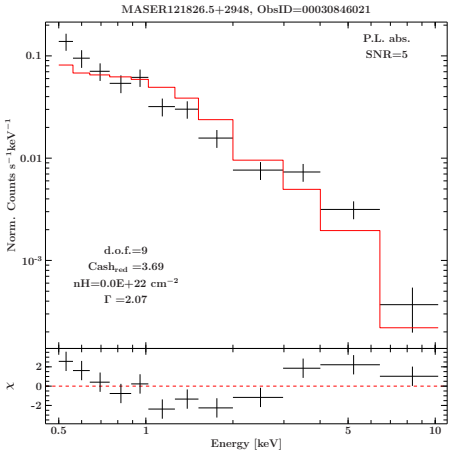

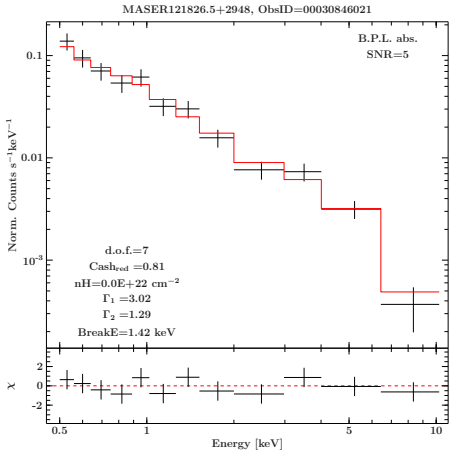

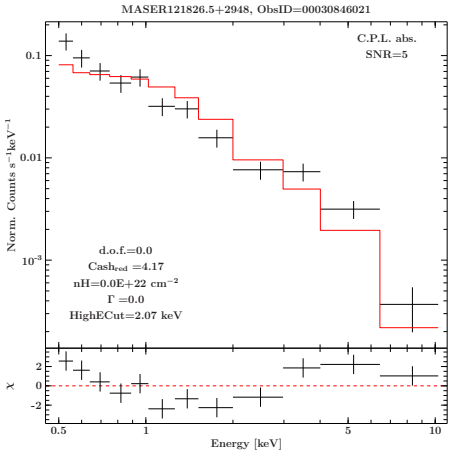

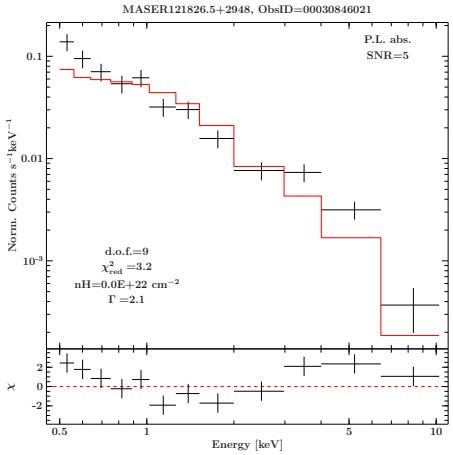

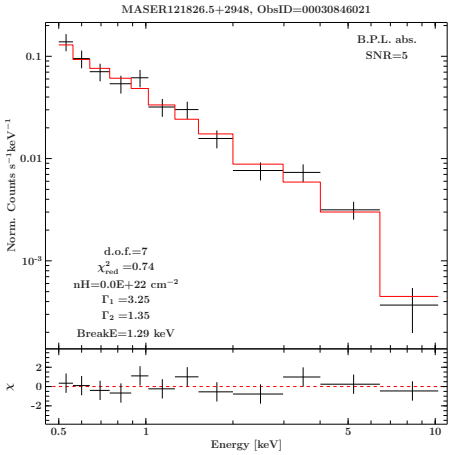

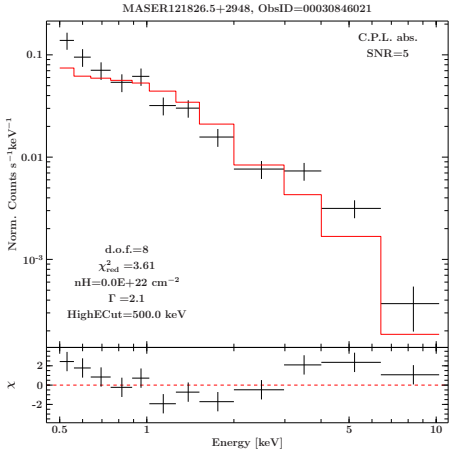
MASER121826.5+2948, ObsID=00030846021
C.P.L. abs.
SNR=5
d.o.f.=8
χ^2_{red} =3.61
nH=0.0E+22 cm^{-2}
Γ =2.1
HighECut=500.0 keV
Norm. Counts s^{-1}keV^{-1}
Energy [keV]

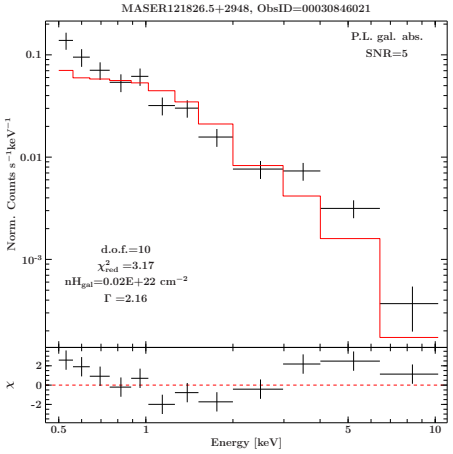
MASER121826.5+2948, ObsID=00030846021
P.L. gal. abs.
SNR=5
d.o.f.=10
χ^2_{red} =3.17
nH$_{gal}$=0.02E+22 cm^{-2}
Γ =2.16
Norm. Counts s^{-1}keV^{-1}
Energy [keV]

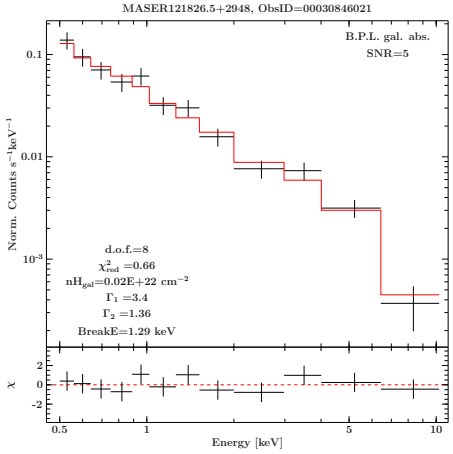
MASER121826.5+2948, ObsID=00030846021
B.P.L. gal. abs.
SNR=5
d.o.f.=8
χ^2_{red} =0.66
nH$_{gal}$=0.02E+22 cm^{-2}
Γ$_1$ =3.4
Γ$_2$ =1.36
BreakE=1.29 keV
Norm. Counts s^{-1}keV^{-1}
Energy [keV]

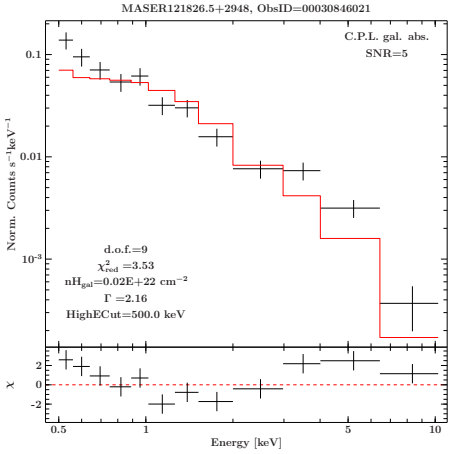
MASER121826.5+2948, ObsID=00030846021
C.P.L. gal. abs.
SNR=5
d.o.f.=9
χ^2_{red} =3.53
nH$_{gal}$=0.02E+22 cm^{-2}
Γ =2.16
HighECut=500.0 keV
Norm. Counts s^{-1}keV^{-1}
Energy [keV]

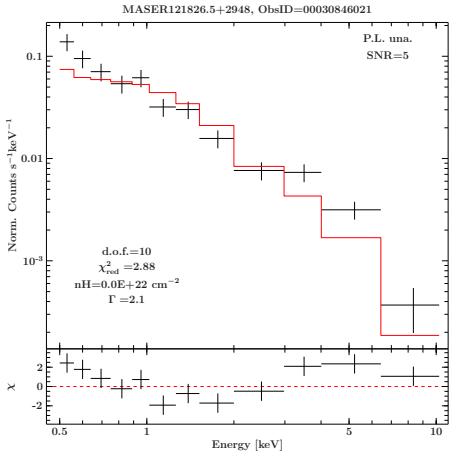
MASER121826.5+2948, ObsID=00030846021
P.L. una.
SNR=5
d.o.f.=10
χ^2_{red} =2.88
nH=0.0E+22 cm^{-2}
Γ =2.1
Norm. Counts s^{-1}keV^{-1}
Energy [keV]

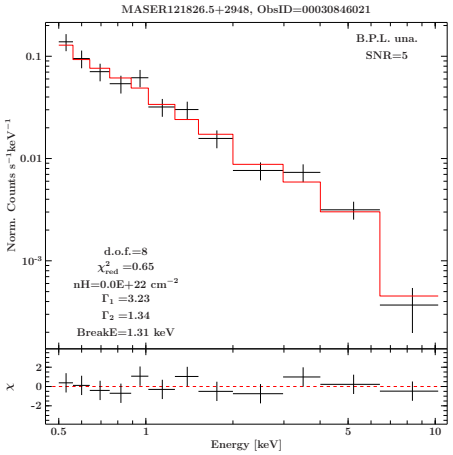
MASER121826.5+2948, ObsID=00030846021
B.P.L. una.
SNR=5
d.o.f.=8
χ^2_{red} =0.65
nH=0.0E+22 cm^{-2}
Γ$_1$ =3.23
Γ$_2$ =1.34
BreakE=1.31 keV
Norm. Counts s^{-1}keV^{-1}
Energy [keV]

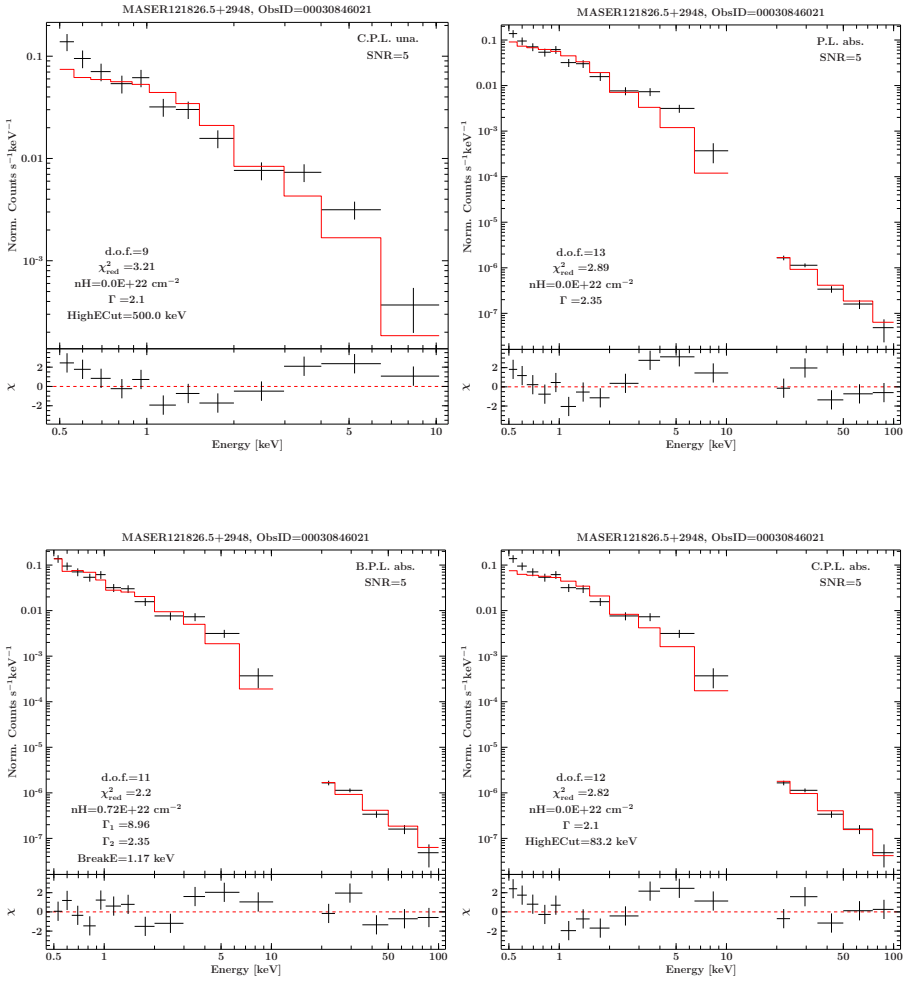
MASER121826.5+2948, ObsID=00030846021
C.P.L. una.
SNR=5
d.o.f.=9
χ^2_{red} =3.21
nH=0.0E+22 cm^{-2}
Γ =2.1
HighECut=500.0 keV
Norm. Counts s^{-1}keV^{-1}
χ
Energy [keV]
MASER121826.5+2948, ObsID=00030846021
P.L. abs.
SNR=5
d.o.f.=13
χ^2_{red} =2.89
nH=0.0E+22 cm^{-2}
Γ =2.35
Norm. Counts s^{-1}keV^{-1}
χ
Energy [keV]
MASER121826.5+2948, ObsID=00030846021
B.P.L. abs.
SNR=5
d.o.f.=11
χ^2_{red} =2.2
nH=0.72E+22 cm^{-2}
Γ$_1$ =8.96
Γ$_2$ =2.35
BreakE=1.17 keV
Norm. Counts s^{-1}keV^{-1}
χ
Energy [keV]
MASER121826.5+2948, ObsID=00030846021
C.P.L. abs.
SNR=5
d.o.f.=12
χ^2_{red} =2.82
nH=0.0E+22 cm^{-2}
Γ =2.1
HighECut=83.2 keV
Norm. Counts s^{-1}keV^{-1}
χ
Energy [keV]

ObsID 00030846022

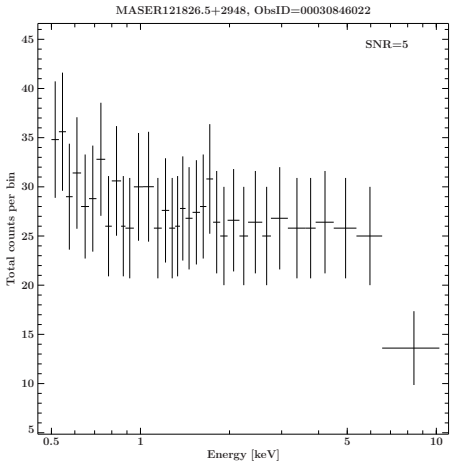

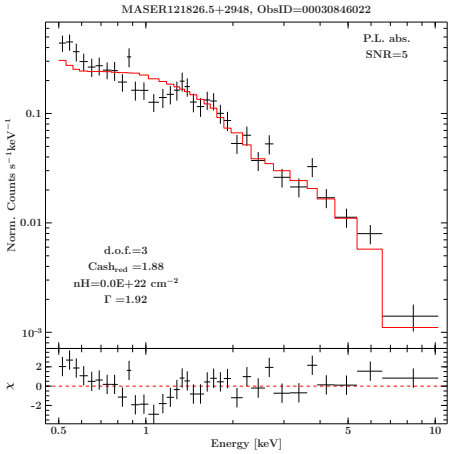

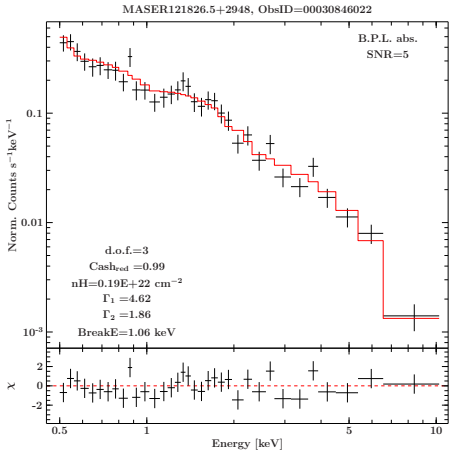

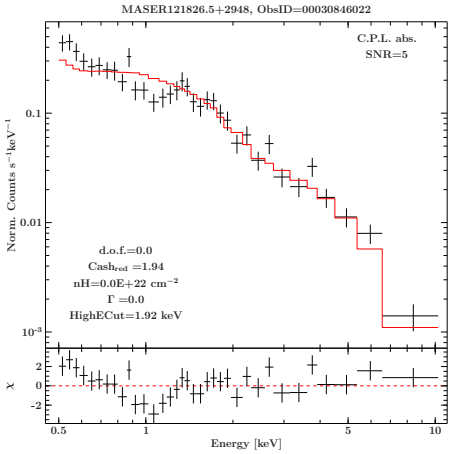

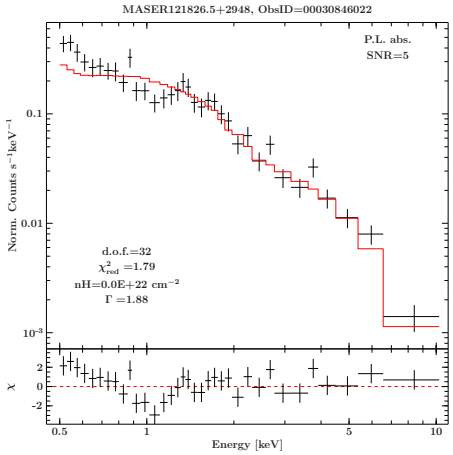

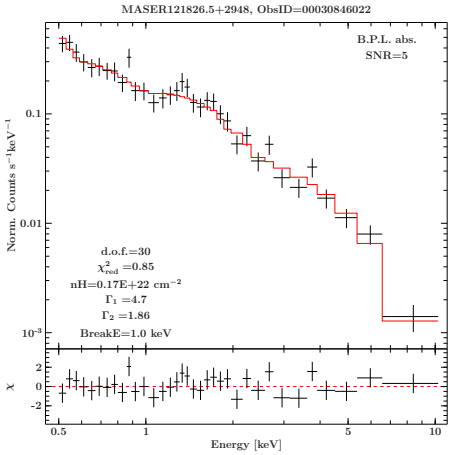

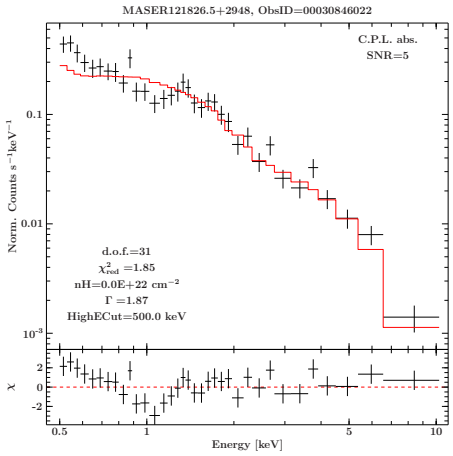
MASER121826.5+2948, ObsID=00030846022
C.P.L. abs.
SNR=5
d.o.f.=31
χ^2_{red} =1.85
nH=0.0E+22 cm^{-2}
Γ =1.87
HighECut=500.0 keV
Norm. Counts s^{-1}keV^{-1}
Energy [keV]

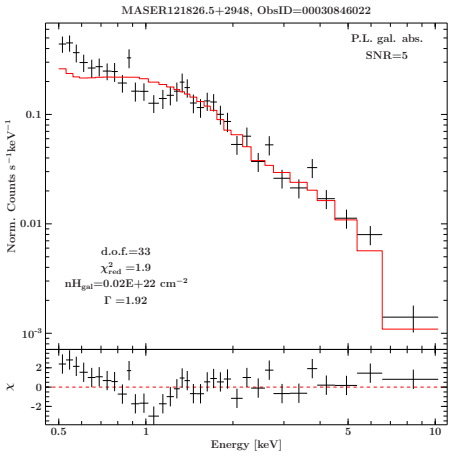
MASER121826.5+2948, ObsID=00030846022
P.L. gal. abs.
SNR=5
d.o.f.=33
χ^2_{red} =1.9
nH$_{gal}$=0.02E+22 cm^{-2}
Γ =1.92
Norm. Counts s^{-1}keV^{-1}
Energy [keV]

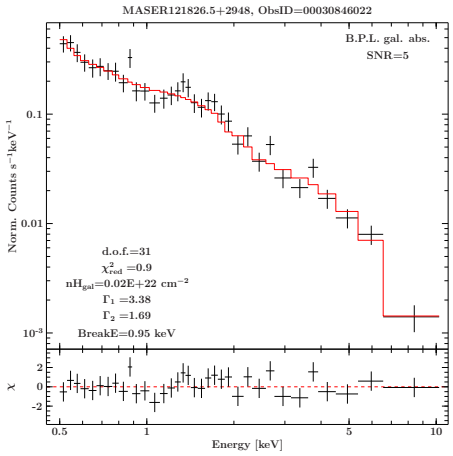
MASER121826.5+2948, ObsID=00030846022
B.P.L. gal. abs.
SNR=5
d.o.f.=31
χ^2_{red} =0.9
nH$_{gal}$=0.02E+22 cm^{-2}
Γ$_1$ =3.38
Γ$_2$ =1.69
BreakE=0.95 keV
Norm. Counts s^{-1}keV^{-1}
Energy [keV]

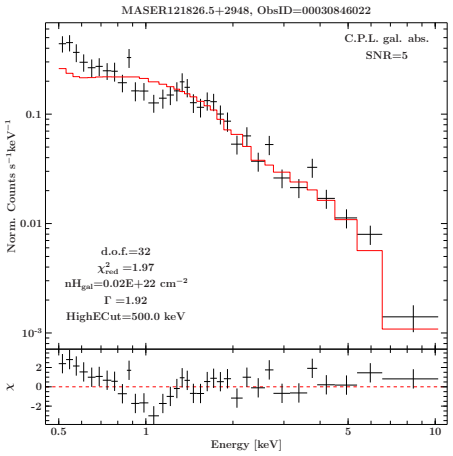
MASER121826.5+2948, ObsID=00030846022
C.P.L. gal. abs.
SNR=5
d.o.f.=32
χ^2_{red} =1.97
nH$_{gal}$=0.02E+22 cm^{-2}
Γ =1.92
HighECut=500.0 keV
Norm. Counts s^{-1}keV^{-1}
Energy [keV]

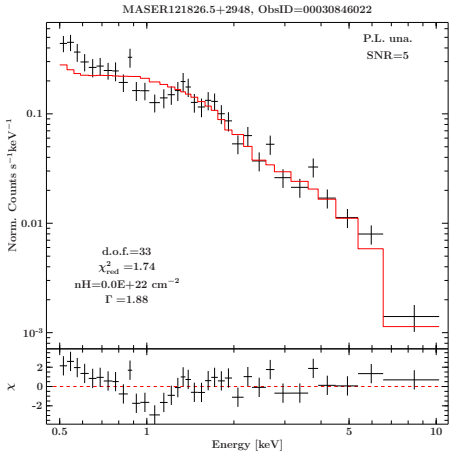
MASER121826.5+2948, ObsID=00030846022
P.L. una.
SNR=5
d.o.f.=33
χ^2_{red} =1.74
nH=0.0E+22 cm^{-2}
Γ =1.88
Norm. Counts s^{-1}keV^{-1}
Energy [keV]

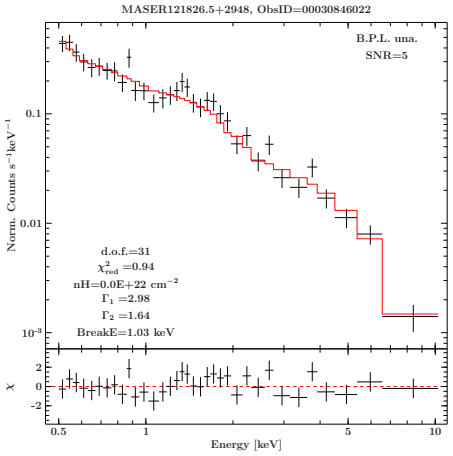
MASER121826.5+2948, ObsID=00030846022
B.P.L. una.
SNR=5
d.o.f.=31
χ^2_{red} =0.94
nH=0.0E+22 cm^{-2}
Γ$_1$ =2.98
Γ$_2$ =1.64
BreakE=1.03 keV
Norm. Counts s^{-1}keV^{-1}
Energy [keV]

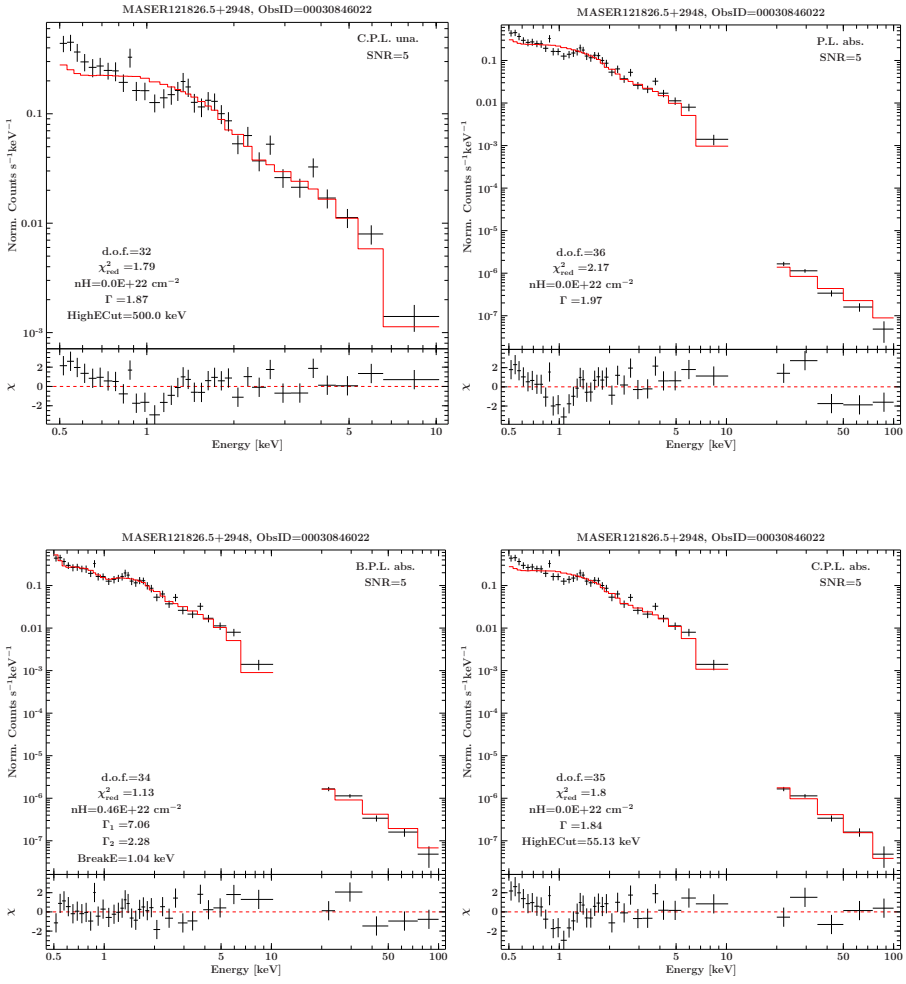
MASER121826.5+2948, ObsID=00030846022
C.P.L. una.
SNR=5
d.o.f.=32
χ^2_{red} =1.79
nH=0.0E+22 cm^{-2}
Γ =1.87
HighECut=500.0 keV
Norm. Counts s^{-1}keV^{-1}
χ
Energy [keV]
MASER121826.5+2948, ObsID=00030846022
P.L. abs.
SNR=5
d.o.f.=36
χ^2_{red} =2.17
nH=0.0E+22 cm^{-2}
Γ =1.97
Norm. Counts s^{-1}keV^{-1}
χ
Energy [keV]
MASER121826.5+2948, ObsID=00030846022
B.P.L. abs.
SNR=5
d.o.f.=34
χ^2_{red} =1.13
nH=0.46E+22 cm^{-2}
Γ_1 =7.06
Γ_2 =2.28
BreakE=1.04 keV
Norm. Counts s^{-1}keV^{-1}
χ
Energy [keV]
MASER121826.5+2948, ObsID=00030846022
C.P.L. abs.
SNR=5
d.o.f.=35
χ^2_{red} =1.8
nH=0.0E+22 cm^{-2}
Γ =1.84
HighECut=55.13 keV
Norm. Counts s^{-1}keV^{-1}
χ
Energy [keV]

ObsID 00030846023

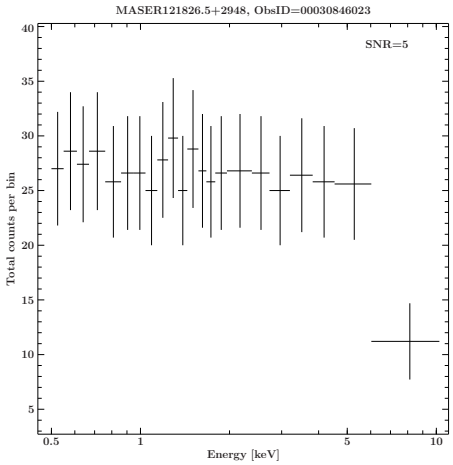

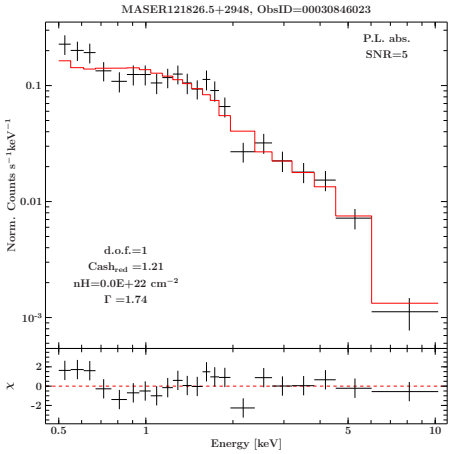

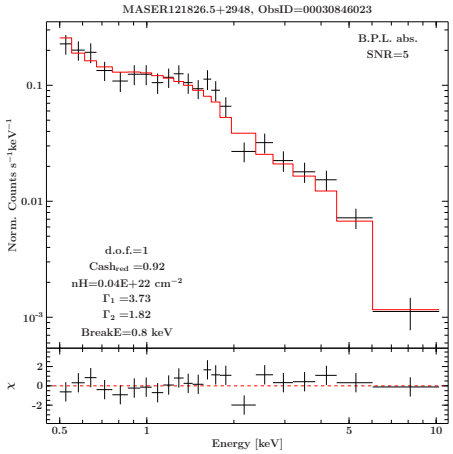

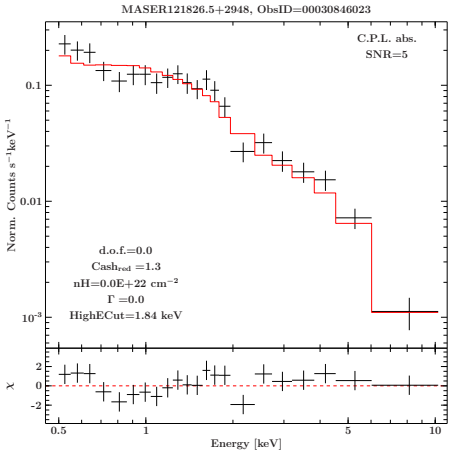

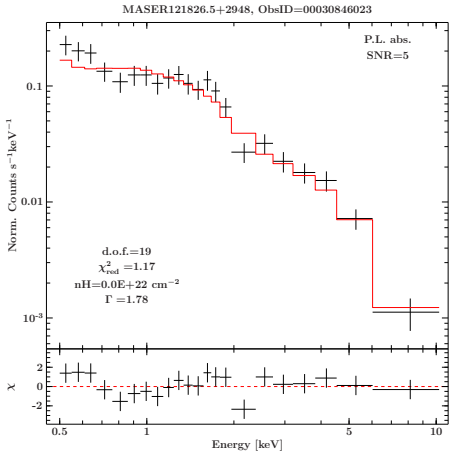

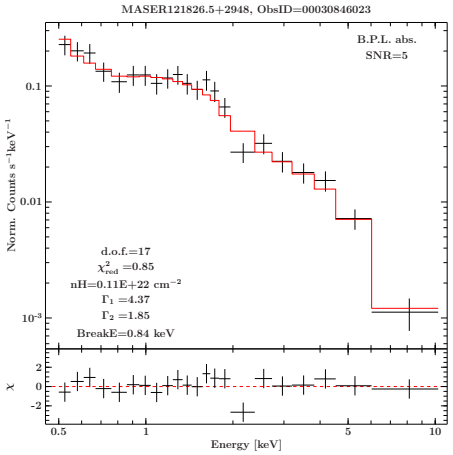

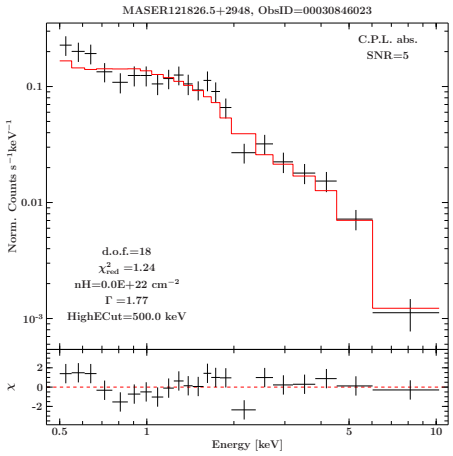
MASER121826.5+2948, ObsID=00030846023
C.P.L. abs.
SNR=5
d.o.f.=18
χ^2_{red} =1.24
nH=0.0E+22 cm^{-2}
Γ =1.77
HighECut=500.0 keV
Norm. Counts s^{-1}keV^{-1}
χ
Energy [keV]

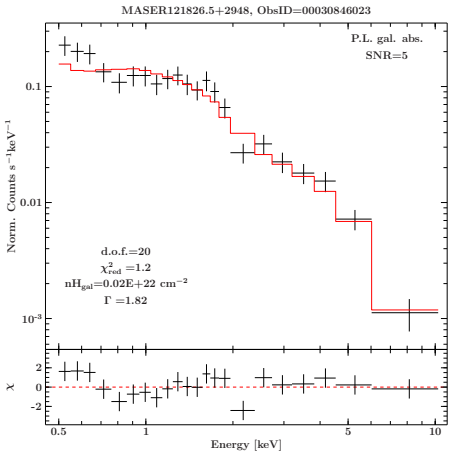
MASER121826.5+2948, ObsID=00030846023
P.L. gal. abs.
SNR=5
d.o.f.=20
χ^2_{red} =1.2
nH_{gal}=0.02E+22 cm^{-2}
Γ =1.82
Norm. Counts s^{-1}keV^{-1}
χ
Energy [keV]

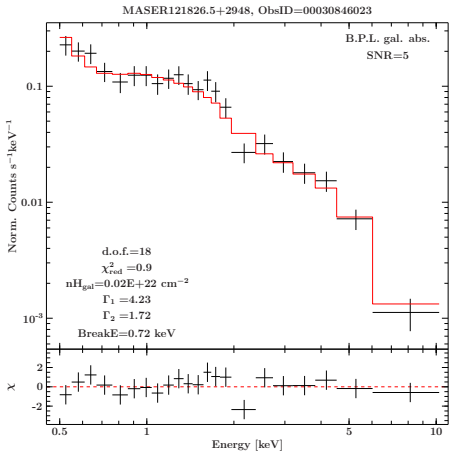
MASER121826.5+2948, ObsID=00030846023
B.P.L. gal. abs.
SNR=5
d.o.f.=18
χ^2_{red} =0.9
nH_{gal}=0.02E+22 cm^{-2}
Γ_1 =4.23
Γ_2 =1.72
BreakE=0.72 keV
Norm. Counts s^{-1}keV^{-1}
χ
Energy [keV]

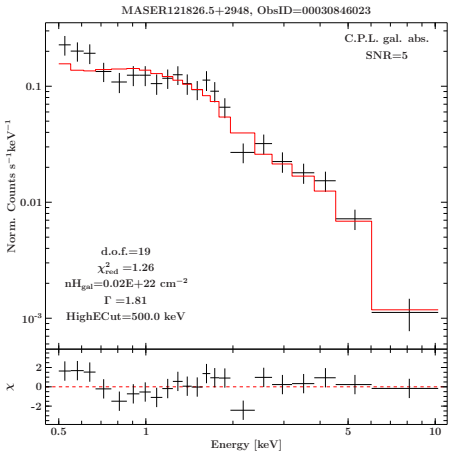
MASER121826.5+2948, ObsID=00030846023
C.P.L. gal. abs.
SNR=5
d.o.f.=19
χ^2_{red} =1.26
nH_{gal}=0.02E+22 cm^{-2}
Γ =1.81
HighECut=500.0 keV
Norm. Counts s^{-1}keV^{-1}
χ
Energy [keV]

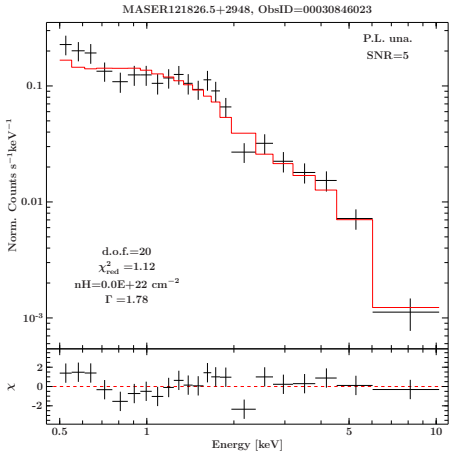
MASER121826.5+2948, ObsID=00030846023
P.L. una.
SNR=5
d.o.f.=20
χ^2_{red} =1.12
nH=0.0E+22 cm^{-2}
Γ =1.78
Norm. Counts s^{-1}keV^{-1}
χ
Energy [keV]

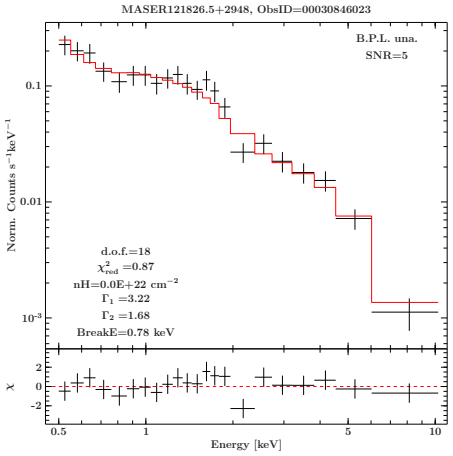
MASER121826.5+2948, ObsID=00030846023
B.P.L. una.
SNR=5
d.o.f.=18
χ^2_{red} =0.87
nH=0.0E+22 cm^{-2}
Γ_1 =3.22
Γ_2 =1.68
BreakE=0.78 keV
Norm. Counts s^{-1}keV^{-1}
χ
Energy [keV]

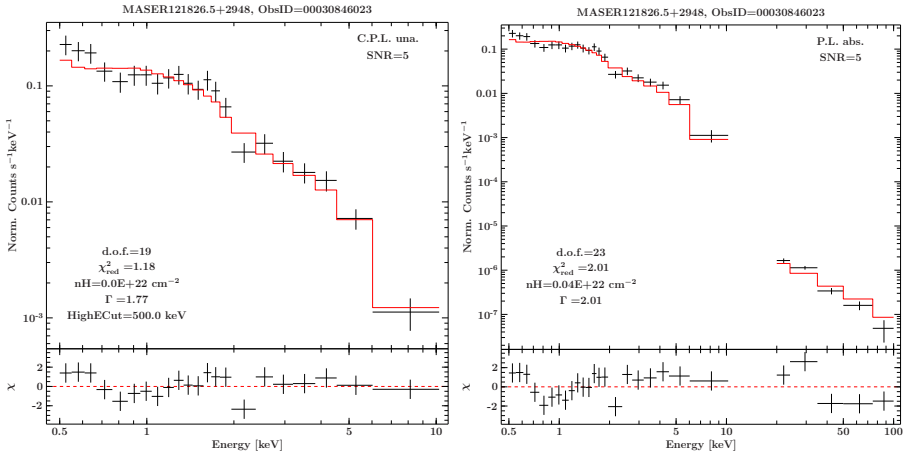
MASER121826.5+2948, ObsID=00030846023
C.P.L. una.
SNR=5
d.o.f.=19
χ^2_{red} =1.18
nH=0.0E+22 cm^{-2}
Γ =1.77
HighECut=500.0 keV
Norm. Counts s^{-1}keV^{-1}
χ
Energy [keV]
MASER121826.5+2948, ObsID=00030846023
P.L. abs.
SNR=5
d.o.f.=23
χ^2_{red} =2.01
nH=0.04E+22 cm^{-2}
Γ =2.01
Norm. Counts s^{-1}keV^{-1}
χ
Energy [keV]

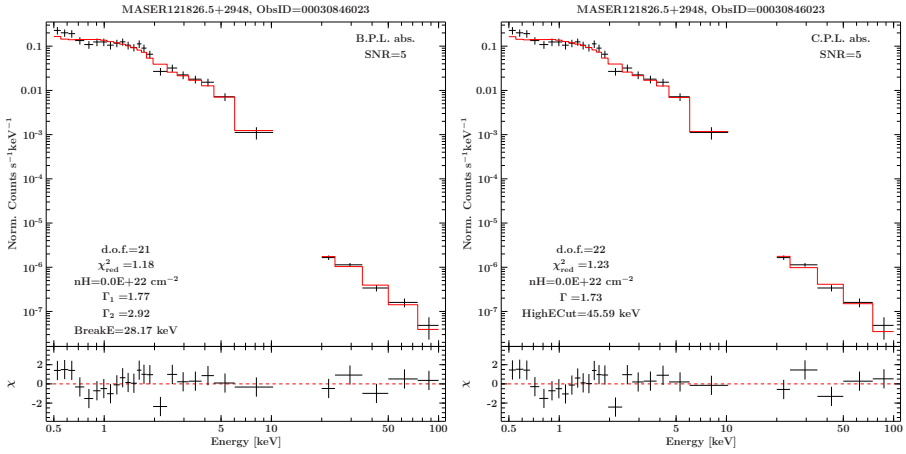
MASER121826.5+2948, ObsID=00030846023
B.P.L. abs.
SNR=5
d.o.f.=21
χ^2_{red} =1.18
nH=0.0E+22 cm^{-2}
Γ$_1$ =1.77
Γ$_2$ =2.92
BreakE=28.17 keV
Norm. Counts s^{-1}keV^{-1}
χ
Energy [keV]
MASER121826.5+2948, ObsID=00030846023
C.P.L. abs.
SNR=5
d.o.f.=22
χ^2_{red} =1.23
nH=0.0E+22 cm^{-2}
Γ =1.73
HighECut=45.59 keV
Norm. Counts s^{-1}keV^{-1}
χ
Energy [keV]

ObsID 00030846025

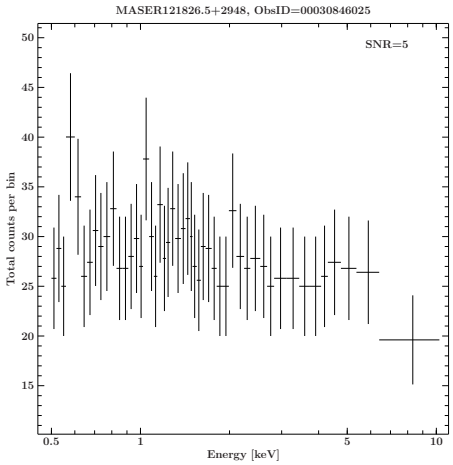

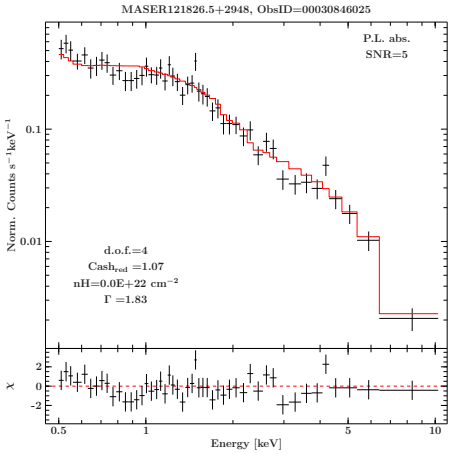

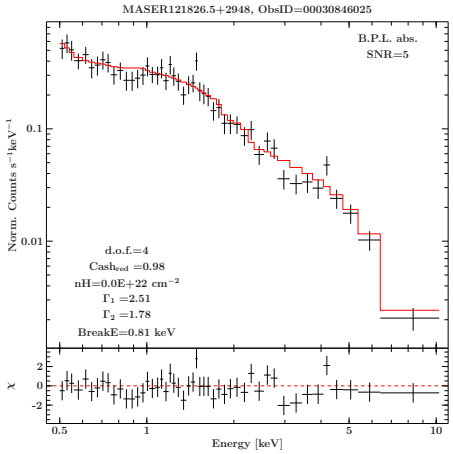

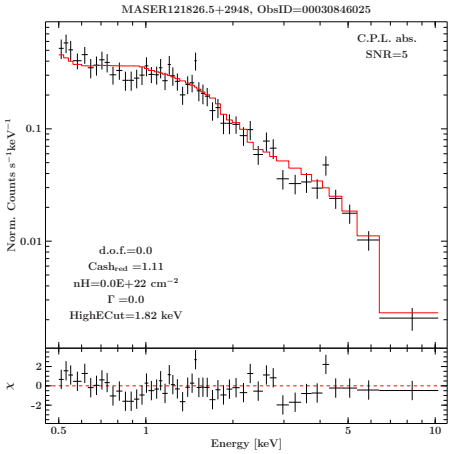

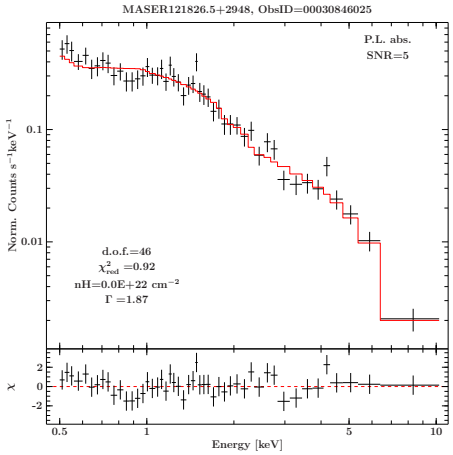

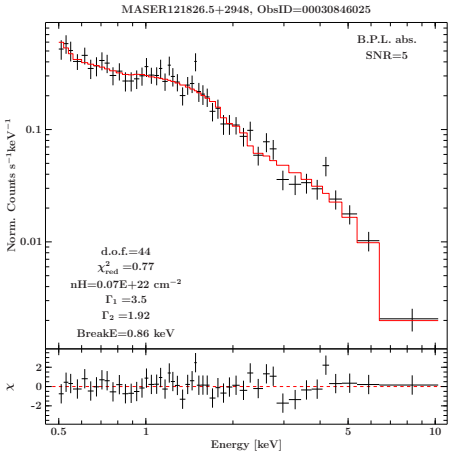

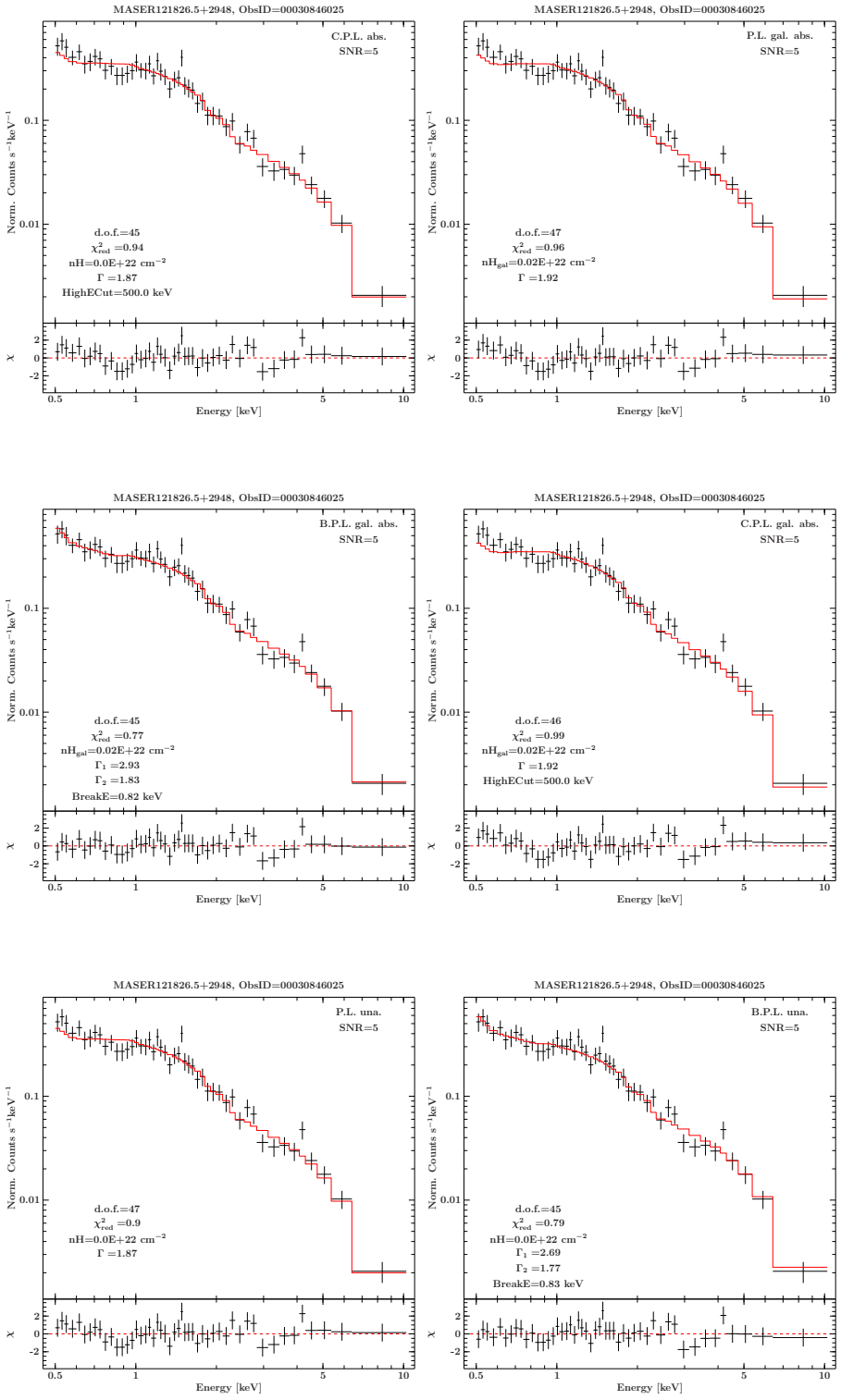
MASER121826.5+2948, ObsID=00030846025
C.P.L. abs.
SNR=5
d.o.f.=45
χ^2_{red} =0.94
nH=0.0E+22 cm^{-2}
Γ =1.87
HighECut=500.0 keV
MASER121826.5+2948, ObsID=00030846025
P.L. gal. abs.
SNR=5
d.o.f.=47
χ^2_{red} =0.96
nH$_{gal}$=0.02E+22 cm^{-2}
Γ =1.92
MASER121826.5+2948, ObsID=00030846025
B.P.L. gal. abs.
SNR=5
d.o.f.=45
χ^2_{red} =0.77
nH$_{gal}$=0.02E+22 cm^{-2}
Γ$_1$ =2.93
Γ$_2$ =1.83
BreakE=0.82 keV
MASER121826.5+2948, ObsID=00030846025
C.P.L. gal. abs.
SNR=5
d.o.f.=46
χ^2_{red} =0.99
nH$_{gal}$=0.02E+22 cm^{-2}
Γ =1.92
HighECut=500.0 keV
MASER121826.5+2948, ObsID=00030846025
P.L. una.
SNR=5
d.o.f.=47
χ^2_{red} =0.9
nH=0.0E+22 cm^{-2}
Γ =1.87
MASER121826.5+2948, ObsID=00030846025
B.P.L. una.
SNR=5
d.o.f.=45
χ^2_{red} =0.79
nH=0.0E+22 cm^{-2}
Γ$_1$ =2.69
Γ$_2$ =1.77
BreakE=0.83 keV
Norm. Counts s^{-1}keV^{-1}
χ
Energy [keV]

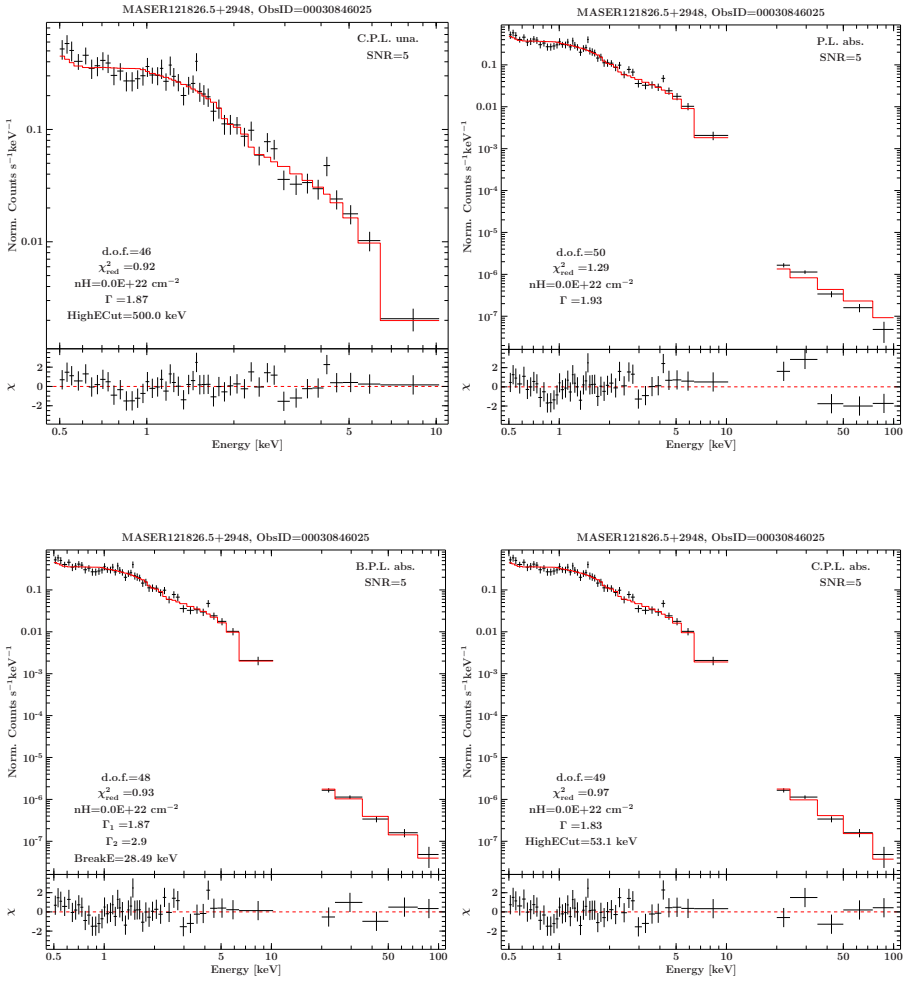
MASER121826.5+2948, ObsID=00030846025
C.P.L. una.
SNR=5
d.o.f.=46
χ^2_{red} =0.92
nH=0.0E+22 cm^{-2}
Γ =1.87
HighECut=500.0 keV
Norm. Counts s^{-1}keV^{-1}
χ
Energy [keV]
MASER121826.5+2948, ObsID=00030846025
P.L. abs.
SNR=5
d.o.f.=50
χ^2_{red} =1.29
nH=0.0E+22 cm^{-2}
Γ =1.93
Norm. Counts s^{-1}keV^{-1}
χ
Energy [keV]
MASER121826.5+2948, ObsID=00030846025
B.P.L. abs.
SNR=5
d.o.f.=48
χ^2_{red} =0.93
nH=0.0E+22 cm^{-2}
Γ_1 =1.87
Γ_2 =2.9
BreakE=28.49 keV
Norm. Counts s^{-1}keV^{-1}
χ
Energy [keV]
MASER121826.5+2948, ObsID=00030846025
C.P.L. abs.
SNR=5
d.o.f.=49
χ^2_{red} =0.97
nH=0.0E+22 cm^{-2}
Γ =1.83
HighECut=53.1 keV
Norm. Counts s^{-1}keV^{-1}
χ
Energy [keV]

ObsID 00030846029

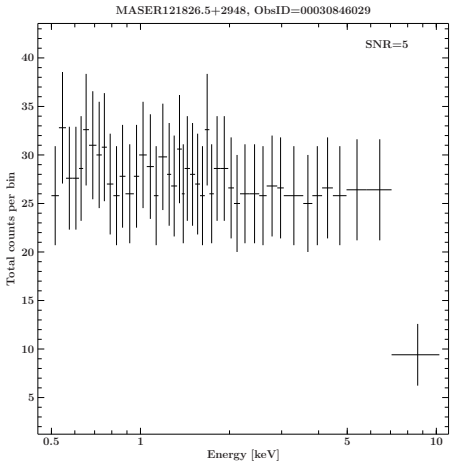

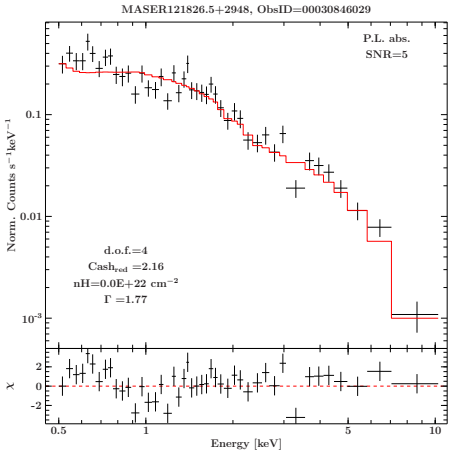

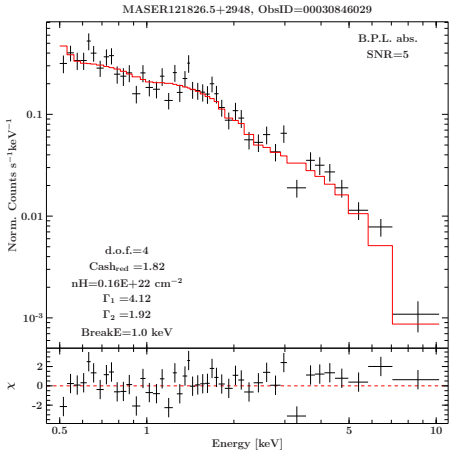

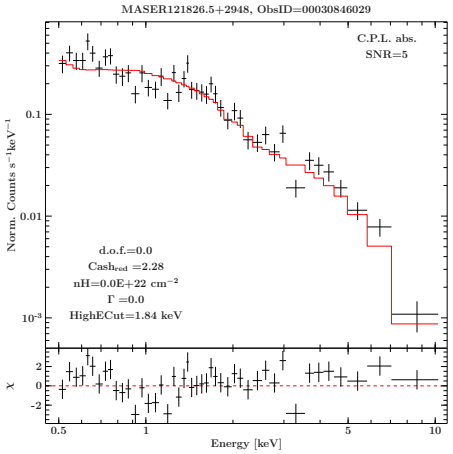

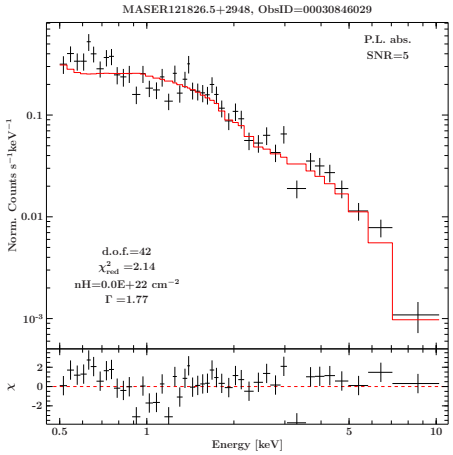

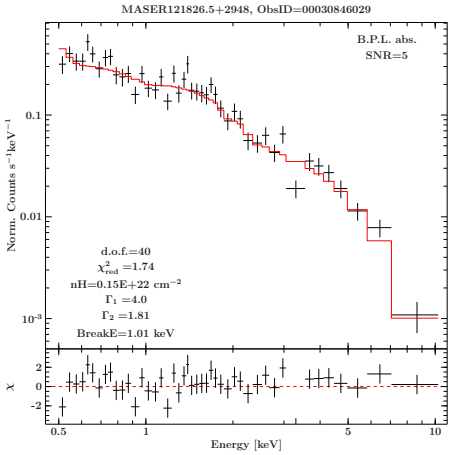

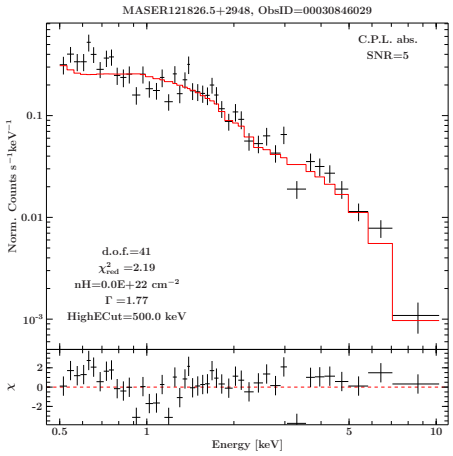
MASER121826.5+2948, ObsID=00030846029
C.P.L. abs.
SNR=5
d.o.f.=41
χ^2_{red} =2.19
nH=0.0E+22 cm^{-2}
Γ =1.77
HighECut=500.0 keV
Norm. Counts s^{-1}keV^{-1}
Energy [keV]

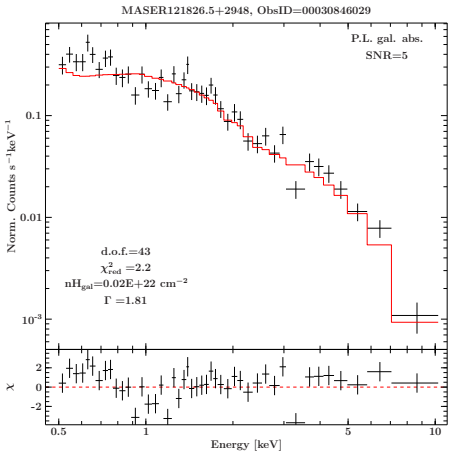
MASER121826.5+2948, ObsID=00030846029
P.L. gal. abs.
SNR=5
d.o.f.=43
χ^2_{red} =2.2
nH$_{gal}$=0.02E+22 cm^{-2}
Γ =1.81
Norm. Counts s^{-1}keV^{-1}
Energy [keV]

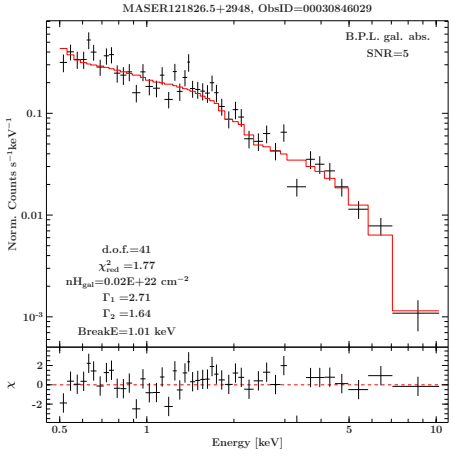
MASER121826.5+2948, ObsID=00030846029
B.P.L. gal. abs.
SNR=5
d.o.f.=41
χ^2_{red} =1.77
nH$_{gal}$=0.02E+22 cm^{-2}
Γ$_1$ =2.71
Γ$_2$ =1.64
BreakE=1.01 keV
Norm. Counts s^{-1}keV^{-1}
Energy [keV]

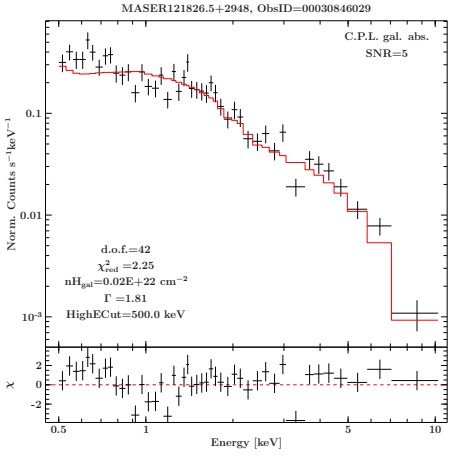
MASER121826.5+2948, ObsID=00030846029
C.P.L. gal. abs.
SNR=5
d.o.f.=42
χ^2_{red} =2.25
nH$_{gal}$=0.02E+22 cm^{-2}
Γ =1.81
HighECut=500.0 keV
Norm. Counts s^{-1}keV^{-1}
Energy [keV]

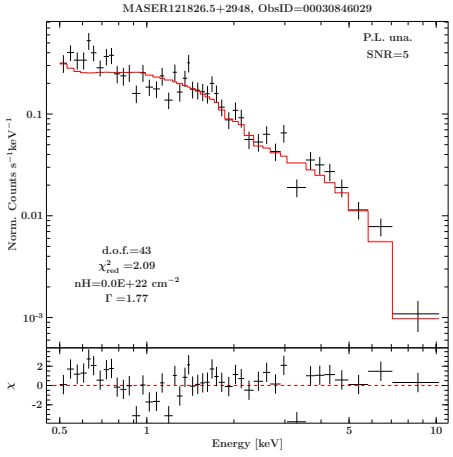
MASER121826.5+2948, ObsID=00030846029
P.L. una.
SNR=5
d.o.f.=43
χ^2_{red} =2.09
nH=0.0E+22 cm^{-2}
Γ =1.77
Norm. Counts s^{-1}keV^{-1}
Energy [keV]

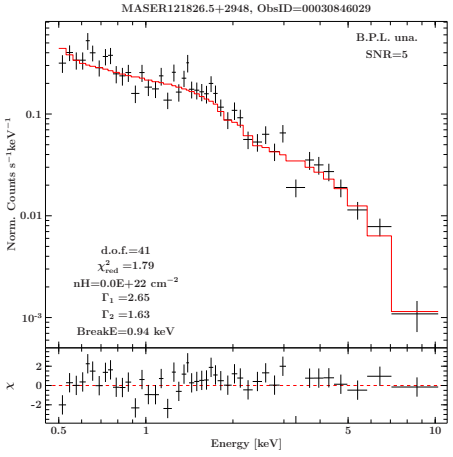
MASER121826.5+2948, ObsID=00030846029
B.P.L. una.
SNR=5
d.o.f.=41
χ^2_{red} =1.79
nH=0.0E+22 cm^{-2}
Γ$_1$ =2.65
Γ$_2$ =1.63
BreakE=0.94 keV
Norm. Counts s^{-1}keV^{-1}
Energy [keV]

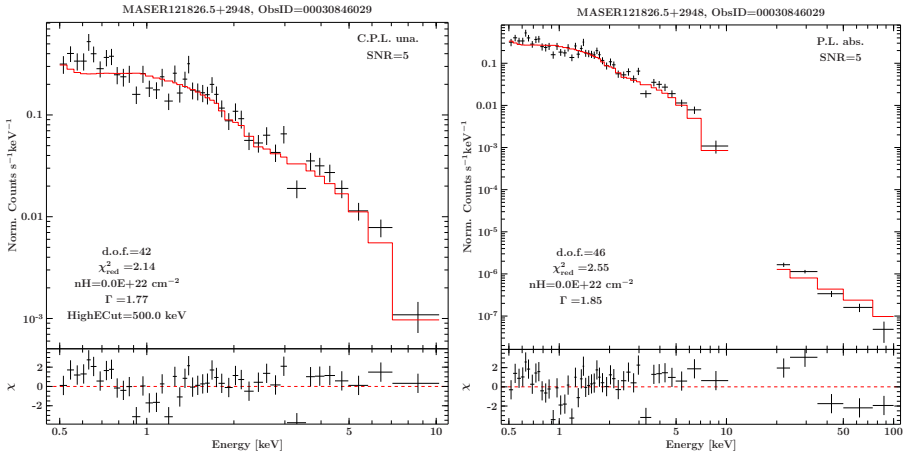
MASER121826.5+2948, ObsID=00030846029
C.P.L. una.
SNR=5
d.o.f.=42
χ^2_{red} =2.14
nH=0.0E+22 cm^{-2}
Γ =1.77
HighECut=500.0 keV
Norm. Counts s^{-1}keV^{-1}
χ
Energy [keV]
MASER121826.5+2948, ObsID=00030846029
P.L. abs.
SNR=5
d.o.f.=46
χ^2_{red} =2.55
nH=0.0E+22 cm^{-2}
Γ =1.85
Norm. Counts s^{-1}keV^{-1}
χ
Energy [keV]

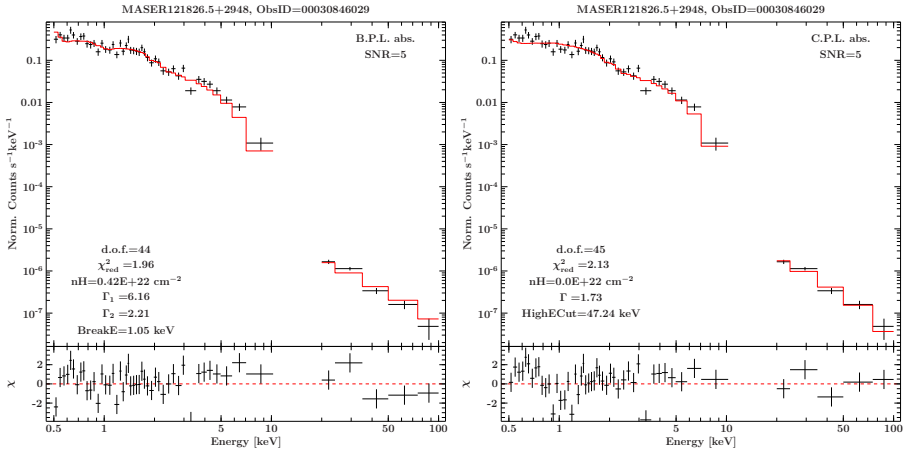
MASER121826.5+2948, ObsID=00030846029
B.P.L. abs.
SNR=5
d.o.f.=44
χ^2_{red} =1.96
nH=0.42E+22 cm^{-2}
Γ$_1$ =6.16
Γ$_2$ =2.21
BreakE=1.05 keV
Norm. Counts s^{-1}keV^{-1}
χ
Energy [keV]
MASER121826.5+2948, ObsID=00030846029
C.P.L. abs.
SNR=5
d.o.f.=45
χ^2_{red} =2.13
nH=0.0E+22 cm^{-2}
Γ =1.73
HighECut=47.24 keV
Norm. Counts s^{-1}keV^{-1}
χ
Energy [keV]

ObsID 00030846030

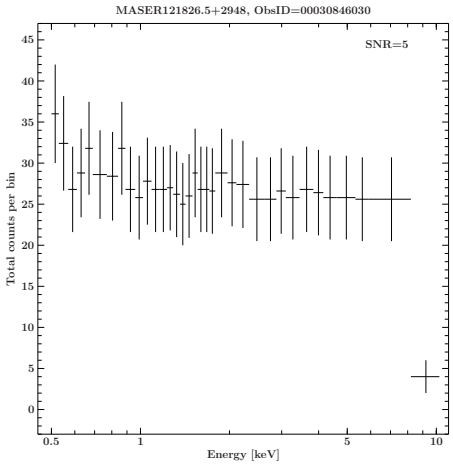

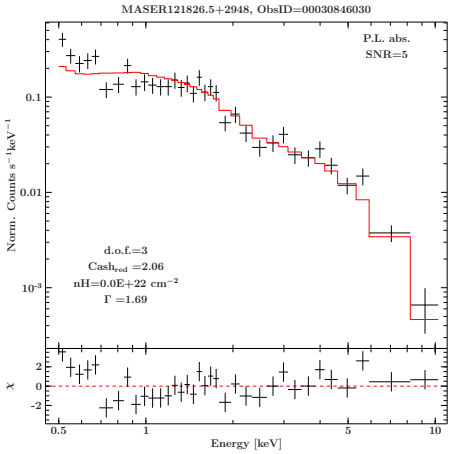

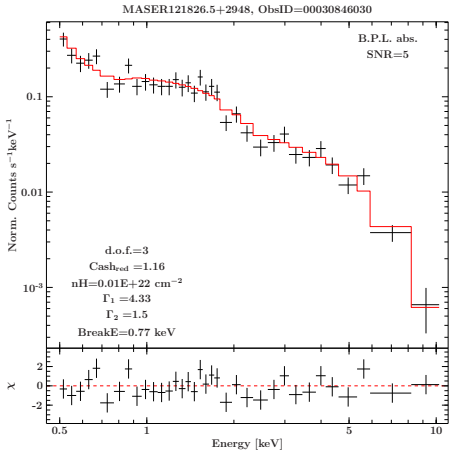

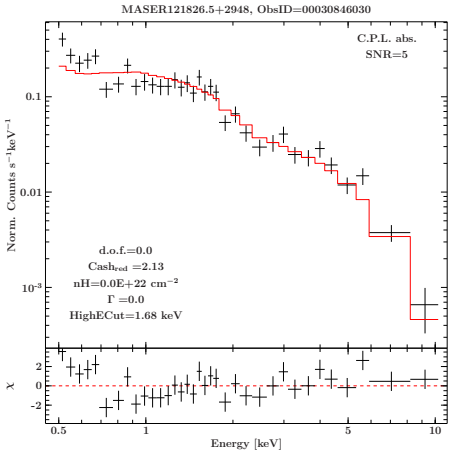

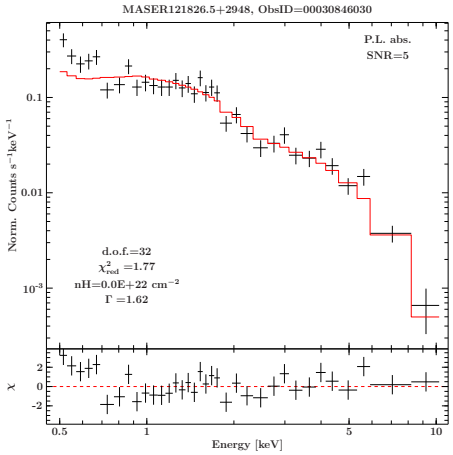

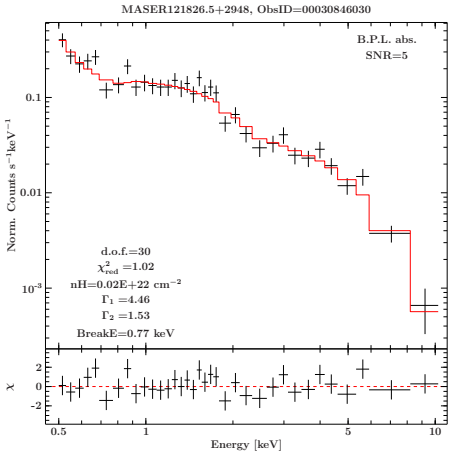

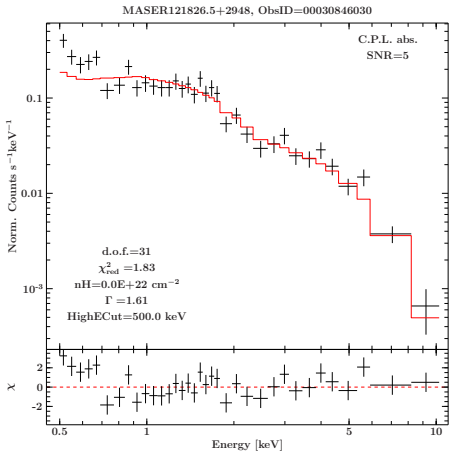
MASER121826.5+2948, ObsID=00030846030
C.P.L. abs.
SNR=5
d.o.f.=31
χ^2_{red} =1.83
nH=0.0E+22 cm^{-2}
Γ =1.61
HighECut=500.0 keV
Norm. Counts s^{-1}keV^{-1}
Energy [keV]

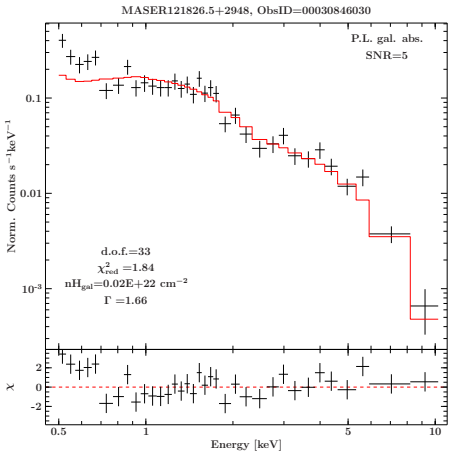
MASER121826.5+2948, ObsID=00030846030
P.L. gal. abs.
SNR=5
d.o.f.=33
χ^2_{red} =1.84
nH$_{gal}$=0.02E+22 cm^{-2}
Γ =1.66
Norm. Counts s^{-1}keV^{-1}
Energy [keV]

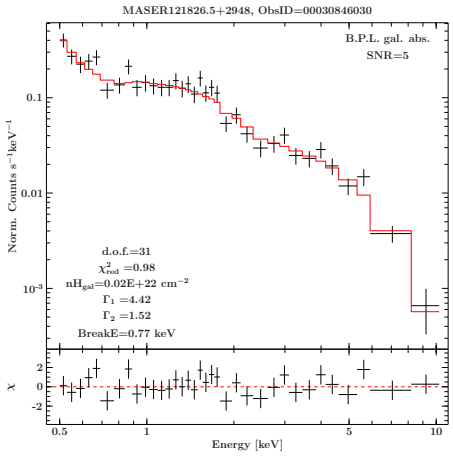
MASER121826.5+2948, ObsID=00030846030
B.P.L. gal. abs.
SNR=5
d.o.f.=31
χ^2_{red} =0.98
nH$_{gal}$=0.02E+22 cm^{-2}
Γ$_1$ =4.42
Γ$_2$ =1.52
BreakE=0.77 keV
Norm. Counts s^{-1}keV^{-1}
Energy [keV]

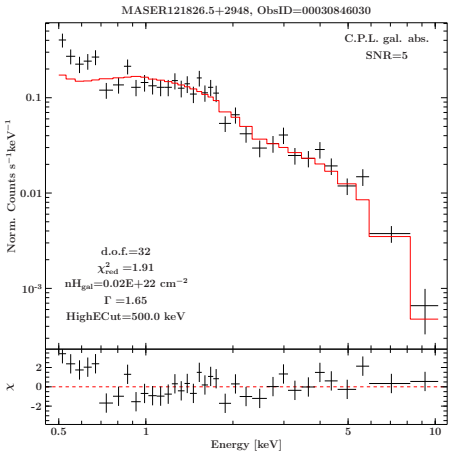
MASER121826.5+2948, ObsID=00030846030
C.P.L. gal. abs.
SNR=5
d.o.f.=32
χ^2_{red} =1.91
nH$_{gal}$=0.02E+22 cm^{-2}
Γ =1.65
HighECut=500.0 keV
Norm. Counts s^{-1}keV^{-1}
Energy [keV]

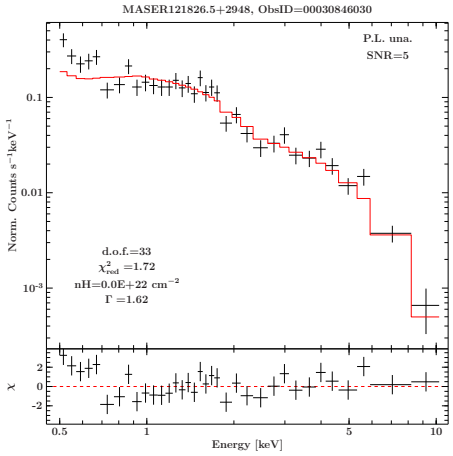
MASER121826.5+2948, ObsID=00030846030
P.L. una.
SNR=5
d.o.f.=33
χ^2_{red} =1.72
nH=0.0E+22 cm^{-2}
Γ =1.62
Norm. Counts s^{-1}keV^{-1}
Energy [keV]

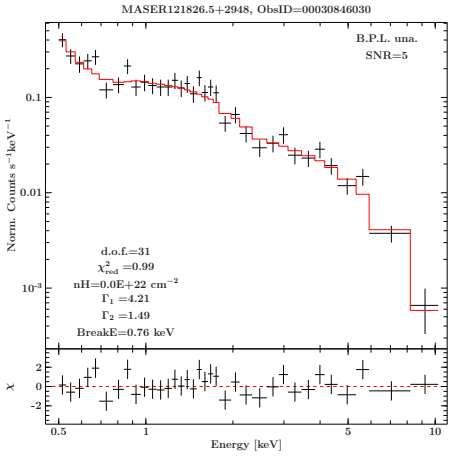
MASER121826.5+2948, ObsID=00030846030
B.P.L. una.
SNR=5
d.o.f.=31
χ^2_{red} =0.99
nH=0.0E+22 cm^{-2}
Γ$_1$ =4.21
Γ$_2$ =1.49
BreakE=0.76 keV
Norm. Counts s^{-1}keV^{-1}
Energy [keV]

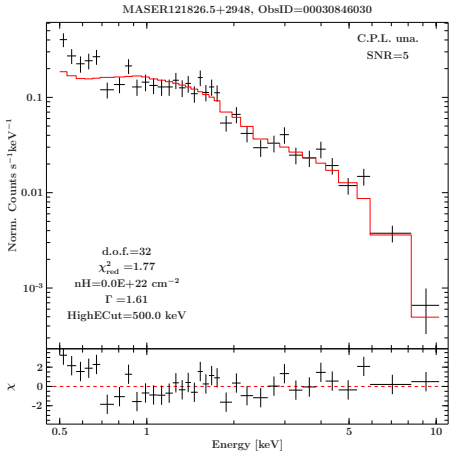
MASER121826.5+2948, ObsID=00030846030
C.P.L. una.
SNR=5
d.o.f.=32
χ^2_{red} =1.77
nH=0.0E+22 cm^{-2}
Γ =1.61
HighECut=500.0 keV
Norm. Counts s^{-1}keV^{-1}
χ
Energy [keV]

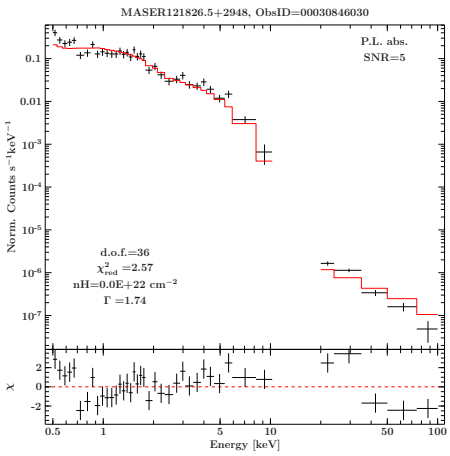
MASER121826.5+2948, ObsID=00030846030
P.L. abs.
SNR=5
d.o.f.=36
χ^2_{red} =2.57
nH=0.0E+22 cm^{-2}
Γ =1.74
Norm. Counts s^{-1}keV^{-1}
χ
Energy [keV]

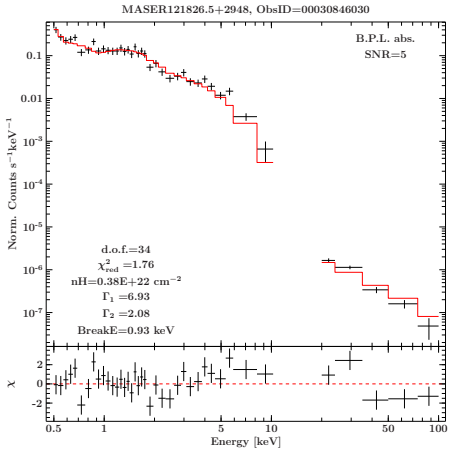
MASER121826.5+2948, ObsID=00030846030
B.P.L. abs.
SNR=5
d.o.f.=34
χ^2_{red} =1.76
nH=0.38E+22 cm^{-2}
Γ_1 =6.93
Γ_2 =2.08
BreakE=0.93 keV
Norm. Counts s^{-1}keV^{-1}
χ
Energy [keV]

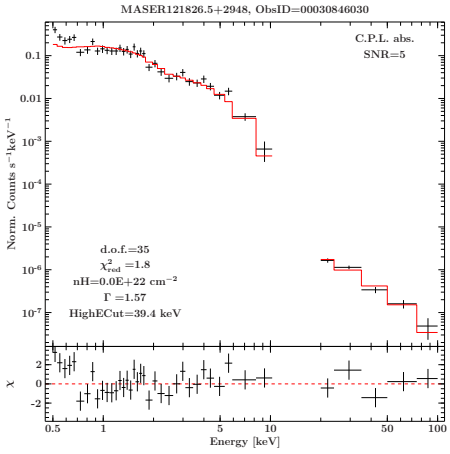
MASER121826.5+2948, ObsID=00030846030
C.P.L. abs.
SNR=5
d.o.f.=35
χ^2_{red} =1.8
nH=0.0E+22 cm^{-2}
Γ =1.57
HighECut=39.4 keV
Norm. Counts s^{-1}keV^{-1}
χ
Energy [keV]

ObsID 00030846034

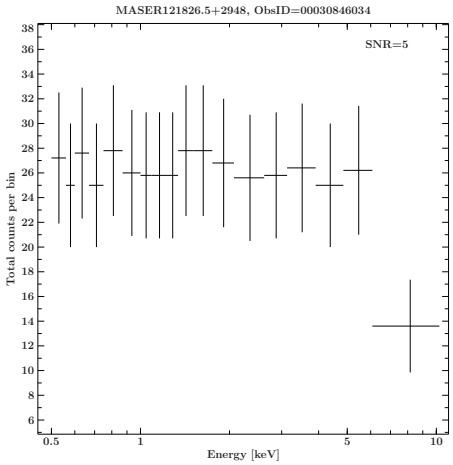

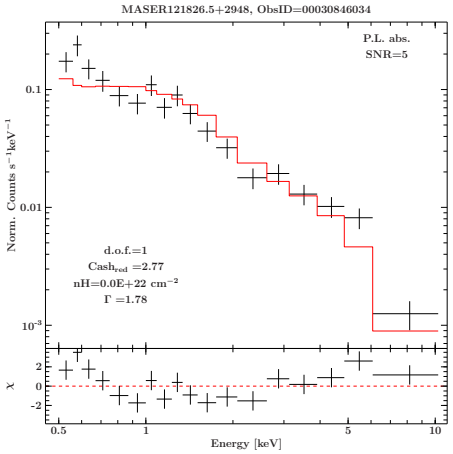

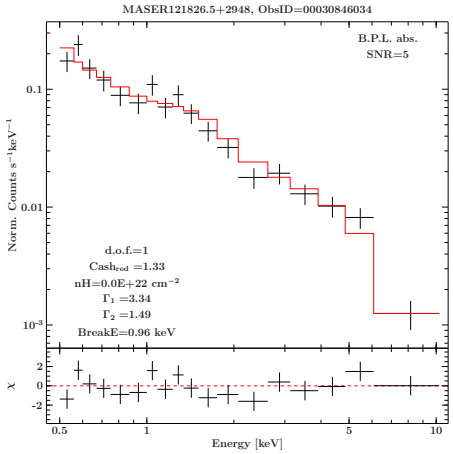

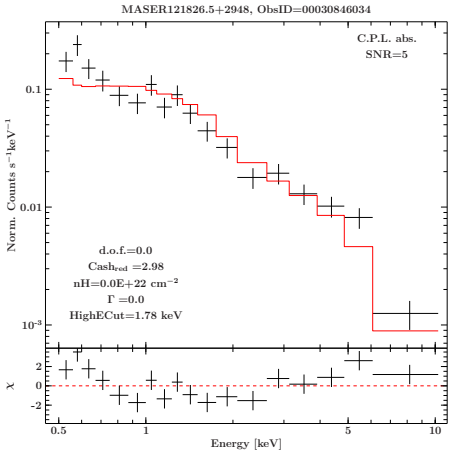

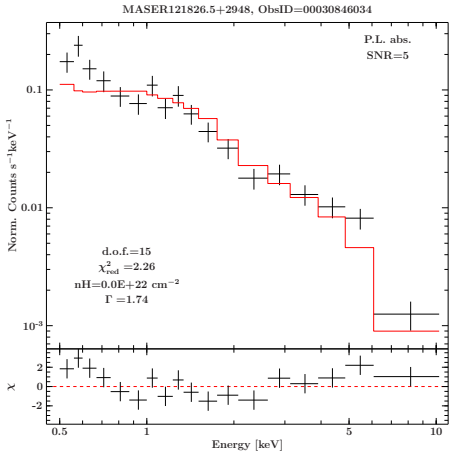

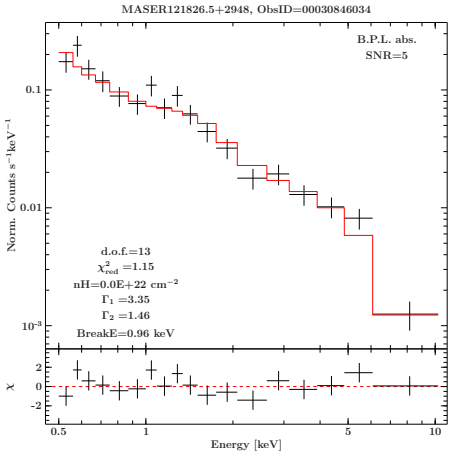

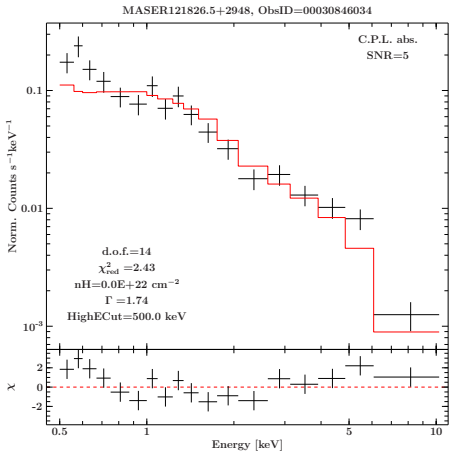
MASER121826.5+2948, ObsID=00030846034
C.P.L. abs.
SNR=5
d.o.f.=14
χ^2_{red} =2.43
nH=0.0E+22 cm^{-2}
Γ =1.74
HighECut=500.0 keV
Norm. Counts s^{-1}keV^{-1}
χ
Energy [keV]

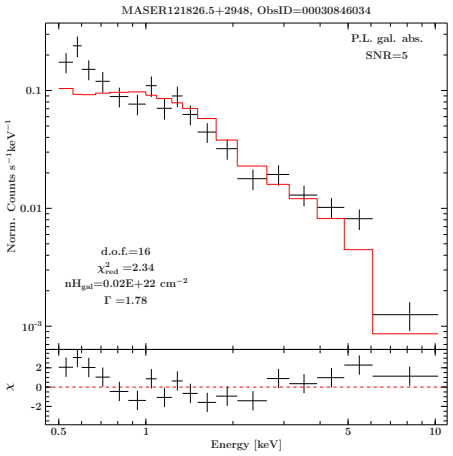
MASER121826.5+2948, ObsID=00030846034
P.L. gal. abs.
SNR=5
d.o.f.=16
χ^2_{red} =2.34
nH$_{gal}$=0.02E+22 cm^{-2}
Γ =1.78
Norm. Counts s^{-1}keV^{-1}
χ
Energy [keV]

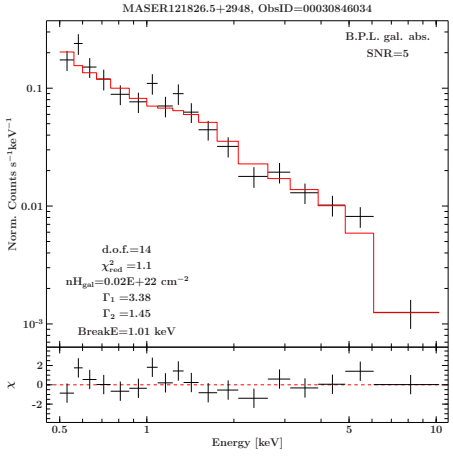
MASER121826.5+2948, ObsID=00030846034
B.P.L. gal. abs.
SNR=5
d.o.f.=14
χ^2_{red} =1.1
nH$_{gal}$=0.02E+22 cm^{-2}
Γ$_1$ =3.38
Γ$_2$ =1.45
BreakE=1.01 keV
Norm. Counts s^{-1}keV^{-1}
χ
Energy [keV]

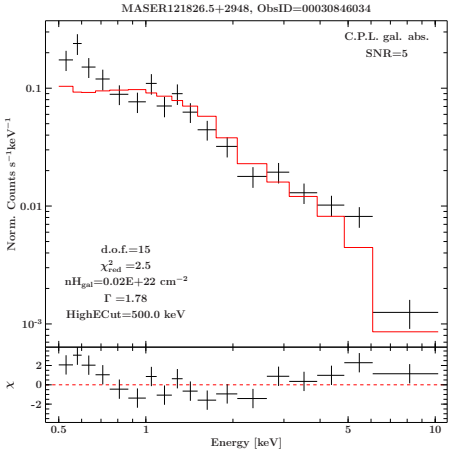
MASER121826.5+2948, ObsID=00030846034
C.P.L. gal. abs.
SNR=5
d.o.f.=15
χ^2_{red} =2.5
nH$_{gal}$=0.02E+22 cm^{-2}
Γ =1.78
HighECut=500.0 keV
Norm. Counts s^{-1}keV^{-1}
χ
Energy [keV]

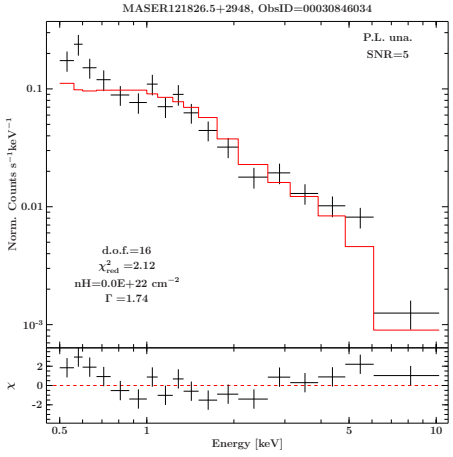
MASER121826.5+2948, ObsID=00030846034
P.L. una.
SNR=5
d.o.f.=16
χ^2_{red} =2.12
nH=0.0E+22 cm^{-2}
Γ =1.74
Norm. Counts s^{-1}keV^{-1}
χ
Energy [keV]

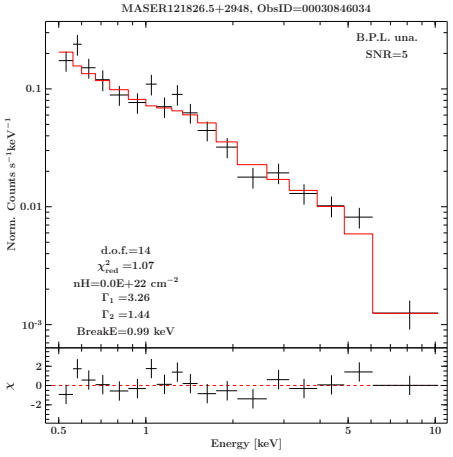
MASER121826.5+2948, ObsID=00030846034
B.P.L. una.
SNR=5
d.o.f.=14
χ^2_{red} =1.07
nH=0.0E+22 cm^{-2}
Γ$_1$ =3.26
Γ$_2$ =1.44
BreakE=0.99 keV
Norm. Counts s^{-1}keV^{-1}
χ
Energy [keV]

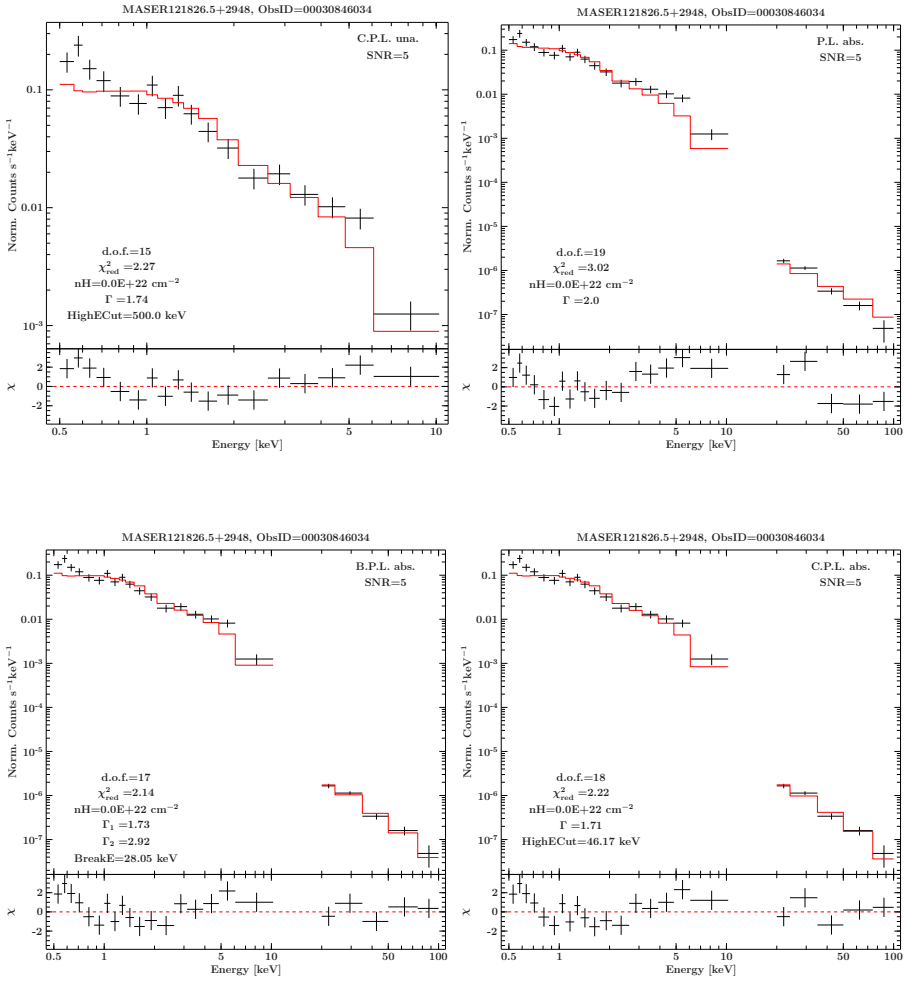
MASER121826.5+2948, ObsID=00030846034
C.P.L. una.
SNR=5
d.o.f.=15
χ^2_{red} =2.27
nH=0.0E+22 cm^{-2}
Γ =1.74
HighECut=500.0 keV
MASER121826.5+2948, ObsID=00030846034
P.L. abs.
SNR=5
d.o.f.=19
χ^2_{red} =3.02
nH=0.0E+22 cm^{-2}
Γ =2.0
MASER121826.5+2948, ObsID=00030846034
B.P.L. abs.
SNR=5
d.o.f.=17
χ^2_{red} =2.14
nH=0.0E+22 cm^{-2}
Γ$_1$ =1.73
Γ$_2$ =2.92
BreakE=28.05 keV
MASER121826.5+2948, ObsID=00030846034
C.P.L. abs.
SNR=5
d.o.f.=18
χ^2_{red} =2.22
nH=0.0E+22 cm^{-2}
Γ =1.71
HighECut=46.17 keV
Norm. Counts s^{-1}keV^{-1}
χ
Energy [keV]

ObsID 00030846035

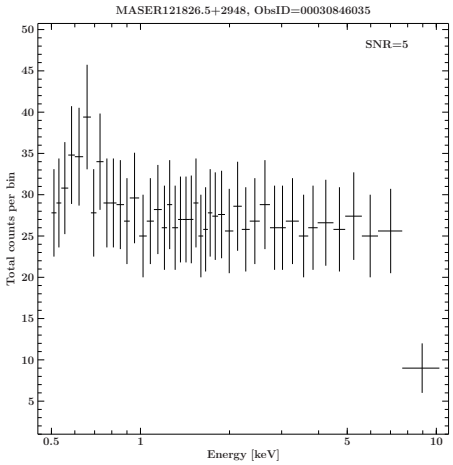

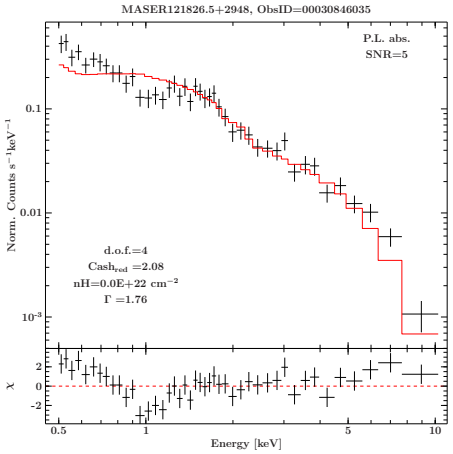

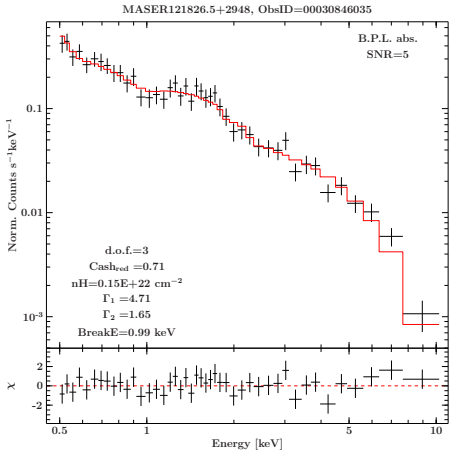

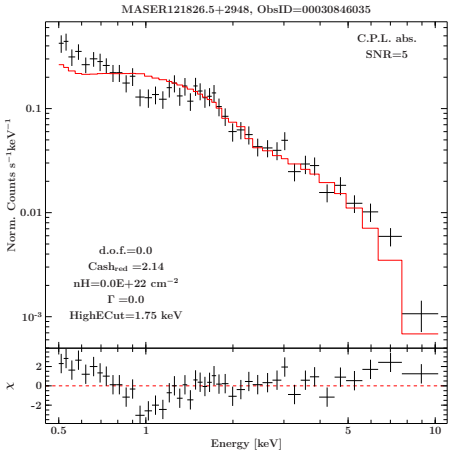

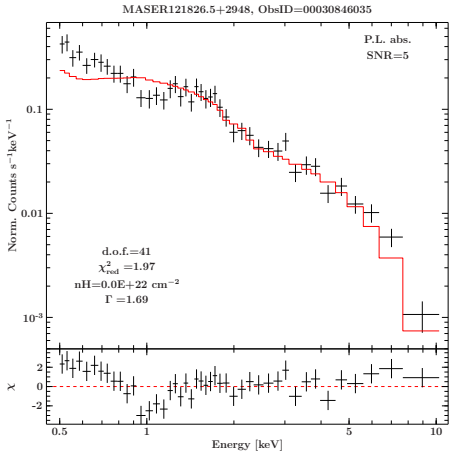

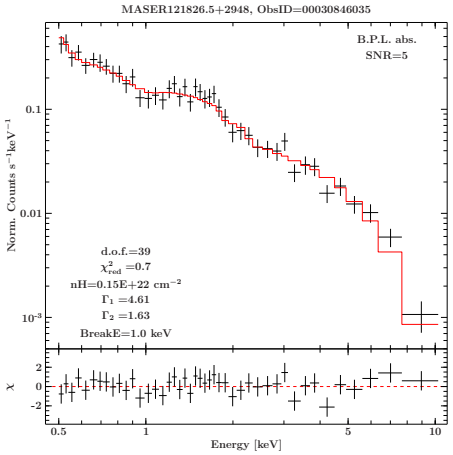

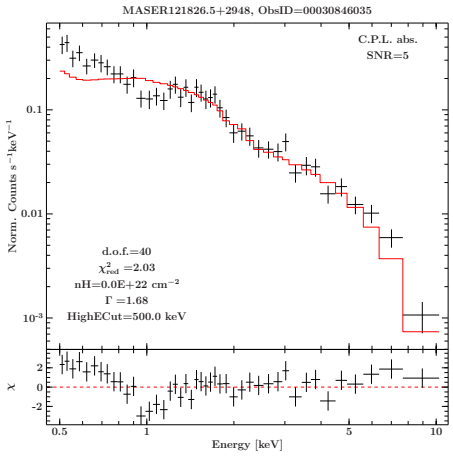
MASER121826.5+2948, ObsID=00030846035
C.P.L. abs.
SNR=5
d.o.f.=40
χ^2_{red} =2.03
nH=0.0E+22 cm^{-2}
Γ =1.68
HighECut=500.0 keV
Norm. Counts s^{-1}keV^{-1}
χ
Energy [keV]

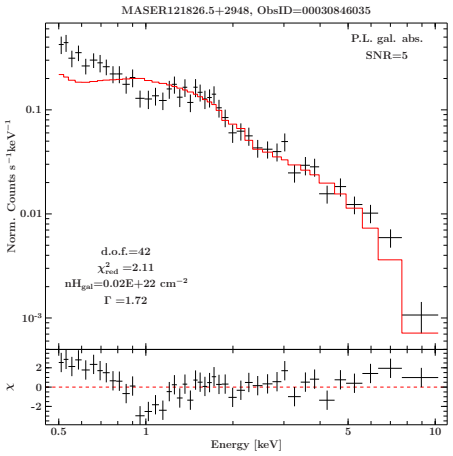
MASER121826.5+2948, ObsID=00030846035
P.L. gal. abs.
SNR=5
d.o.f.=42
χ^2_{red} =2.11
nH$_{gal}$=0.02E+22 cm^{-2}
Γ =1.72
Norm. Counts s^{-1}keV^{-1}
χ
Energy [keV]

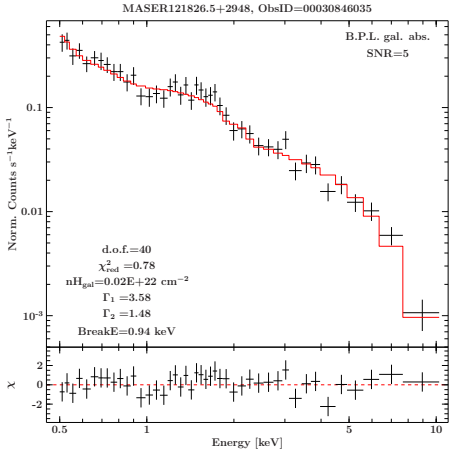
MASER121826.5+2948, ObsID=00030846035
B.P.L. gal. abs.
SNR=5
d.o.f.=40
χ^2_{red} =0.78
nH$_{gal}$=0.02E+22 cm^{-2}
Γ$_1$ =3.58
Γ$_2$ =1.48
BreakE=0.94 keV
Norm. Counts s^{-1}keV^{-1}
χ
Energy [keV]

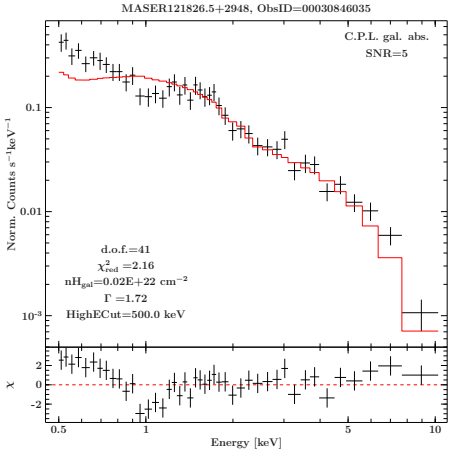
MASER121826.5+2948, ObsID=00030846035
C.P.L. gal. abs.
SNR=5
d.o.f.=41
χ^2_{red} =2.16
nH$_{gal}$=0.02E+22 cm^{-2}
Γ =1.72
HighECut=500.0 keV
Norm. Counts s^{-1}keV^{-1}
χ
Energy [keV]

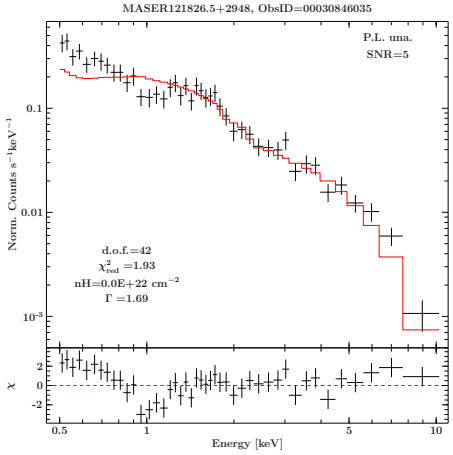
MASER121826.5+2948, ObsID=00030846035
P.L. una.
SNR=5
d.o.f.=42
χ^2_{red} =1.93
nH=0.0E+22 cm^{-2}
Γ =1.69
Norm. Counts s^{-1}keV^{-1}
χ
Energy [keV]

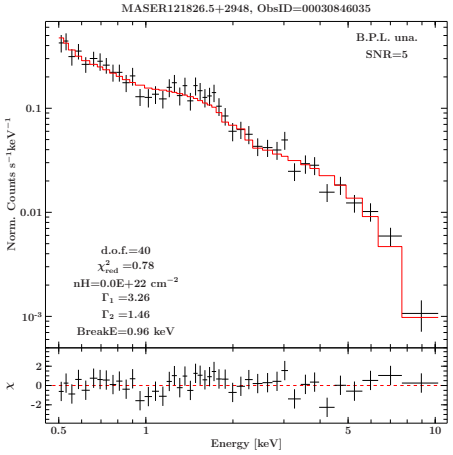
MASER121826.5+2948, ObsID=00030846035
B.P.L. una.
SNR=5
d.o.f.=40
χ^2_{red} =0.78
nH=0.0E+22 cm^{-2}
Γ$_1$ =3.26
Γ$_2$ =1.46
BreakE=0.96 keV
Norm. Counts s^{-1}keV^{-1}
χ
Energy [keV]

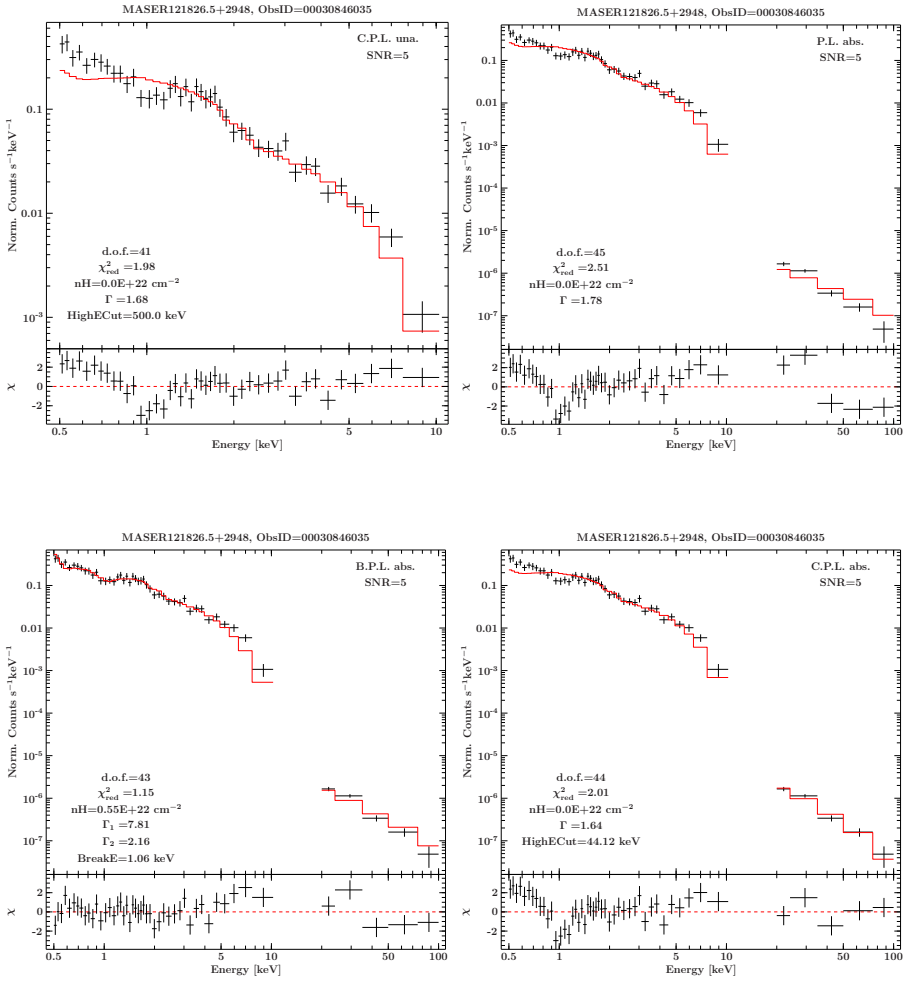
MASER121826.5+2948, ObsID=00030846035
C.P.L. una.
SNR=5
d.o.f.=41
χ^2_{red} =1.98
nH=0.0E+22 cm^{-2}
Γ =1.68
HighECut=500.0 keV
MASER121826.5+2948, ObsID=00030846035
P.L. abs.
SNR=5
d.o.f.=45
χ^2_{red} =2.51
nH=0.0E+22 cm^{-2}
Γ =1.78
MASER121826.5+2948, ObsID=00030846035
B.P.L. abs.
SNR=5
d.o.f.=43
χ^2_{red} =1.15
nH=0.55E+22 cm^{-2}
Γ$_1$ =7.81
Γ$_2$ =2.16
BreakE=1.06 keV
MASER121826.5+2948, ObsID=00030846035
C.P.L. abs.
SNR=5
d.o.f.=44
χ^2_{red} =2.01
nH=0.0E+22 cm^{-2}
Γ =1.64
HighECut=44.12 keV
Norm. Counts s^{-1}keV^{-1}
χ
Energy [keV]

ObsID 00030846036

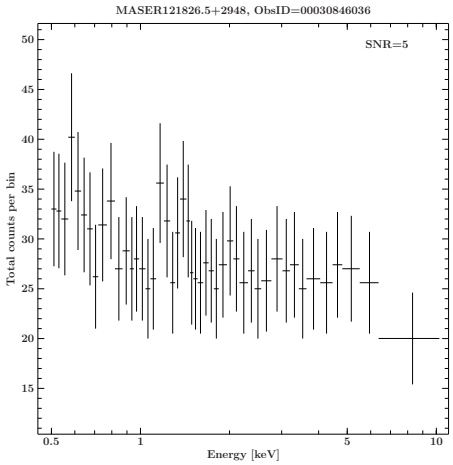

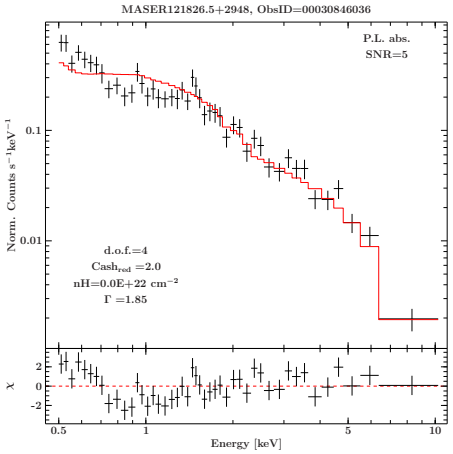

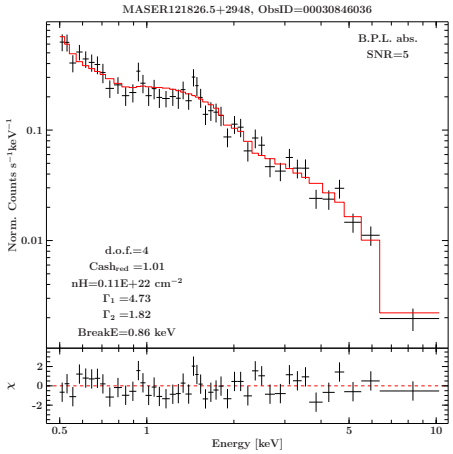

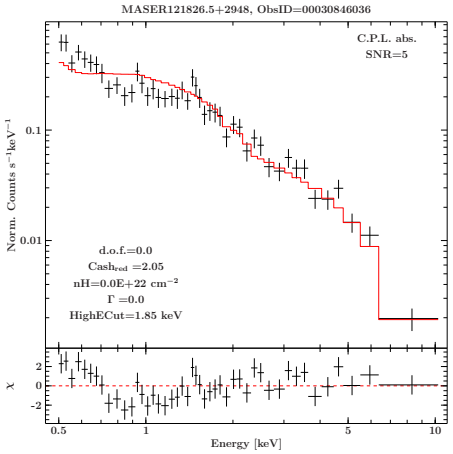

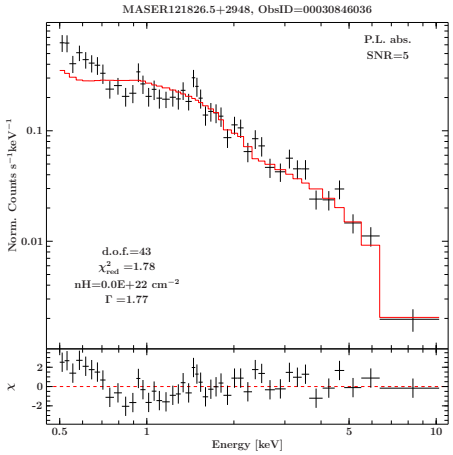

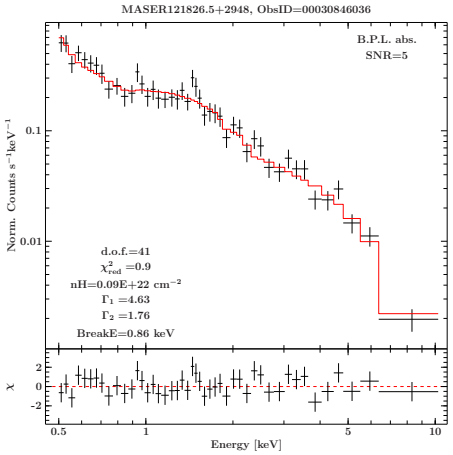

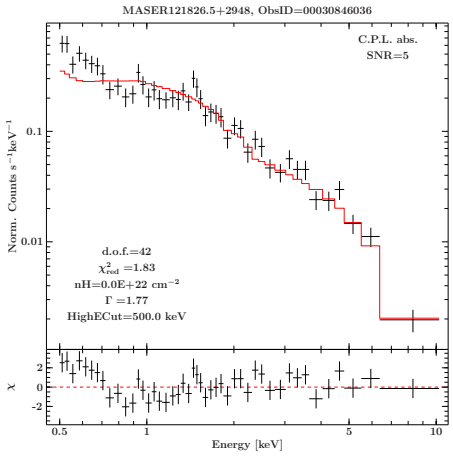
MASER121826.5+2948, ObsID=00030846036
C.P.L. abs.
SNR=5
d.o.f.=42
χ^2_{red} =1.83
nH=0.0E+22 cm^{-2}
Γ =1.77
HighECut=500.0 keV
Norm. Counts s^{-1}keV^{-1}
χ
Energy [keV]

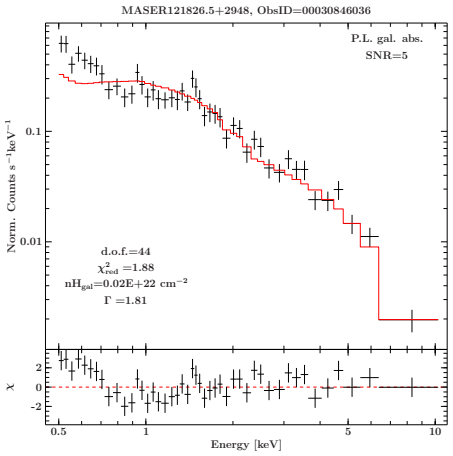
MASER121826.5+2948, ObsID=00030846036
P.L. gal. abs.
SNR=5
d.o.f.=44
χ^2_{red} =1.88
nH$_{gal}$=0.02E+22 cm^{-2}
Γ =1.81
Norm. Counts s^{-1}keV^{-1}
χ
Energy [keV]

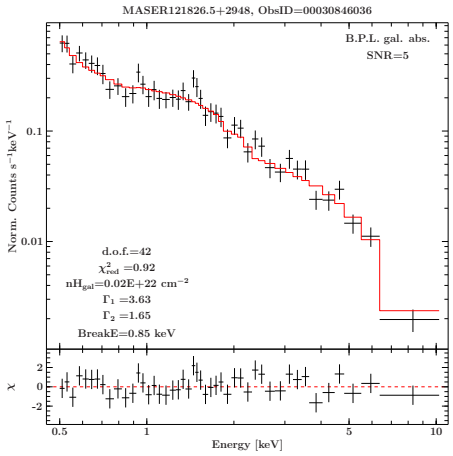
MASER121826.5+2948, ObsID=00030846036
B.P.L. gal. abs.
SNR=5
d.o.f.=42
χ^2_{red} =0.92
nH$_{gal}$=0.02E+22 cm^{-2}
Γ$_1$ =3.63
Γ$_2$ =1.65
BreakE=0.85 keV
Norm. Counts s^{-1}keV^{-1}
χ
Energy [keV]

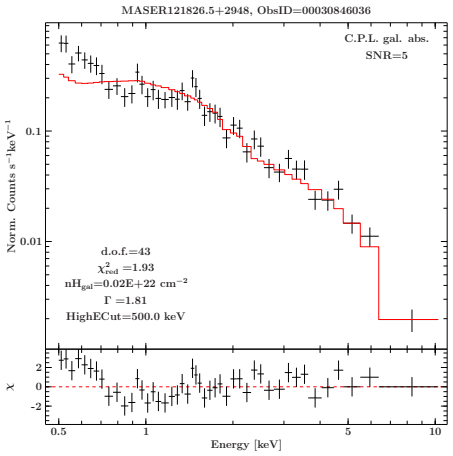
MASER121826.5+2948, ObsID=00030846036
C.P.L. gal. abs.
SNR=5
d.o.f.=43
χ^2_{red} =1.93
nH$_{gal}$=0.02E+22 cm^{-2}
Γ =1.81
HighECut=500.0 keV
Norm. Counts s^{-1}keV^{-1}
χ
Energy [keV]

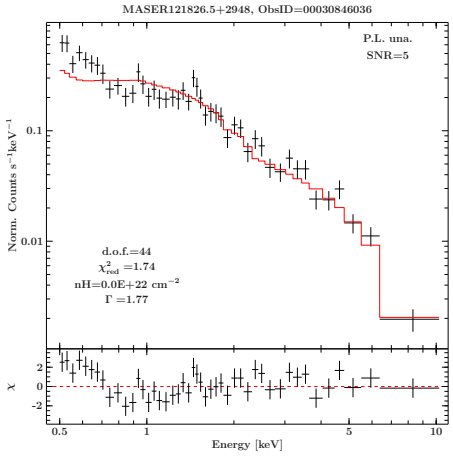
MASER121826.5+2948, ObsID=00030846036
P.L. una.
SNR=5
d.o.f.=44
χ^2_{red} =1.74
nH=0.0E+22 cm^{-2}
Γ =1.77
Norm. Counts s^{-1}keV^{-1}
χ
Energy [keV]

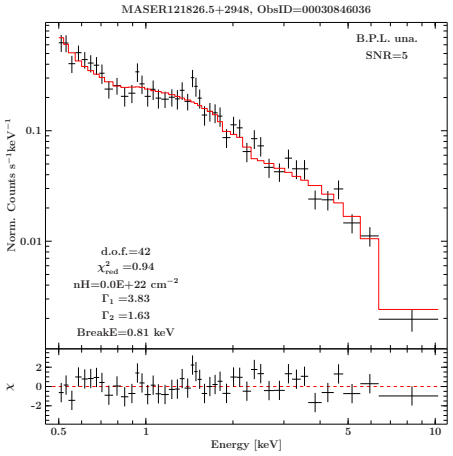
MASER121826.5+2948, ObsID=00030846036
B.P.L. una.
SNR=5
d.o.f.=42
χ^2_{red} =0.94
nH=0.0E+22 cm^{-2}
Γ$_1$ =3.83
Γ$_2$ =1.63
BreakE=0.81 keV
Norm. Counts s^{-1}keV^{-1}
χ
Energy [keV]

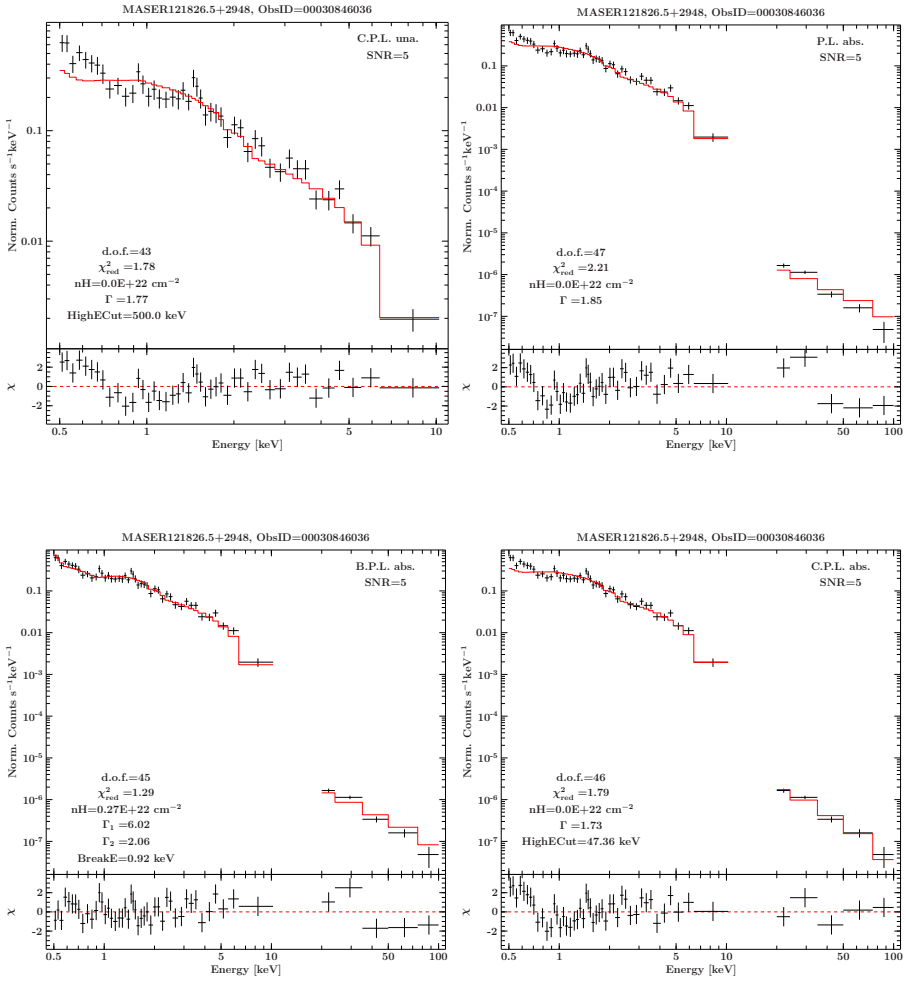
MASER121826.5+2948, ObsID=00030846036
C.P.L. una.
SNR=5
d.o.f.=43
χ^2_{red} =1.78
nH=0.0E+22 cm^{-2}
Γ =1.77
HighECut=500.0 keV
MASER121826.5+2948, ObsID=00030846036
P.L. abs.
SNR=5
d.o.f.=47
χ^2_{red} =2.21
nH=0.0E+22 cm^{-2}
Γ =1.85
MASER121826.5+2948, ObsID=00030846036
B.P.L. abs.
SNR=5
d.o.f.=45
χ^2_{red} =1.29
nH=0.27E+22 cm^{-2}
Γ$_1$ =6.02
Γ$_2$ =2.06
BreakE=0.92 keV
MASER121826.5+2948, ObsID=00030846036
C.P.L. abs.
SNR=5
d.o.f.=46
χ^2_{red} =1.79
nH=0.0E+22 cm^{-2}
Γ =1.73
HighECut=47.36 keV
Norm. Counts s^{-1}keV^{-1}
χ
Energy [keV]

ObsID 00030846037

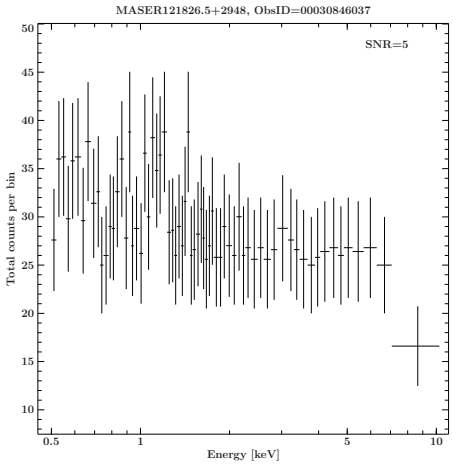

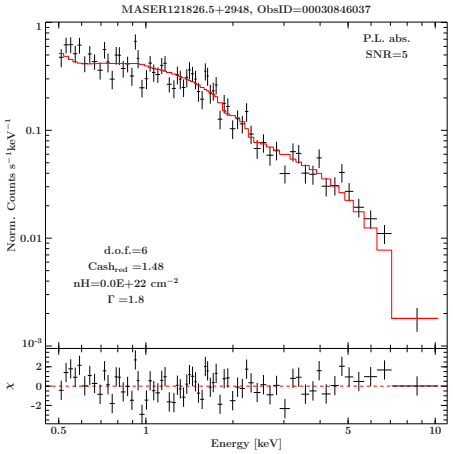

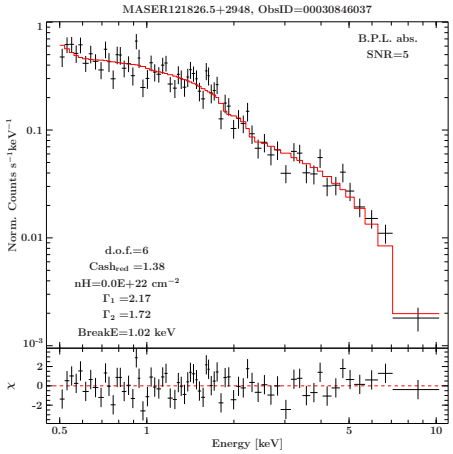

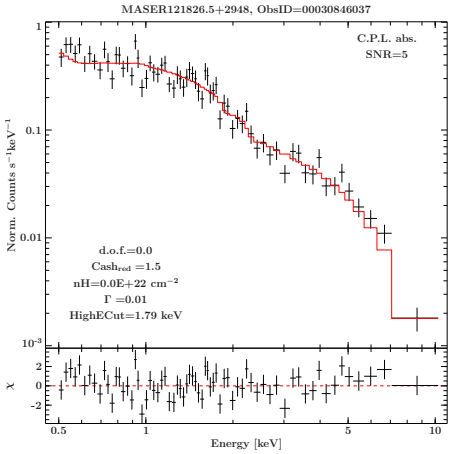

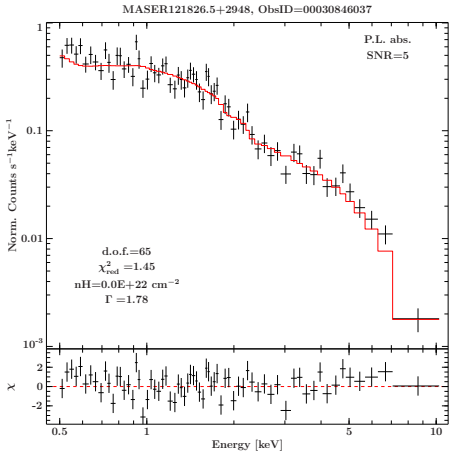

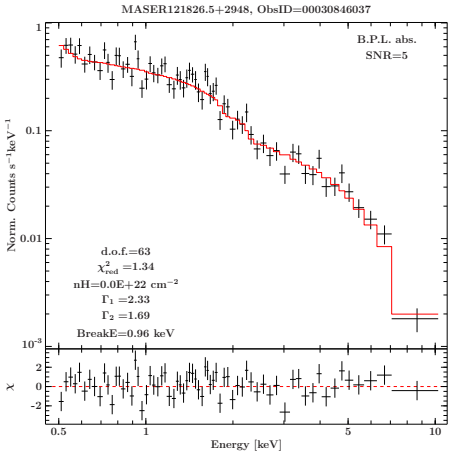

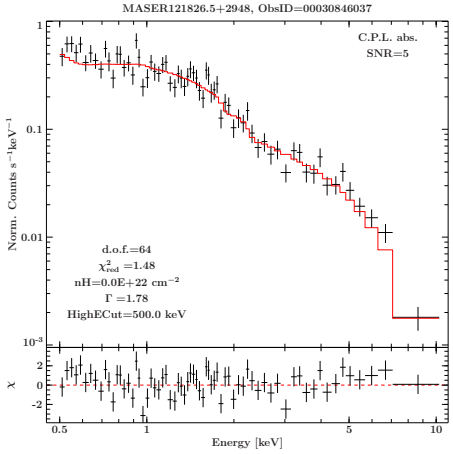
MASER121826.5+2948, ObsID=00030846037
C.P.L. abs.
SNR=5
d.o.f.=64
χ^2_{red} =1.48
nH=0.0E+22 cm^{-2}
Γ =1.78
HighECut=500.0 keV
Norm. Counts s^{-1}keV^{-1}
χ
Energy [keV]

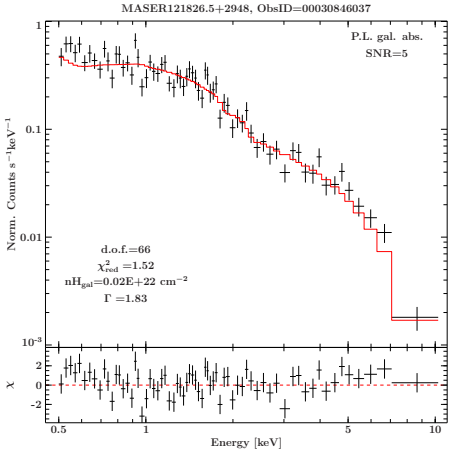
MASER121826.5+2948, ObsID=00030846037
P.L. gal. abs.
SNR=5
d.o.f.=66
χ^2_{red} =1.52
nH$_{gal}$=0.02E+22 cm^{-2}
Γ =1.83
Norm. Counts s^{-1}keV^{-1}
χ
Energy [keV]

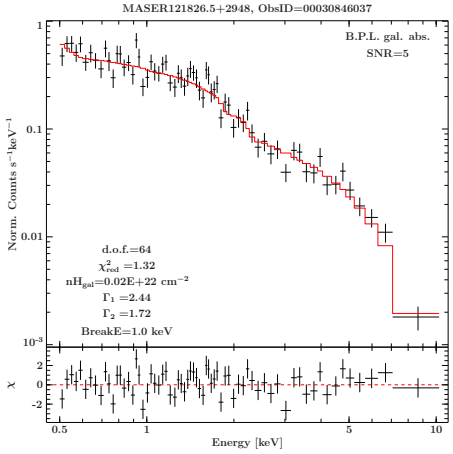
MASER121826.5+2948, ObsID=00030846037
B.P.L. gal. abs.
SNR=5
d.o.f.=64
χ^2_{red} =1.32
nH$_{gal}$=0.02E+22 cm^{-2}
Γ$_1$ =2.44
Γ$_2$ =1.72
BreakE=1.0 keV
Norm. Counts s^{-1}keV^{-1}
χ
Energy [keV]

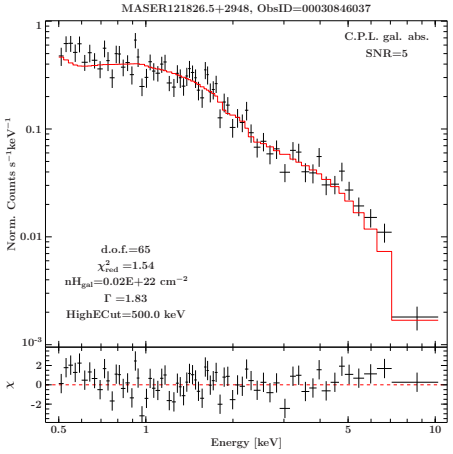
MASER121826.5+2948, ObsID=00030846037
C.P.L. gal. abs.
SNR=5
d.o.f.=65
χ^2_{red} =1.54
nH$_{gal}$=0.02E+22 cm^{-2}
Γ =1.83
HighECut=500.0 keV
Norm. Counts s^{-1}keV^{-1}
χ
Energy [keV]

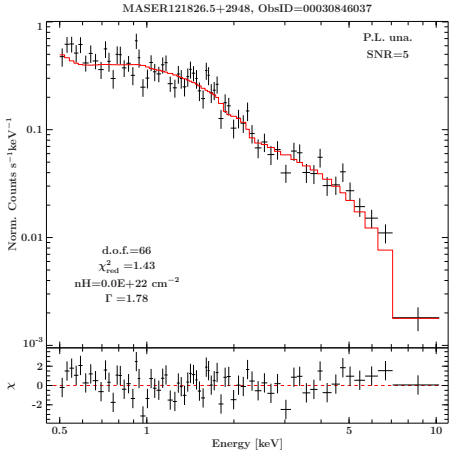
MASER121826.5+2948, ObsID=00030846037
P.L. una.
SNR=5
d.o.f.=66
χ^2_{red} =1.43
nH=0.0E+22 cm^{-2}
Γ =1.78
Norm. Counts s^{-1}keV^{-1}
χ
Energy [keV]

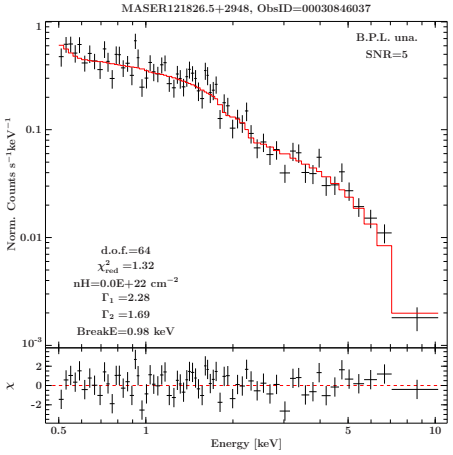
MASER121826.5+2948, ObsID=00030846037
B.P.L. una.
SNR=5
d.o.f.=64
χ^2_{red} =1.32
nH=0.0E+22 cm^{-2}
Γ$_1$ =2.28
Γ$_2$ =1.69
BreakE=0.98 keV
Norm. Counts s^{-1}keV^{-1}
χ
Energy [keV]

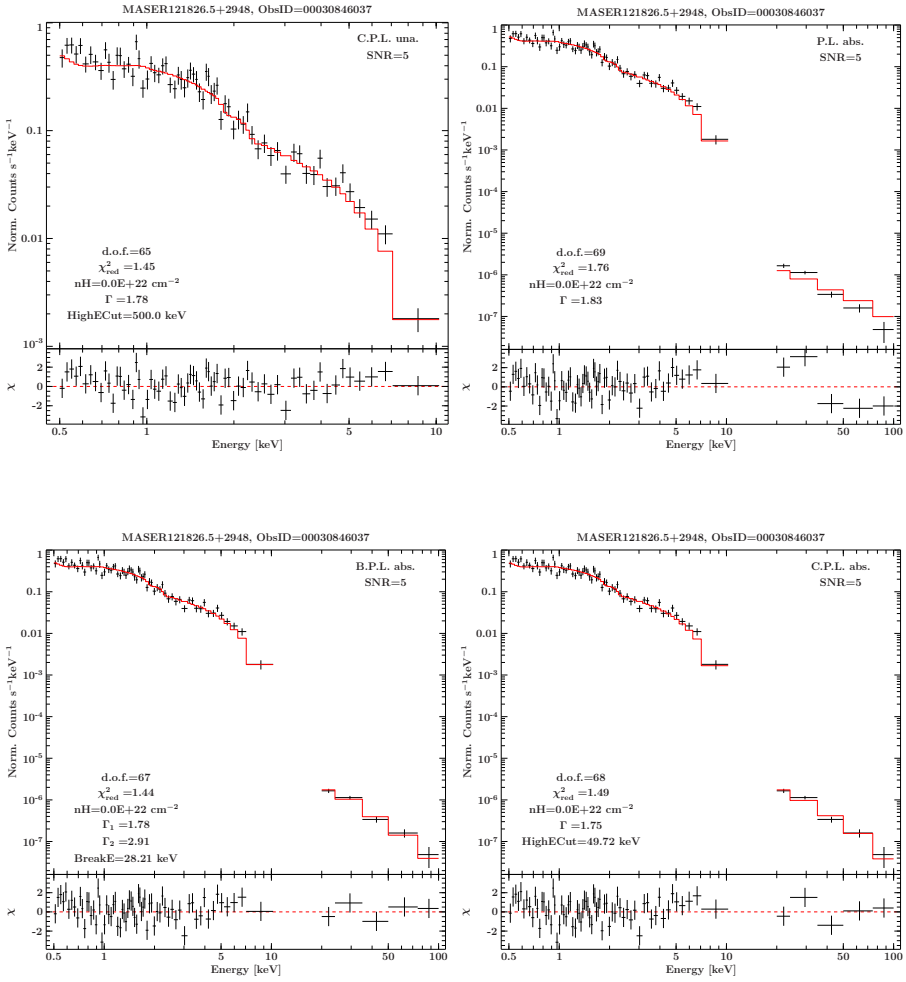
MASER121826.5+2948, ObsID=00030846037
C.P.L. una.
SNR=5
d.o.f.=65
χ^2_{red} =1.45
nH=0.0E+22 cm^{-2}
Γ =1.78
HighECut=500.0 keV
Norm. Counts s^{-1}keV^{-1}
χ
Energy [keV]
MASER121826.5+2948, ObsID=00030846037
P.L. abs.
SNR=5
d.o.f.=69
χ^2_{red} =1.76
nH=0.0E+22 cm^{-2}
Γ =1.83
Norm. Counts s^{-1}keV^{-1}
χ
Energy [keV]
MASER121826.5+2948, ObsID=00030846037
B.P.L. abs.
SNR=5
d.o.f.=67
χ^2_{red} =1.44
nH=0.0E+22 cm^{-2}
Γ_1 =1.78
Γ_2 =2.91
BreakE=28.21 keV
Norm. Counts s^{-1}keV^{-1}
χ
Energy [keV]
MASER121826.5+2948, ObsID=00030846037
C.P.L. abs.
SNR=5
d.o.f.=68
χ^2_{red} =1.49
nH=0.0E+22 cm^{-2}
Γ =1.75
HighECut=49.72 keV
Norm. Counts s^{-1}keV^{-1}
χ
Energy [keV]

ObsID 00030846038

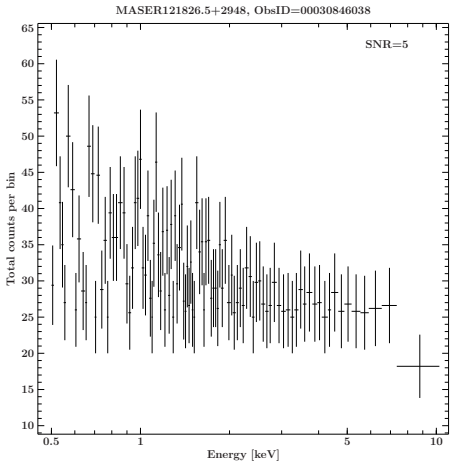

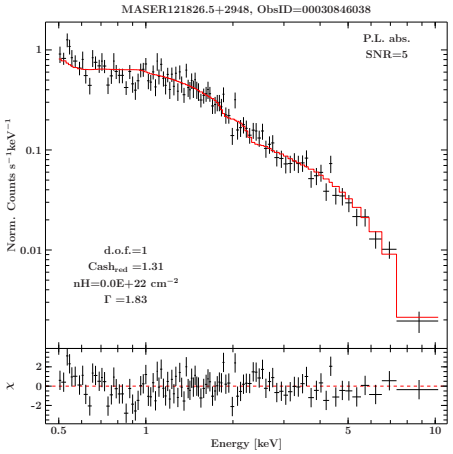

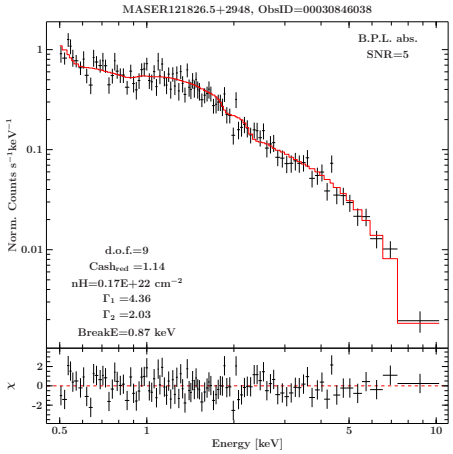

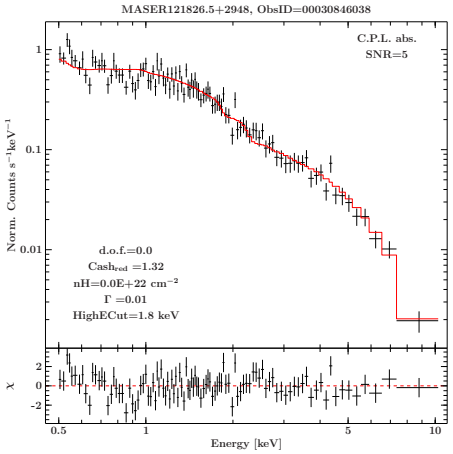

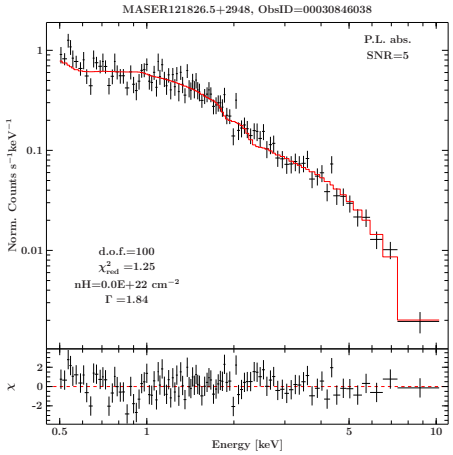

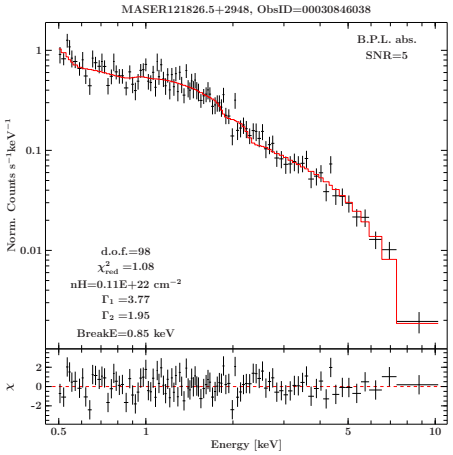

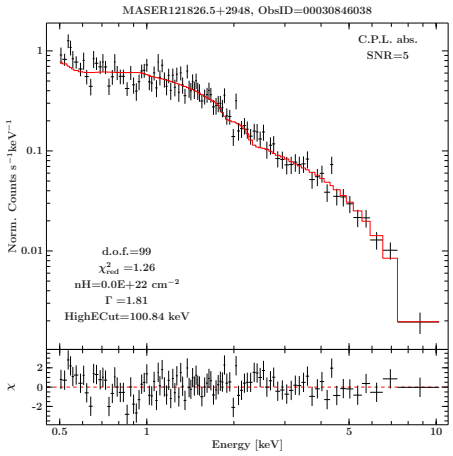
MASER121826.5+2948, ObsID=00030846038
C.P.L. abs.
SNR=5
d.o.f.=99
χ^2_{red} =1.26
nH=0.0E+22 cm^{-2}
Γ =1.81
HighECut=100.84 keV
Norm. Counts s^{-1}keV^{-1}
χ
Energy [keV]

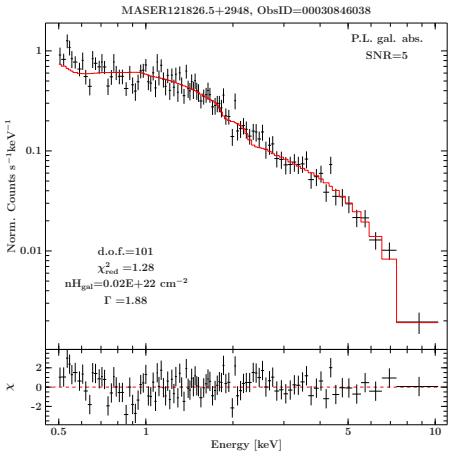
MASER121826.5+2948, ObsID=00030846038
P.L. gal. abs.
SNR=5
d.o.f.=101
χ^2_{red} =1.28
nH$_{gal}$=0.02E+22 cm^{-2}
Γ =1.88
Norm. Counts s^{-1}keV^{-1}
χ
Energy [keV]

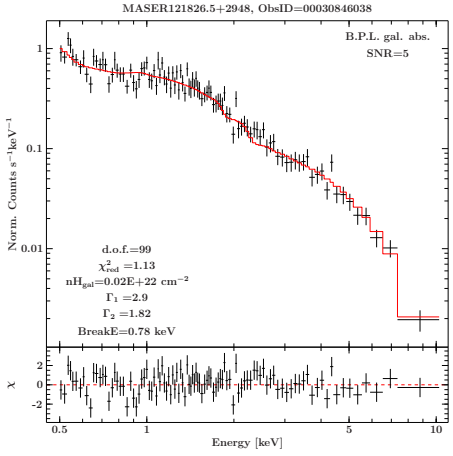
MASER121826.5+2948, ObsID=00030846038
B.P.L. gal. abs.
SNR=5
d.o.f.=99
χ^2_{red} =1.13
nH$_{gal}$=0.02E+22 cm^{-2}
Γ$_1$ =2.9
Γ$_2$ =1.82
BreakE=0.78 keV
Norm. Counts s^{-1}keV^{-1}
χ
Energy [keV]

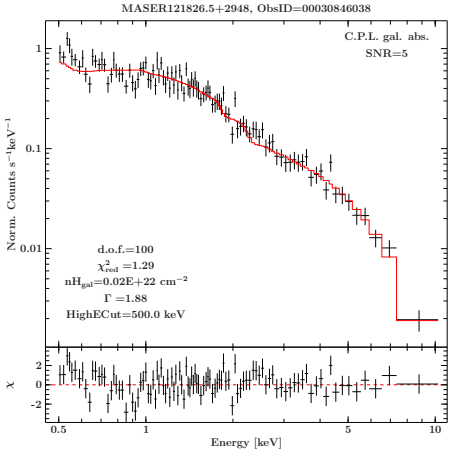
MASER121826.5+2948, ObsID=00030846038
C.P.L. gal. abs.
SNR=5
d.o.f.=100
χ^2_{red} =1.29
nH$_{gal}$=0.02E+22 cm^{-2}
Γ =1.88
HighECut=500.0 keV
Norm. Counts s^{-1}keV^{-1}
χ
Energy [keV]

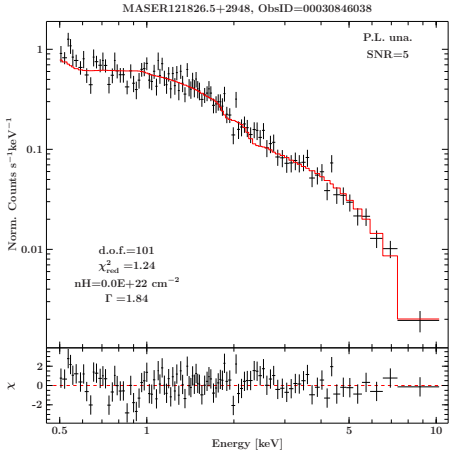
MASER121826.5+2948, ObsID=00030846038
P.L. una.
SNR=5
d.o.f.=101
χ^2_{red} =1.24
nH=0.0E+22 cm^{-2}
Γ =1.84
Norm. Counts s^{-1}keV^{-1}
χ
Energy [keV]

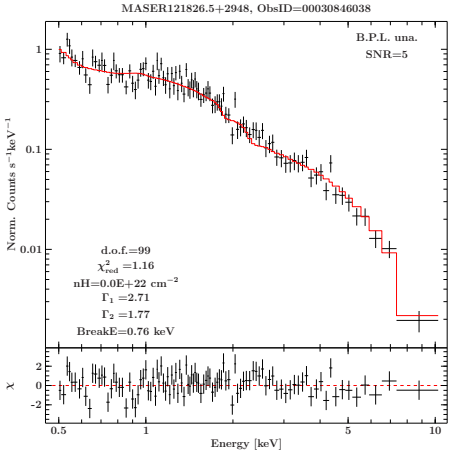
MASER121826.5+2948, ObsID=00030846038
B.P.L. una.
SNR=5
d.o.f.=99
χ^2_{red} =1.16
nH=0.0E+22 cm^{-2}
Γ$_1$ =2.71
Γ$_2$ =1.77
BreakE=0.76 keV
Norm. Counts s^{-1}keV^{-1}
χ
Energy [keV]

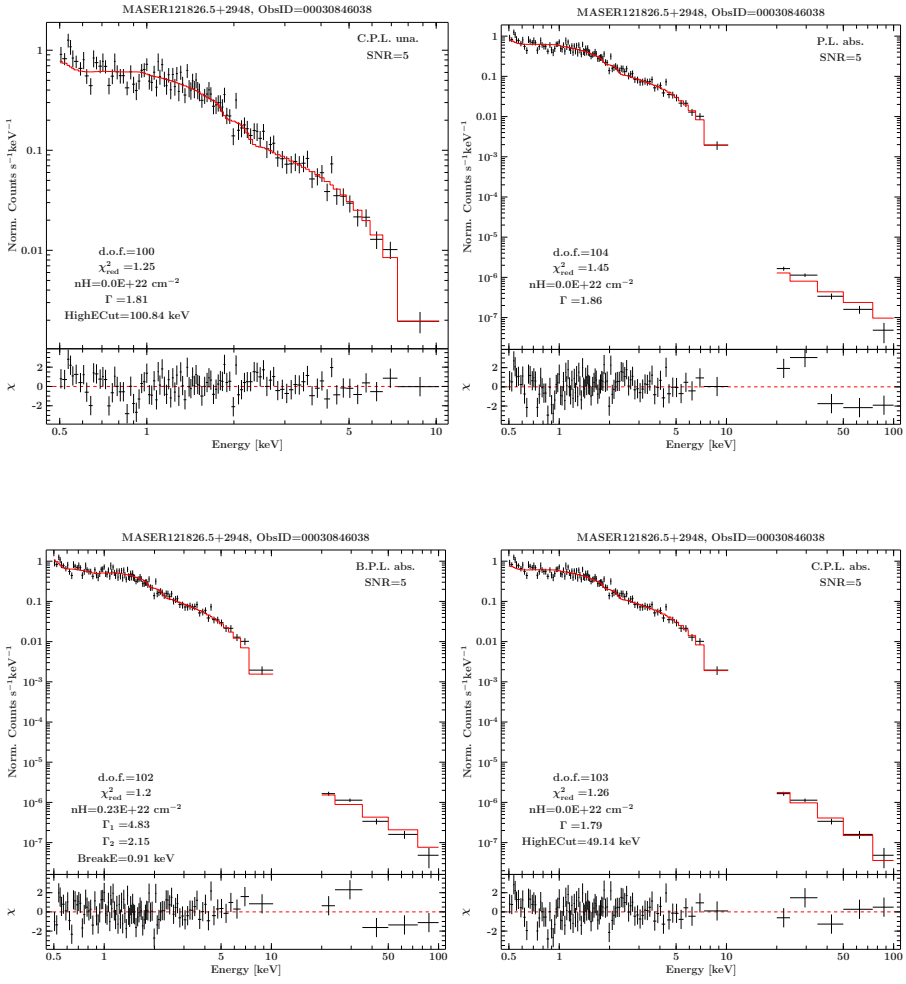
MASER121826.5+2948, ObsID=00030846038
C.P.L. una.
SNR=5
d.o.f.=100
χ^2_{red} =1.25
nH=0.0E+22 cm^{-2}
Γ =1.81
HighECut=100.84 keV
Norm. Counts s^{-1}keV^{-1}
χ
Energy [keV]
MASER121826.5+2948, ObsID=00030846038
P.L. abs.
SNR=5
d.o.f.=104
χ^2_{red} =1.45
nH=0.0E+22 cm^{-2}
Γ =1.86
Norm. Counts s^{-1}keV^{-1}
χ
Energy [keV]
MASER121826.5+2948, ObsID=00030846038
B.P.L. abs.
SNR=5
d.o.f.=102
χ^2_{red} =1.2
nH=0.23E+22 cm^{-2}
Γ_1 =4.83
Γ_2 =2.15
BreakE=0.91 keV
Norm. Counts s^{-1}keV^{-1}
χ
Energy [keV]
MASER121826.5+2948, ObsID=00030846038
C.P.L. abs.
SNR=5
d.o.f.=103
χ^2_{red} =1.26
nH=0.0E+22 cm^{-2}
Γ =1.79
HighECut=49.14 keV
Norm. Counts s^{-1}keV^{-1}
χ
Energy [keV]

ObsID 00030846039

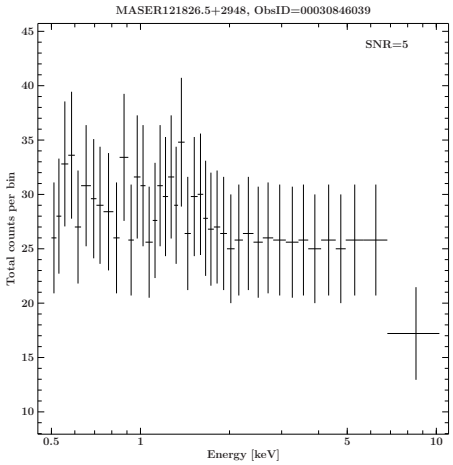

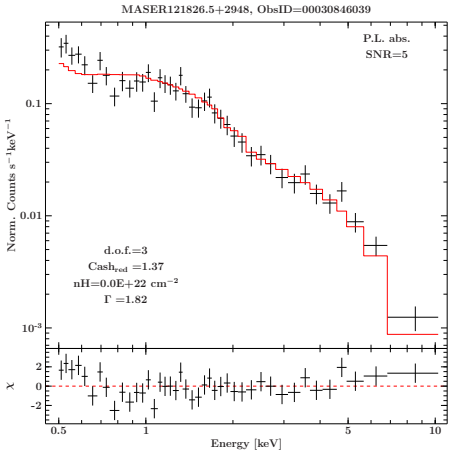

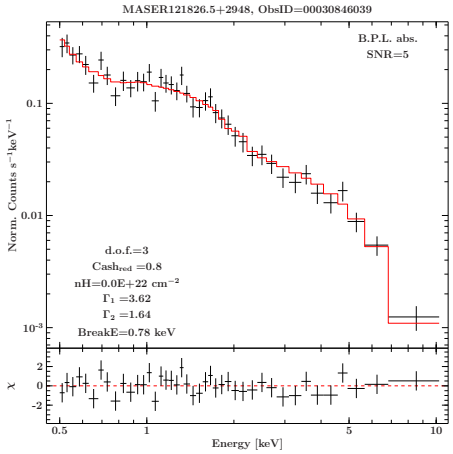

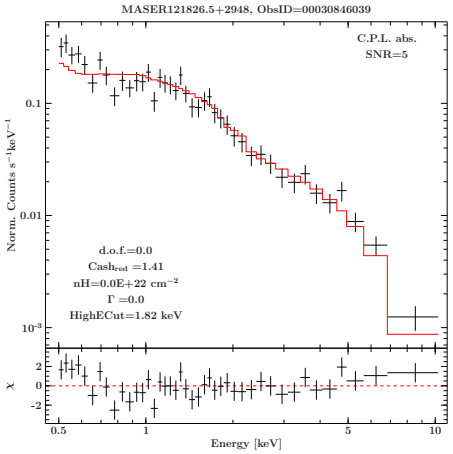

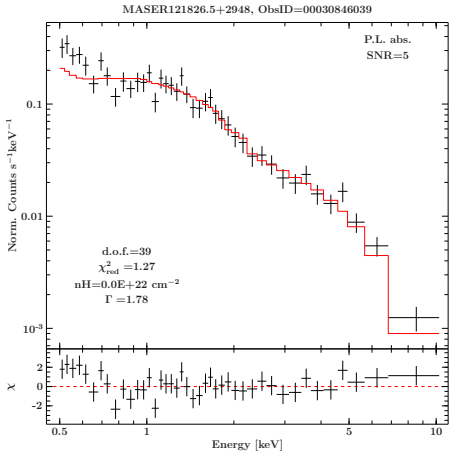

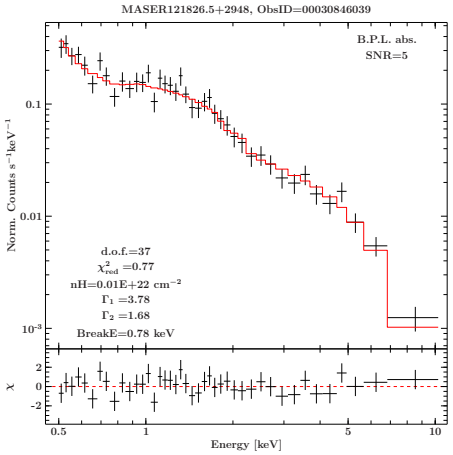

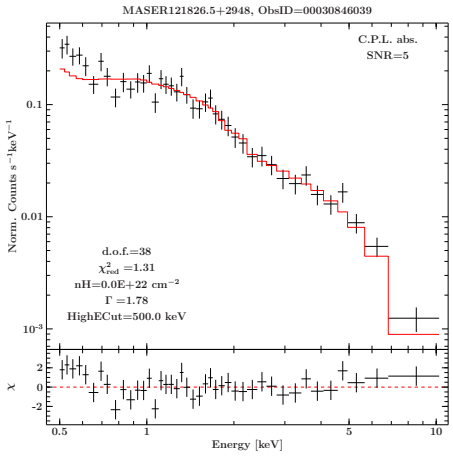
MASER121826.5+2948, ObsID=00030846039
C.P.L. abs.
SNR=5
d.o.f.=38
χ^2_{red} =1.31
nH=0.0E+22 cm^{-2}
Γ =1.78
HighECut=500.0 keV
Norm. Counts s^{-1}keV^{-1}
χ
Energy [keV]

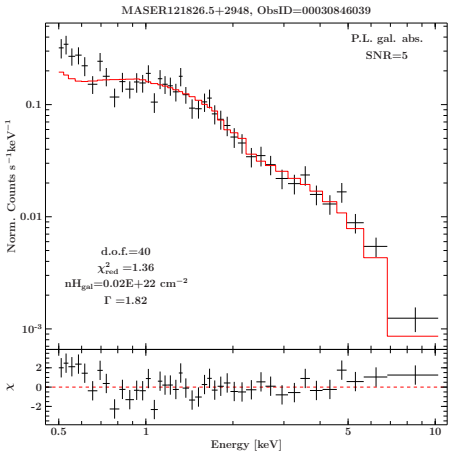
MASER121826.5+2948, ObsID=00030846039
P.L. gal. abs.
SNR=5
d.o.f.=40
χ^2_{red} =1.36
nH$_{gal}$=0.02E+22 cm^{-2}
Γ =1.82
Norm. Counts s^{-1}keV^{-1}
χ
Energy [keV]

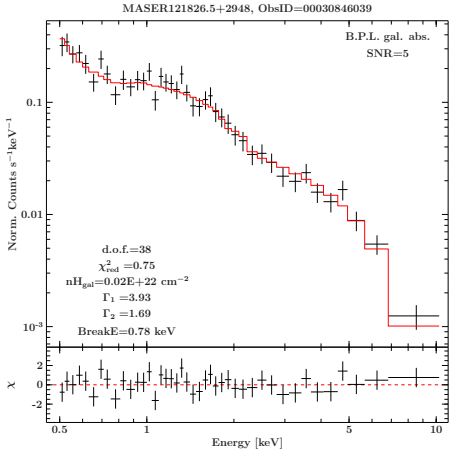
MASER121826.5+2948, ObsID=00030846039
B.P.L. gal. abs.
SNR=5
d.o.f.=38
χ^2_{red} =0.75
nH$_{gal}$=0.02E+22 cm^{-2}
Γ$_1$ =3.93
Γ$_2$ =1.69
BreakE=0.78 keV
Norm. Counts s^{-1}keV^{-1}
χ
Energy [keV]

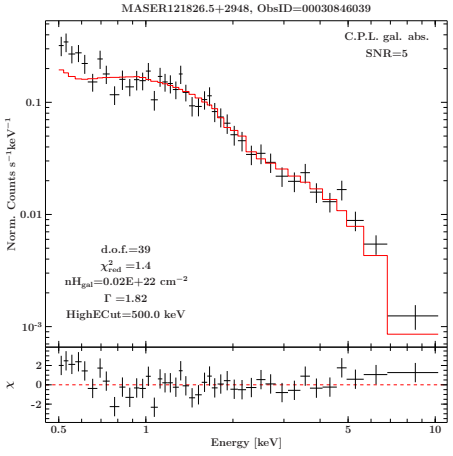
MASER121826.5+2948, ObsID=00030846039
C.P.L. gal. abs.
SNR=5
d.o.f.=39
χ^2_{red} =1.4
nH$_{gal}$=0.02E+22 cm^{-2}
Γ =1.82
HighECut=500.0 keV
Norm. Counts s^{-1}keV^{-1}
χ
Energy [keV]

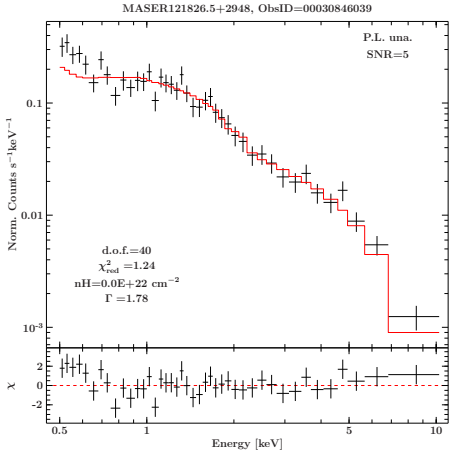
MASER121826.5+2948, ObsID=00030846039
P.L. una.
SNR=5
d.o.f.=40
χ^2_{red} =1.24
nH=0.0E+22 cm^{-2}
Γ =1.78
Norm. Counts s^{-1}keV^{-1}
χ
Energy [keV]

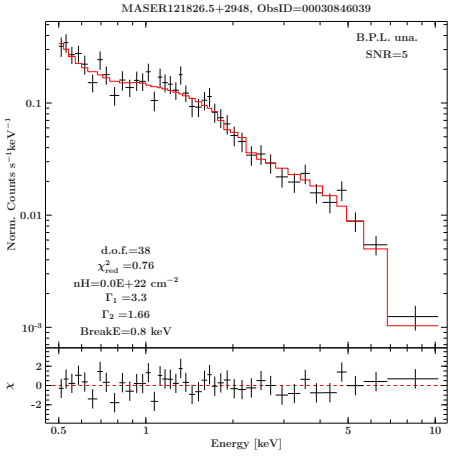
MASER121826.5+2948, ObsID=00030846039
B.P.L. una.
SNR=5
d.o.f.=38
χ^2_{red} =0.76
nH=0.0E+22 cm^{-2}
Γ$_1$ =3.3
Γ$_2$ =1.66
BreakE=0.8 keV
Norm. Counts s^{-1}keV^{-1}
χ
Energy [keV]

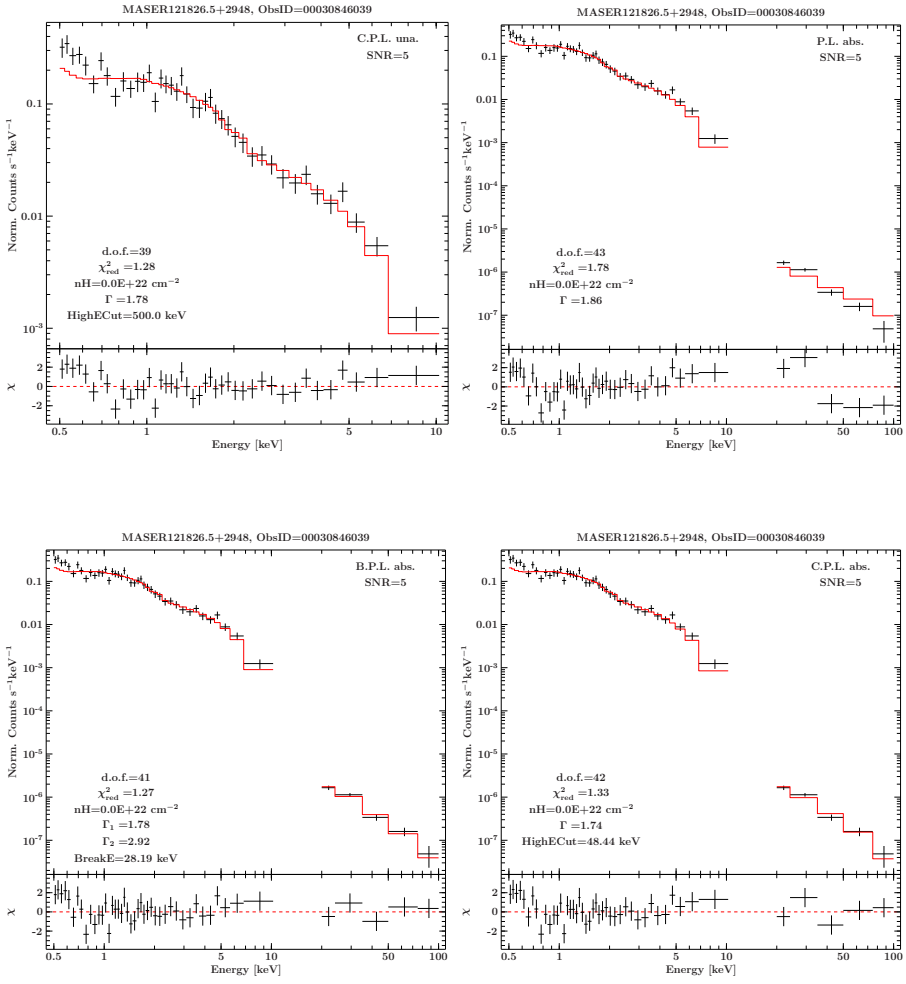
MASER121826.5+2948, ObsID=00030846039
C.P.L. una.
SNR=5
d.o.f.=39
χ^2_{red} =1.28
nH=0.0E+22 cm^{-2}
Γ =1.78
HighECut=500.0 keV
MASER121826.5+2948, ObsID=00030846039
P.L. abs.
SNR=5
d.o.f.=43
χ^2_{red} =1.78
nH=0.0E+22 cm^{-2}
Γ =1.86
MASER121826.5+2948, ObsID=00030846039
B.P.L. abs.
SNR=5
d.o.f.=41
χ^2_{red} =1.27
nH=0.0E+22 cm^{-2}
Γ$_1$ =1.78
Γ$_2$ =2.92
BreakE=28.19 keV
MASER121826.5+2948, ObsID=00030846039
C.P.L. abs.
SNR=5
d.o.f.=42
χ^2_{red} =1.33
nH=0.0E+22 cm^{-2}
Γ =1.74
HighECut=48.44 keV
Norm. Counts s^{-1}keV^{-1}
χ
Energy [keV]

ObsID 00030846040

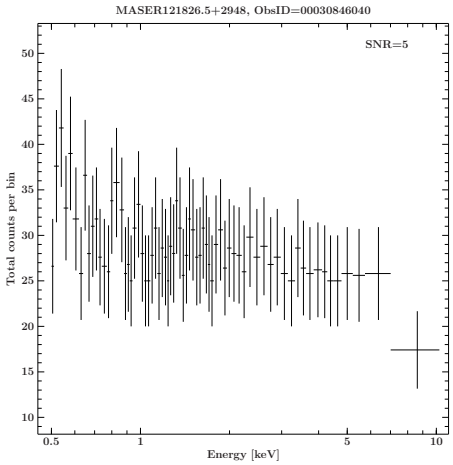

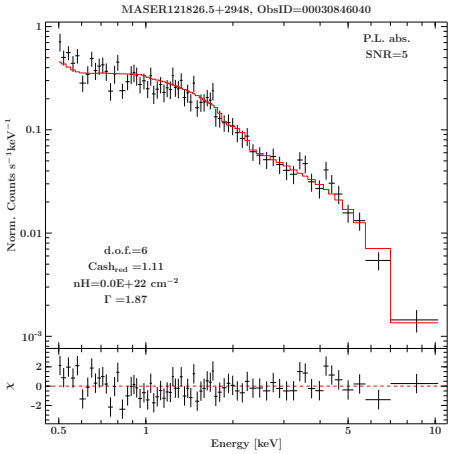

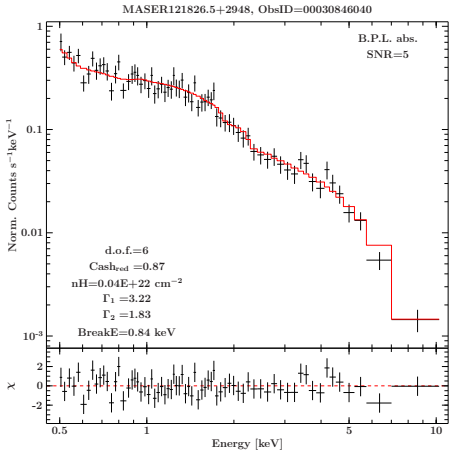

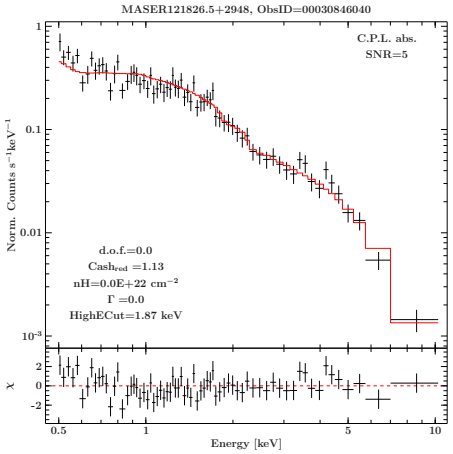

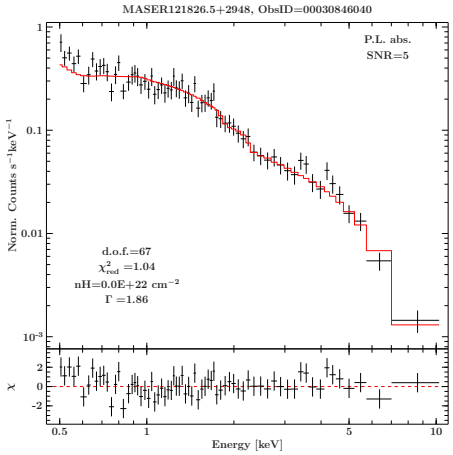

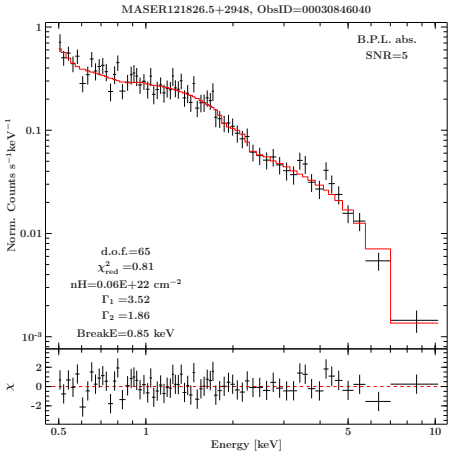

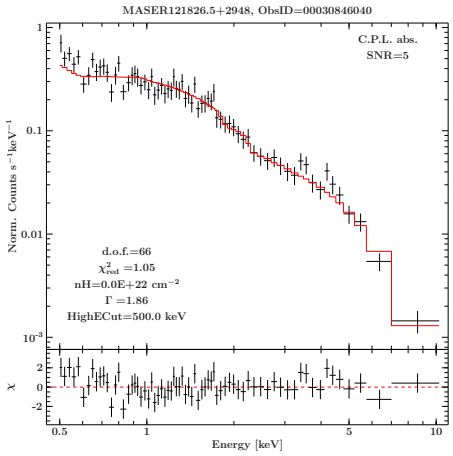
MASER121826.5+2948, ObsID=00030846040
C.P.L. abs.
SNR=5
d.o.f.=66
χ^2_{red} =1.05
nH=0.0E+22 cm^{-2}
Γ =1.86
HighECut=500.0 keV
Norm. Counts s^{-1}keV^{-1}
χ
Energy [keV]

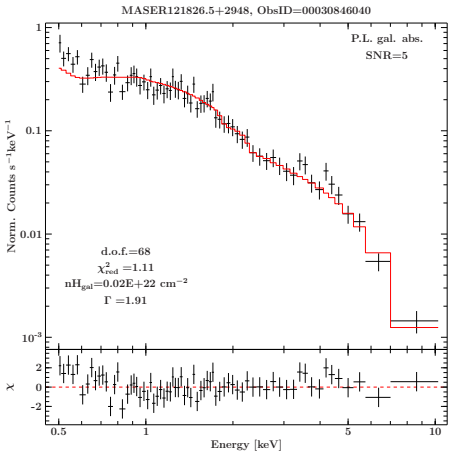
MASER121826.5+2948, ObsID=00030846040
P.L. gal. abs.
SNR=5
d.o.f.=68
χ^2_{red} =1.11
nH$_{gal}$=0.02E+22 cm^{-2}
Γ =1.91
Norm. Counts s^{-1}keV^{-1}
χ
Energy [keV]

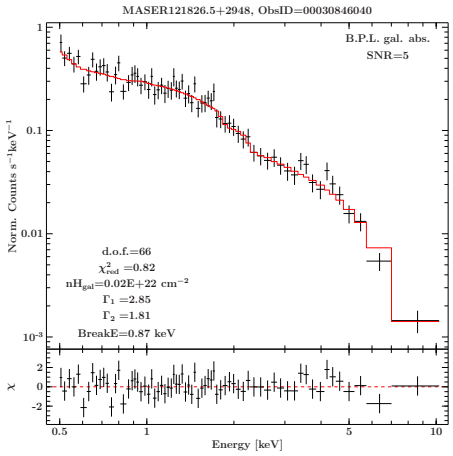
MASER121826.5+2948, ObsID=00030846040
B.P.L. gal. abs.
SNR=5
d.o.f.=66
χ^2_{red} =0.82
nH$_{gal}$=0.02E+22 cm^{-2}
Γ$_1$ =2.85
Γ$_2$ =1.81
BreakE=0.87 keV
Norm. Counts s^{-1}keV^{-1}
χ
Energy [keV]

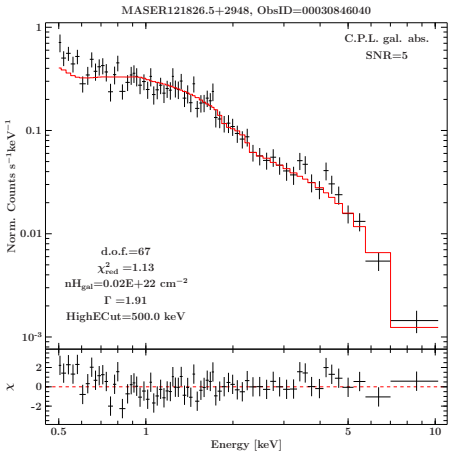
MASER121826.5+2948, ObsID=00030846040
C.P.L. gal. abs.
SNR=5
d.o.f.=67
χ^2_{red} =1.13
nH$_{gal}$=0.02E+22 cm^{-2}
Γ =1.91
HighECut=500.0 keV
Norm. Counts s^{-1}keV^{-1}
χ
Energy [keV]

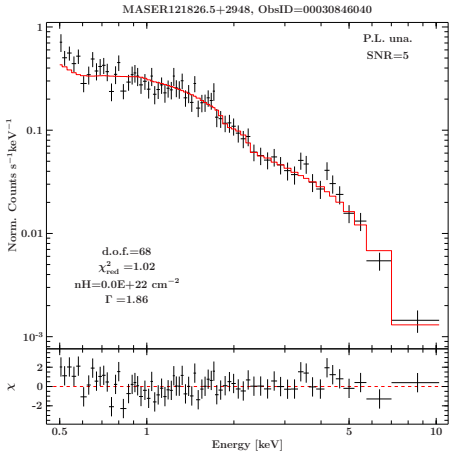
MASER121826.5+2948, ObsID=00030846040
P.L. una.
SNR=5
d.o.f.=68
χ^2_{red} =1.02
nH=0.0E+22 cm^{-2}
Γ =1.86
Norm. Counts s^{-1}keV^{-1}
χ
Energy [keV]

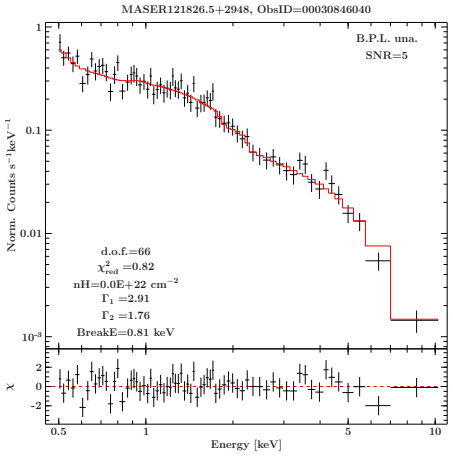
MASER121826.5+2948, ObsID=00030846040
B.P.L. una.
SNR=5
d.o.f.=66
χ^2_{red} =0.82
nH=0.0E+22 cm^{-2}
Γ$_1$ =2.91
Γ$_2$ =1.76
BreakE=0.81 keV
Norm. Counts s^{-1}keV^{-1}
χ
Energy [keV]

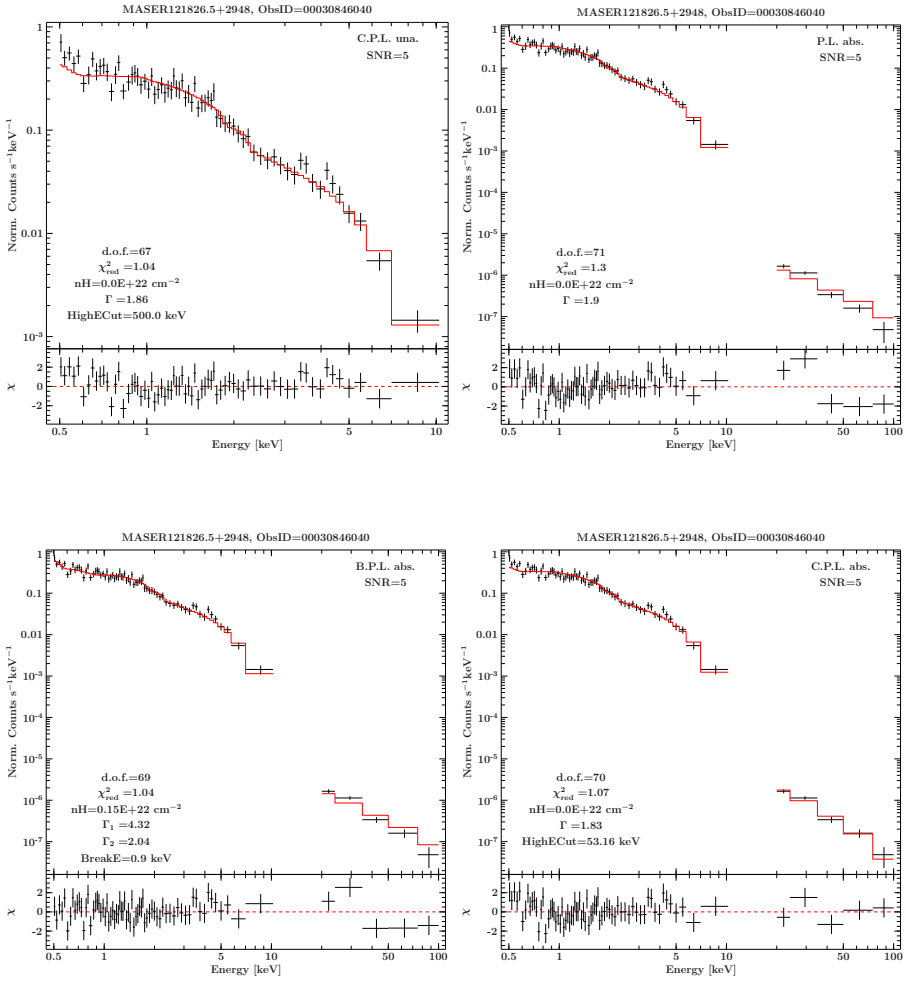
MASER121826.5+2948, ObsID=00030846040
C.P.L. una.
SNR=5
d.o.f.=67
χ^2_{red} =1.04
nH=0.0E+22 cm^{-2}
Γ =1.86
HighECut=500.0 keV
MASER121826.5+2948, ObsID=00030846040
P.L. abs.
SNR=5
d.o.f.=71
χ^2_{red} =1.3
nH=0.0E+22 cm^{-2}
Γ =1.9
MASER121826.5+2948, ObsID=00030846040
B.P.L. abs.
SNR=5
d.o.f.=69
χ^2_{red} =1.04
nH=0.15E+22 cm^{-2}
Γ_1 =4.32
Γ_2 =2.04
BreakE=0.9 keV
MASER121826.5+2948, ObsID=00030846040
C.P.L. abs.
SNR=5
d.o.f.=70
χ^2_{red} =1.07
nH=0.0E+22 cm^{-2}
Γ =1.83
HighECut=53.16 keV
Norm. Counts s^{-1}keV^{-1}
χ
Energy [keV]

A.2. Remaining spectral model fitting plots for MASER050819.7+1721

ObsID 00037118001

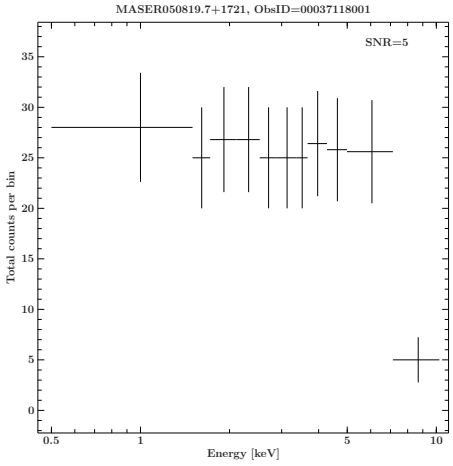

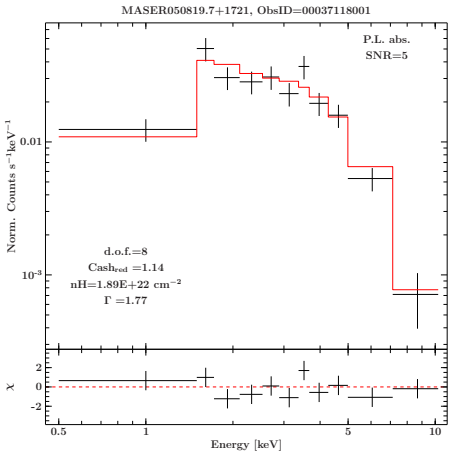

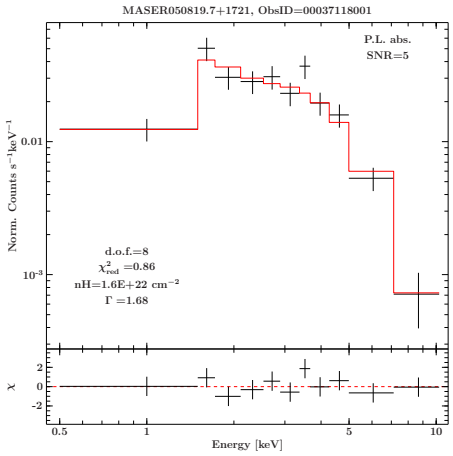

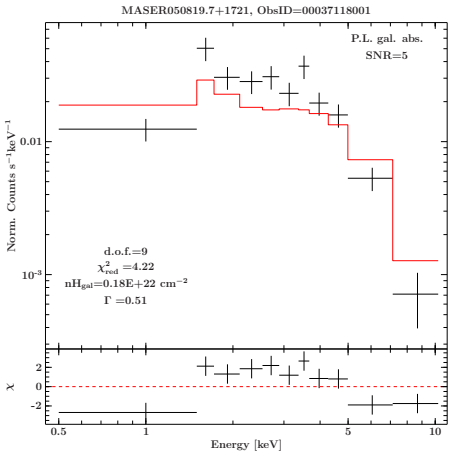

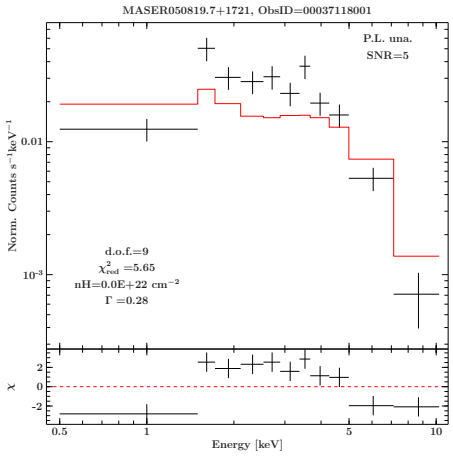

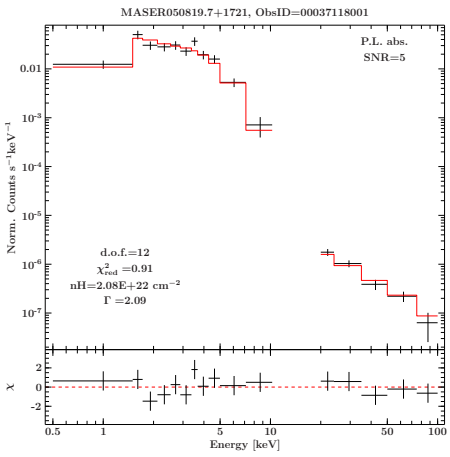

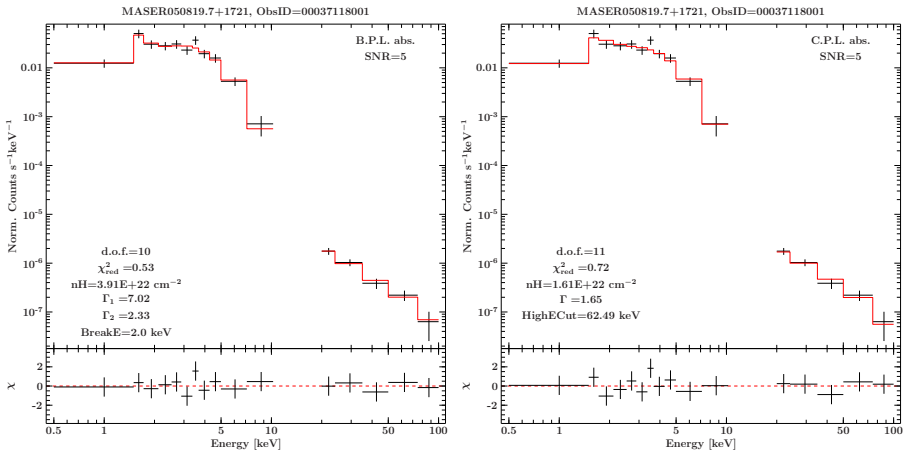
MASER050819.7+1721, ObsID=00037118001
B.P.L. abs.
SNR=5
d.o.f.=10
χ^2_{red} =0.53
nH=3.91E+22 cm^{-2}
Γ_1 =7.02
Γ_2 =2.33
BreakE=2.0 keV
Norm. Counts s^{-1}keV^{-1}
χ
Energy [keV]
MASER050819.7+1721, ObsID=00037118001
C.P.L. abs.
SNR=5
d.o.f.=11
χ^2_{red} =0.72
nH=1.61E+22 cm^{-2}
Γ =1.65
HighECut=62.49 keV
Norm. Counts s^{-1}keV^{-1}
χ
Energy [keV]

ObsID 00037118003

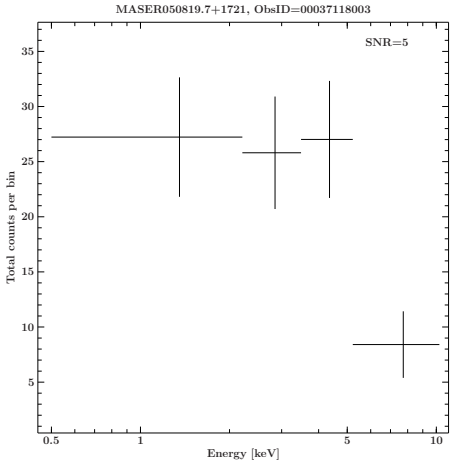

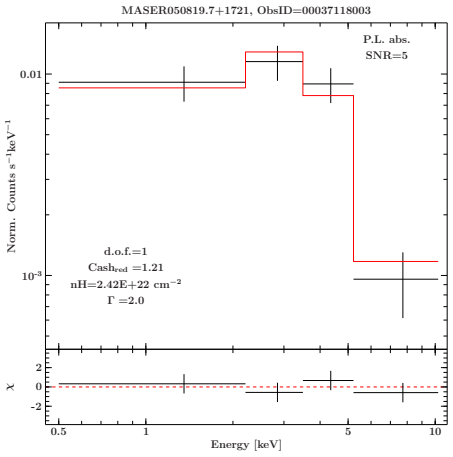

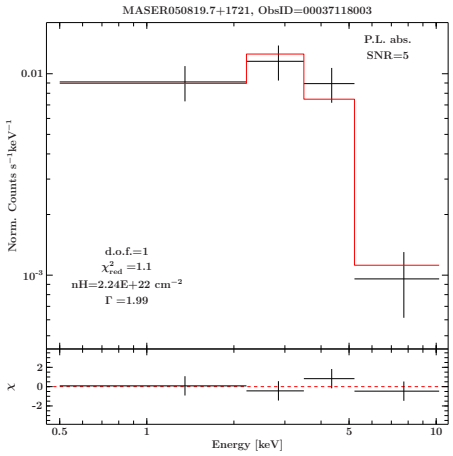

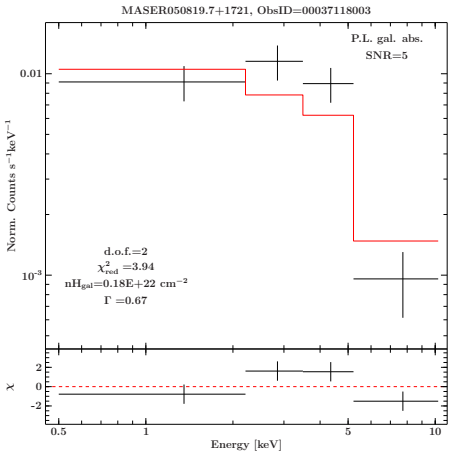

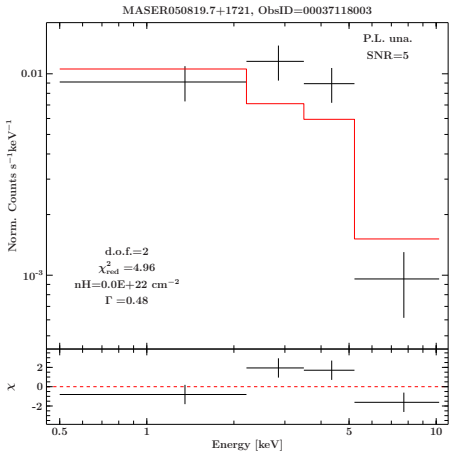

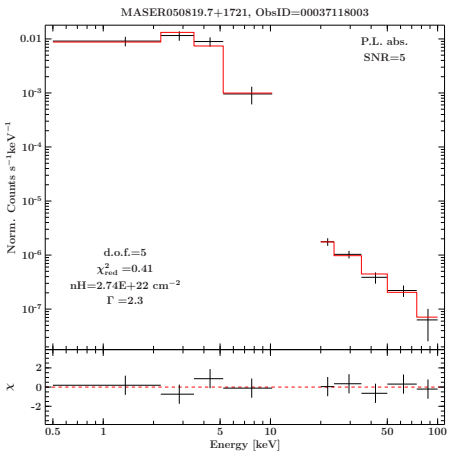

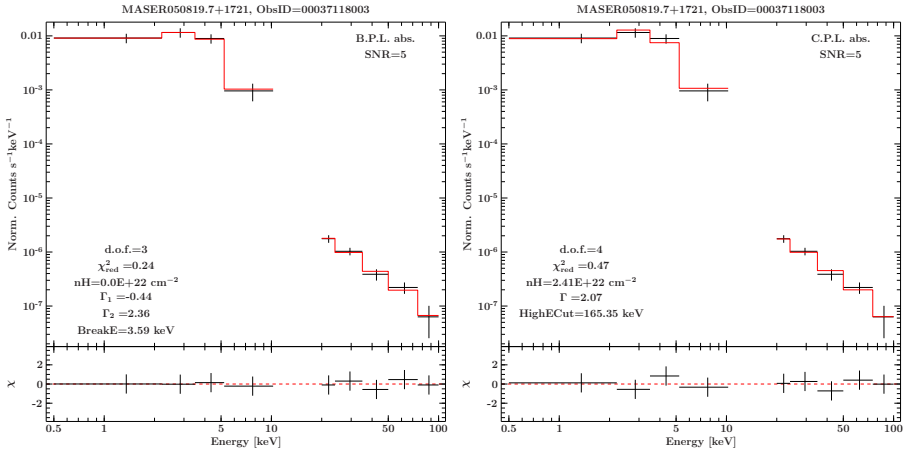
MASER050819.7+1721, ObsID=00037118003
B.P.L. abs.
SNR=5
d.o.f.=3
χ^2_{red} =0.24
nH=0.0E+22 cm^{-2}
Γ_1 =-0.44
Γ_2 =2.36
BreakE=3.59 keV
Norm. Counts s^{-1}keV^{-1}
χ
Energy [keV]
MASER050819.7+1721, ObsID=00037118003
C.P.L. abs.
SNR=5
d.o.f.=4
χ^2_{red} =0.47
nH=2.41E+22 cm^{-2}
Γ =2.07
HighECut=165.35 keV
Norm. Counts s^{-1}keV^{-1}
χ
Energy [keV]

ObsID 00037118004

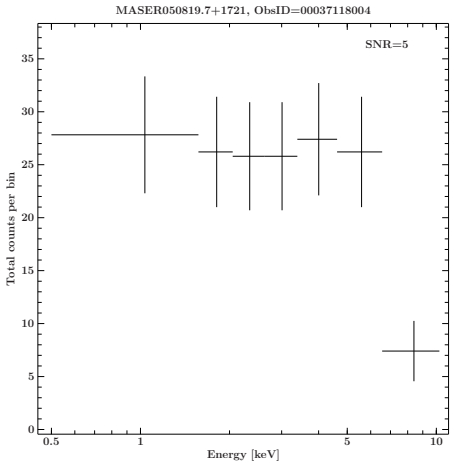

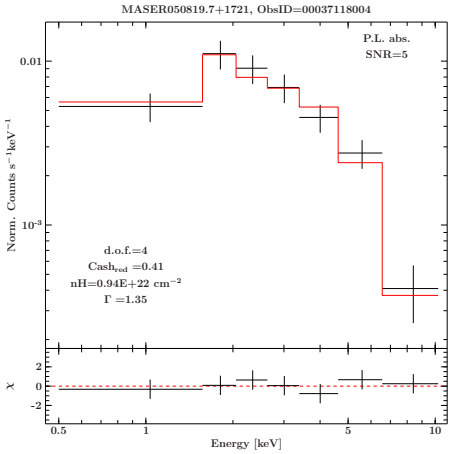

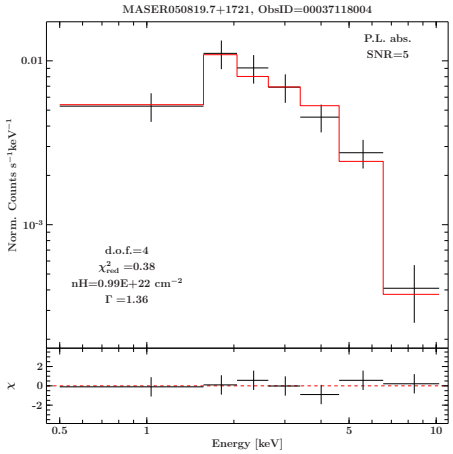

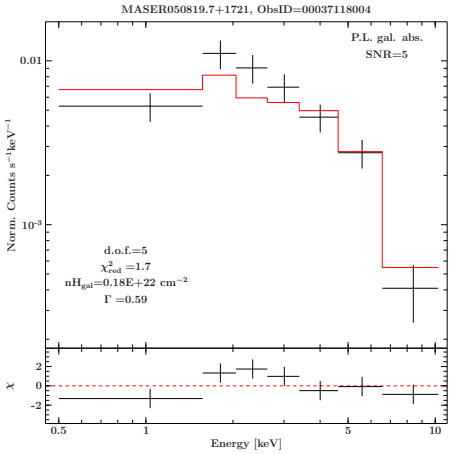

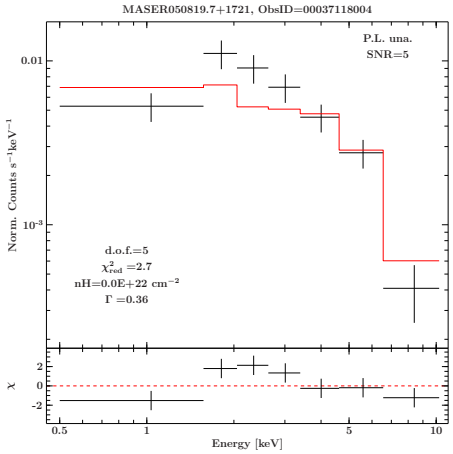

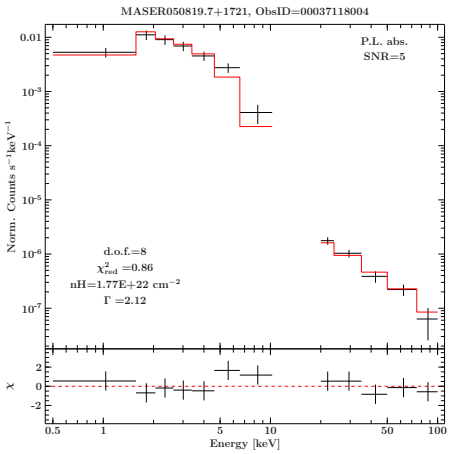

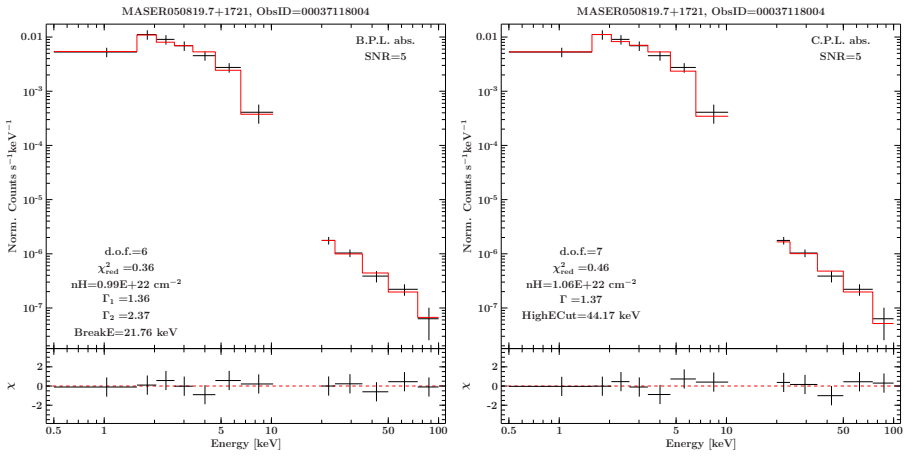
MASER050819.7+1721, ObsID=00037118004
B.P.L. abs.
SNR=5
d.o.f.=6
χ^2_{red} =0.36
nH=0.99E+22 cm^{-2}
Γ_1 =1.36
Γ_2 =2.37
BreakE=21.76 keV
Norm. Counts s^{-1}keV^{-1}
χ
Energy [keV]
MASER050819.7+1721, ObsID=00037118004
C.P.L. abs.
SNR=5
d.o.f.=7
χ^2_{red} =0.46
nH=1.06E+22 cm^{-2}
Γ =1.37
HighECut=44.17 keV
Norm. Counts s^{-1}keV^{-1}
χ
Energy [keV]

Summarized PHAs of ObsIDs 00037118001 to 00037118004

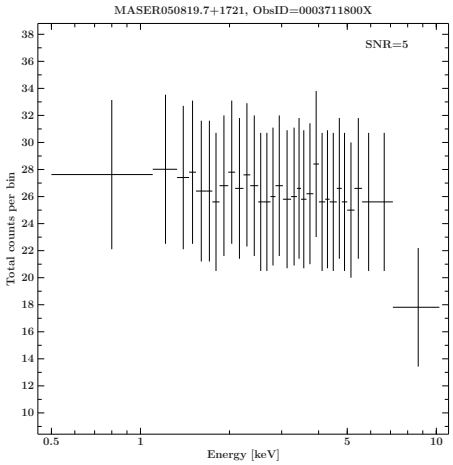

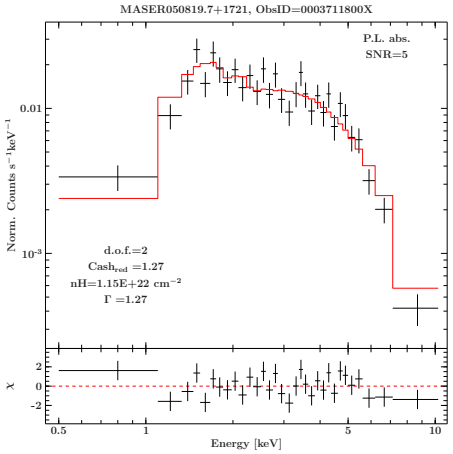

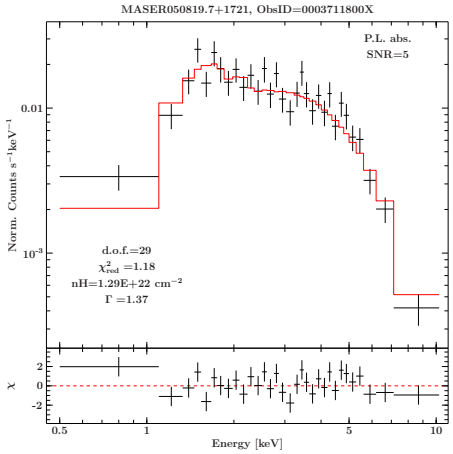

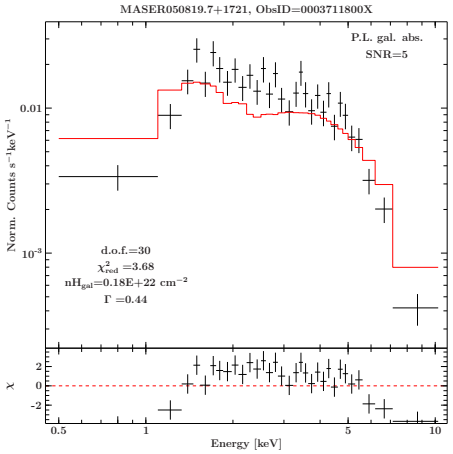

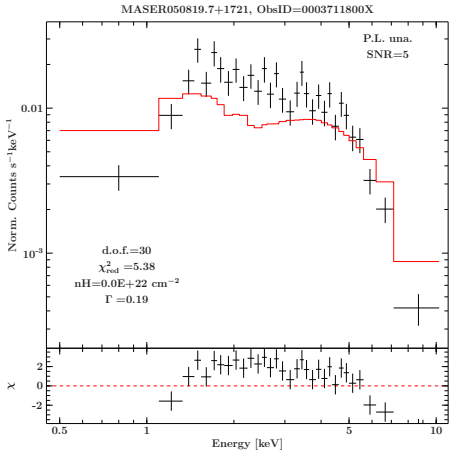

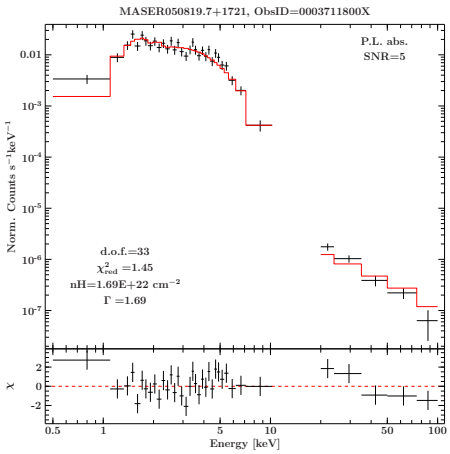

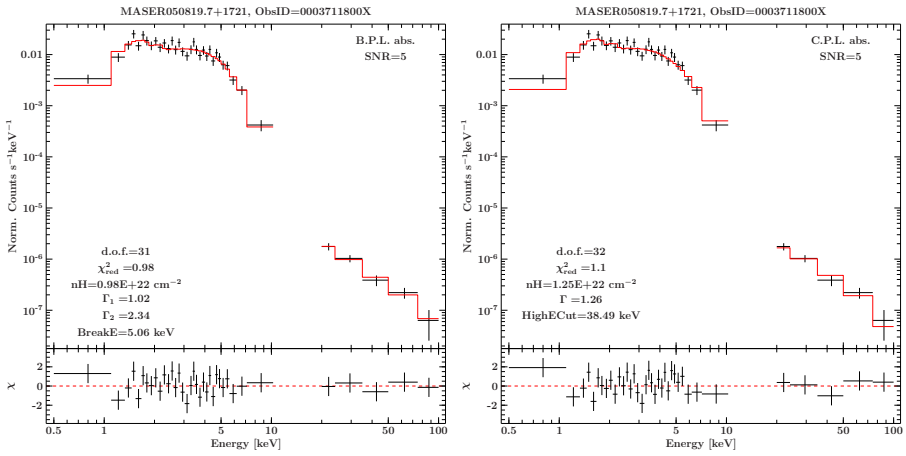
MASER050819.7+1721, ObsID=0003711800X
B.P.L. abs.
SNR=5
d.o.f.=31
χ^2_{red} =0.98
nH=0.98E+22 cm^{-2}
Γ_1 =1.02
Γ_2 =2.34
BreakE=5.06 keV
Norm. Counts s^{-1}keV^{-1}
Energy [keV]
MASER050819.7+1721, ObsID=0003711800X
C.P.L. abs.
SNR=5
d.o.f.=32
χ^2_{red} =1.1
nH=1.25E+22 cm^{-2}
Γ =1.26
HighECut=38.49 keV
Norm. Counts s^{-1}keV^{-1}
Energy [keV]

REFERENCES

Balzano, V. A. (1983). Star-burst galactic nuclei. *Astrophysical Journal*, 268:602–627.

Boggs, S., Bregman, J., Carlstrom, J., Daou, D., Donahue, M., Gies, D., Lockman, F., McCammon, D., Pipher, J., Pollacco, D., Ridgway, S., and Stern, R. (2012). "2012 senior review of operating missions in the nasa astrophysics division. Technical report, NASA.

Braatz, J. (online 28.05.2012). `https://safe.nrao.edu/wiki/bin/view/Main/PrivateWaterMaserList`.

Braatz, J. A., Reid, M. J., Humphreys, E. M. L., Henkel, C., Condon, J. J., and Lo, K. Y. (2010). The Megamaser Cosmology Project. II. The Angular-diameter Distance to UGC 3789. *ApJ*, 718:657–665.

Cash, W. (1979). Parameter estimation in astronomy through application of the likelihood ratio. *ApJ*, 228:939–947.

Castangia, P., Tilak, A., Kadler, M., Henkel, C., Greenhill, L., and Tueller, J. (2010). X-ray vs. H_2O maser emission in AGN. *X-ray Astronomy 2009; Present Status, Multi-Wavelength Approach and Future Perspectives*, 1248:347–350.

Claussen, M. J., Diamond, P. J., Braatz, J. A., et al. (1998). *ApJ*, 500:L129.

Contini, T., Considere, S., and Davoust, E. (1998). Starbursts in barred spiral galaxies III. Definition of a homogeneous sample of starburst nucleus galaxies. *Astronomy and Astrophysics Supplement*, 130:285–298.

Davis, J. E. (2001). The Formal Underpinnings of the Response Functions Used in X-Ray Spectral Analysis. *ApJ*, 548:1010–1019.

Dolan, J. F. (1972). The Direct Reduction of Astronomical X-Ray Spectra. *Ap&SS*, 17:472–481.

Elitzur, M. (1982). Physical characteristics of astronomical masers. *Reviews of Modern Physics*, 54:1225–1260.

Gehrels, N. (1986). Confidence limits for small numbers of events in astrophysical data. *ApJ*, 303:336–346.

Gehrels, N., Chincarini, G., Giommi, P., Mason, K. O., Nousek, J. A., Wells, A. A., White, N. E., Barthelmy, S. D., Burrows, D. N., Cominsky, L. R., Hurley,

K. C., Marshall, F. E., Mészáros, P., Roming, P. W. A., Angelini, L., Barbier, L. M., Belloni, T., Campana, S., Caraveo, P. A., Chester, M. M., Citterio, O., Cline, T. L., Cropper, M. S., Cummings, J. R., Dean, A. J., Feigelson, E. D., Fenimore, E. E., Frail, D. A., Fruchter, A. S., Garmire, G. P., Gendreau, K., Ghisellini, G., Greiner, J., Hill, J. E., Hunsberger, S. D., Krimm, H. A., Kulkarni, S. R., Kumar, P., Lebrun, F., Lloyd-Ronning, N. M., Markwardt, C. B., Mattson, B. J., Mushotzky, R. F., Norris, J. P., Osborne, J., Paczynski, B., Palmer, D. M., Park, H.-S., Parsons, A. M., Paul, J., Rees, M. J., Reynolds, C. S., Rhoads, J. E., Sasseen, T. P., Schaefer, B. E., Short, A. T., Smale, A. P., Smith, I. A., Stella, L., Tagliaferri, G., Takahashi, T., Tashiro, M., Townsley, L. K., Tueller, J., Turner, M. J. L., Vietri, M., Voges, W., Ward, M. J., Willingale, R., Zerbi, F. M., and Zhang, W. W. (2004). The Swift Gamma-Ray Burst Mission. *ApJ*, 611:1005–1020.

Gillessen, S. and Harney, H. L. (2005). Significance in gamma-ray astronomy - the Li & Ma problem in Bayesian statistics. *A&A*, 430:355–362.

Godet, O., Beardmore, A. P., Abbey, A. F., Osborne, J. P., Page, K. L., Tyler, L., Burrows, D. N., Evans, P., Starling, R., Wells, A. A., Angelini, L., Campana, S., Chincarini, G., Citterio, O., Cusamano, G., Giommi, P., Hill, J. E., Kennea, J., LaParola, V., Mangano, V., Mineo, T., Moretti, A., Nousek, J. A., Pagani, C., Perri, M., Capalbi, M., Romano, P., Tagliaferri, G., and Tamburelli, F. (2007). The in-flight spectroscopic performance of the Swift XRT CCD camera during 2006-2007. In *Society of Photo-Optical Instrumentation Engineers (SPIE) Conference Series*, volume 6686 of *Society of Photo-Optical Instrumentation Engineers (SPIE) Conference Series*.

Gordon, J. P., Zeiger, H. J., and Townes, C. H. (1954). Molecular Microwave Oscillator and New Hyperfine Structure in the Microwave Spectrum of NH_3. *Physical Review*, 95:282–284.

Greenhill, L. J. (2007). Masers in AGN environments. In Chapman, J. M. and Baan, W. A., editors, *IAU Symposium*, volume 242 of *IAU Symposium*, pages 381–390.

Greenhill, L. J., Henkel, C., Becker, R., Wilson, T. L., and Wouterloot, J. G. A. (1995). Centripetal acceleration within the subparsec nuclear maser disk of NGC4258. *A&A*, 304:21.

Greenhill, L. J., Tilak, A., and Madejski, G. (2008). Prevalence of High X-Ray Obscuring Columns among AGNs that Host H_2O Masers. *ApJ*, 686:L13–L16.

Hanke, M. (2007). High-resolution X-ray Spectroscopy of the Black Hole Cygnus X-1 with the Chandra X-ray Observatory. Diploma Thesis, Dr. Karl Remeis-Sternwarte Bamberg.

Herrnstein, J. R., Moran, J. M., Greenhill, L. J., Diamond, P. J., Inoue, M., Nakai, N., Miyoshi, M., Henkel, C., and Riess, A. (1999). A 4 % geometric distance to the galaxy NGC4258 from orbital motions in a nuclear gas disk. *Nature*, 400:539–541.

Houck, J. C. (2012). ISIS 1.0 Technical Manual. `http://space.mit.edu/cxc/isis/manual.html`.

Jahoda, K., Swank, J. H., Giles, A. B., Stark, M. J., Strohmayer, T., Zhang, W., and Morgan, E. H. (1996). In-orbit performance and calibration of the Rossi X-ray Timing Explorer (RXTE) Proportional Counter Array (PCA). In Siegmund, O. H. and Gummin, M. A., editors, *Society of Photo-Optical Instrumentation Engineers (SPIE) Conference Series*, volume 2808 of *Society of Photo-Optical Instrumentation Engineers (SPIE) Conference Series*, pages 59–70.

Jansen, F., Lumb, D., Altieri, B., Clavel, J., Ehle, M., Erd, C., Gabriel, C., Guainazzi, M., Gondoin, P., Much, R., Munoz, R., Santos, M., Schartel, N., Texier, D., and Vacanti, G. (2001). XMM-Newton observatory. I. The spacecraft and operations. *A&A*, 365:L1–L6.

Kadler, M. (2012). Extragalactic jets. Lecture, University of Wuerzburg.

Kandalyan, R. A. and Al-Zyout, M. M. (2010). Extragalactic H_2O maser sources and their properties. *Astrophysics*, 53:329–341.

Kompaneets, A. S. (1957). *Soviet Phys. JETP Lett*, 4:730.

Kondratko, P. T., Greenhill, L. J., and Moran, J. M. (2006). Discovery of Water Maser Emission in Five AGNs and a Possible Correlation Between Water Maser and Nuclear 2-10 keV Luminosities. *ApJ*, 652:136–145.

Krolik, J. H. (1998). *Active Galactic Nuclei: From the Central Black Hole to the Galactic Environment*. Princeton University Press.

Kuo, C. Y., Braatz, J. A., Condon, J. J., Impellizzeri, C. M. V., Lo, K. Y., Zaw, I., Schenker, M., Henkel, C., Reid, M. J., and Greene, J. E. (2011). The megamaser cosmology project. iii. accurate masses of seven supermassive black holes in active galaxies with circumnuclear megamaser disks. *The Astrophysical Journal*, 727(1):20.

Li, T.-P. and Ma, Y.-Q. (1983). Analysis methods for results in gamma-ray astronomy. *ApJ*, 272:317–324.

Lo, K. Y. (2005). Mega-Masers and Galaxies. *ARA&A*, 43:625–676.

Madejski, G., Done, C., Życki, P. T., and Greenhill, L. (2006). X-Ray Emission from Megamaser Galaxy IC 2560. *ApJ*, 636:75–82.

Mitsuda, K., Bautz, M., Inoue, H., Kelley, R. L., Koyama, K., Kunieda, H., Makishima, K., Ogawara, Y., Petre, R., Takahashi, T., Tsunemi, H., White, N. E., Anabuki, N., Angelini, L., Arnaud, K., Awaki, H., Bamba, A., Boyce, K., Brown, G. V., Chan, K.-W., Cottam, J., Dotani, T., Doty, J., Ebisawa, K., Ezoe, Y., Fabian, A. C., Figueroa, E., Fujimoto, R., Fukazawa, Y., Furusho, T., Furuzawa, A., Gendreau, K., Griffiths, R. E., Haba, Y., Hamaguchi, K., Harrus, I., Hasinger, G., Hatsukade, I., Hayashida, K., Henry, P. J., Hiraga, J. S., Holt, S. S., Hornschemeier, A., Hughes, J. P., Hwang, U., Ishida, M., Ishisaki, Y., Isobe, N., Itoh, M., Iyomoto, N., Kahn, S. M., Kamae, T., Katagiri, H., Kataoka, J., Katayama, H., Kawai, N., Kilbourne, C., Kinugasa, K., Kissel, S., Kitamoto, S., Kohama, M., Kohmura, T., Kokubun, M., Kotani, T., Kotoku, J., Kubota, A., Madejski, G. M., Maeda, Y., Makino, F., Markowitz, A., Matsumoto, C., Matsumoto, H., Matsuoka, M., Matsushita, K., McCammon, D., Mihara, T., Misaki, K., Miyata, E., Mizuno, T., Mori, K., Mori, H., Morii, M., Moseley, H., Mukai, K., Murakami, H., Murakami, T., Mushotzky, R., Nagase, F., Namiki, M., Negoro, H., Nakazawa, K., Nousek, J. A., Okajima, T., Ogasaka, Y., Ohashi, T., Oshima, T., Ota, N., Ozaki, M., Ozawa, H., Parmar, A. N., Pence, W. D., Porter, F. S., Reeves, J. N., Ricker, G. R., Sakurai, I., Sanders, W. T., Senda, A., Serlemitsos, P., Shibata, R., Soong, Y., Smith, R., Suzuki, M., Szymkowiak, A. E., Takahashi, H., Tamagawa, T., Tamura, K., Tamura, T., Tanaka, Y., Tashiro, M., Tawara, Y., Terada, Y., Terashima, Y., Tomida, H., Torii, K., Tsuboi, Y., Tsujimoto, M., Tsuru, T. G., Turner, M. J. L. ., Ueda, Y., Ueno, S., Ueno, M., Uno, S., Urata, Y., Watanabe, S., Yamamoto, N., Yamaoka, K., Yamasaki, N. Y., Yamashita, K., Yamauchi, M., Yamauchi, S., Yaqoob, T., Yonetoku, D., and Yoshida, A. (2007). The X-Ray Observatory Suzaku. *PASJ*, 59:1–7.

Miyoshi, M., Moran, J., Herrnstein, J., Greenhill, L., Nakai, N., Diamond, P., and Inoue, M. (1995). Evidence for a black hole from high rotation velocities in a sub-parsec region of NGC4258. *Nature*, 373:127–129.

Molendi, S. and Maccacaro, T. (1994). The variable soft X-ray excess of MKN 766. *A&A*, 291:420–424.

Neufeld, D. A., Maloney, P. R., and Conger, S. (1994). Water maser emission from X-ray-heated circumnuclear gas in active galaxies. *ApJ*, 436:L127.

Nowak, M. A. (2009). X-ray spectroscopy: in theory and practice. Lecture, Dr. Karl Remeis-Sternwarte Bamberg.

Osterbrock, D. E. (2005). *Astrophysics of Gaseous Nebulae and Active Galactic Nuclei*. Palgrave Macmillan.

Peck, A. B., Henkel, C., Ulvestad, J. S., Brunthaler, A., Falcke, H., Elitzur, M., Menten, K. M., and Gallimore, J. F. (2003). The Flaring H_2O Megamaser and Compact Radio Source in Markarian 348. *ApJ*, 590:149–161.

Peterson, B. M. (1997). *An Introduction to Active Galactic Nuclei*. Cambridge University Press.

Predehl, P., Andritschke, R., Böhringer, H., Bornemann, W., Bräuninger, H., Brunner, H., Brusa, M., Burkert, W., Burwitz, V., Cappelluti, N., Churazov, E., Dennerl, K., Eder, J., Elbs, J., Freyberg, M., Friedrich, P., Fürmetz, M., Gaida, R., Hälker, O., Hartner, G., Hasinger, G., Hermann, S., Huber, H., Kendziorra, E., von Kienlin, A., Kink, W., Kreykenbohm, I., Lamer, G., Lapchov, I., Lehmann, K., Meidinger, N., Mican, B., Mohr, J., Mühlegger, M., Müller, S., Nandra, K., Pavlinsky, M., Pfeffermann, E., Reiprich, T., Robrade, J., Rohé, C., Santangelo, A., Schächner, G., Schanz, T., Schmid, C., Schmitt, J., Schreib, R., Schrey, F., Schwope, A., Steinmetz, M., Strüder, L., Sunyaev, R., Tenzer, C., Tiedemann, L., Vongehr, M., and Wilms, J. (2010). eROSITA on SRG. In *Society of Photo-Optical Instrumentation Engineers (SPIE) Conference Series*, volume 7732 of *Society of Photo-Optical Instrumentation Engineers (SPIE) Conference Series*.

Reid, M. J., Braatz, J. A., Condon, J. J., Greenhill, L. J., Henkel, C., and Lo, K. Y. (2009). The Megamaser Cosmology Project. I. Very Long Baseline Interferometric Observations of UGC 3789. *ApJ*, 695:287–291.

Riess, A. G., Macri, L., Casertano, S., Lampeitl, H., Ferguson, H. C., Filippenko, A. V., Jha, S. W., Li, W., and Chornock, R. (2011). A 3% Solution: Determination of the Hubble Constant with the Hubble Space Telescope and Wide Field Camera 3. *ApJ*, 730:119.

Sawada-Satoh, S., Kameno, S., Nakamura, K., Namikawa, D., Shibata, K. M., and Inoue, M. (2008). Positional Coincidence of H_2O Maser and a Plasma-Obscuring Torus in Radio Galaxy NGC 1052. *ApJ*, 680:191–199.

Schmahl, E. (2005). The Cash Statistic and Forward Fitting. `hesperia.gsfc.nasa.gov/~schmahl/cash/cash_oddities.html`.

Tarchi, A. (2012). AGN and Megamasers. *ArXiv e-prints*.

Titarchuk, L. (1994). Generalized Comptonization models and application to the recent high-energy observations. *ApJ*, 434:570–586.

Titarchuk, L. and Lyubarskij, Y. (1995). Power-Law Spectra as a Result of Comptonization of the Soft Radiation in a Plasma Cloud. *ApJ*, 450:876.

Urry, C. M. and Padovani, P. (1995). Unified Schemes for Radio-Loud Active Galactic Nuclei. *PASP*, 107:803.

Véron-Cetty, M.-P. and Véron, P. (2006). A catalogue of quasars and active nuclei: 12th edition. *Astronomy and Astrophysics*, 455:773–777.

Wardle, M. and Yusef-Zadeh, F. (2012). The Origin of Keplerian Megamaser Disks. *ArXiv e-prints*.

Weigert, A., Wendker, H. J., and Wisotzki, L. (2009). *Astronomie und Astrophysik: Ein Grundkurs*. Wiley VCH.

Weinreb, S., Barrett, A. H., Meeks, M. L., and Henry, J. C. (1963). Radio Observations of OH in the Interstellar Medium. *Nature*, 200:829–831.

Weisskopf, M. C., Tananbaum, H. D., Van Speybroeck, L. P., and O'Dell, S. L. (2000). Chandra X-ray Observatory (CXO): overview. In Truemper, J. E. and Aschenbach, B., editors, *Society of Photo-Optical Instrumentation Engineers (SPIE) Conference Series*, volume 4012 of *Society of Photo-Optical Instrumentation Engineers (SPIE) Conference Series*, pages 2–16.

Wilms, J. (2010). Active Galactic Nuclei. Lecture, Dr. Karl Remeis-Sternwarte Bamberg.

Zhang, J. S., Henkel, C., Guo, Q., Wang, H. G., and Fan, J. H. (2010). On The Nuclear Obscuration of H_2O Maser Galaxies. *ApJ*, 708:1528–1536.

Zhang, J. S., Henkel, C., Guo, Q., and Wang, J. (2012). Radio properties of H_2O maser host galaxies. *A&A*, 538:A152.

Zhang, J. S., Henkel, C., Kadler, M., Greenhill, L. J., Nagar, N., Wilson, A. S., and Braatz, J. A. (2006). Extragalactic H2O masers and X-ray absorbing column densities. *A&A*, 450:933–944.